Improving the Nuclear Tracer Imaging Centrifuge Method for Measuring In-Situ Capillary Pressures and Comparisons with Other Methods

by

Pål Ove Sukka

A dissertation submitted to the Department of Physics and Technology, University of Bergen to obtain the Candidatus Scientarium Degree, December 16th 2004

Summary

This thesis is a part of the study of oil recovery mechanisms in chalk reservoirs, performed by the Reservoir Physics Group at the Department of Physics and Technology, University of Bergen.

The capillary pressure scanning curves are of great importance in any oil recovery process, in order to evaluate the endpoint saturations for the various fluid displacements involved, to obtain fluid displacement characteristics, determining potentials for enhanced oil production and to get input information to reservoir simulations to predict the oil production. In addition, the primary drainage P_c-curve gives valuable information on the microscopic fluid distribution in the reservoir transition zone. The relationship between saturations and pressure differentials (i.e. capillary pressure) determines and describes the displacement efficiency under various oil production scenarios.

The main objective of this work has been to improve the Nuclear Tracer Imaging Centrifuge (NTIC) Method, developed at the Department of Physics and Technology, University of Bergen. This NTIC Method is capable of measuring in-situ capillary pressures at reservoir conditions with respect to pressure and temperature. The apparatus consists of a centrifuge with swinging buckets and an imaging system using nuclear tracers to measure local in-situ saturations while the cores are spinning in the centrifuge.

There are several advantages of the NTI Centrifuge Method compared to the existing methods: Crude oil may be used, even at reservoir conditions, capillary end effects are directly measurable and measurements are performed while the centrifuge is spinning, hence there is no need to remove the core plugs in order to obtain in-situ saturation information. This last item implies that there are in principle no restrictions in the selection of oil to be used. Most importantly, however; no assumptions are needed to calculate the capillary pressure curves, since the saturations are directly measured at specific locations with given capillary pressures.

In this thesis, the NTIC Method is described and the measuring capability and the reproducibility of the technique are demonstrated. The NTIC-system has been modified by improving the experimental set-up and gating the detector; hence the background radiation has been minimized and the primary drainage capillary pressure curve has been obtained.

Previously obtained results have indicated a need for an improved method for measuring capillary pressure in reservoir rocks. Emphasis in the early part of the project was therefore to compare the measurements achieved by use of the improved NTI Centrifuge Method to results obtained by existing methods; the Direct Measurement of Saturation (DMS) method with magnetic resonance imaging and the conventional centrifuge method; the industry standard method. Results obtained by using the conventional centrifuge method corroborated the results obtained by using the NTIC Method. A summary and comparison of other existing techniques are included.

Recently, the impacts on the capillary pressure functions at various wettability conditions have been emphasized. Hence, the wettability on some of the core plugs have been altered by using Ekofisk crude oil, to less water-wet conditions, in order to investigate the impacts from wettability on the capillary pressure measurements. Capillary pressure curves obtained by using the DMS method demonstrated consistent trends when moving towards less water-wet conditions, with respect to changes in the shape of the P_c-curves and shift in end point saturations for spontaneous imbibition. Hysteresis effects were clearly observed from the secondary drainage and imbibition data.

Experiments have been performed both at the University of Bergen, and at ConocoPhillips Research Centre in Bartlesville, Oklahoma, USA.

Acknowledgements

There are many people to thank for helping me throughout my study for this Candidatus Scientiarum Degree. First of all I would like to express my gratitude to my supervisor, Professor Arne Graue, for his guidance, support, enlightening discussions and motivation.

I would like to thank Professor Kristoffer Kolltveit, Associate Professor Jan R. Lien and Professor Arne Skauge for their theoretical contributions throughout this work.

Thanks to Eirik Aspenes and Robert W. Moe for invaluable help getting started, and for their theoretical and experimental contributions.

Thanks to my fellow students for a memorable period of study and a great social set. Especially I would like to thank Else Birkeland Johannesen, Jostein Skretting, Geir Ersland and Martin Fernø for a very good and valuable cooperation.

Thanks to the employees at the Department of Physics and Technology and at the Centre for Integrated Petroleum Research (CIPR) for providing irreproachable working conditions. Especially I would like to thank Chief Engineer Kåre Njøten, and Kåre Slettebakken and Leif Egil Sandnes at the mechanical workshop.

I would like to thank Rich Treinen, Eugene Spinler, James J. Howard, Ken Farmer, Jim Stevens and Johnny Jack at ConocoPhillips Research Centre for all their contributions and for making my visits to Bartlesville memorable.

Thanks to my family and friends for their encouragement, understanding and support.

Finally, I want to express a sincere appreciation to my girlfriend Karin Nilsen Tysnes for her invaluable support and love during the long hours of total involvement with my work.

Bergen, 10th of December 2004

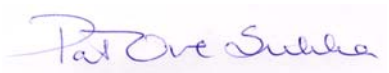

Pål Ove Sukka

Table of Contents

Introduction

In core analysis, the centrifuge has been used to determine capillary pressure curves since the original work reported by Hassler and Brunner, nearly 60 years ago [1]. Most of this work, however, has measured the amount of fluid expelled as a function of rotational speed and fit these volumes to a variety of models. Even if this method is fast compared to other existing methods, the indirect calculation of saturations may produce a saturation error of 10 % due to interpretation of the experimental data [2].

Because of the vitality of obtaining correct capillary pressure curves in order to enhance the understanding of oil recovery processes, much effort has been made to improve the capillary pressure measurements. In this study, three different ways of obtaining the capillary pressure curves have been used: The conventional centrifuge method, the Direct Measurement of Saturation (DMS) method, developed by Spinler and Baldwin [3], and finally; the improved Nuclear Tracer Imaging Centrifuge (NTIC) Method.

A total of 20 1.5”-diameter core samples have been prepared at the University of Bergen. The core material is Rørdal chalk, obtained at the Portland quarry in Ålborg, Denmark. Eight plugs from chalk material obtained in the late 1990’s and 12 core plugs from chalk material obtained in June 2003 have been used in this study. The wettability on 12 of these plugs has been altered to less water-wet conditions by a multidirectional flow of crude oil at elevated temperature, in order to investigate the impacts of wettability on the P_c-curves.

US activity:
Six plugs (4 less water-wet and 2 strongly water-wet) were shipped to the ConocoPhillips Research Centre, Bartlesville, USA, where the DMS method was used to obtain imbibition- and secondary drainage capillary pressure curves. The plan was that after finishing these measurements, the cores should be returned to the University of Bergen. Here, the conventional- and the improved NTIC Method were intended to be used for the very same plugs, both by use of decane and octadecane, in order to compare the data. Because more attention was required on other parts of the project, and because the plugs could not be returned before an elevated temperature wettability test had been obtained on-site, these comparisons were not performed.

UoB activity:
The conventional- and the improved NTIC Method were performed on some of the 14 plugs at the University of Bergen. The improvements of the NTIC-system were more time consuming than expected. Also, after two months of preparation, the centrifuge core holder receiving-cups turned out not to handle the certified maximum speed of rotation, and they broke; hence an experiment that had lasted for two months was ruined. Therefore, the available time was not sufficient to perform all the initially planned experiments, and only the primary drainage capillary pressure curve was obtained by use of the NTIC Method.

Part 1

Theory

CHAPTER 1

Parameter Definitions and Core Analysis

Reservoir physics implies fluid flow in a porous media. Therefore, as an introduction to this thesis, some of the most important parameters governing this process are discussed.

1.1 Porosity – Definition and Classification

Theoretically, any rock may act as a reservoir for oil and gas; that is, as long as it possesses two essential properties: It must have pores to contain hydrocarbons, and the pores must be connected in a way to allow the movement of fluids. In other words, the rock must have porosity and permeability.

Porosity is the first of these essential attributes of a reservoir. The pore space or voids within a reservoir may contain water, gas or oil. This parameter is conventionally symbolized by the Greek letter phi (φ), and is often expressed as a percentage:

$$Porosity\ (\%) = \frac{volume\ of\ voids}{total\ volume\ of\ rock} \times 100 \qquad (1.1.1)$$

Porosity can be classified as effective or isolated porosity. The effective porosity includes catenary and cul-de-sac (dead-end) pores, vugs and fractures, all which hydrocarbons can emerge from. Isolated pores (closed pores) are unable to yield hydrocarbons, having invaded an open pore subsequently closed by compaction or cementation [4].

Porosity is a changing parameter. Two main types can be defined according to their time of formation. Primary pores are those formed when sediments are deposited. Secondary pores are those developed in a rock after deposition, due to solution, compaction and cementation. Many minerals may leach out of a rock, but volumetrically, carbonate solution is the most significant [4]. Thus solution-induced porosity is quite common in limestone, which I've been working on in this thesis.

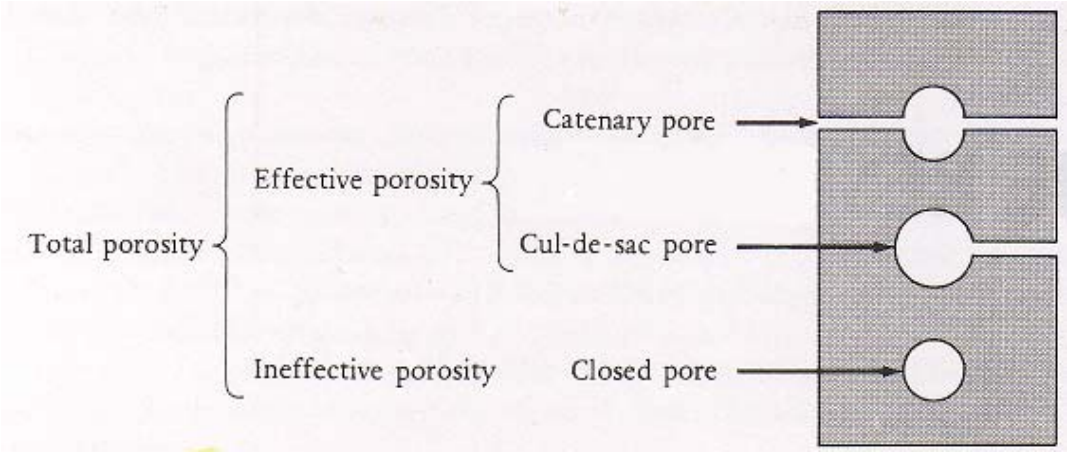

Figure 1.1.1: Different types of porosity (Selley, 1998).

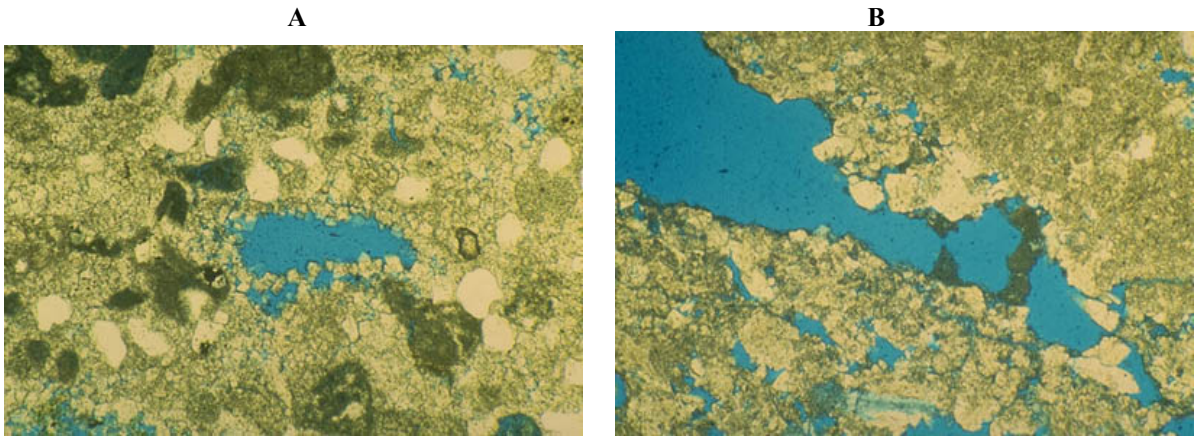

Figure 1.1.2: Pictures of vugs (A) and fractures (B); contributors to the porosity [5].

1.2 Absolute Permeability - Definition

The second essential requirement of a reservoir is permeability. This is defined as the ability of fluids to flow through a porous material [6]. As mentioned in part 1.1, the ratio of total to effective porosity is of extreme importance, being directly related to the permeability of the rock. This parameter is symbolized by K, and is found by use of Darcy's law:

$$Q = \frac{K(P_1 - P_2)A}{\mu L}, \qquad (1.2.1)$$

where Q = rate of flow [cm^3/s]
K = permeability [Darcy]
($P_1 - P_2$) = pressure drop across the sample [atm]
A = cross sectional area of flow [cm^2]
L = length of the sample [cm]
μ = viscosity of the fluid [cP]

Even if the unit of permeability is Darcy, most reservoirs have permeabilities much less than this; therefore the millidarcy (mD) is commonly used.

1.3 Relative Permeability

When more than one phase is present in a porous medium, this will affect the fluid flow. (Given the fluids are immiscible.) Each fluid will have an effective permeability equal or less the absolute permeability, because the cross-section of the fluid flow is reduced due to the presence of more than one fluid [7]. The relative permeability is defined as the ratio of the effective to the absolute permeability (i: oil / water / gas)

$$k_{ri} = \frac{K_{eff,i}}{K_{abs}}, \qquad (1.3.1)$$

where k_{ri} and $K_{eff,i}$ are the relative- and the effective permeability to fluid i, respectively, and K_{abs} is the absolute permeability.

Relative permeability is closely related to fluid saturation, as shown in Figure 1.3.1.

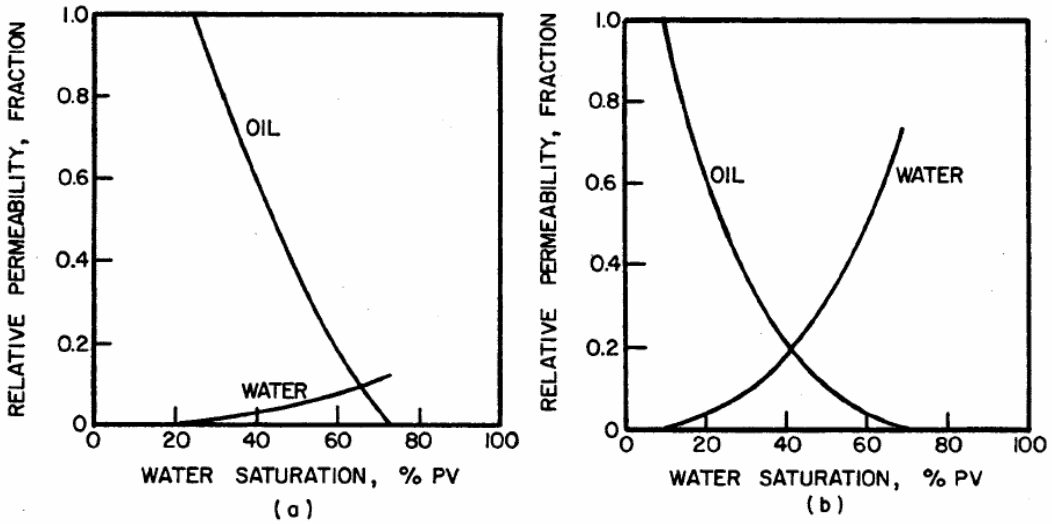

Figure 1.3.1: Examples on relative permeability curves of (a): a water-wet system, and (b): an oil-wet system (Craig, 1971).

From this figure, it is seen that at initial water saturation, S_{wi}, the relative permeability to oil is near 1, while for water it is 0. The water (if being the wetting phase) occupies the smallest pores, and creates a thin film at the rock surfaces. But since the water phase does not have a continuous path throughout the medium, the k_{rw} is 0. On the other hand, because of this film is so thin, it does not contribute to a large restriction for the oil-flow. That is why k_{ro} is close to 1. When S_{wi} is increasing (in this case; imbibition), the water film is getting thicker, and suddenly it prevent the oil (non-wetting phase) from being continuous. The non-wetting fluid (oil) is trapped in the middle of the pores; snap-off. That is why the k_{ro} – curve in the imbibition process will be steeper than is the case in a drainage process. This is called hysteresis. This hysteresis effect will not occur for the wetting phase (here: water). When the oil no longer forms a continuous path throughout the porous medium, the remaining oil will be found as droplets in the middle of the pores. We are now at residual oil saturation, S_{or}.

1.4 Wettability – Definition and Its Effects on Core Analysis

1.4.1 Definition

Wettability is defined as "the tendency of one fluid to spread on or adhere to a solid surface in the presence of other immiscible fluids" [8]. In a rock / oil / brine system, it is a measure of the preference that the rock has for either the oil or water. When the rock is *water-wet*, there is a tendency for water to occupy the small pores and to contact the majority of the rock surface.

Similarly, in an *oil-wet* system, the rock is preferentially in contact with the oil; the location of the two fluids is reversed from the water-wet case, and oil will occupy the small pores and contact the majority of the rock surface. One can further classify a system to have non-uniform wettability; either fractional or mixed wettability. In *fractional wettability*, crude oil components are strongly adsorbed in certain areas of the rock; certain areas of the rock are strongly oil-wet, while the rest is strongly water-wet. The term *mixed-wettability* indicates a certain type of fractional wettability; the larger pores are oil-wet while the smallest pores are water-wet, or vice versa [9]. It is important to note, however, that the term wettability is used for the wetting preference of the rock, and does not necessarily refer to the fluid that is in contact with the rock at any given time.

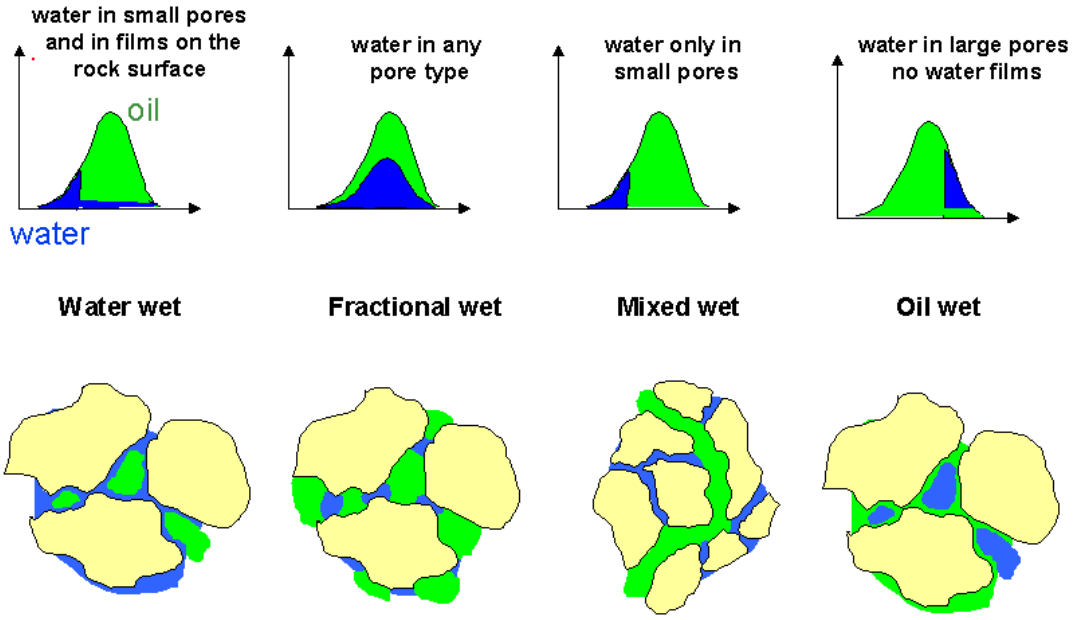

Figure 1.4.1.1: The relationship between different types of wettability and pore distribution (with permission from Norsk Hydro, SCAL-manual).

To demonstrate the wetting preference of a rock, one can allow water to imbibe into a core originally filled with refined oil. If the water displaces the oil, it is an indication that the rock prefers to be in contact with the water rather than oil. That is: the core is water-wet. Similarly, a core saturated with water is oil-wet if oil imbibes into the core and displaces water from the rock surface. If the rock to not have any strong preference for either oil or water, it is classified to be of *neutral / intermediate wettability*.

Originally, most reservoir minerals are water-wet. This can be altered by the adsorption of polar compounds and / or the deposition of organic matter that was originally in the crude oil, see Figure 1.4.1.2. Surfactants in the crude oil are generally believed to be polar compounds that contain oxygen, nitrogen and / or sulphur. These compounds are most prevalent in the heavier fractions of crude oil, such as the resins and asphaltenes. In addition, the degree to which the wettability is altered is also determined by factors as pressure, temperature, mineral surface and brine chemistry [10-15].

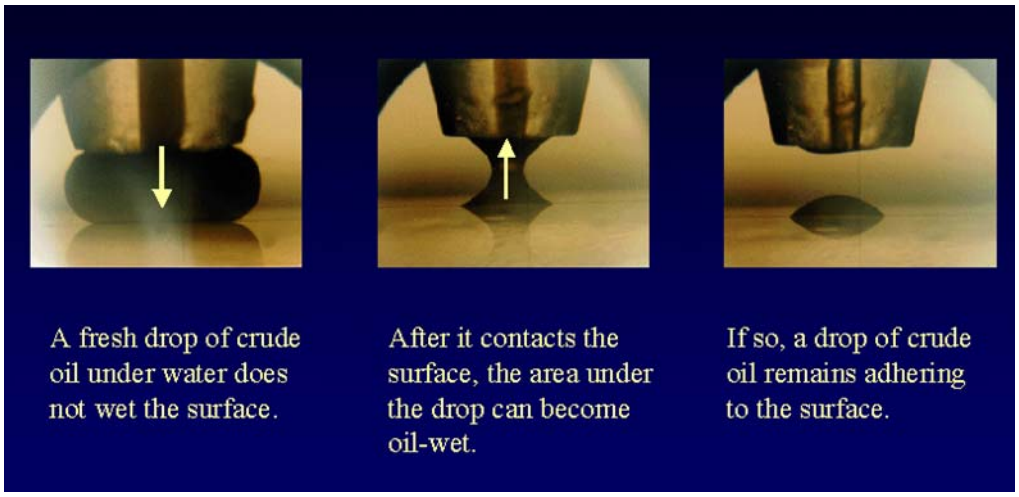

Figure 1.4.1.2: Adhesion of crude oil under brine (with permission from Norsk Hydro, SCAL-manual).

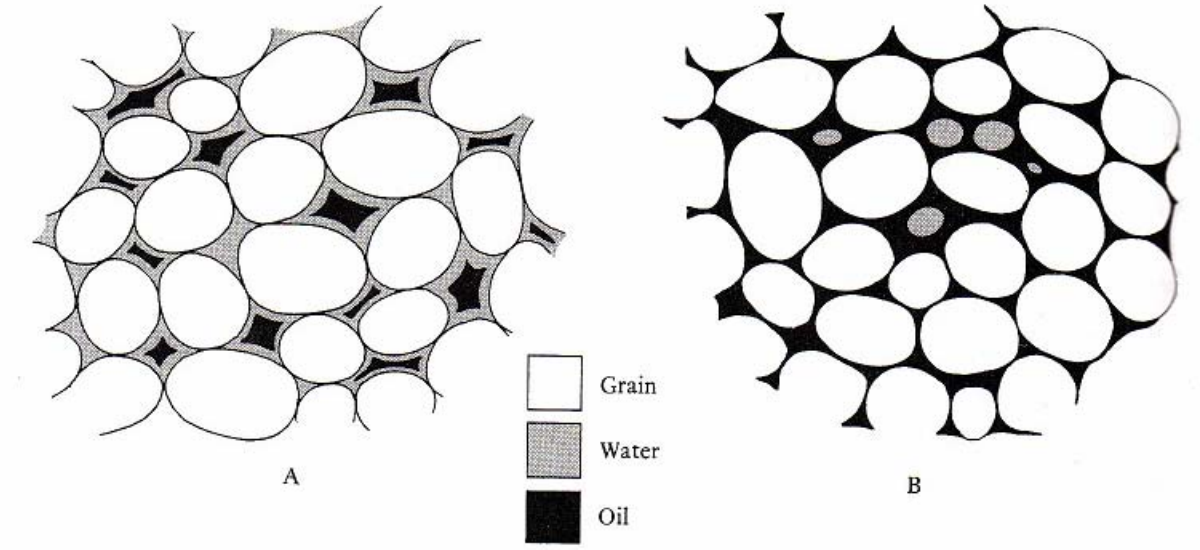

Figure 1.4.1.3: The concept of wettability in reservoirs. (A): A water-wet reservoir. (B): An oil-wet reservoir. (Selley, 1998)

The wettability of a rock / fluid system is important because it is a major factor controlling the location, flow and distribution of fluids in a reservoir. Hence the wettability of a core will affect almost all types of core analyses, including capillary pressure, relative permeability, water flood behaviour, etc.

1.4.2 Impacts on Capillary Pressure

The capillary pressure / saturation relationship is shown to depend on the interaction of wettability, pore structure and saturation history. Unfortunately, no simple relationship exists that relates the capillary pressure determined at two different wettabilities. Since a porous medium can generally not be modelled as a set of capillary tubes, an apparent contact angle calculated from either the displacement capillary pressure curve or the complete capillary pressure curve would only be a rough estimate of the actual contact angle [10]. Experiments have shown that in a **uniformly wetted porous medium** (e.g. teflon core), the drainage capillary pressure is insensitive to the wettability when the contact angle is less than 50^o, see Figure 1.4.2.1. This insensitivity is a result of e.g. the extremely rough surfaces of the porous medium, which makes the effective contact angle zero [13], see Figure 1.4.2.2.

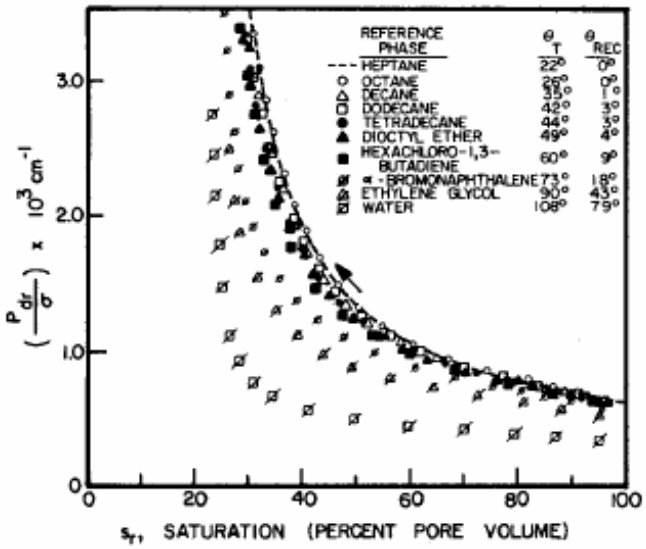

Figure 1.4.2.1: Effect of contact angle on drainage capillary pressure curves, air/liquid in teflon cores. S_T is the reference liquid saturation, θ_T is the contact angle measured on a flat surface and θ_{REC} is the receding contact angle measured with a liquid drop on a roughened teflon surface (Anderson, 1987).

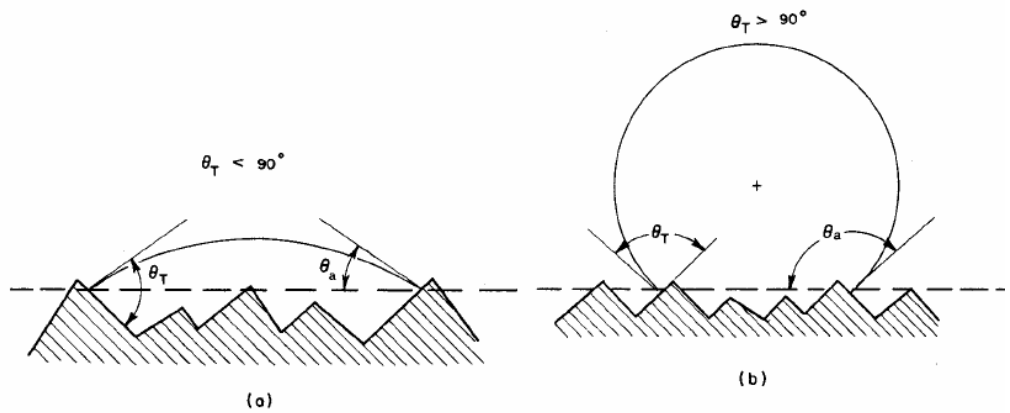

Figure 1.4.2.2: Effects of surface roughness on apparent contact angle θ_a. θ_T is the contact angle measured on a smooth surface. (a) The droplet is the wetting fluid, so $\theta_T < 90^o$. (b) The droplet is the non-wetting fluid, $\theta_T > 90^o$ (Anderson, 1987).

The positive part of the imbibition capillary pressure curve measured in a uniformly wetted core is found to be insensitive when the contact angle is less than about 20^o, for the same reasons as above.

The S_{or} is found to be affected by the wettability, and the minimum S_{or} occurs when a uniformly wetted system is slightly oil-wet to neutrally wet. This S_{or} is found after many PV's of water being flushed through the system [13].

However, in 1999, Graue et al. showed that when altering the wettability of outcrop chalk plug by aging, the spontaneous brine imbibition rate and endpoint were significantly reduced. This process, however, did not reduce the total movable oil, i.e. spontaneous imbibition plus forced displacement. In fact, the total movable oil was slightly increased with reduced water wettability, at the cost of higher differential pressure. It was found that drainage capillary pressure curves for decreasing water-wet conditions exhibited lower drainage capillary pressure, sharper curvature for the drainage curves near S_{wi} and higher S_{wi} at the less water-wet conditions. Forced imbibition showed a consistent development for the negative capillary pressure curves. At less water-wet conditions, the capillary pressure curves became flatter and the residual oil saturations exhibited a consistent trend of smaller values when moving towards less water-wet conditions [16], see Figure 1.4.2.3 and Figure 1.4.2.4. These results are most likely obtained by use of cores where the **wettability is not totally uniform.**

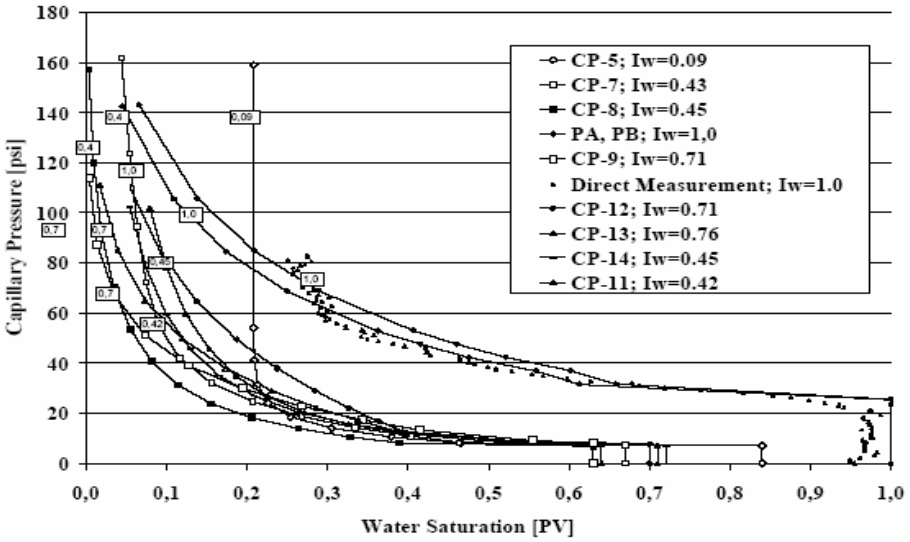

Figure 1.4.2.3: Primary and secondary drainage capillary pressure curves, obtained with Hassler Brunner saturations, the centrifuge method (Graue, 1999).

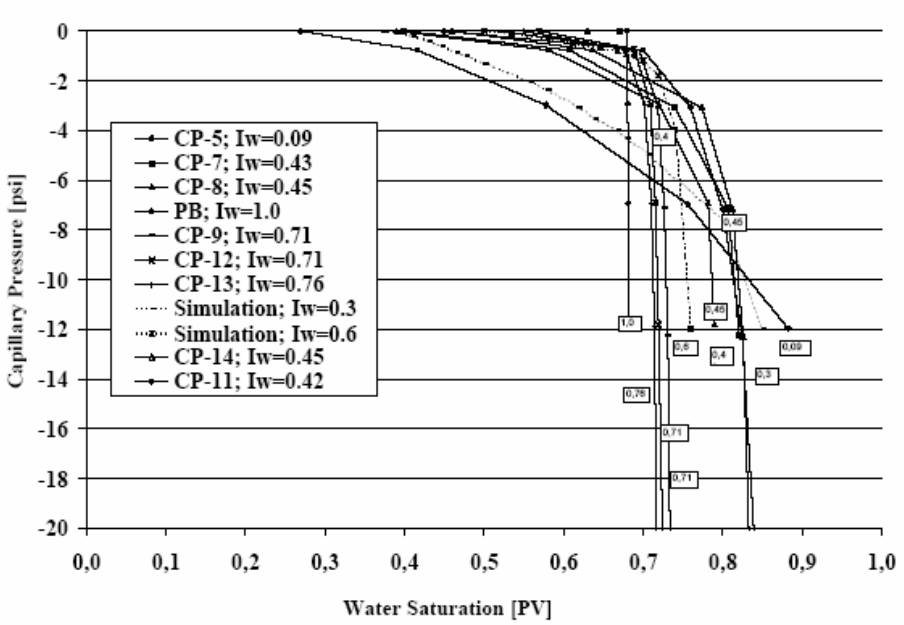

Figure 1.4.2.4: Negative capillary pressure curves, obtained by Hassler Brunner saturations, the centrifuge method (Graue, 1999).

1.5 Measurement of the Wettability

There are several methods that can be used to measure wettability. This section describes three quantitative methods in use today: Contact angle, Amott (and Amott-Harvey) method and the U.S. Bureau of Mines (USBM) method. The contact angle measures the wettability of a specific surface, while the Amott and USBM methods measure the average wettability of a core [11]. The methods are summarized for comparison in Table 1.1.

1.5.1 Contact Angle

The contact angle is the best wettability measurement when pure fluids and artificial cores are used, because there is no possibility of surfactants or other compounds altering the wettability. In this method, the contact angle, θ_c, is measured (see Figure 1.5.1.1). But since this method is limited to use on specific surfaces, and not on core material, this method can not be used in measurements in this thesis.

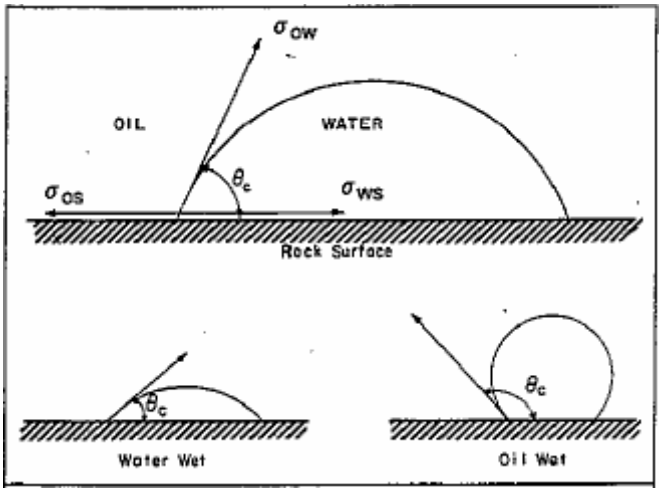

Figure 1.5.1.1: Wettability of the oil/water/rock system, (Anderson 1986).

1.5.2 Amott and Amott-Harvey Method

The Amott method combines spontaneous imbibition and forced displacement to measure the average wettability of a core. This method is based on the fact that the wetting fluid will generally imbibe spontaneously into the core, displacing the non-wetting one [17]. The test results by the Amott method is expressed by

- The ratio of the water volume displaced by spontaneous imbibition of oil, to the total water volume displaced by oil (both through spontaneous and forced imbibition); "the displacement-by-oil ratio".

$$\delta_o = \frac{V_{wsp}}{V_{wt}} \tag{1.5.2.1}$$

- The ratio of the oil volume displaced by spontaneous imbibition of water, to the total oil volume displaced by water (both through spontaneous and forced imbibition); "the displacement-by-water ratio".

$$\delta_w = \frac{V_{osp}}{V_{ot}} \tag{1.5.2.2}$$

This test may be done by use of the capillary pressure curve, as Figure 1.5.2.1 shows (For further description of his curve, see Chapter 2.1):

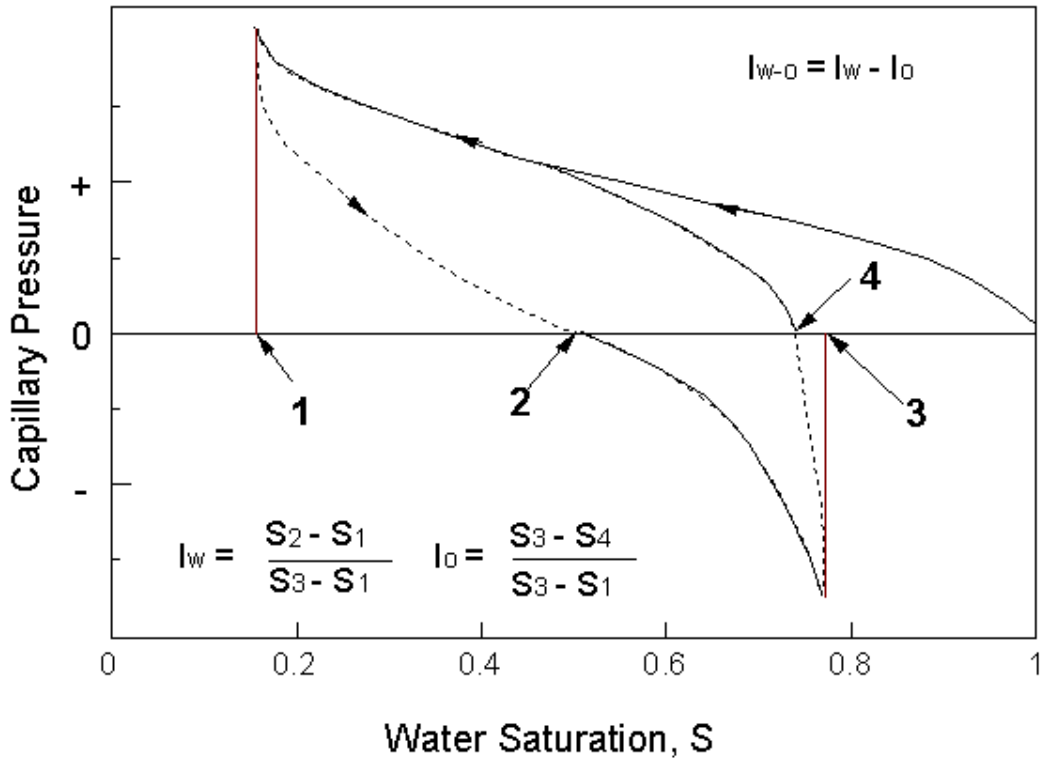

Figure 1.5.2.1: Amott method by using capillary pressure curve. (Note: here δ is replaced by I) (Skjæveland, 2000).

We often use a modification of the Amott wettability test; *The Amott-Harvey relative displacement index*, I (note: do not mix with I in Figure 1.5.2.1). This index is the displacement-by-water ratio minus the displacement-by-oil ratio:

$$I = \delta_w - \delta_o = \frac{V_{osp}}{V_{ot}} - \frac{V_{wsp}}{V_{vt}} \qquad (1.5.2.3)$$

This combination of the two ratios gives a single wettability index, where I = +1 indicates a complete water-wet system, while I = -1 indicate a complete oil-wet system. The main problem with the Amott tests and its modifications is that they are insensitive near neutral wettability.

1.5.3 USBM Method

The third qualitative method to measure the wettability is the USBM method [18]. As the Amott test, this method also measures the average wettability of the core. A major advantage over the Amott wettability test is that it is more sensitive near neutral wettability. On the other hand, a disadvantage is that this method can only be used on plug-size samples, since these must be spun in a centrifuge [18].

The USBM method uses the ratio of areas under the drainage- and the imbibition- capillary pressure curves to calculate a wettability index: (See Figure 1.5.3.1)

$$W = \log\left(\frac{A_1}{A_2}\right) \qquad (1.5.3.1)$$

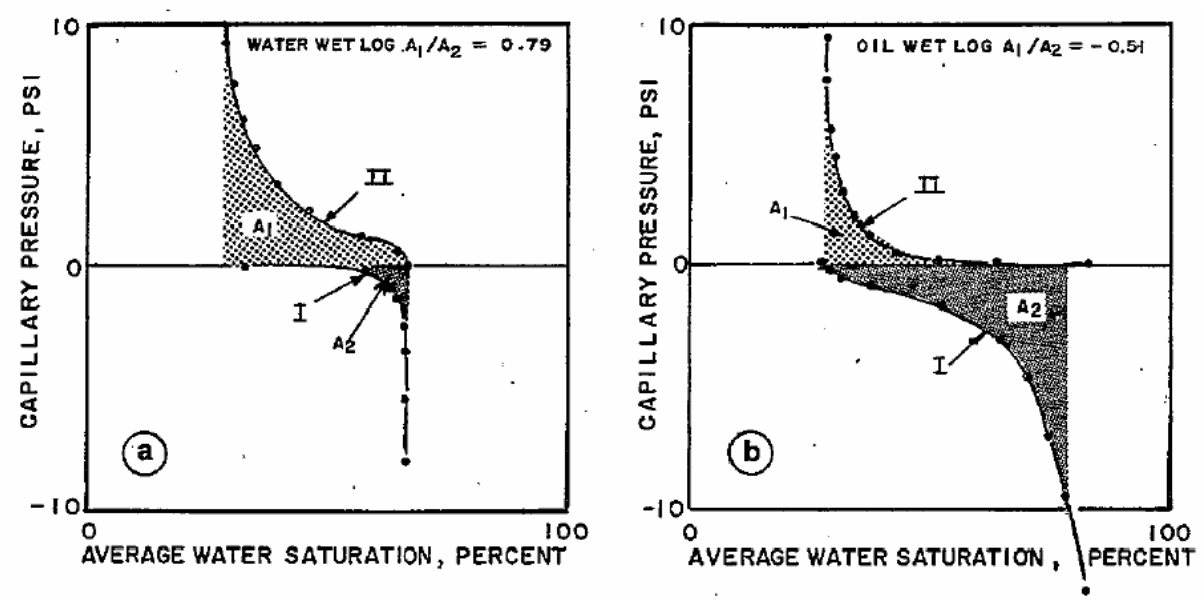

Figure 1.5.3.1: The necessary areas to calculate the wettability index by the USBM method. a: a water-wet core, and b: an oil-wet core (Anderson 1986).

As can be seen from equation (1.5.3.1); when W < 0: the core is oil-wet, and when W > 0: the core is water-wet.

In 1985, Sharma and Wunderlich developed a modification of the USBM method that allows a calculation of both the Amott and USBM wettability indices [19]. This method has some advantages over the standard USBM method: The resolution of the USBM method is improved by accounting for the saturation changes that occur at zero capillary pressure, and the Amott index is also calculated. The Amott method will sometimes indicate if a system is non-uniformly wetted [11].

To sum up: A comparison of the wettability criteria for the three methods is shown in Table 1.1:

Table 1.1: Approximate relationship between wettability, contact angle and the USBM, Amott and Amott-Harvey wettability indexes (Anderson 1986).

	Water-Wet	Neutrally Wet	Oil-Wet
Contact angle			
Minimum	0°	60 to 75°	105 to 120°
Maximum	60 to 75°	105 to 120°	180°
USBM wettability index	*W* near 1	*W* near 0	*W* near −1
Amott wettability index			
Displacement-by-water ratio	Positive	Zero	Zero
Displacement-by-oil ratio	Zero	Zero	Positive
Amott-Harvey wettability index	$0.3 \le I \le 1.0$	$-0.3 < I < 0.3$	$-1.0 \le I \le -0.3$

1.6 Diffusion, Dispersion and Adsorption

When tracers are used in miscible displacement experiments (miscible brine - brine experiments), it is important to be familiar with the concepts of adsorption, diffusion and dispersion.

Molecular **diffusion** is defined as the transport of molecules in the absence of bulk flow. When two miscible phases are brought in contact, the phases will mix, due to the random movement of the molecules in each phase. The rate of mixing due to diffusion is expressed by Fick's first and second law [20]:

- **Ficks 1. law**: The flux J of diffusing *particles* (not necessarily atoms) is proportional to the *gradient* of their *concentration*, or

$$J_i = -D \cdot \nabla c_i \tag{1.6.1}$$

The index **i** refers to the particular particle with number **i** observed; ***D*** is the diffusion coefficient of that particle and ***c*** is the concentration.

- **Ficks 2. law**: The *temporal change* in concentration at a given point is proportional to the 2^{nd} *derivative of the concentration,* or

$$\frac{\partial c}{\partial t} = div\left(D \cdot \nabla c\right) = D \cdot \Delta c \tag{1.6.2}$$

In a porous medium, the diffusion coefficient, D, has to be corrected for the formation factor, F, and the porosity, ϕ. This correction is given by

$$D' = \frac{D}{F \times \phi} \tag{1.6.3}$$

During bulk flow, convection induced mixing will contribute in addition to the molecular diffusion. This process is strongly dependent on the interstitial velocity, v. **Dispersion** is defined as this combination of molecular diffusion and mixing induced by convection, and is described by

$$\frac{\partial c}{\partial t} = D \cdot \Delta c - v \cdot \nabla c \tag{1.6.4}$$

The time and velocity dependency of this dispersion process causes the concentration front of a miscible displacement process to have a certain mixing zone. The size of this mixing zone will be affected by fractures, dead-end pores, different permeable layers, adsorption of injected tracer, etc. See Figure 1.6.1.

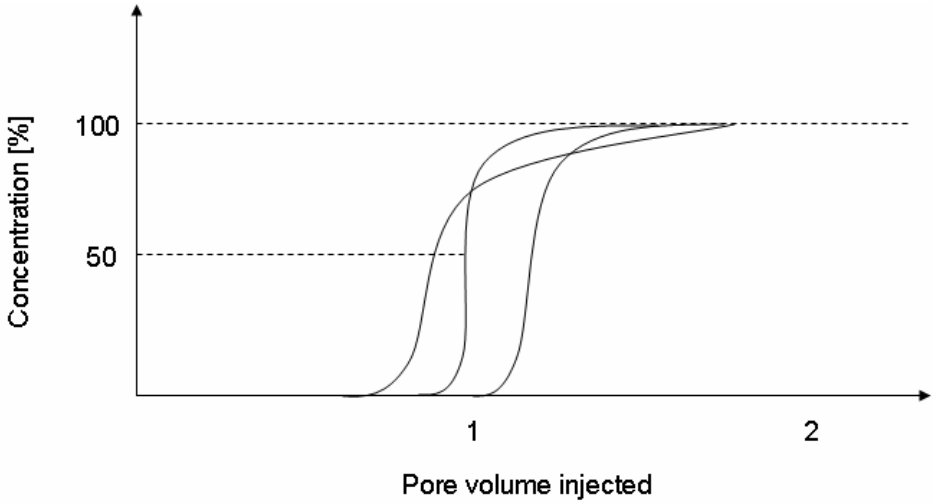

Figure 1.6.1: Examples of effluent profiles from miscible displacement

Adsorption is a process where the molecules adsorb on the solid material, and the level of adsorption depends on salinity, pH, temperature and wettability. This is a reversible process; if the concentration of the adsorbed component is reduced in the solution, there will be a desorption.

For complementary information on these phenomena, see [21].

CHAPTER 2

Capillary Pressure

Consideration of the wettability of pores leads us to the concept of capillarity.

2.1 Introduction to Capillary Pressure

Capillary pressure is an important parameter in the study of a porous medium containing two or more immiscible fluids. Together with viscous and gravitational forces, the capillary forces control the distribution as well as the flow of the immiscible phases in the porous medium. When two immiscible fluids are in contact across a curved interface, a pressure difference exists between the fluids. This so-called capillary pressure (P_c) is the combined result of interfacial tensions and curvature. The general definition of capillary pressure (see Figure 2.1.1) is described by:

$$P_c = P_{nw} - P_w \qquad (2.1.1)$$

where P_c - capillary pressure
P_{nw} - pressure in the non-wetting phase
and P_w - pressure in the wetting phase

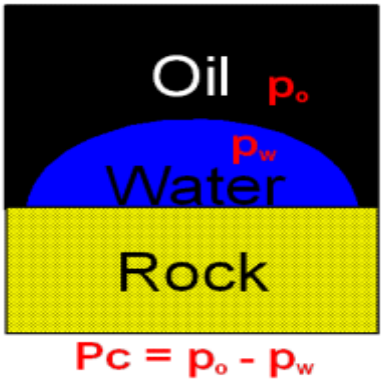

Figure 2.1.1: This figure shows the definition of capillary pressure; oil being the non-wetting phase, and water the wetting phase.

In a rock-fluid-system, the curvature and thereby P_c is dependent on the adherence preference of the fluids to the rock surface. This is why capillary pressure and wettability are inseparable.

Capillarity is the phenomenon whereby liquid is drawn up a capillary tube (see Figure 2.1.2). The capillary pressure equals the difference between the ambient pressure and the hydrostatic pressure of the water column.

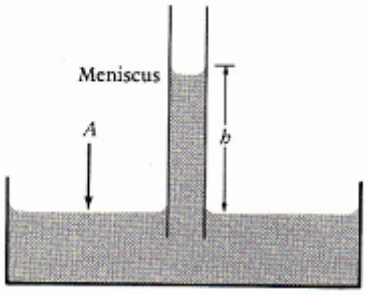

Figure 2.1.2: Capillary tube in a liquid-filled tank. The pressure on the water level (A) equals the pressure due to the hydrostatic head of water (h) minus the capillary pressure across the meniscus (Selley, 1998).

The relationship between the height of the column and P_c can be described by following equation

$$P_c = (\rho_{nw} - \rho_w)gh \qquad (2.1.2)$$

where $(\rho_{nw} - \rho_w)$ is the density difference between the two phases in contact.

The capillary pressure increases with decreasing tube diameter (see Figure 2.1.3), due to another definition of P_c:

$$P_c = \frac{2\sigma \cos\theta}{r} \qquad (2.1.3)$$

where σ – the surface tension between the two phases in contact
θ – the contact angle between the solid surface and the tangent to the interface between the two phases in contact.
r – the radius of the capillary tube.

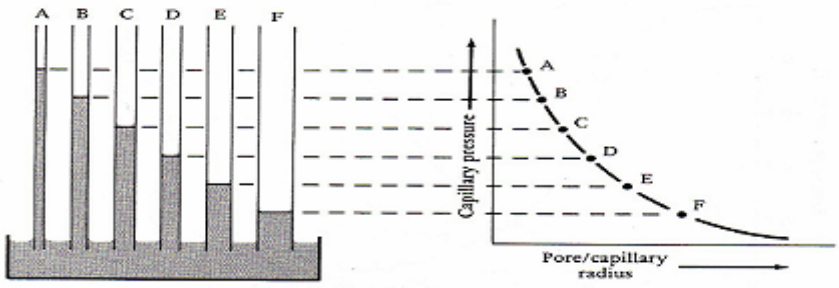

Figure 2.1.3: Capillary tubes of various diameters showing that there is a proportional relationship between the heights of the liquid column and the diameter of the tubes (Selley, 1998).

An example of a capillary pressure curve is shown in Figure 2.1.4.

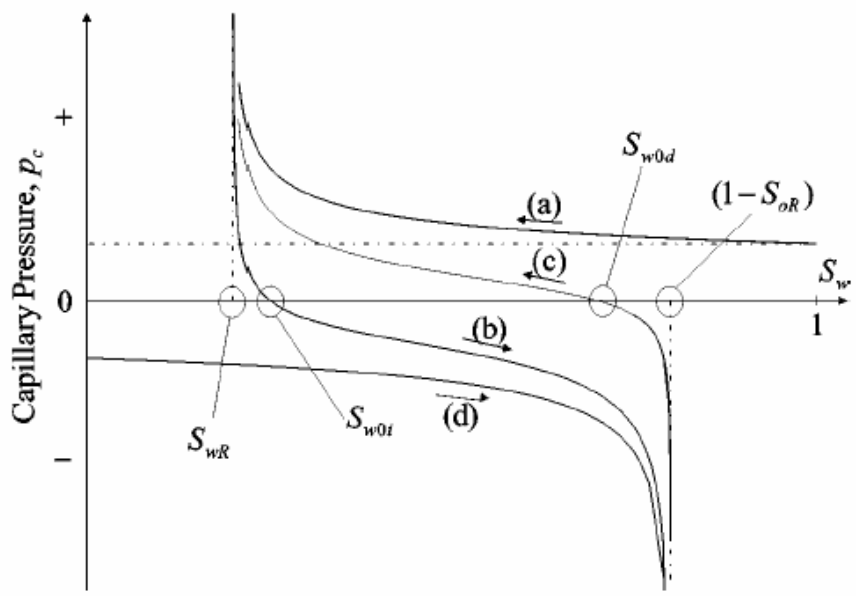

Figure 2.1.4: This figure shows the capillary pressure, P_c, as a function of the wetting phase saturation, S_w. (a): primary drainage; (b): (secondary) imbibition; (c) secondary drainage and (d) primary imbibition (Skjæveland et al., 2000).

Normally it is assumed that the initial migration of oil into the reservoir is a drainage process. Hence the original water distribution in a reservoir as a function of height is described by the primary drainage curve. For a non-wetting fluid to enter a porous medium that is 100% saturated with a wetting fluid, the pore throat has to be passed. The capillary entry pressure is defined as the pressure needed to initiate desaturation of a pore system. This threshold pressure is normally related to the primary drainage curve, or when a non-wetting fluid is forced into a pore system. The threshold pressure corresponds to the pore throats with largest radius.

As the pressure of the non-wetting phase is being increased, that is: increasing P_c [from equation (2.1.1)], smaller pores are being drained, leading to a decreasing S_w. This process continues until irreducible wetting phase saturation (S_{wi}) is approached. At this point, no further invasion by the second fluid is possible at any pressure. There is now a thin, discontinuous film at the rock surface. This primary drainage curve relates to curve (a) in figure 2.1.4.

When S_{wi} has been reached, the porous media is allowed to spontaneous imbibe the wetting fluid. The non-wetting phase is then displaced, and S_w is increasing. This corresponds to the positive part of curve (b). The spontaneous process will occur until P_c equals zero. From Figure 2.1.4, one can see that the drainage and imbibition curves are not coincident. The difference in the curves is called *hysteresis*, and is due to differences in advancing and receding contact angle (contact angle hysteresis), surface roughness and surface heterogeneity [13]. After P_c has reached 0, S_w may increase even more, by forcing the wetting phase into the porous medium. This relates to the negative part of the imbibition curve; the forced imbibition curve. This may be done until all the remaining non-wetting phase is trapped in the centre of the pores; this phase will then no longer be continuous. The saturation is now $S_w = 1 - S_{nwr}$.

By applying a pressure on the non-wetting phase, S_w may decrease and the secondary drainage curve (c) is obtained. This curve together with the imbibition curve provides valuable information with respect to wettability characteristics.

In geological terms, the capillary pressure of a reservoir increases with decreasing pore size, or more specifically, pore throat diameter. Therefore, the pore size distribution will affect the shape of the capillary pressure curve, which gives the relationship between saturation and P_c. This relationship is sketched in Figure 2.1.5.

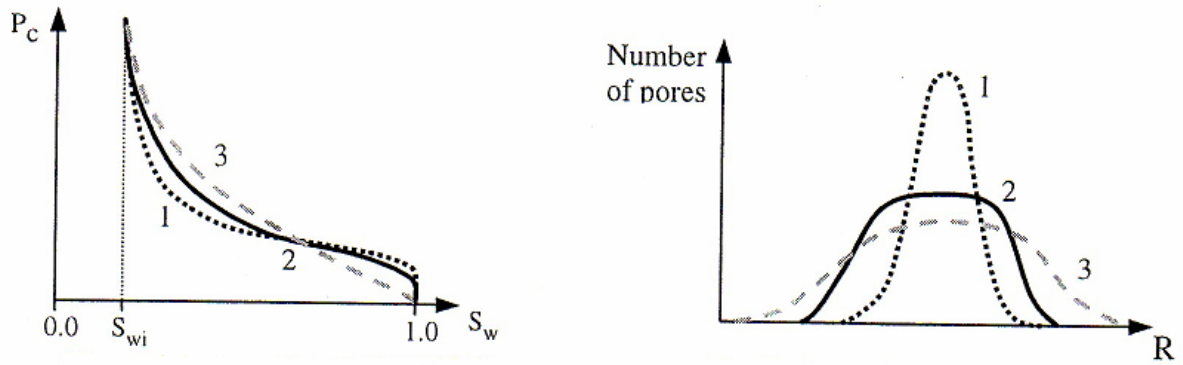

Figure 2.1.5: A general relationship between pore size distribution and capillary pressure curves (Selley, 1998).

The sorting of the deposited sediments will affect the pore size distribution. The figure above indicate that a well sorted rock sample, which gives a narrow pore size distribution (1) (uniform pore diameters), leads to a significant change in saturation in a limited P_c-interval. Once the entry pressure has been exceeded, fluid invasion increases rapidly for a minor pressure increase until S_{wi} is reached. This curve is typical for a good quality reservoir.

On the other hand, if the rock sample is poorly sorted, there will be a wide range of pore sizes (3). The result is that the wetting phase saturation declines almost uniformly with increasing pressure. This curve indicates a very poor reservoir quality [4].

Capillary pressure data is important, primarily, for determining the amount of hydrocarbons as a function of height above the water-oil contact (see Figure 2.1.6) [22].

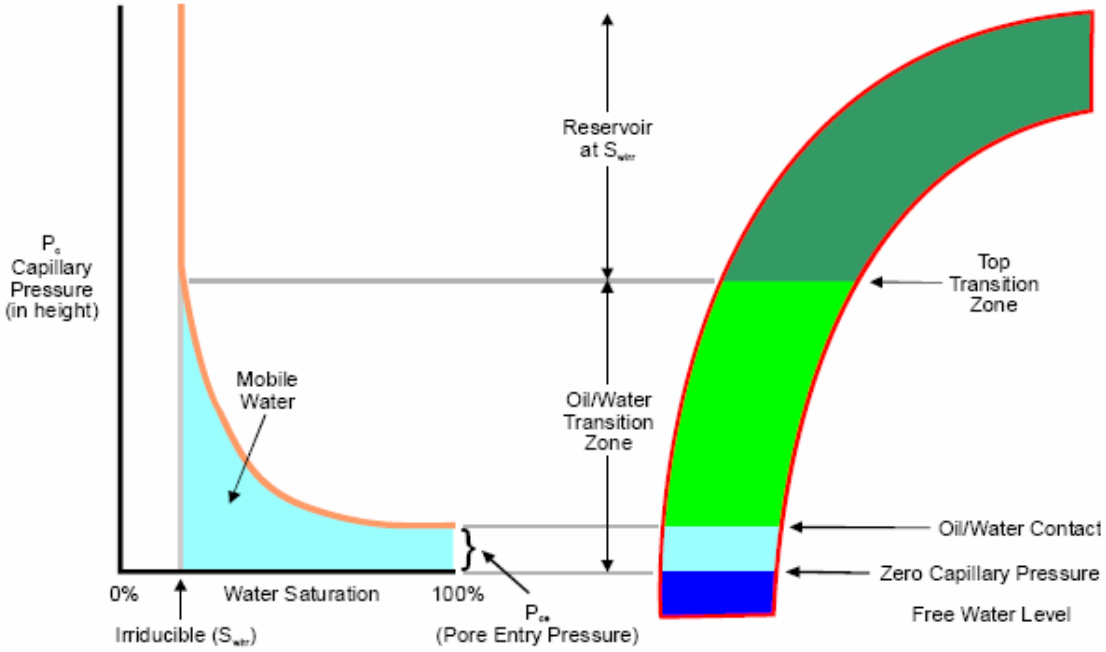

Figure 2.1.6: Relationship between the Pc curve and the different zones of a reservoir (Holmes, 2002).

It is often necessary to compare capillary pressure curves measured on different cores from the same reservoir. Because capillary pressure is affected by both permeability and porosity, it is necessary to correct for these effects before a proper comparison can be made. This is generally done with dimensionless, empirical capillary pressure function, known as the Leveretts J-function [23].

$$J(P_c) = \frac{P_c}{\sigma \times \cos\theta} \times \sqrt{\frac{k}{\phi}} \qquad (2.1.4)$$

This function can also be used to convert laboratory measured capillary pressure to reservoir capillary pressure, as long as the interfacial tension, σ, and the contact angle, θ, between the two fluids in contact are known, both in the reservoir and in the laboratory [7]. Assuming permeability and porosity are constant;

$$\frac{P_{c,res}}{P_{c,lab}} = \frac{(\sigma \times \cos\theta)_{res}}{(\sigma \times \cos\theta)_{lab}} \qquad (2.1.5)$$

2.2 Capillary Pressure Measurements

The capillary pressure curve for each specific rock/oil/water combination is an important parameter in predicting potential hydrocarbon recovery from a reservoir. Capillary pressure is one of the most important input parameters for numerical simulations and extensive efforts have been dedicated to the improvement of the experimental measurements of capillary pressure [24].

There are several methods to measure capillary pressure curves. Today, essentially five methods of measuring P_c for small core samples are in common use. These methods are

1 the semi-permeable plate method,
2 the mercury injection method,
3 the dynamic capillary-pressure method,
4 the evaporation method, and
5 the centrifuge method.

The semi-permeable plate method allows any combination of fluids, but this is a time consuming (days – weeks) and tedious method. While most methods use a single phase fluid or an oil-water system, *the mercury injection method* uses liquid mercury. Mercury intrusion provides questionable results due to the use of mercury in a vacuum to mimic water/oil behaviour, although it is a time-saving method [25]. On the other hand – this method has the advantage of determining the pore size distribution [the drainage capillary pressure curve describes the interaction between the injected mercury and the porous network in the rock. Hence a certain capillary pressure level can easily be converted to an adequate (minimum) radius of the pores entered by mercury]. The use of mercury leads to a permanent loss of the core sample, and therefore this method is not to prefer. *The dynamic method* is based on obtained data by simultaneous steady flow of oil and gas through a core sample, at a predetermined level of pressure difference of the two fluids. *The evaporation method* is seldom used.

2.2.1 The Conventional Centrifuge Method

In this thesis, *the centrifuge method* is investigated. This method more closely represents the actual reservoir because of the wettability characteristics of the oil-water system used. The concept of this method is that during centrifugation, the rotational speed generates a high g-force, which again gives a capillary pressure profile across the core (it should be noticed that in this procedure the centrifugal force is applied directly to the liquid in the rock).

Say we have a water-wet core sample. As the angular velocity of the centrifuge increases, the higher density of the water to the oil makes the water leave the sample at its outer radius as it is simultaneously replaced by the oil. At each different angular velocity, equilibrium will form. The measurements are done one data point at a time, where the average saturation of the core can be determined at the different accelerations to which it is subjected by collecting and measuring the liquid that leaves the core with the aid of a stroboscope device. From the data obtained, it is possible to determine the relation between capillary pressure and saturation of the core [1].

Similarly, imbibition capillary pressure may be measured by letting water displace oil. The displacement will then be in the opposite direction, with receiving tubes mounted at the end closest to the centre of rotation. The centrifuge technique measures produced amount of fluid at a given rotational level. It is worth noticing that this fluid volume can only be related to *mean saturation* in the plug, while the plug will have a saturation gradient due to different levels of capillary pressure along the plug.

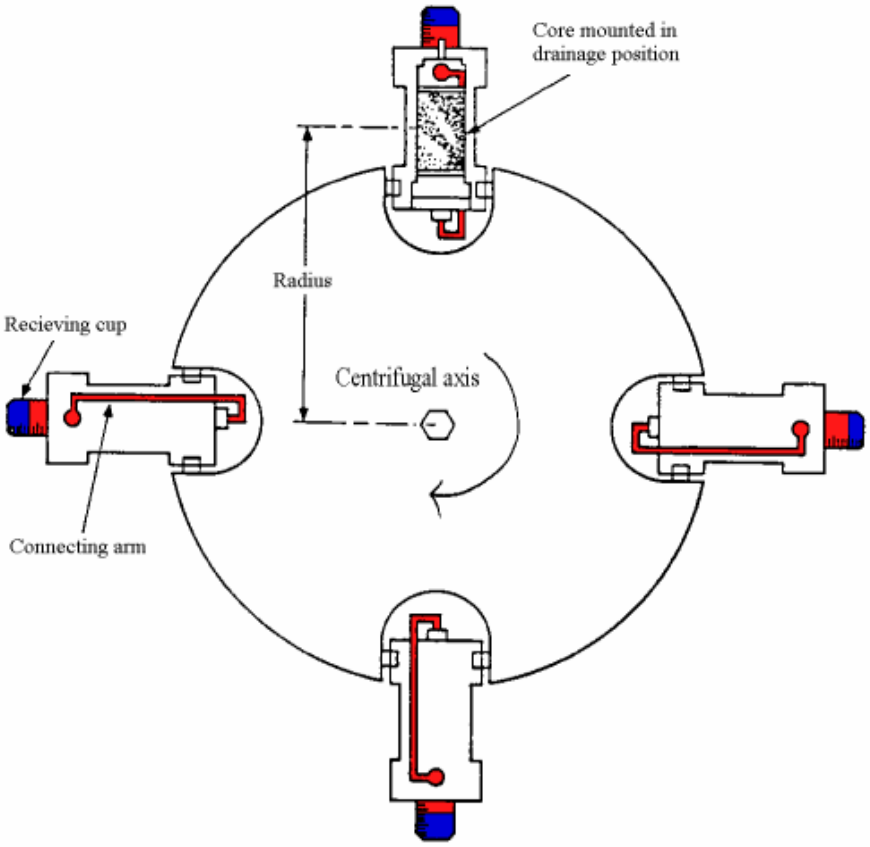

Figure 2.2.1.1: Measuring capillary pressure by use of the centrifuge method. This figure illustrates core holders containing core plugs under drainage mode (with permission from Norsk Hydro, SCAL-manual).

Let us first regard the capillary pressure as the independent variable that determines the saturation, so that the relation between capillary pressure and saturation of a given core is expressed by a function $S(p)$. This function gives the saturation s in the core at equilibrium when the capillary pressure is p. We further assume we have a cylindrical core of length L, containing a liquid with density ρ, which is subjected to an acceleration g. If the capillary pressure at the outlet of the core is zero, then at a distance h above the lower face, the capillary pressure will be ρgh and the saturation $S(\rho gh)$. The average saturation of the core is given by

$$\bar{s} = \frac{1}{L}\int_0^L S(\rho gh)dh \qquad (2.2.1.1)$$

Substituting ρgh with x, we get

$$\bar{s} = \frac{1}{L}\int_0^{\rho gL} S(x)\frac{1}{\rho g}dx = \frac{1}{\rho gL}\int_0^{\rho gL} S(x)dx \qquad (2.2.1.2)$$

We then define

$$z = \rho gL \qquad (2.2.1.3)$$

Hence z equals the **capillary pressure at the inlet endface** of the core. By combining (2.2.1.2) and (2.2.1.3):

$$\bar{s} = \frac{1}{z}\int_0^z S(x)dx \quad \Rightarrow \quad z\bar{s} = \int_0^z S(x)dx \tag{2.2.1.4}$$

This implies

$$S(z) = \frac{d}{dz}(z\bar{s}) = \bar{s} + z\frac{d\bar{s}}{dz} \tag{2.2.1.5}$$

The capillary pressure curve $s = S(p)$ for the core can be obtained by centrifuging the plug at different speeds. This corresponds to different values of z, and the average saturation of the core $\bar{s}$ can be measured for each different value of z. If the core contains two fluids (e.g. oil and water) the capillary pressure at the inlet endface (z) may be calculated at each angular velocity directly by

$$z = \Delta\rho\omega^2 RL \Rightarrow P_{ci} = \Delta\rho\omega^2 RL$$

which is based upon equation (2.2.1.3): g has been replaced by the centripetal acceleration, $\omega^2 R$, where R is the distance from the centre of rotation to the centre of the core sample and ω is the angular speed of rotation, defined as

$$\omega = \frac{2\pi(RPM)}{60}$$

From equation (2.2.1.5) it is seen that by plotting a curve of $z\bar{s}$ against z, and measuring slopes of tangents to this curve, we get the capillary pressure curve [1].

Equation (2.2.1.5) is often referred to as **the classical Hassler-Brunner solution**, and is commonly expressed as:

$$S_{w,HB}(P_{ci}) = S_w(P_{ci}) = \bar{S}_w(P_{ci}) + P_{ci}\frac{d\bar{S}_w(P_{ci})}{dP_{ci}}, \tag{2.2.1.6}$$

where P_{ci} is the capillary pressure at the inlet endface of the core plug (P_{ci}=z).

In these calculations, it has been assumed that the core is subjected to the same acceleration throughout its length (i.e. a linear field distribution). Since a centrifuge is being used, this is not strictly true, see Figure 2.2.1.2.

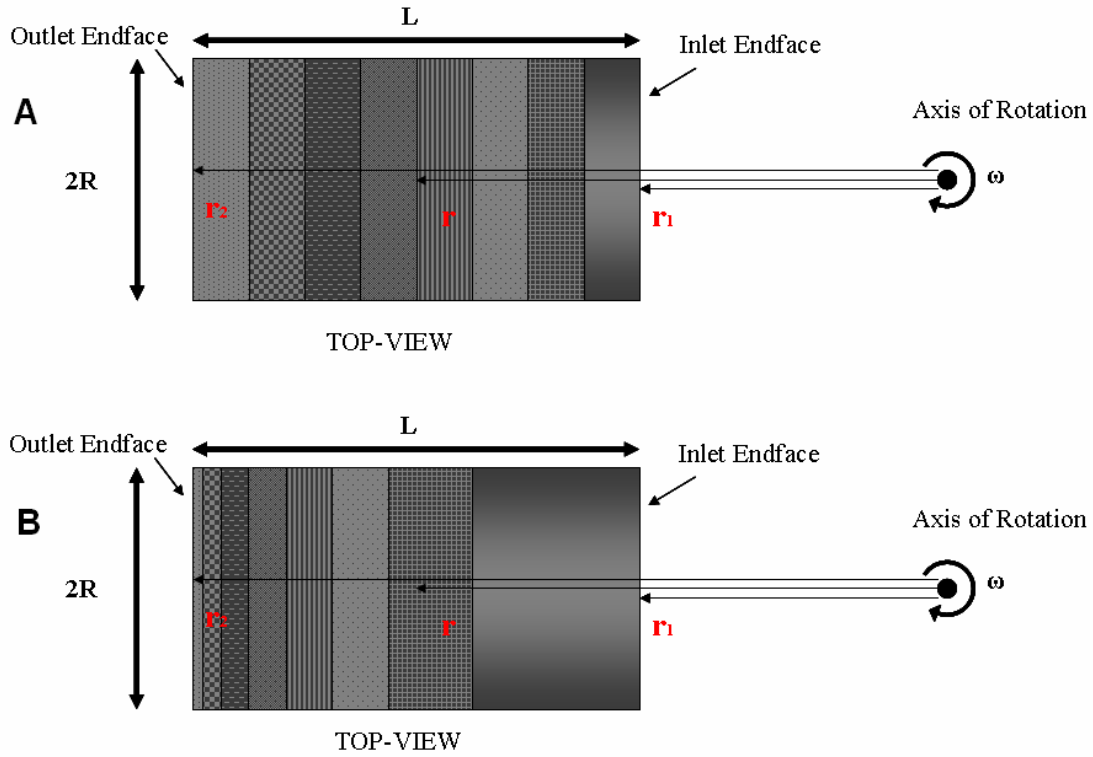

Figure 2.2.1.2: A: Assumption of a linear field distribution. B: Assumption of one-dimensional distribution for centrifugal field.

If the variation of the centrifugal field with the distance from the axis of rotation is taken into account, equation (2.2.1.4) gets a bit more complicated. Hassler and Brunner showed that the following equations hold instead of (2.2.1.4) [1]:

$$z\bar{s} = \cos^2\frac{1}{2}\theta\int_0^z \frac{S(x)dx}{\sqrt{1-\frac{x}{z}\sin^2\theta}} \qquad (2.2.1.7)$$

with

$$z = \frac{1}{2}\Delta\rho\omega^2\left(r_2^{\,2} - r_1^{\,2}\right) \qquad (2.2.1.8)$$

and

$$\cos\theta = \frac{r_1}{r_2} \qquad (2.2.1.9)$$

r_1 and r_2 are the distances from the axis of rotation to the two ends of the core, and ω is the angular velocity of the centrifuge. Equation (2.2.1.7) cannot be solved as simply for the unknown function S(x) as (2.2.1.4). But equation (2.2.1.4) is a good approximation of equation (2.2.1.7), hence its solution given by equation (2.2.1.6) can be taken as a first approximation to the solution of equation (2.2.1.7). The calculation of the capillary pressure, however, is modified to equation (2.2.1.8).

The conventional centrifuge method allows the capillary pressure curves of small consolidated core samples to be determined quickly and conveniently. The curves may further be extended to rather large values of capillary pressure; hence this method is very attractive compared to other techniques. However, this method suffers from some disadvantages. The most pressing problems with the centrifuge technique are focused on the validity of the fundamental assumptions associated with the Hassler-Brunner equations. These include [26]:

1. The assumption of zero-capillary pressure at the outlet endface of core plug. Much effort has been done to investigate this assumption, but so far, no conclusions have been drawn.
2. Not taking into account that core sample heterogeneity might affect the flow mechanisms.
3. The assumption of no vertical gravitational acceleration effects on the horizontal centrifugal field. Chen and Ruth showed that gravitational effects are pronounced when measurements are performed at low speed for high permeability and porosity core samples [27].
4. The assumption of a one-dimensional distribution of a centrifugal field inside the core plug. This assumption has turned out to be inaccurate and radial effects should be taken into account [26], [28].

Therefore, there have been several attempts to come up with a method for direct measurement of capillary pressure using the centrifuge.

The major reasons for the lack of literature reporting of water/oil capillary pressure data that include development of complete primary drainage, imbibition and secondary drainage curves, are the difficulty, expense and time to obtain them. These negatives can be significantly reduced by direct measurement of saturation profiles in plugs.

Ruth and Chen [29] summarized the numerous models that have been proposed over 50 years for approximating the saturation at one face from a sample from centrifuged effluent volumes. But, in every case, the model chosen to interpret the data influences the calculated capillary pressure curve [30].

In the early 1990's, Chardaire-Riviere, C., et al. tried to obtain the saturation profile in the porous plug while centrifuging. The technique was to continuously record the local saturation variation along the core, while centrifuging at any given time. The experimental procedure consisted in recording flight times of ultrasonic waves at three locations along the core, for then to determine the local saturation by a simple specific calibration. This led to correspondence between the ultrasonic signal and saturation [31]. Figure 2.2.1.3, Figure 2.2.1.4 and Figure 2.2.1.5 illustrates the set-up of her experiment, the calibration curve and the final P_c curve, respectively.

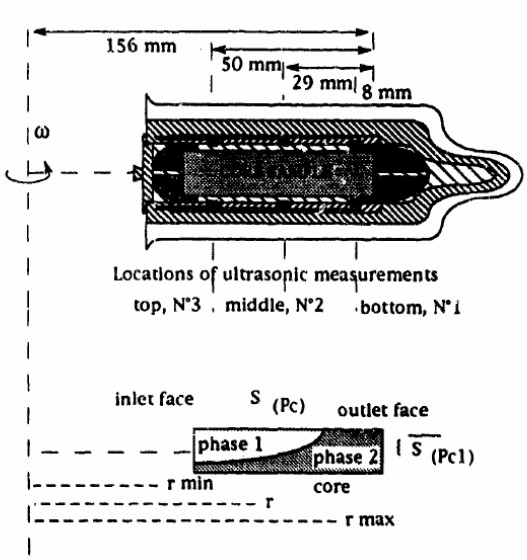

Figure 2.2.1.3: Centrifuge method set-up (Chardaire-Riviere et al., 1992).

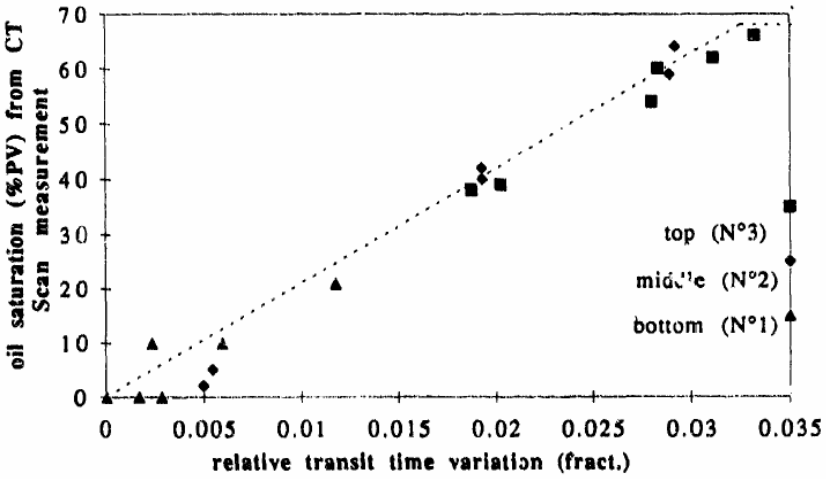

Figure 2.2.1.4: Calibration curve of oil saturation versus the corresponding values for relative transit time variations (Chardaire-Riviere et al., 1992).

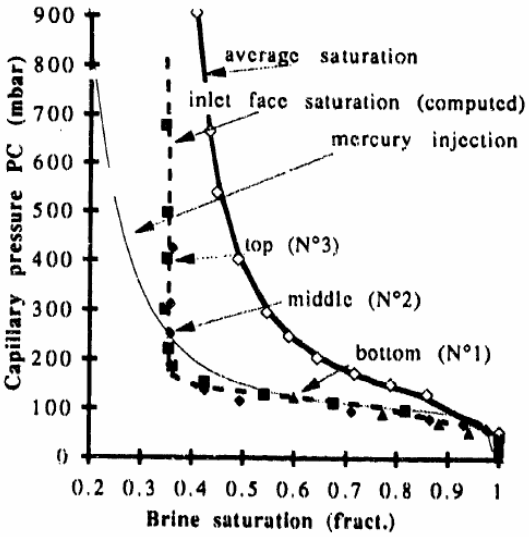

Figure 2.2.1.5: Capillary pressure curves for oil / brine drainage in a Berea sandstone sample (Chardaire-Riviere et al., 1992).

2.2.2 Direct Measurement of Saturation

Obtaining the saturation profile in the porous plug while spinning has been looked upon as an expensive and cumbersome process, as mentioned in the previous chapter. In 1997, Spinler and Baldwin introduced an alternative method of doing this. The **Direct Measurement of Saturation (DMS) method** directly measures an oil/water saturation profile within a porous rock that is established under a known pressure gradient as measured from a free-water level established along the height of the rock plug (see Figure 2.2.2.1).

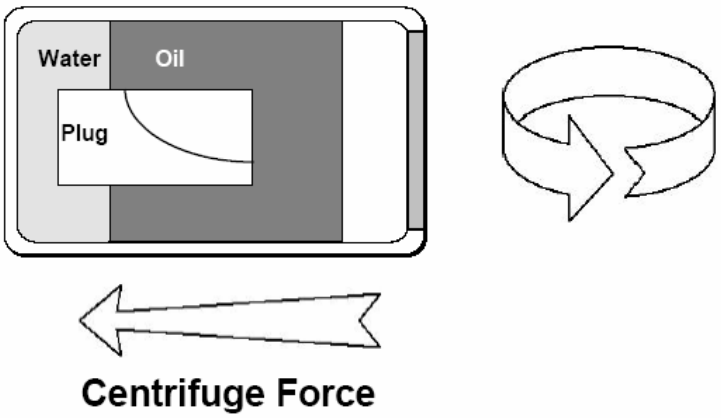

Figure 2.2.2.1: This figure is a simplified illustration of a plug with free water level in a large volume centrifuge cell with a saturation profile (Spinler, 1997).

The development of a capillary pressure curve in porous rock occurs as the fluid saturation changes with the varying pressure induced by the centrifuge, and the density difference between hydrocarbons and water. The difficulty has been in determining saturation profiles in the rock while it is spinning.

Spinler and Baldwin came up with a procedure to solidify the oil phase while centrifuging and map the water in the rock by using Magnetic Resonance Imaging (MRI) outside the centrifuge. The high definition capability of MRI makes it suitable for imaging fluids in porous rocks on a fraction of a millimetre scale [32]. By solidifying the hydrocarbon, redistribution of the water in the rock is prevented. Since solid state hydrocarbon has a short relaxation time, it is not imaged. Hence, in this system, the water is imaged, and the octadecane (which is a convenient hydrocarbon in this method) solidifies at 27 degrees Celsius and is not imaged. It is therefore necessary to keep the laboratory ambient temperature below 27 degrees Celsius. To prevent evaporation of the water while imaging, the plug is kept in a sealed plastic centrifuge bottle.

One disadvantage of this system is that the water (if being the wetting phase) has a relaxation time that is dependent on the size of the pore spaces it occupies. At low water saturation this is not noticeable, but in the regions of high water saturation, the relaxation time is increasing significantly and affects the standard image intensity. This effect is corrected by use of a calibration curve; the intensity map of water distribution is directly converted to water saturation (Figure 2.2.1.1 and Figure 2.2.2.3). One aspect to be aware of is the fact that there is a small volume change (approximately 2 %) due to hydrocarbon contraction during freezing. This is corrected by adjusting the water saturation [25].

To calculate the capillary pressure by this method, one needs to consider the variation of the centrifugal field with the distance from the axis of rotation (shown in Figure 2.2.1.2, B). Hence the following equation is being used:

$$P_c = \frac{1}{2}\Delta\rho\omega^2\left(r_2^{\,2} - r_1^{\,2}\right) \qquad (2.2.2.1)$$

where $\Delta\rho$: density difference [kg/m^3]
ω : angular velocity
r_2 : the reference point; the distance from the centre to the free water level [m]
r_1 : is the distance from centre to point of interest [m]

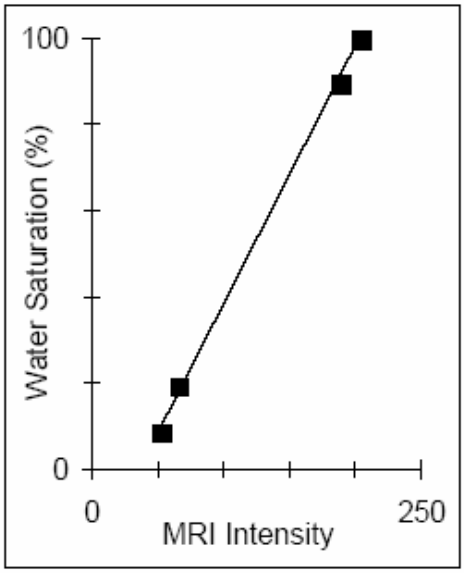

Figure 2.2.2.2: An example of a calibration curve for chalk, air-water centrifuge desaturation and imbibition (Spinler, 1997).

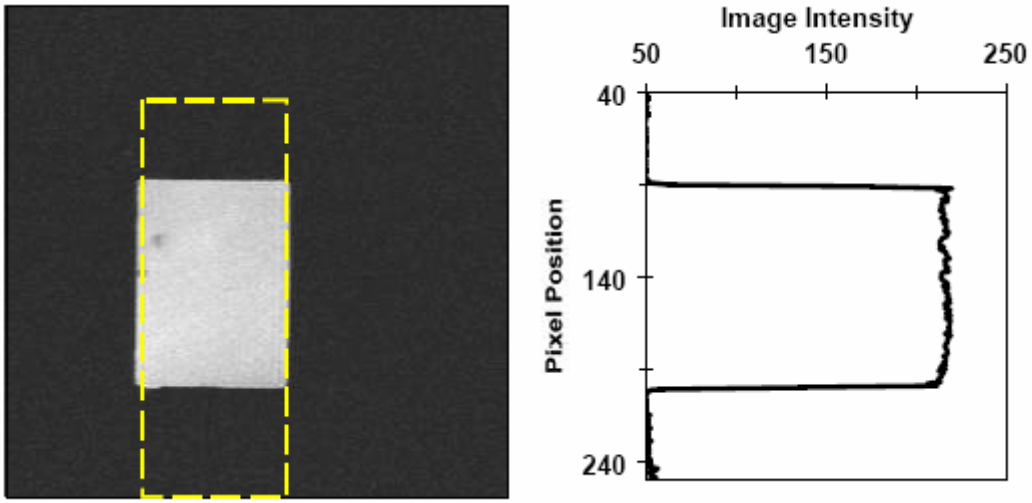

Figure 2.2.2.3: Left: MRI image of 100 % water saturated chalk plug. Dashed area corresponds to image area. Right: Image intensity map of the boxed area in the image to the left (Spinler, 1997).

Capillary pressure as a function of position in the sample and the achievable pressure range is determined by the speed of the centrifuge, distance from the free water level and the sample length. Development of both the positive and negative portions of a capillary pressure scanning curve simultaneously (see Figure 2.2.2.4) is enabled by positioning the free water level along the length of the plug. The free water level is the position where the oil and water pressures are equal (capillary pressure equal to zero), and this level is imaged with the plug, which enables an accurate calculation of capillary pressures in the plug. Movement of the free water level is minimized during imbibition and drainage by using a centrifuge cell with a bulk volume significantly larger than the pore volume of the plug. The ability to obtain positive capillary pressure curves for tight rocks such as chalk will impact our understanding and numerical modelling of fluid flow in such media, and will certainly better define the Improved Oil Recovery opportunities available.

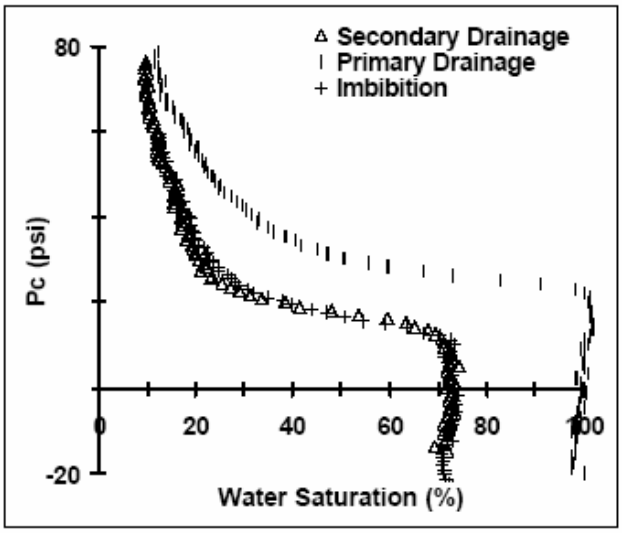

Figure 2.2.2.4: Capillary pressure curves for chalk plug. No hysteresis is found of the bounding curves (Spinler, 1997).

This method reduces or eliminates most of the limitations for other capillary pressure measurement techniques. The measurement of saturation is direct and independent of interpretive models which might influence the results, and since numerous data point are obtained concurrently throughout the sample, the measurements are rapid.

In addition to use octadecane and brine as fluids, Spinler and Baldwin came up with another technique to directly measure the saturation profiles in the cores. Here D_2O and pentadecane (melting point of 8 degrees Celsius) were used instead of brine and octadecane. The D_2O does not image, so the images showed only pentadecane. If the sample plugs used in the test are water-wet, the pentadecane is not in directly contact with the surface, and therefore, it has a constant relaxation time, independent of its local saturation or effective pore size. This means that the MRI spin echo image or local intensity is directly proportional to saturation [3].

To sum up:

- This DMS method eliminates the need for assumed or indirect determination of fluid saturations
- By positioning the free water level along the height of the plug, both negative and positive portions of the capillary pressure curve are measured from one centrifuge run. As a consequence, the direct measurement of capillary pressure curves has potential as a valuable additional tool for the oil industry.

- Freezing of oil phase while centrifuging permits determination of the water saturations in the core plug without fluid redistribution
- The use of centrifuge for pressure development coupled with direct saturation measurement appears to provide an accurate and rapid method for determining capillary pressure curves in porous medium.

Application of laboratory data from core analysis to reservoir studies can be seriously handicapped by the quality of data. Non-uniformity in the properties of rock samples, i.e. porosity and wettability, is often a major source of poor quality information. As pointed out in Chapter 1.5, the wettability state of a rock sample can be measured by a number of means that are assumed to provide an average wettability for the sample. However, wettability variations can occur, but they can not be seen except on a pore level [33]. Such variations can have as much if not more impact on fundamental laboratory measurements like relative permeability and capillary pressure curves. Another advantage of this Direct Measurement of Saturation method compared to other methods is its possibility of analysing such heterogeneities within a single plug. Variation of wettability within the sample cannot be seen from an Amott test on the full plug [32].

Figure 2.2.2.5 and Figure 2.2.2.6 show examples on variation in porosity within a plug; distinct bands that represent zones of varying porosity, and these variations will also affect the desaturation process. The sample is originally 100 % saturated with brine, and is then desaturated step-wise with air, by use of a centrifuge.

Without imaging, the non-uniformity of the plug would not have been known, and data such as primary drainage capillary pressure curve would have been compromised by using conventional techniques. By knowing that areas of different porosity exist, it is possible to separately evaluate the desaturation of different porosity areas [32].

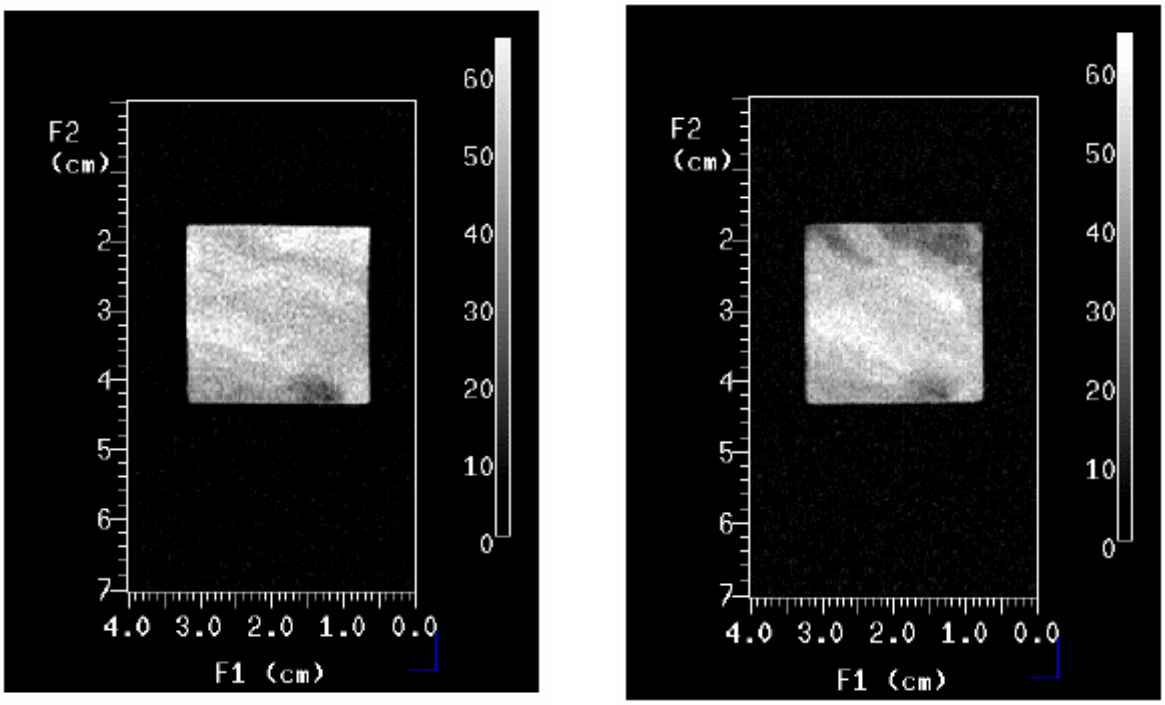

Figure 2.2.2.5 Left: A sample saturated 100% with brine. The greyer zones are areas of less porosity. Right: The sample is being partly desaturated with air, seen as darker spots in zones of higher porosity (Spinler et al., 1999).

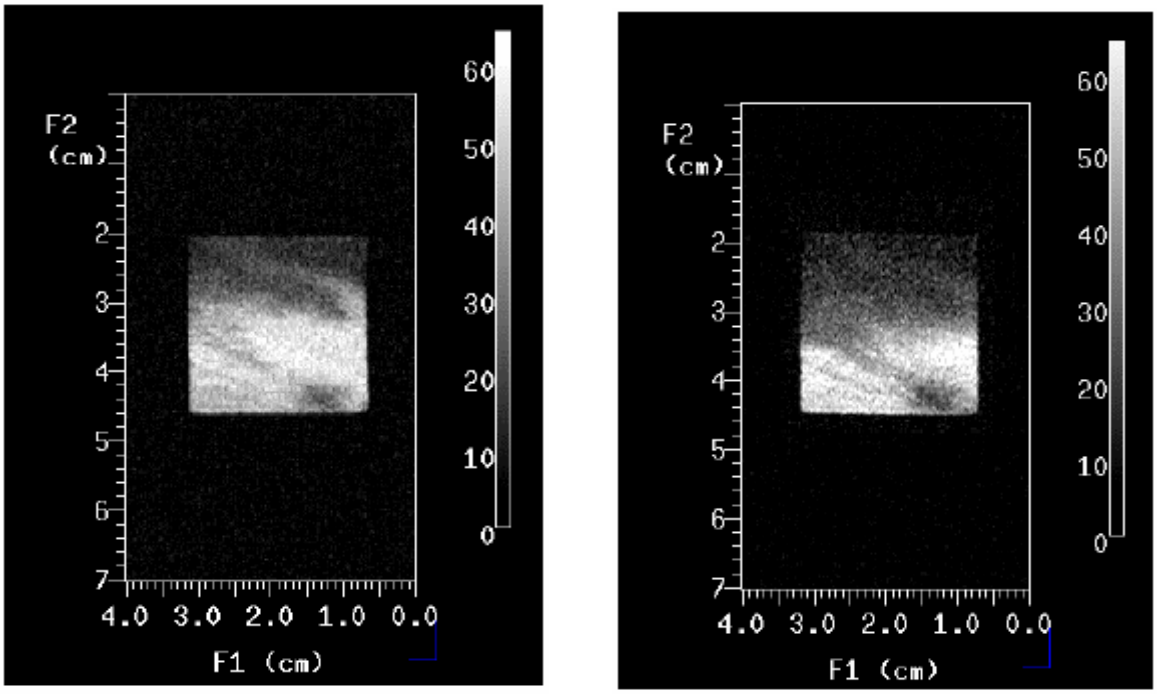

Figure 2.2.2.6: Left: The desaturation continuous, preferentially in the higher porosity areas. Right: The plug is at an equilibrium desaturated state with air (Spinler et al., 1999).

The chalk plug illustrated in the figures above had a porosity that varied from 23 to 27%. Intensities of the different porosity areas have been measured, converted to water saturation and plotted versus pressure as calculated from the standard centrifuge equation as a function of position within the plug. The results of these measurements were two distinct primary drainage capillary pressure curves, shown in Figure 2.2.2.7.

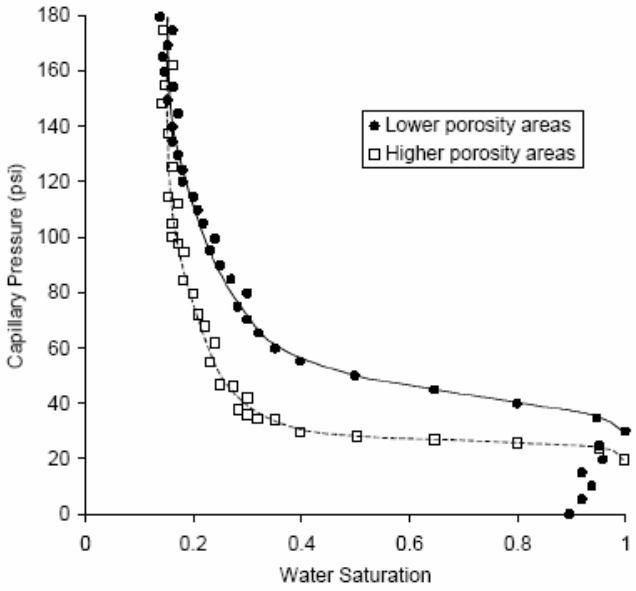

Figure 2.2.2.7: Primary drainage capillary pressure curves at air brine equilibrium from manual readings of saturation data from different porosity zones of sample (Spinler et al., 1999).

In addition to porosity, the saturation profiles can give valuable information on wettability. Figure 2.2.2.8 shows a most unusual feature of the fluid distribution; the concave downward shape of the saturation distribution within the plug from side edge to side edge. This feature suggests that the properties within the plug vary from the interior to the edges. To evaluate this anomaly, one can determine imposition capillary pressure curves for different positions (columns) within the plug as indicated by the vertical lines on the figure.

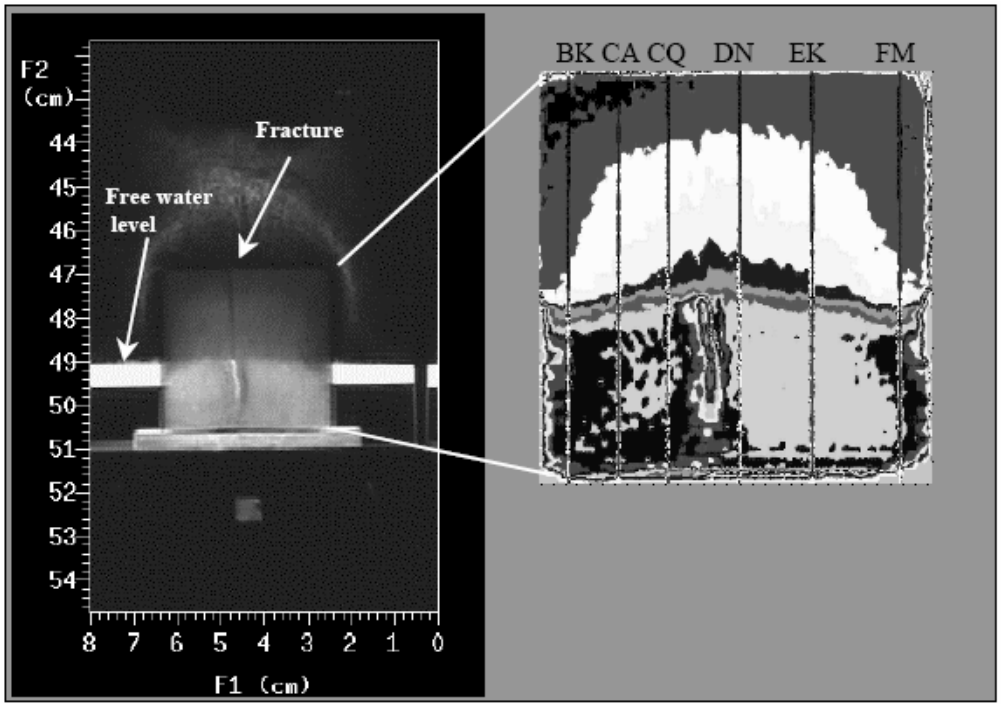

Figure 2.2.2.8: The MRI image of a chalk plug after centrifuging. The free water level can be seen outside of plug and in fracture. The letters above identify positions within the plug for imbibition Pc curves (Spinler et al., 1999).

Spinler et al. showed by the different capillary pressure curves that the apparent wettability of the plug varied from strongly water-wet at the centre to moderately water-wet near the edges. The variation of wettability within this plug was probably a result of the core preparation process. The core was aged in crude oil after it had been flushed to initial water saturation with crude oil. The soaking process in crude oil probably altered the outside of the plug to a more neutral state than is the case for the interior part. This effect has now been reduced by a modified process of altering wettability [34].

Both of these examples illustrate the proficiency of Direct Measurement of Saturation for capillary pressure measurement. No other technology can obtain such data from highly heterogeneous rock samples.

All methods of measuring capillary pressure have some weaknesses, and the DMS method is no exception. The possibility of a non-uniform wettability distribution within the core, as described above, may influence the results, since the curve is measured along the length of the core. Another problem is the position of the sample while imaging. With a resolution of 25 points pr centimetre there is not much movement needed to get off by a few points. And since the calculations are made point by point, this very well might affect the measurements.

The fact that the buckets in the centrifuge are not totally horizontal while spinning will result in a tilted free water level. The consequence of this is that the capillary pressure curves are dependent on position.

In 2002, Graue, Bognø, et al. came up with another method of measuring capillary pressure curves; the Nuclear Tracer Imaging Centrifuge Method [35]. A major part of this thesis has been to improve this method. The description and improvements are described in Chapter 9.

CHAPTER 3

NMR

In this thesis, Nuclear Magnetic Resonance (NMR) and NMR Imaging (MRI) were performed to calculate fluid distribution in Rørdal chalk samples. This chapter is devoted to the discussion of the basic concepts of NMR. The major part of the information has been found in *Lien, J.R., "En kort innføring i NMR-logging", 1995*, and *Coates, G.R., et al. "NMR-logging, Principles & Application", 1998.* [36]-[37].

3.1 NMR - Basics

Hydrogen is abundant in both water and hydrocarbons. The nucleus of a hydrogen is a proton; a positively charged particle, and this spinning particle represents a current loop that generates a magnetic dipole moment, μ, with two poles (north and south) aligned with the spin axis. The magnetic dipole moment is defined by equation (3.1.1).

$$\mu = I \cdot A \tag{3.1.1}$$

,

where I is the current of an electrical loop, with enclosed area A. This circular motion leads to an associated angular moment, L, defined by

$$L = | m\vec{r} \times \vec{v} | \tag{3.1.2}$$

where m is the mass of the moving object with velocity $\vec{v}$ relative to an axis in distance $\vec{r}$. In the case of a proton, μ and L are parallel, and their relationship is

$$\vec{\mu} = \gamma \vec{L} \tag{3.1.3}$$

where γ is the gyromagnetic ratio. When many hydrogen atoms are present and no external magnetic field exists, the hydrogen nuclear spin axes are randomly aligned, as seen in Figure 3.1.1.

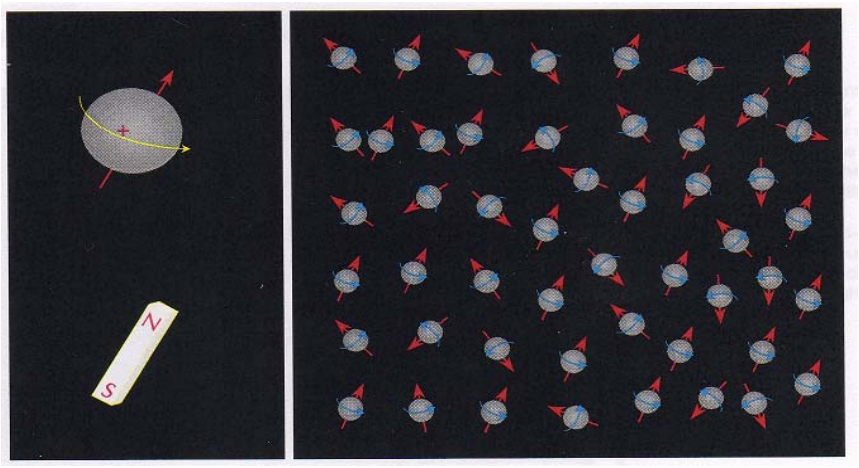

Figure 3.1.1: A hydrogen nuclei behave as though they are tiny bar magnets aligned with the spin axis of the nuclei. In the absence of an external magnetic field, the nuclear magnetic axes are randomly aligned (Coates, 1998).

When a magnetic dipole moment is immersed in a static magnetic field, B_0, this will exert a torque, τ, on the nucleus that acts to align the nuclear spin axis with B_0. τ is defined by

$$\vec{\tau} = \vec{\mu} \times \vec{B}_0 \tag{3.1.4}$$

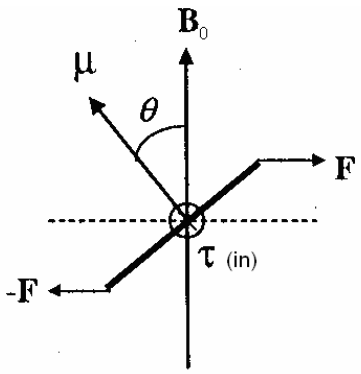

Figure 3.1.2: A magnetic dipole moment in a static magnetic field (Lien, 2002).

The magnetic dipole moment is said to be in equilibrium when μ and B_0 are parallel, and from equation (3.1.4) one can see that τ is then zero. If an external force is applied to the system, μ can be moved out of equilibrium; hence its potential energy, U, is changed. U is defined by:

$$U = -\vec{\mu} \cdot \vec{B}_0 \tag{3.1.5}$$

Depending on θ (see Figure 3.1.2) the energy varies from $+\mu B_0$ (labile equilibrium) to $-\mu B_0$ (stable equilibrium). It can further be shown that following equation is valid:

$$U = -\gamma \hbar m_z B_0 \tag{3.1.6}$$

where $\hbar$ is Planck's constant (modified) and m_z is the spin quantum number. According to quantum mechanics, when a proton is subjected to an external magnetic field, the proton is forced into one of two energy states; one parallel (β) and one anti-parallel (α) to B_0. That is;

m_z may have two possible values: $\pm\frac{1}{2}$. Because of the two possible values of m_z, there is an energy difference between the two levels:

$$\Delta U = E_\beta - E_\alpha = \gamma\hbar B_0 \tag{3.1.7}$$

This is illustrated in Figure 3.1.3.

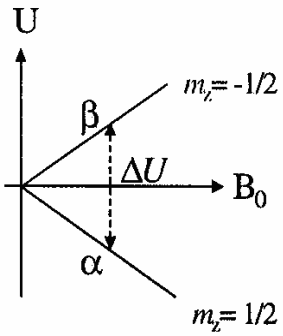

Figure 3.1.3: The two possible energy levels for a proton in an external magnetic field (Lien, 2002).

For a transition from level α to level β to occur, a photon of energy corresponding to the difference in potential energy between the two states is required. According to Planck's law, the frequency of the photon is given by

$$\Delta U = hf \tag{3.1.8}$$

Combining (3.1.7) and (3.1.8), and the fact that $\hbar = \frac{h}{2\pi}$, gives

$$f = \frac{\gamma}{2\pi} B_0 \tag{3.1.9}$$

When a torque is applied to a spinning object, the following theorem ("spinnsatsen") is given by the classical mechanics:

$$\vec{\tau} = \frac{d\vec{L}}{dt} = \vec{\mu} \times \vec{B}_0 \tag{3.1.10}$$

This implies that $d\vec{L}$ is perpendicular to both $\vec{\mu}$ and $\vec{L}$. That is; the axis of the object moves perpendicular to the torque in a motion called precession. In this example, the nucleus will precess around B_0. This is called the *Larmor precession*.

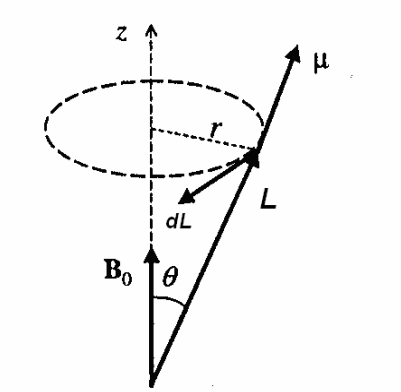

Figure 3.1.4: Precession of μ and L around B_0 (modified, Lien, 2002).

By using equations (3.1.3) and (3.1.10) together with the fact that $r = L\sin\theta$ (from Figure 3.1.4), one can find the angular velocity of $\vec{L}$:

$$\vec{\tau} = \vec{\mu} \times \vec{B}_0 = \mu B_0 \sin\theta = \frac{dL}{dt} = \omega_L r = \omega_L L \sin\theta = \omega_L \frac{\mu}{\gamma}\sin\theta \qquad (3.1.11)$$

The angular velocity may then be written as:

$$\omega_L = \gamma B_0 \qquad (3.1.12)$$

This implies the precession frequency is given by:

$$f_L = \frac{\omega_L}{2\pi} = \frac{\gamma}{2\pi} B_0 \qquad (3.1.13)$$

This frequency, f_L, is called the *Larmor frequency*. From equation (3.1.9) one can see that this equals the frequency of the photon required to excite protons from state α to state β. In order to actually make this happen, the angle between the magnetic dipole momentum and the axis of the static field $\vec{B}_0$ has to be changed. This is done by applying an oscillating magnetic field, $\vec{B}_1$, orthogonal to the static field $\vec{B}_0$ and $\vec{L}$. To maintain this orthogonal direction, the frequency of $\vec{B}_1$ must equal the Larmor frequency of the protons relative to $\vec{B}_0$. $\vec{B}_1$ will affect the rotation of $\vec{L}$, and according to equation (3.1.10), this will exert another torque on μ:

$$\vec{\tau}_1 = \vec{\mu} \times \vec{B}_1 = \frac{d\vec{L}_1}{dt} \qquad (3.1.14)$$

Figure 3.1.5 shows that $d\vec{L}_1$ is perpendicular to $d\vec{L}$, because $\vec{B}_1$ is perpendicular to $\vec{B}_0$.

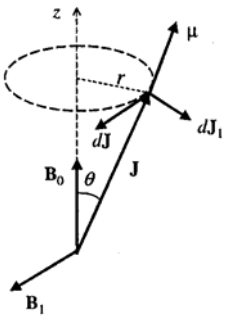

Figure 3.1.5: By applying a magnetic field B_1, perpendicular to B_0 and L, the angular momentum is moved away from B_0 (Lien, 2002).

From the quantum mechanics point of view, if a proton is at the low-energy state, it may absorb energy provided by $\vec{B}_1$ and jump to a the high-energy state. The application of $\vec{B}_1$ also causes the protons to precess in phase with one another. This change in energy state and in-phase precession caused by $\vec{B}_1$ is called *nuclear magnetic resonance*.

3.2 Relaxation

A sample, containing hydrogen or hydrocarbons, is magnetized when exposed by a static magnetic field, $\vec{B}_0$. In such a process, more spins are precessing parallel to $\vec{B}_0$ than anti-parallel (see Figure 3.2.1). The difference between the number aligned parallel and anti-parallel to $\vec{B}_0$ forms the net magnetization, $\vec{M}_0$, which provides the signal measured by NMR and MRI devices. When the sample has come to equilibrium in the $\vec{B}_0$ field, the net magnetization is defined by equation (3.2.1).

$$\vec{M}_0 = \sum_i^N \mu_i \qquad (3.2.1)$$

$\vec{M}_0$ consists of three components; M_x, M_y and M_z, the z-axis being defined as the direction of $\vec{B}_0$. In this state, $\vec{M}_0$ equals M_z, the magnetization along the $\vec{B}_0$ axis.

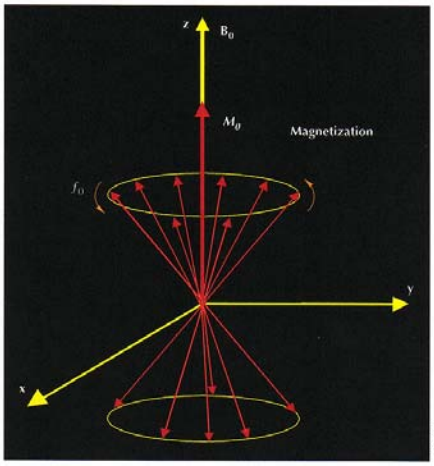

Figure 3.2.1: When many protons are precessing in an external magnetic field, a net magnetization, $\vec{M}_0$, will be exhibited (Coates, 1998).

As pointed out in Chapter 3.1, the system can be brought from one state to another by applying a pulsed oscillating magnetic field $\vec{B}_1$, orthogonal to $\vec{B}_0$ and $\vec{L}$, and $\vec{B}_1$ is precessing with the Larmor frequency. Angular-pulse terms, such as π pulse (or 180° pulse) and a π/2 pulse (or 90° pulse), refer to the angle through which magnetization is tipped by $\vec{B}_1$. The system is then brought to a higher energy state, and the direction of the magnetization is changed.

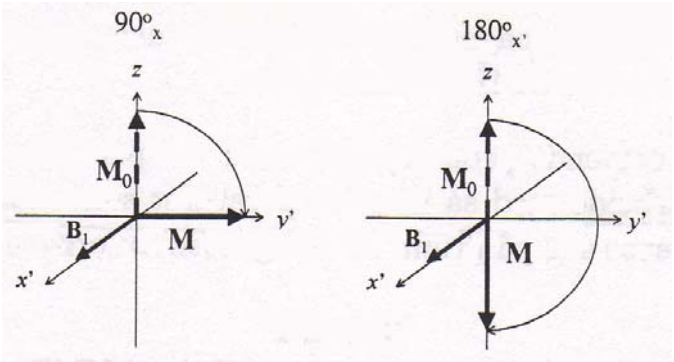

Figure 3.2.2: Left: a $90°_{x'}$-pulse, right: an $180°_{x'}$-pulse. In both cases, M_0 is originally aligned along the z-axis, and is then tipped 90° and 180° about the x-axis, respectively (Lien, 2002).

When the $\vec{B}_1$-field is turned off, the excited protons will return to their original state; the α-state, and the net magnetization will decrease; $\vec{M} \rightarrow \vec{M}_0$. This process is defined as *relaxation*.

3.2.1 T_1 Relaxation

As mentioned earlier, $\vec{M}$ consists of three components; M_x, M_y and M_z. In equilibrium, M_x and M_y equals zero, and $M_0 = M_z$. When applying an oscillating magnetic field, $\vec{B}_1$, $\vec{M}_0$ is no longer in equilibrium; that is M_x, $M_y \neq 0$, and the change in M_z is defined by

$$\frac{dM_z}{dt} = -\frac{M_z - M_0}{T_1} \qquad (3.2.1.1)$$

T_1, *the longitudinal relaxation time*, is related to the time of the relaxation process. When applying a $90^{o}_{x'}$-pulse, $\vec{M}_0$ is flipped to the xy-plane. Solution of (3.2.1.1) leads to

$$M_z = M_0\left[1 - \exp\left(-t/T_1\right)\right] \qquad (3.2.1.2)$$

When applying a $180^{o}_{x'}$-pulse, the net magnetization is flipped to the negative z-direction, and solution of (3.2.1.1) yields

$$M_z = M_0\left[1 - 2\exp\left(-t/T_1\right)\right] \qquad (3.2.1.3)$$

Figure 3.2.1.1 shows the relaxation curves of equation (3.2.1.2) and (3.2.1.3), respectively.

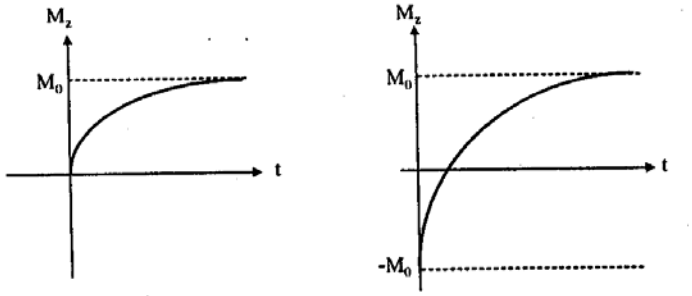

Figure 3.2.1.1: The relaxation curves of equation (3.2.1.2) and (3.2.1.3), respectively (Lien, 2002).

All spins do not relax simultaneously. The process behaves much like nuclear decay of radioactive isotopes, with the relaxation occurring exponential with time. The parameter T_1 is measured by *the inversion recovery method*.

This method is illustrated in Figure 3.2.1.2.

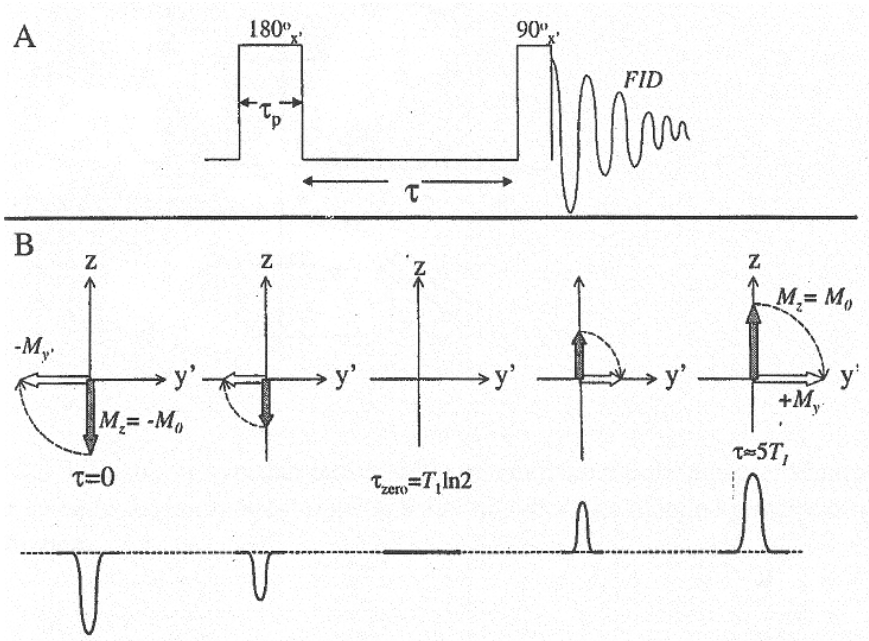

Figure 3.2.1.2: The inversion recovery method (Lien, 2002).

This figure illustrates the pulse-sequence. First, an $180^{o}_{x'}$-pulse is applied so that the magnetization vector, $\vec{M}$, is flipped in the negative z-direction (inversion). Then, after a given time τ, relaxation has taken place, and by applying a $90^{o}_{x'}$-pulse, a transverse magnetization is detectable in the (x', y')-plane. By repeating this process with different values of τ, the longitudinal decay curve can be found point-wise, as $\vec{M}$ versus time. These points can then be adjusted to an exponential function, and a value of T_1 may be found. The pulse-sequence in this method is given by

$$[180^{o}_{x'} - \tau - 90^{o}_{x'}]$$

(At the bottom of Figure 3.2.1.2; the final pulse after the Fourier-transformation.)

3.2.2 T_2 Relaxation

A system in equilibrium will have $\vec{M} = \vec{M}_0$, that is; the magnetization vector is situated along the z-axis. When a $90^o_{x'}$-pulse is applied on the system, the magnetization-vector is flipped down in the (x', y')-plane. This implies $M_z = 0$, and further the amount of nucleus in the α-state equals the amount of nucleus in the β-state (see Figure 3.1.3), $n_\alpha = n_\beta$.

As previously mentioned, the magnetic dipole momentum, $\vec{\mu}$, is either parallel or anti-parallel to the z-axis. The reason for $\vec{M}$ suddenly being allowed to be situated in the (x', y')-plane is that the dipole momentums of the nucleus are being gathered while precessing parallel to $\vec{B}_0$; there is a *phase-coherence*, see Figure 3.2.2.1. This phase coherency will gradually vanish, even if $n_\alpha = n_\beta$. In this process (*transversal relaxation*), there is no exchange of energy to the environment; the exchange of energy happens between the nucleuses: The rate of α → β equals the rate of β → α.

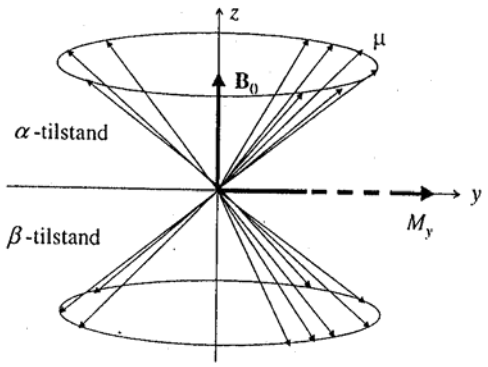

Figure 3.2.2.1: The gathering of magnetic dipole momentum, (Lien, 2002).

Like the longitudinal relaxation, this transversal relaxation is described by the rate of decreasing magnetization:

$$\frac{dM_x}{dt} = -\frac{M_x}{T_2} \quad \text{and} \quad \frac{dM_y}{dt} = -\frac{M_y}{T_2} \tag{3.2.2.1}$$

Solving these equations gives:

$$M_x = M_y = M_0 \exp\left(-\frac{t}{T_2}\right) \tag{3.2.2.2}$$

T_2 is called the *transversal relaxation time,* or *spin-spin relaxation time*. M_z can not return to equilibrium $\vec{M}_0$ as long as M_x, $M_y \neq 0$. This means that $T_1 \geq T_2$. To measure T_2, a pulse sequence is needed. The fare most used is the *CPMG-sequence*, or the *spin-echo sequence* (see Figure 3.2.2.2 and Figure 3.2.2.3).

The nucleuses will affect one another; hence the magnetic field on each nucleus will not be homogenous. Nevertheless, some nucleus will sense exact the same field, and these are called *isochromates*. All the isochromates will together form the total magnetization, $\vec{M}$. Those nucleuses that sense a stronger field than the applied field $\vec{B}_0$ will rotate faster than the Larmor-frequency, and those who sense a weaker field will rotate slower. This leads to the isochromates being spread out like a fan.

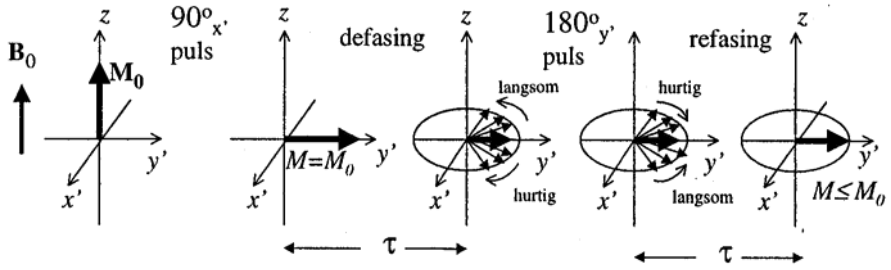

Figure 3.2.2.2: The CPMG method for measuring the T_2. An illustration of the fan-shaped distribution of the isochromates (Lien, 2002).

The CPMG sequence starts out with applying a $90^{o}_{x'}$-pulse. When this pulse is turned off, the phase coherent precession starts to dephase. After a period τ, an $180^{o}_{y'}$-pulse is applied, hence the dephasing due to the inhomogeneous magnetic field is reversed and starts to rephrase (the "faster" isochromates is now situated behind the "slower" ones, this is called an *echo*). After another period τ the transversal magnetization has rephased, and the x-and y-components of $\vec{M}$ is being measured. This value is smaller than at t = 0 (see Figure 3.2.2.2). By repeating this echo-sequence, the transversal relaxation curve of type (3.2.2.2) is found point-wise.

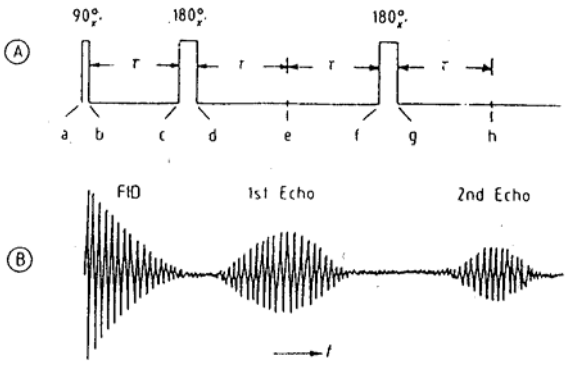

Figure 3.2.2.3: Illustration of the CPMG-sequence. τ is called the echo-time (Lien, 2002).

The CPMG-sequence is denoted

$$\left[90^{o}_{x'} - \tau - \left(180^{o}_{y'} - 2\tau\right)_n\right]$$

3.3 NMR Measurements

Petrophysical information, such as porosity, saturation, pore size distribution, permeability and hydrocarbon typing can be extracted from NMR-measurements [37]. In this section, a closer look is taken upon how to calculate the first three properties. For further information on the concepts of a NMR-instrument, see *Coates, G.R., et al "NMR logging Principles & Application", 1998*, and *Lien, J.R., "En kort innføring i NMR-logging", 2002, [36]-[37]*.

3.3.1 Pore Size Distribution

The pore volume in a porous media can be divided into a surface volume, δS, and a bulk volume, 1-δS. The surface volume is the thin section (thickness δ) that wets the rock surface. The bulk volume is by far the larger of these two volumes, as indicated in Figure 3.3.1.1.

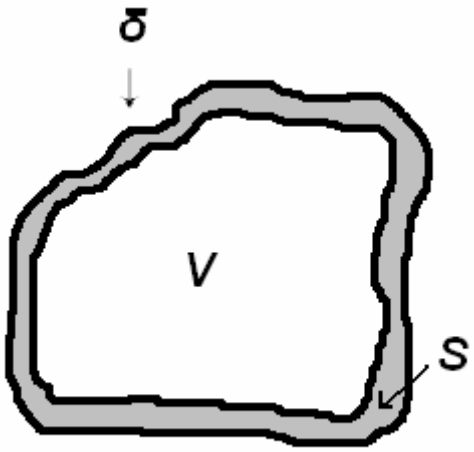

Figure 3.3.1.1: The pore volume can be divided into a surface volume and a bulk volume. V is the total pore volume.

With the assumption that there is only one phase present in the pore, the relaxation time can be described by the following equation:

$$\frac{1}{T_i} = \left(1 - \frac{\delta \cdot S}{V}\right)\frac{1}{T_{ib}} + \frac{\delta \cdot S}{V}\frac{1}{T_{is}}, \text{ i = 1, 2} \qquad (3.3.1.1)$$

where T_{ib} and T_{is} is the bulk and surface relaxation time, respectively. The fact that the thickness of δ is only a few molecule diameters leads to the following approximation; bulk volume ≈ 1. In addition, the relaxation in the surface volume is substantially faster than in the bulk volume. This leads to a modification of equation (3.3.1.1):

$$\frac{1}{T_i} = \frac{\delta \cdot S}{V}\frac{1}{T_{is}} \tag{3.3.1.2}$$

The surface relaxivity, $\rho = \frac{\delta}{T_{is}}$, indicates the strength of the relaxation processes taking place at the pore surface. This parameter has been shown to be independent on pore size. The relaxation times, T_1 and T_2, are then related to the volume:surface-ratio, i.e. the pore diameter, d:

$$d = \frac{V}{S} = \rho T_{1,2} \tag{3.3.1.3}$$

Since the process of measuring T_2 is faster than is the case for T_1, the pore size distribution is generally done by T_2 measurement by the CPMG sequence. From equation (3.3.1.3); one pore size is indicated by one specific T_2-value. But - in a porous media, there are a large number of different pore sizes, hence the curve obtained by the CPMG sequence will include several values of T_2, and not fit the exponential function given by equation (3.2.2.2). The data is then adjusted a multi exponential function, given by

$$M(t) = M_0 \sum_j^n a_j(T_{2j}) \exp(-\frac{t}{T_{2j}}), \tag{3.3.1.4}$$

Where the population coefficient $a_j(T_{2j})$ represents the contribution of pores with relaxation time T_{2j}, and n is the chosen number of T_2 values (often n = 100). To solve equation (3.3.1.4) with respect to $a_j(T_{2j})$ when M(t) is known is an inverse problem, and in order to avoid unstable solutions, the T_2 values are pre-selected. The distribution of the $a_j(T_{2j})$ coefficients is proportional to the pore size distribution.

3.3.2 Porosity

The porosity can easily be found by summing the entire pore size distribution

$$\phi = c\sum_j^n a_j(T_{2j}), \tag{3.3.2.1}$$

where c is is a constant, found by calibrating the brine saturating the porous media.

As mentioned in Chapter 2.2.2, it is possible to visually see variations in porosity by looking at MRI images. In Figure 2.2.2.5 it was shown that there were some zones, having a greyish colour. These zones indicated areas of less porosity.

3.3.3 Saturation

The experiments presented in this thesis, are performed on Rørdal chalk cores. Normally, the pores in these core samples are fairly uniform in size, which gives a narrow pore size distribution [38]. Hence the exponential curve detected by the CPMG sequence has a small T_2 range. When water and i.e. decane is filling the pore space, the T_2 distributions for these two phases are totally separated (see Figure 3.3.3.1). This is beneficial when calculating the saturations; this is done by integrating the area under each peak, and calculating the ratio of intensity due to water to the total intensity.

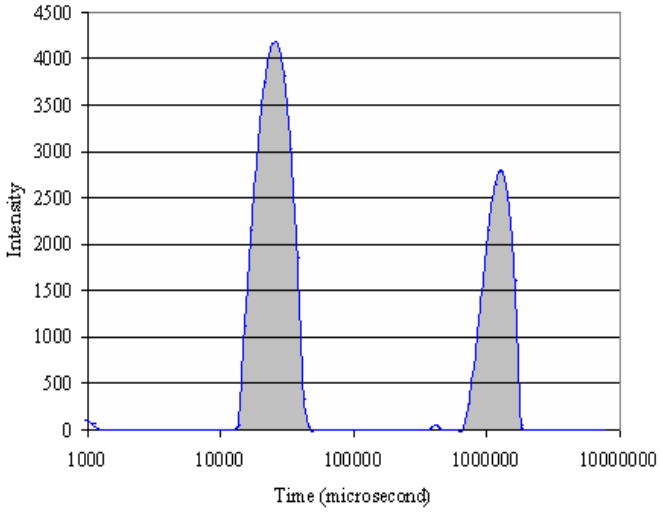

Figure 3.3.3.1: The T_2 distribution for a Portland chalk core.

However, if the core sample is containing vugs (see Chapter 1.1), the pore size distribution is no longer that narrow; hence the T_2 range of the CPMG sequence increases. This may further lead to a case where the T_2 distributions for these two phases are no longer totally separated, and problems calculating the saturation of each phase may occur (see Figure 3.3.3.2).

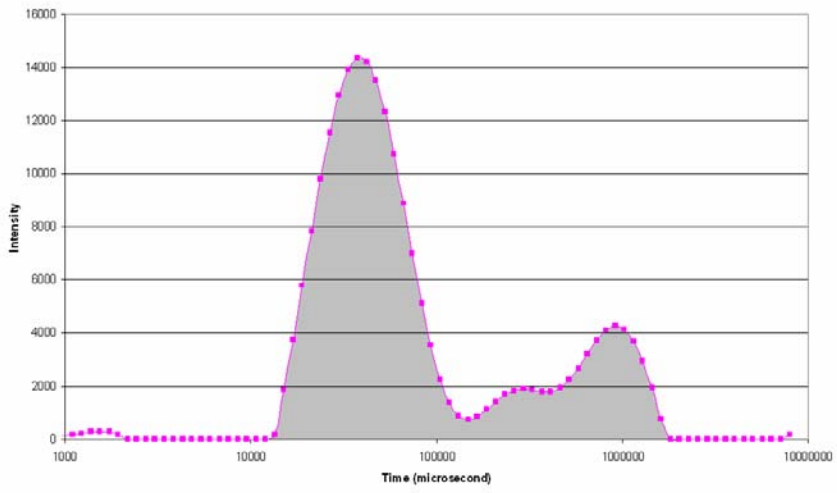

Figure 3.3.3.2: The T_2 distribution in a Portland chalk core containing vugs.

Part 2

Experimental Procedures

CHAPTER 4

Procedures for Core Analysis

4.1 Core Material

Reservoir core material is very expensive to obtain. Thus in order to do extensive core analysis, it is necessary to use analogues from outcrop material which possess the same characteristics found in the reservoir rock. In 1995, Lie et al. examined different outcrop chalks in order to obtain an analogue to the Ekofisk field reservoir rock. Among these, Rørdal chalk from the Portland quarry in Ålborg, Denmark, was examined and found to be a good analogue [38]. Hence in this thesis, the Rørdal chalk has been used to represent the Ekofisk Field reservoir rock. This rock consists of coccolith deposits from Maastrichtian age (that is; 75-61 Ma), the same age as the Tor field (part of the Ekofisk field), with 99% calcite and 1% quartz [39]. All the core samples were drilled in the same direction from large chalk blocks to obtain analogous material and to ensure the same orientation relative to bedding planes or laminations. The outcrop rock is originally strongly water-wet, the porosity is in the order of 40-50 % and the permeability varies from 1 to 10 mDarcy.

The core plugs being used in this thesis are partly taken from Rørdal chalk obtained in the late 1990's and partly from material obtained in June 2003.

4.2 Fluids

The fluids being used in this thesis are given in Table 4.1:

Table 4.1: Fluid Properties

Name	Type/ content	Density [g/cm^3]	Viscosity at 20^o C [cP]	Other
Brine	- Distillate water - 5% wt NaCl - 5% wt $CaCl_2$ - 0.0001% wt NaN_3	1.057	1.09	The minerals are added to minimize interactions between water and rock surface, NaN_3 is added to prevent bacterial growth
Ekofisk Oil	-Crude oil from Ekofisk Field	0.85	14.3	This is being stored in an oil drum, and is turned several times before tapping
n-Decane ($C_{10}H_{22}$)	-Mineral oil	0.73	0.92	Purity of ~95%
Decahydronapthalene (Decalin, $C_{10}H_{18}$)	- Mineral oil	0.90		Purity of ~95 %
Octadecane ($C_{18}H_{38}$)	-Mineral oil	0.777	2.46[a]	Purity of ~95 %
Lamp oil	-Mineral oil	0.740	1.43	Purity of ~95 %

[a]: viscosity at ~40^{o}C

4.3 Equipment used in Core Analysis

The pumps being used for displacement experiments are computerized QX Series Metering Pumps, giving data on pressure and rate, see Figure 4.3.1.

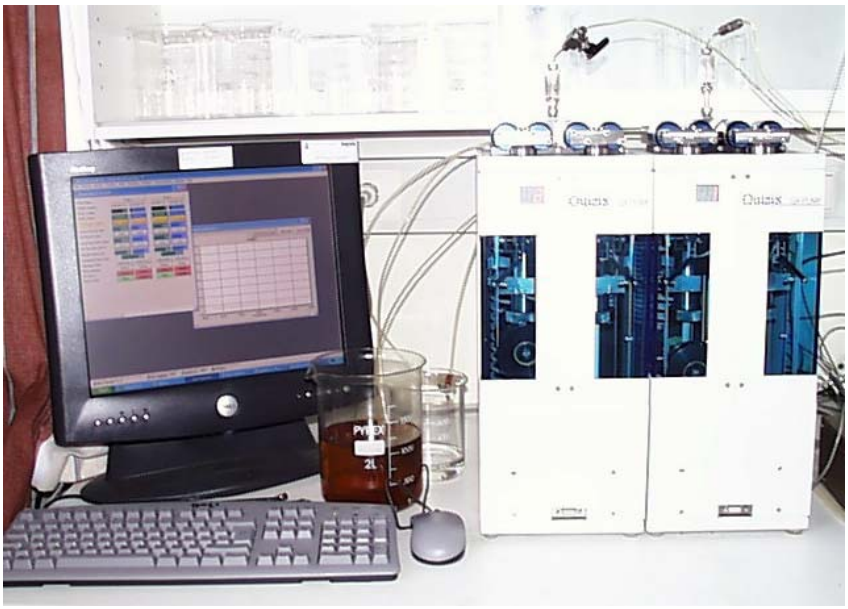

Figure 4.3.1: The computerized QX Series Metering Pump

Validyne Pressure Transducers were used for pressure measurements, and backpressure was established by use of a Gas Dome Backpressure Regulator; Temco BP50.

Regular Hassler Core holders were used for oil and water displacements, see Figure 4.3.2.

Figure 4.3.2: Hassler Core holder

Injection of crude oil into core samples was done by use of an accumulator.

4.4 Measuring the Porosity

To obtain measurements of porosity, the following procedure was used. First, the core plugs were dried for 90°C for 3 days to remove potential moisture. The cores were then measured (length, diameter and weight) and then vacuum evacuated to ~10mBar and saturated with degassed brine. The equipment used for vacuum evacuation is shown in Figure 4.4.1

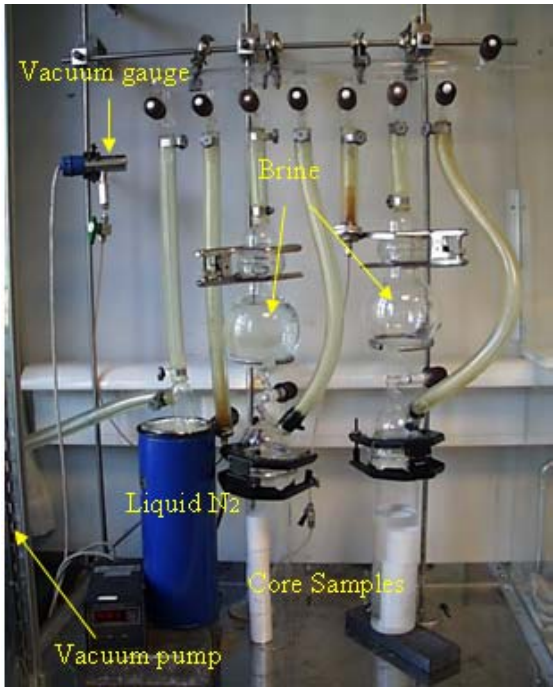

Figure 4.4.1: Equipment used in vacuum evacuation.

The core samples were left submerged in degassed brine for approximately 12 hours to maximize the saturation of the effective pore system. Then, once again the weights of the samples were measured, and the effective porosity (see Chapter 1.1) was calculated by use of equation (4.4.1).

$$\phi_{eff} = \frac{m_{totally\ \ saturated} - m_{dry}}{\rho \times V_b} \qquad (4.4.1)$$

The cores were then again stored in brine for another week to reach ionic equilibrium with the rock constituents.

4.5 Measuring the Permeability

The core permeability to brine was being measured by use of a biaxial core holder, (see Figure 4.3.2), with a slight confinement pressure. The brine was injected at three different rates, and the differential pressure was measured. The permeability was found by use of equation (1.2.1). Because of the fragile nature of chalk material, net confinement pressure should not exceed 10 bar. This was to ensure that the cores were kept within the elastic compression region.

4.6 Altering the Wettability by Aging

Earlier, the wettability has been altered by submersing core samples in the crude oil at elevated temperature for various length of time. But, as pointed out in Chapter 2.2.2, this may result in a variation in wettability within the core [32]. The core illustrated in Figure 2.2.2.8 was aged in crude oil after it had been flushed to initial water saturation with crude oil. The soaking process in crude oil probably altered the outside of the plug to a less water-wet state whether was the case for the interior part. This effect has now been reduced by a modified process of altering wettability [34]. This new process has been used in this thesis.

The modified aging process started out with crude oil drainage (Ekofisk oil; composition has been measured to be 0.90 wt. % asphaltenes, 53 wt. % saturated hydro carbons, 35 wt. % aromatics and 12 wt. % nitrogen-sulphur-oxygen containing components [40]). The drainage was performed at 80^{o}C with constant pressure of approximately 2 bar/cm. This pressure corresponded to capillary pressure values near S_{wi} on a capillary pressure curve. To keep the temperature stable, this process was done inside a hot cabinet, illustrated in Figure 4.6.1. The drainage process was stopped when $S_w \approx 23$ % in order to keep the S_{wi} similar in all experiments. Saturation calculation was done by material balance. When S_{wi} was reached, the direction of flow was reversed, and another pore volume of crude oil was injected. This was done to reduce the end effects of the drainage process.

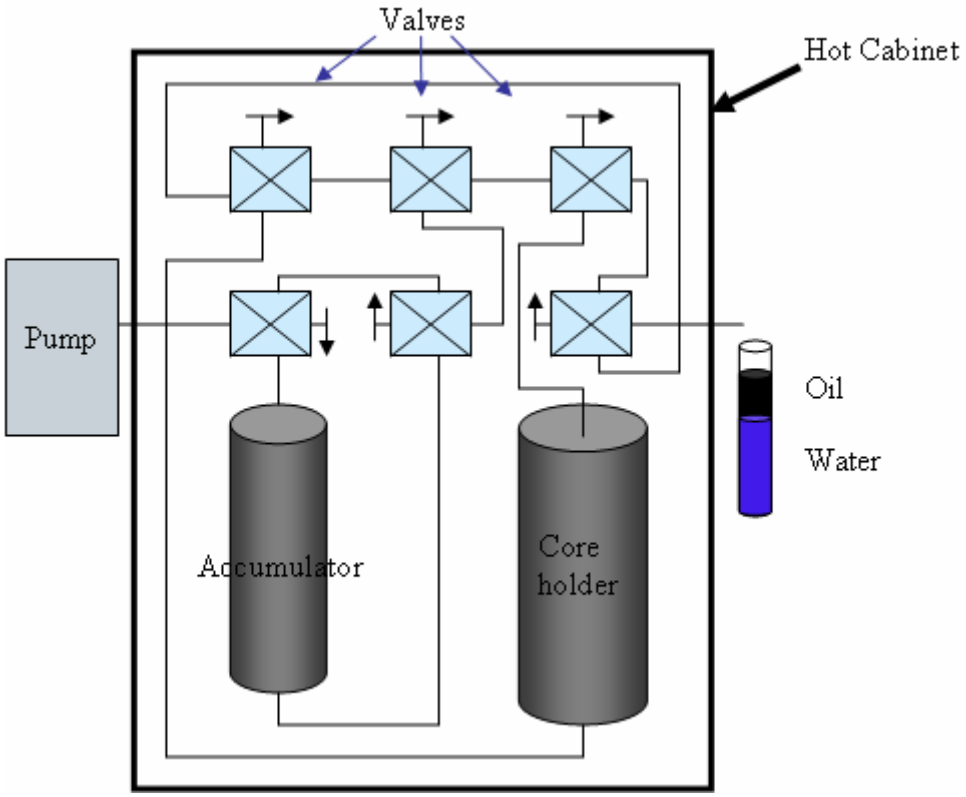

Figure 4.6.1: Illustration of the laboratory oven. The flow direction of the oil is determined by use of the valves.

Wettability was altered by continuously flushing crude oil through the core plugs, still at 80°C. Aging at elevated temperature has been shown to be substantially more effective than aging at room temperature [41]. Another reason for applying a stable temperature as long as the crude oil was inside the rock was to prevent possible wax problems with this crude oil. The direction of flow was reversed during this process, in order to achieve as uniform wettability distribution as possible. The reason for using crude oil was the contents of heavy components, such as asphaltenes and resins. Mineral oil, such as decane, has been shown not to alter the wettability [41]. To ensure the absorption of components, the flow rate in this aging process was set to 1.5 ml/h (corresponding to 3 ml/h for 2''. In this thesis 1.5'' cores have been used) (Torsvik, Haugland, Private Communication).

To obtain Amott indices of approximately $I_w = 0.3$ and $I_w = 0.6$, the length of the aging process was set to 6 days and 2 days, respectively.

After aging, a miscible displacement of the crude oil with decalin and then decane was carried out (at the same temperature). There were two reasons for doing this. Firstly, this was performed in order to stop the aging process. Secondly, to obtain reproducible results it was desirable to deal with the same mineral oil; that is decane. The miscible displacement process was performed by first inject 5 PV decahydronaphtalene (decalin), and then inject another 5 PV n-decane. Decalin was used as a buffer between the crude oil and n-decane to prevent asphaltene precipitation [42]. The core samples were then submersed in n-decane at 80°C to get a gradually cooling to room temperature.

4.7 Wettability Measurement – Amott Test

After the aging process was completed, an Amott test was performed to measure the wettability. The reason for not doing a complete Amott-Harvey test, including the oil imbibition test, was that previous work has shown that the current alteration of wettability does not lead to a spontaneous displacement of water by oil ([34] and [43]).

The core sample was placed in graduated imbibition cells, and the amount of oil spontaneous displaced by water was measured (see Figure 4.7.1). After approximately 1000 hours, or when the spontaneous production of oil had stopped, the cores were being placed in core holders and forced displacement was carried out to obtain S_{or}. Again, this was done at a pressure of 2 bar/cm and a confinement pressure of 17 bar. The Amott index was calculated as described in Chapter 1.5.2.

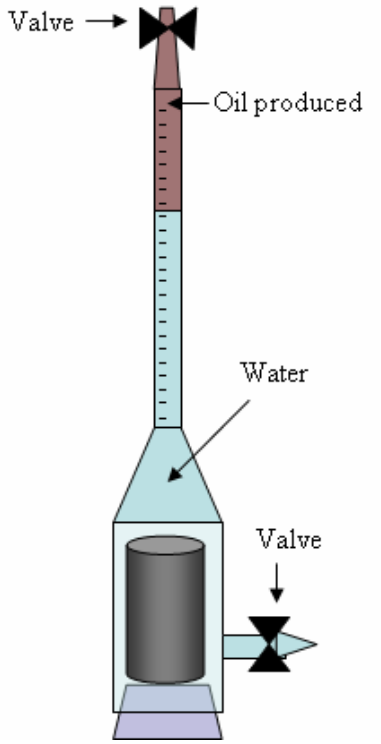

Figure 4.7.1: A graduated imbibition cell. The volume of oil displaced spontaneously by water is measured.

CHAPTER 5

The Procedure of the DMS Method

The DMS method, Direct Measurement of Saturation, was used to measure capillary pressure curves, at various wettabilities. This method utilizes MRI imaging and an oil phase that solidifies at room temperature to obtain the P_c scanning curves directly, at only one centrifuge rotational speed. The principles of this test are described in Chapter 2.2.2. There are some limitations due to radial and gravity effects [26], [44]. Chen and Ruth showed that gravitational effects are negligible if the centrifuge is run above 500 RPM [27]. Since these experiments are run above this critical RPM, this approach may be used satisfactorily. The radial effect, however, (illustrated in Figure 5.1) is not taken into account in the calculations of the capillary pressure. This effect is although reduced by using the image analyzer program (to be discussed in Chapter 6).

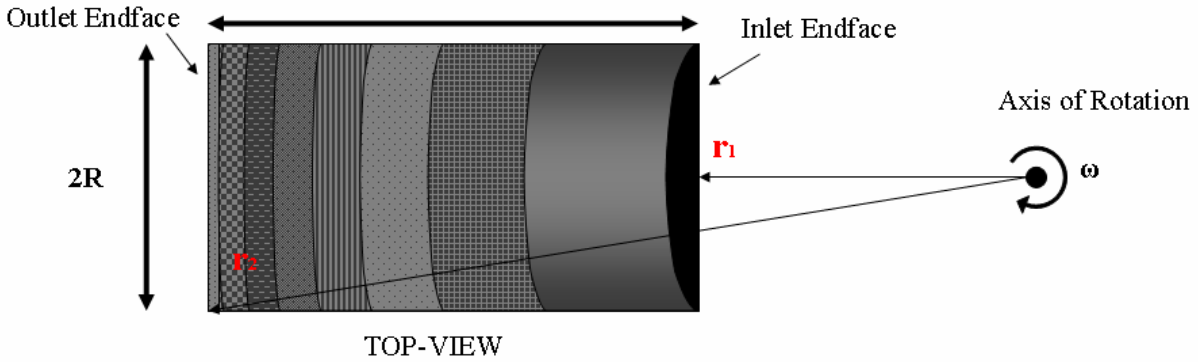

Figure 5.1: An illustration of the radial effect; the radial distribution due to centrifugal field.

A total of six core plugs; 4 that have been aged and 2 strongly water-wet (all chalk), were shipped to ConocoPhillips ResearchCenter, Bartlesville, OK, USA. The aging procedure is described in Chapter 4.6.

5.1 Core Preparation

The core samples that had been aged were shipped to the Research Centre at S_{or}, with decane as the oil phase. The cores had been water flooded after preparation for safety reasons due to the shipping (shipping the cores at S_{or} submerged in water is safer than shipping the cores at S_{wi} submerged in oil). After doing NMR measurements to verify/calibrate the saturations (see Chapter 6.1), the samples were drained to S_{wi}. The decane was then replaced by octadecane. Since the octadecane solidifies at 28.2°C, this process was done in an oven, at 45°C. The set-up is shown in Figure 5.1.1.

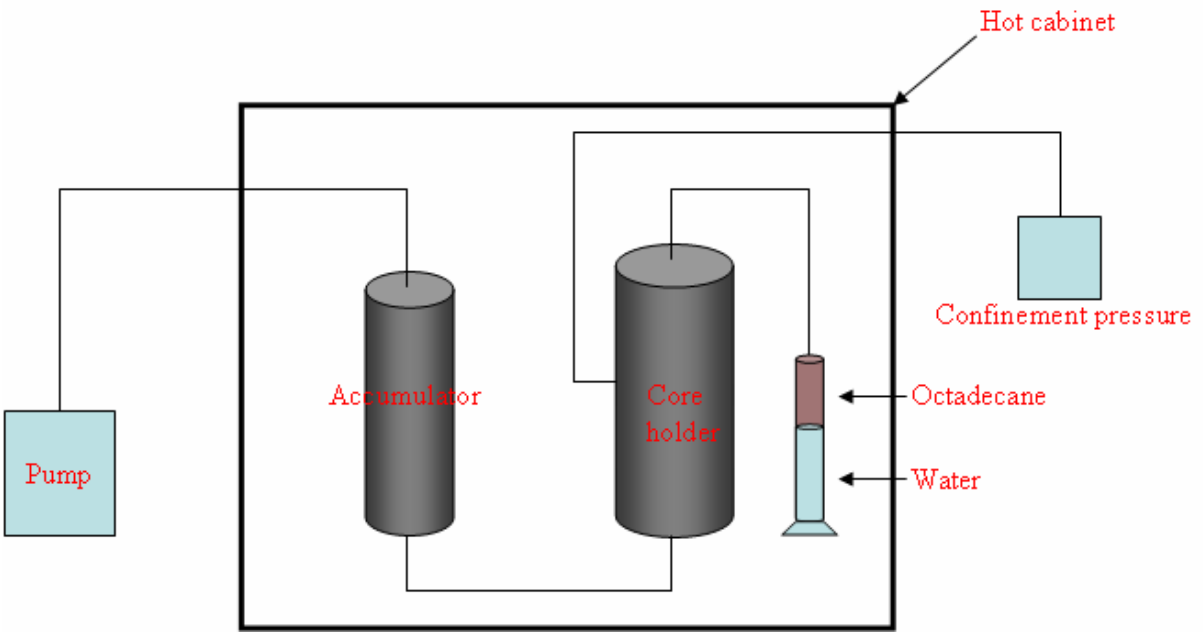

Figure 5.1.1: The set-up for the replacement of decane by octadecane. The accumulator is filled with octadecane.

After this replacement process, the samples were cooled in a refrigerator for approximately 12 hours, to make sure the octadecane had solidified. The samples were submerged in octadecane. This was to prevent air-gaps due to a decreasing volume of octadecane (2 %) when solidifying. The oil phase could then be considered immobile. A teflon sleeve was mounted around the core sample, so that fluids only may flow through the inlet and outlet of the core (see Figure 5.1.2). NMR measurements were then carried out to see whether there was any decane left within the samples; to check the efficiency of the octadecane-decane replacement. At this point, when the octadecane had solidified, it was necessary to obtain a fluid saturated image by the MRI on each core sample in order to establish the necessary calibration curve (see Chapter 2.2). [Preferentially, an MRI image of 100% water saturated core should have been taken in order to get an adequate calibration curve. But since the samples had been aged before arriving the research centre, this was unfortunately not achievable (Since $S_{or} > 0$).]

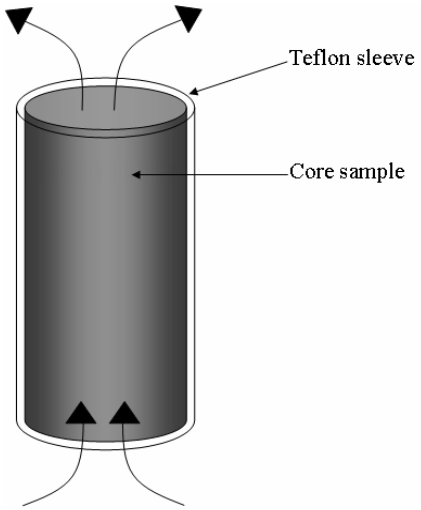

Figure 5.1.2: A teflon sleeve is mounted around the core sample. In this way, fluids may only flow through the inlet and outlet of the core.

5.2 The Centrifuge Experiment

5.2.1 Imbibition P_c Measurement

Before starting the centrifuge experiment, one needed to set the free water level, in order to establish a reference point (where $P_c = 0$). Based on earlier experiments [24], one could assume that a maximum negative capillary pressure at -15 psi (~ -1 bar) was needed. A spreadsheet was used to calculate the free water level (see Appendix A). To achieve the maximum capillary pressure as noted above, the free water level was found to be at the middle of the core (see Figure 5.2.1.1). Since the cores at this point were at S_{wi}, this would give us both the positive and negative part of the imbibition capillary pressure curve.

The density of brine at room temperature was calculated to be 1.057g/cm^3. In this experiment, the centrifuge was brought up to a temperature of 35^{o}C to liquefy the octadecane. In order to calculate the amount of water needed to obtain this free water level, the density of brine at this temperature was needed. From tables, one could find the density of octadecane at T=35^{o}C to be 0.7714 g/cm^3, and at room temperature ρ=0.777 g/cm^3. $\rho_{brine,T=35^oC}$ was ***estimated*** by equation (5.2.1.1).

$$\rho_{brine,T=35^oC} = \rho_{brine,T=22^oC} \times \frac{\rho_{octadecane,T=35^oC}}{\rho_{octadecane,T=22^oC}} \qquad (5.2.1.1)$$

Solving this equation gave $\rho_{brine,T=35^oC} \approx 1{,}053$ g/cm^3.

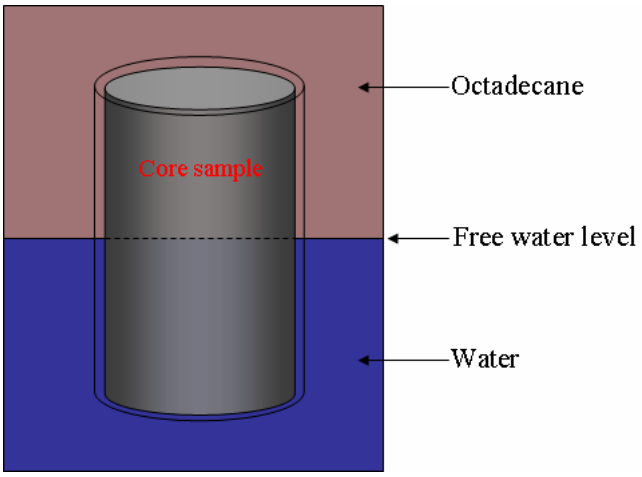

Figure 5.2.1.1: The free water level is set at the middle of the core.

The cores were mounted in a centrifuge core holder at room temperature. The calculated amount of water was added to achieve a free-water-level height along half the length of the core plug. As mentioned in Chapter 2.2, the free-water-level should essentially be constant throughout the spinning since the centrifuge cell had a bulk volume significantly larger than the pore volume of the plug. Additional octadecane was added to immerse the core in fluid (see Figure 5.2.1.2).

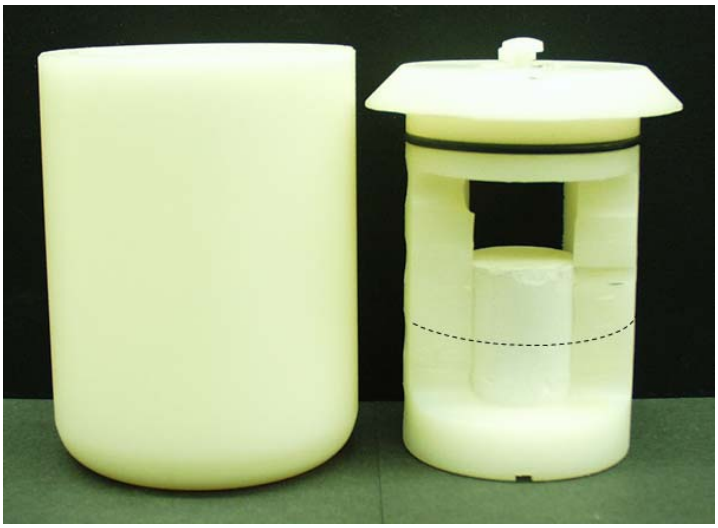

Figure 5.2.1.2: The centrifuge core holder. The free water level is indicated by the stippled curve. Octadecane was surrounding the plug above this curve.

The centrifuge, a Sorvall RC 26 Plus, with swinging buckets, was spinning at 2400 RPM while at room temperature (after balancing the buckets). The temperature was brought to 35^{o}C and held for 8 days to reach equilibrium (Rich Treinen, Private Communication). By increasing the temperature after the centrifuge reached the desired rotational speed, the oil phase became mobile with both spontaneous and forced imbibition starting upon exceeding the 28.2^{o}C melting point of octadecane. Spontaneous imbibition occurred in the area above the free water level, forced imbibition in the part of the core below the free water level. Prior to the MRI measurements (sagital image) the plugs were cooled to 15^{o}C while at speed in the centrifuge (overnight), allowing the oil phase to solidify and thus become immobile. The recorded data provided the in-situ saturation information necessary to generate both the positive and negative part of the capillary pressure imbibition curve. The plugs were weighed before and after spinning to calculate the saturations.

A forced imbibition was then carried out at a maximum displacement pressure of 12 bar (2 bar/cm) to bring the core samples to S_{or}. Trying to establish a uniform S_{or}, a subsequent water flooding was performed in both directions. The core plugs were then again imaged.

5.2.2 Secondary Drainage P_c Measurement

The core samples were mounted in the centrifuge core holders in the exact same position as the previous experiment. To achieve the same capillary pressure as in the imbibition P_c measurement, enough water was added to maintain a free water level of half the length of the core plug.

The centrifuge was spinning at 2400 RPM while at room temperature. The temperature was brought to 35^{o}C and hold for 8 days to reach equilibrium. After cooling to 15^{o}C, the centrifuge was stopped and the core plugs were imaged. Again, the plugs were weighed before and after spinning to calculate the saturations.

5.3 Wettability Measurement

Because of lack of time, the wettabilities of the core samples were not measured before shipping. Hence this needed to be done after the centrifuge experiments. Since these measurements were performed several months after finishing the P_c experiments, NMR measurements were performed to calculate the saturations. The plugs were then drained with octadecane to S_{wi}. The maximum displacement pressure was 12 bar, and confinement pressure was set to 17 bar.

The two strongly water-wet core samples had been exposed to air, hence they needed to be water flooded with a backpressure of 10 bar (Johnnie Jack, Private Communication). The set-up is shown in Figure 5.3.1. The displacement- and confinement pressure was now 22 bar and 27 bar, respectively.

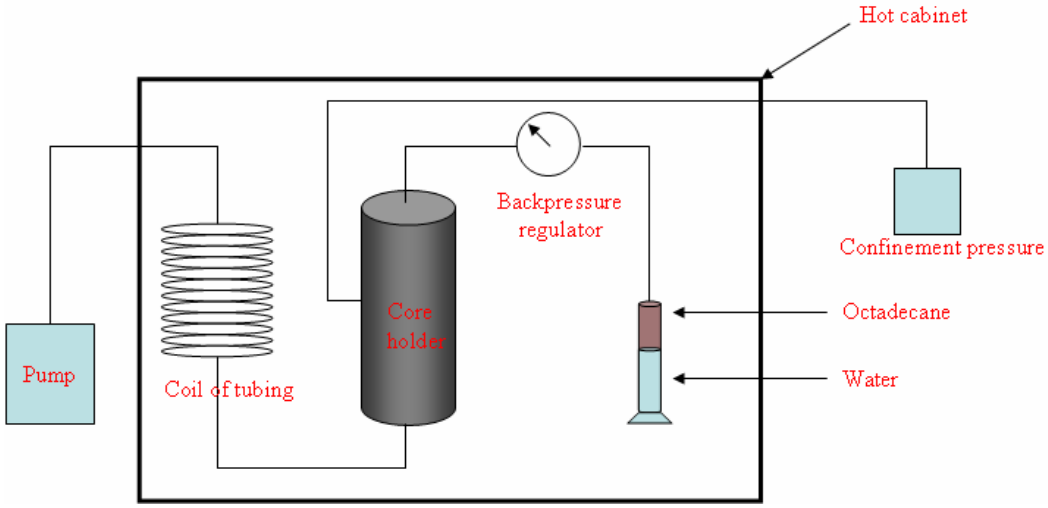

Figure 5.3.1: The set-up for removing air from core samples. A backpressure regulator of 10 bar is being used to compress the air.

After removing the air, the core samples were again drained to S_{wi}. They were then placed in imbibition cells inside an oven at 35°C, and the amount of oil spontaneously being produced by water imbibition was measured. The saturations were found by measuring the weight before and after spontaneous imbibition, corroborating to material balance calculations.

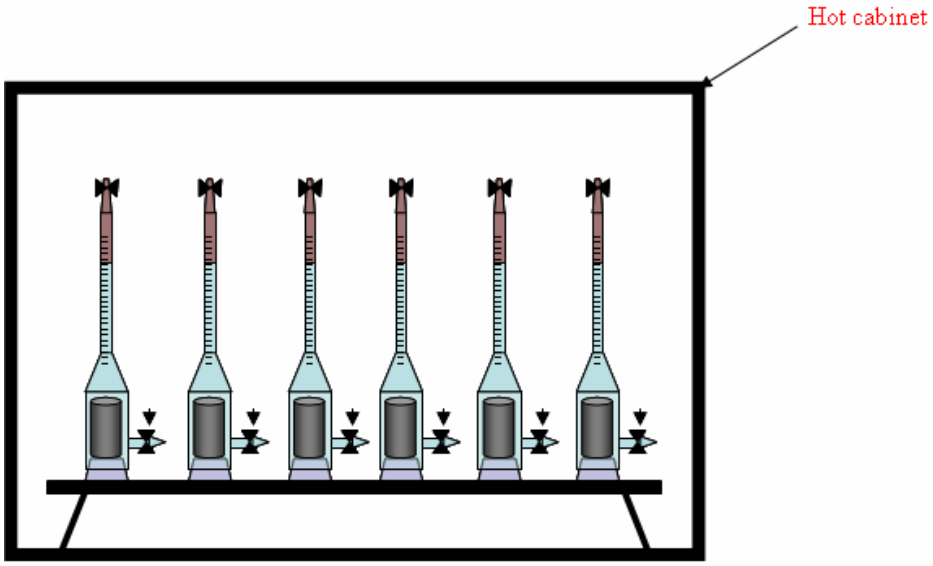

Figure 5.3.2: The imbibition tests are done inside an oven, at a temperature of 35°C.

After approximately 1000 hours, or when oil was no longer being produced, forced imbibition was performed and the Amott indices were calculated as described in Chapter 1.5.2.

CHAPTER 6

NMR and MRI Procedures

To verify the average saturations of the core samples and the replacement process of decane by octadecane (as mentioned in Chapter 5), NMR spectroscopy was used by relating the T_2-relaxation time to saturations, i.e. calculating the saturation of each phase. MRI tomography was used as the high spatial resolution imaging technique required to measure the saturation of the cores for the DMS method described in Chapter 2.2.2 and Chapter 5. These measurements were done at the ConocoPhillips Research Centre, Bartlesville, OK, USA.

6.1 NMR Measurements

First, the NMR instrument, a MARAN, bench top 10MHz spectrometer, was calibrated to the core samples. From chapter 3.3.1, there is a relation between pore surface/volume ratio and the measured T_2-relaxation time. The cores being aged had a water saturation of $1\text{-}S_{or}$ (decane being the hydrocarbon) whilst the strongly water-wet cores were 100 % water (brine) saturated. Salts like NaCl and $CaCl_2$ do primarily not contribute to significantly changes in T_2.

To prevent vaporizing, the cores were wrapped up in a plastic film before measurements were done. T_2 was measured by a standard CPMG-sequence. To achieve an optimal signal, an inversion recovery sequence was run for each core. The parameters used are listed in Table 6.1.

Table 6.1: The parameters used in NMR measurements

Core Sample	PO6	PO7	PO9	PO10	PO11	PO13
State	Aged 6 days	Aged 2 days	Aged 2 days	Aged 6 days	100% S_w	100% S_w
S_w	$1\text{-}S_{or}$	$1\text{-}S_{or}$	$1\text{-}S_{or}$	$1\text{-}S_{or}$	1	1
RG	25	25	25	25	25	25
RD	2000000	2000000	2000000	2000000	2000000	2000000
τ	500	500	500	500	500	500
90 pulse	28	28	28	27,25	27,8	28
Number of scan	128	128	128	128	128	128

The echo train data were fitted to a multi exponential model (equation 3.3.1.4), and the resultant distribution could be shown graphically, as illustrated in Figure 6.1.1.

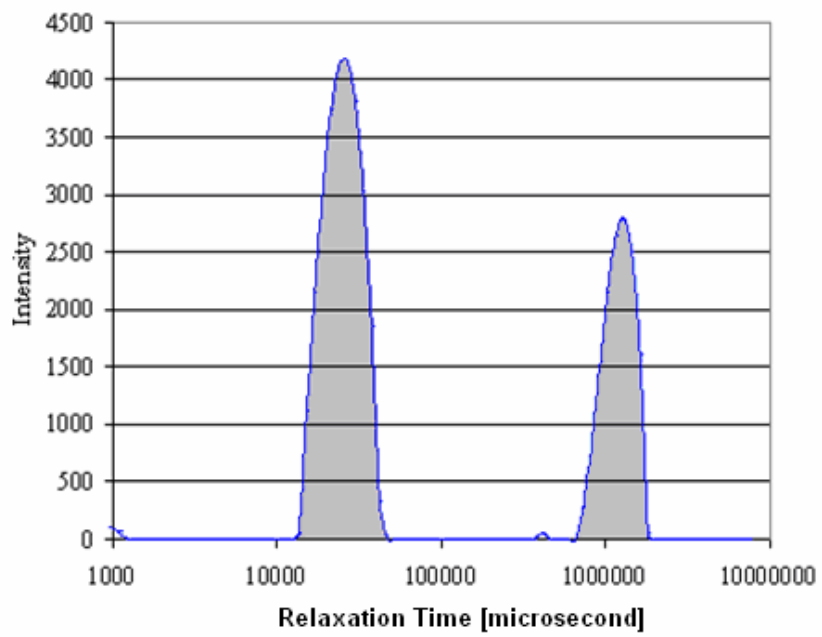

Figure 6.1.1: One example of the T_2 distribution.

The lowest values of T_2 represent water, and the higher values represent decane. The T_2 relaxations values due to water and decane were summarized and the water saturations were found by calculating the ratio of the sum of the intensities representing water to total intensity.

Since octadecane was solidified at room temperature, the replacement process of decane by octadecane was verified when the 2nd peak disappeared, as seen in Figure 6.1.2.

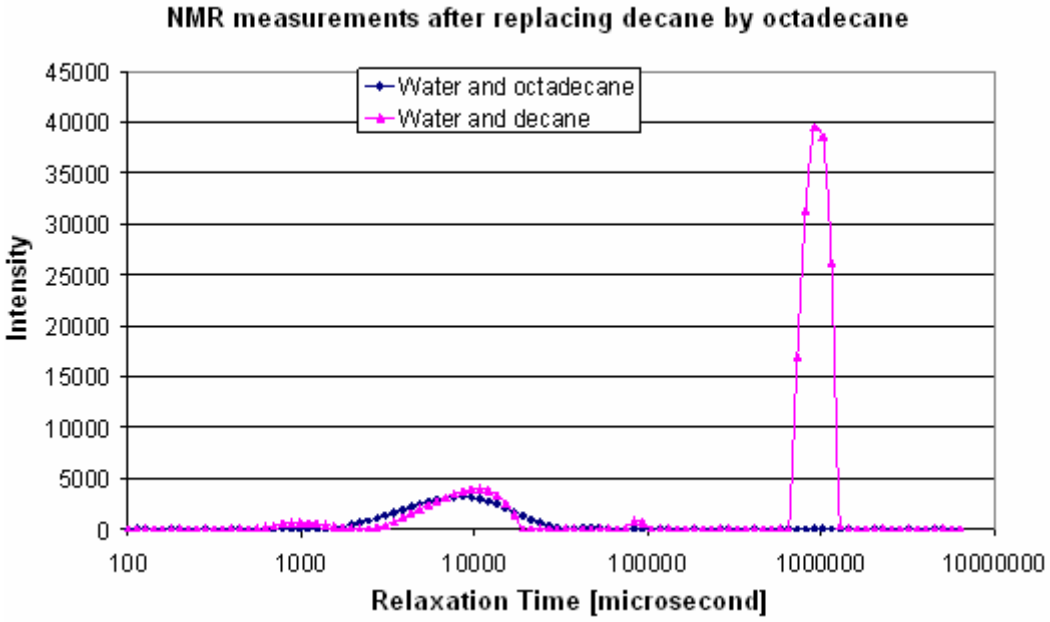

Figure 6.1.2: Octadecane replacing decane.

6.2 MRI procedures

The magnetic resonance imager used was a Varian 85/310 CSI. It had a 31 cm bore, a superconducting magnet [which created a static magnetic field (denoted B_1 in chapter 3.1) of 2 Tesla] and operated at 85.55 MHz for hydrogen protons. A 9 cm I.D. saddle coil was used as both transmitting and receiving coil. The amount of fluid hydrogen protons was obtained by use of a Hahn spin-echo sequence with a 4 ms echo time and a 2.0 second recovery time. A sagital image, as shown in Figure 6.2.1, was taken for each core. That is: One slice, approximately 4 mm thick, was obtained through the centre axis of the plug. This is the basis for MRI derived saturation distributions presented in this thesis.

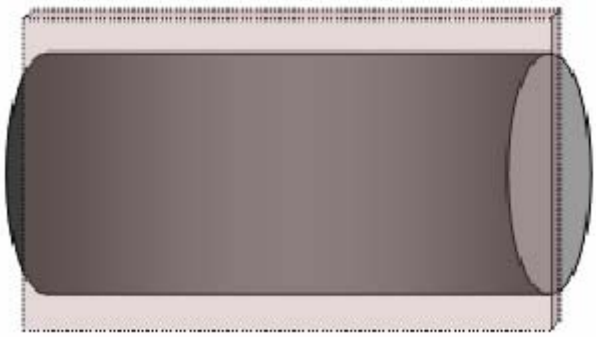

Figure 6.2.1: An illustration of the orientation of a sagital image. A 4 mm thick slice is obtained through the centre of the sample.

As already mentioned, octadecane solidifies at room temperature. Hence it does not image by MRI, and imaging of the plug at laboratory conditions of 23^{o}C made it possible to obtain the water saturation distribution directly from the image intensities. As can be seen in Figure 6.2.1, the sagital image is a rectangle aligned in parallel with the centrifugal force produced in the centrifuge. The field of view was 9 cm x 8 cm with a pixel resolution of 0.35 x 0.62 mm.16 repetitive measurements were averaged at each image pixel. The images consisted of 255 levels of grey in a 256x256 display. The intensities of the individual pictures were adjusted to produce a presentable visual display (using the same vertical scale for each core).

At this point, however, it was necessary to be accurate on positioning the core before imaging, as previously mentioned in Chapter 5. The orientation of the core had to be exact the same at every image, in all three dimensions. If this was not fulfilled, a comparison of the images could be affected.

The images obtained from the MRI were exported as an 8 bit .tiff-file, and processed in an image analyzing program; ImageJ [45]. The images were sectioned into a column of rectangular volume elements, with an average height of 3 pixels. 10 pixels (3 mm) on each side of the rectangle were not included in the volume elements in order to eliminate edge effects often observed at the sides of the plug (Rich Treinen, Private Communication) (see Figure 6.2.2). By doing this, the previously discussed radial effect (see Chapter 5) is reduced, even if it is not taken into account in the calculations of the capillary pressure. Each volume element had a bulk volume of 0.2 cm^3; the pore volume depended on the porosity. The number of volume elements depended on the core length. In this thesis 35 measurements of saturation were obtained along the length of each core plug.

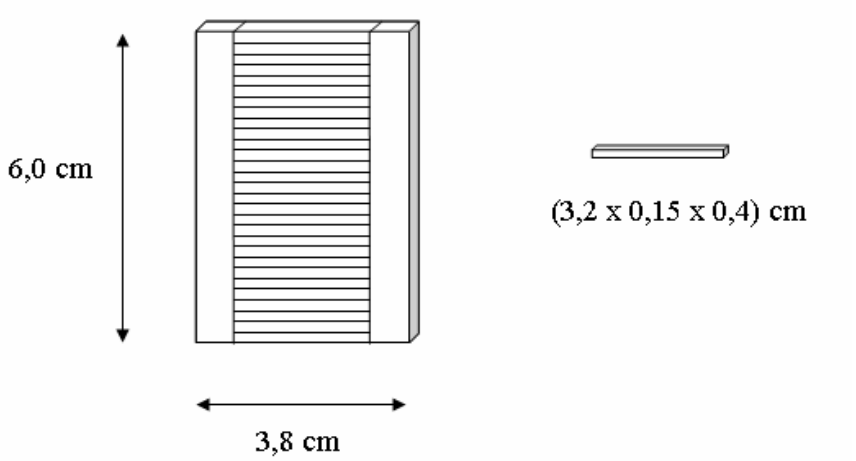

Figure 6.2.2: The column of rectangular volume elements and volume element size.

The images were not representative with respect to length and width, so they needed to be calibrated to the actual values. ImageJ was then used to calculate the average intensities of each volume element. By use of the image at S_{wi} (known average saturation) and assuming zero intensity in dry core, the saturation was calculated by a calibration curve.

The free water level described in Chapter 5 was seen from the images, and the height after centrifuging could easily be measured. This gave the reference point r_2 which is needed to calculate the capillary pressure by the following equation

$$P_c = \frac{1}{2}\Delta\rho\omega^2\left(r_2^{\,2} - r_1^{\,2}\right), \qquad (6.2.1)$$

where $\Delta\rho$ is the density difference between the two phases, ω is the angular velocity, r_2 is the radius from the centre of rotation to the FWL, and r_1 is the radius from the centre of rotation to the point of interest.

Inasmuch as both the saturation and capillary pressure of each point was known, the capillary pressure curve could be drawn.

Part 3

Results and Discussion

CHAPTER 7

Preparation of Core Plugs for Special Core Analysis

A total of 20 1½"-diameter core samples have been prepared as described in Chapter 4. The results of standard core analysis and imbibition-tests are presented in this chapter.

7.1 Porosity and Permeability

Core plug data and the measured porosity and permeability of each plug is presented in Table 7.1

Table 7.1: Results from standard core analysis.

Core	Length [cm]	±	Diameter [cm]	±	m_{dry} [g]	±	m_{sat} [g]	±	V_p [cm3]	±	Porosity [%]	±	Abs. Perm [mD]	±
PO6	6,00	0,01	3,78	0,01	96,8	0,1	128,7	0,1	30,2	0,2	44,8	0,4	4,4	0,1
PO7	6,00	0,01	3,79	0,01	95,6	0,1	128,0	0,1	30,7	0,2	45,4	0,4	6,3	0,1
PO9	5,99	0,01	3,78	0,01	95,5	0,1	127,5	0,1	30,3	0,2	45,0	0,4	3,5	0,1
PO10	6,00	0,01	3,78	0,01	96,0	0,1	128,0	0,1	30,3	0,2	45,0	0,4	6,9	0,1
PO11	6,02	0,01	3,78	0,01	96,8	0,1	129,0	0,1	30,5	0,2	45,1	0,4	6,8	0,1
PO13	5,99	0,01	3,78	0,01	95,9	0,1	128,0	0,1	30,4	0,2	45,2	0,4	9,4	0,1
PO15	5,97	0,01	3,81	0,01	94,4	0,1	125,6	0,1	29,5	0,2	43,4	0,4	3,1	0,1
PO16	6,02	0,01	3,81	0,01	94,5	0,1	125,6	0,1	29,4	0,2	42,9	0,4	3,3	0,1
PO17	6,03	0,01	3,81	0,01	95,7	0,1	127,7	0,1	30,3	0,2	44,1	0,4	3,7	0,1
PO18	6,02	0,01	3,81	0,01	97,0	0,1	128,2	0,1	29,5	0,2	43,1	0,4	3,9	0,1
PO21	6,01	0,01	3,83	0,01	98,8	0,1	131,3	0,1	30,7	0,2	44,4	0,4	1,2	0,1
PO22	6,01	0,01	3,82	0,01	97,6	0,1	130,1	0,1	30,7	0,2	44,7	0,4	4,1	0,1
PO23	6,05	0,01	3,82	0,01	98,4	0,1	130,6	0,1	30,5	0,2	44,0	0,4	4,6	0,1
PO25	6,04	0,01	3,83	0,01	99,3	0,1	131,2	0,1	30,2	0,2	43,4	0,4	3,4	0,1
PO26	6,01	0,01	3,81	0,01	97,8	0,1	130,2	0,1	30,7	0,2	44,8	0,4	3,6	0,1
PO27	6,02	0,01	3,81	0,01	97,4	0,1	130,0	0,1	30,8	0,2	45,0	0,4	3,9	0,1
PO28	6,00	0,01	3,82	0,01	98,2	0,1	130,5	0,1	30,6	0,2	44,5	0,4	3,8	0,1
PO29	6,00	0,01	3,83	0,01	99,1	0,1	131,6	0,1	30,7	0,2	44,5	0,4	4,7	0,1
PO30	6,02	0,01	3,79	0,01	97,1	0,1	128,7	0,1	29,9	0,2	44,5	0,4	4,5	0,1
PO31	6,01	0,01	3,79	0,01	97,5	0,1	129,0	0,1	29,8	0,2	44,3	0,4	3,4	0,1

As mentioned in Chapter 4.1, the core material is Rørdal Chalk. The cores PO21 to PO29 are from material obtained in the late 1990's, while the rest of the samples are of material obtained in June 2003. From Table 7.1, one can see that the porosity values are rather homogenous. The permeabilities, on the other hand, are not that uniform. The reasons for this might be heterogeneities within the core material (e.g. vugs), uncertainties related to the used instruments, etc. In Chapter 7.2, a qualitative analysis of the newer core samples is reported.

7.2 Qualitative Analysis of Core Plug Samples

By looking at epoxy-prepared chalk samples (of new type) through a microscope, one could clearly see vugs, see Figure 7.2.1. (A vug = a cavity, void or large pore in a rock that is commonly lined with mineral precipitates [5]). One is normally not able to see these vugs in such a microscope (James Howard, Private Communication).

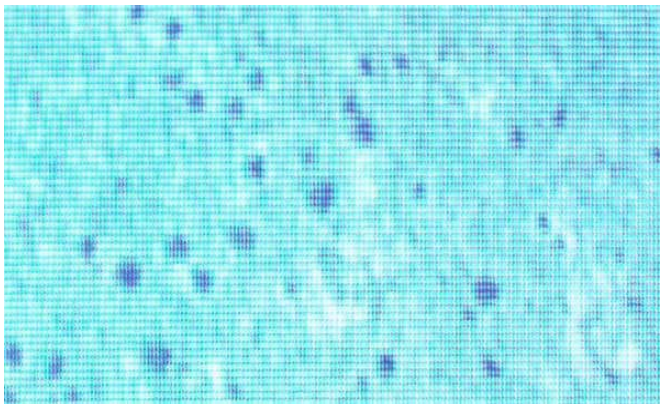

Figure 7.2.1: The chalk sample seen through a microscope. The darker spots are vugs.

By using an electron microscope instead of an optical microscope, the enlargement increases. Unfortunately, the samples have not been polished well enough to get perfect images. However, the vugs can easily be seen, hence measurements of the dimensions, the components, etc. could be performed.

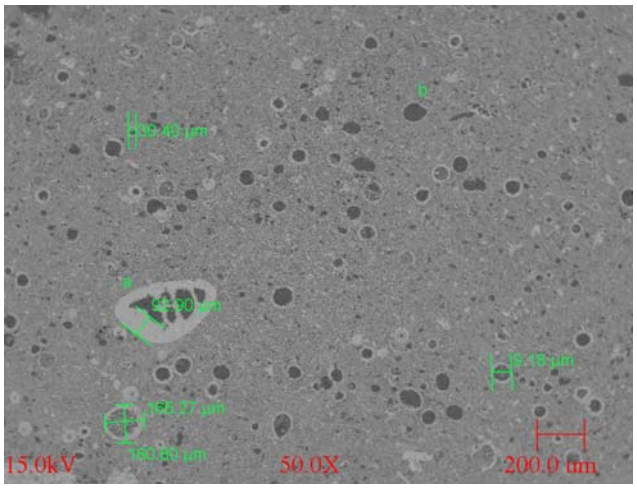

Figure 7.2.2: Electron-microscope image of sample 1. As indicated in the figure, some of the dimensions are measured.

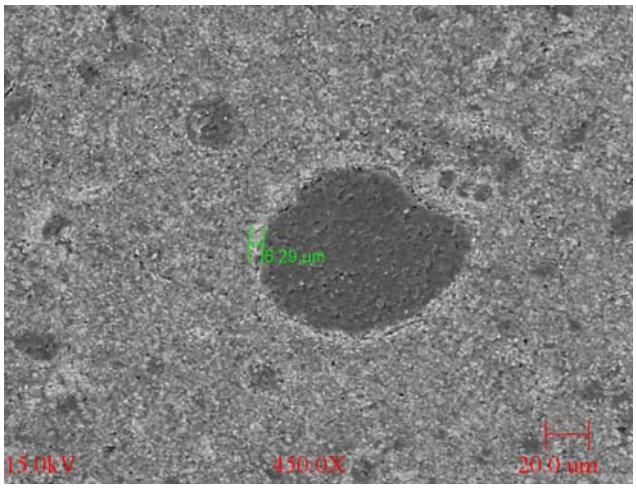

Figure 7.2.3: Enlargement of point 'b' in Figure 7.2.2. The dimension of the layer at the pore-wall is measured.

Through an electron microscope, the smaller vugs are also detectable. There seems to be a variety in the sizes of the vugs. In the figure above, one can see the existence of a layer at the pore-wall. This layer is present in most of the vugs (see Figure 7.2.2). The thicknesses of these layers are found to vary from 6 to 25 µm. According to some measurements, these layers contain no Magnesium (Mg), which indicates that these layers are not Dolomite, but more likely Calcite.

A closer look at some sections of the samples by using an Energy Dispersive Spectrum (EDS), yields improved qualitative measurements, see Figure 7.2.4 and Figure 7.2.5.

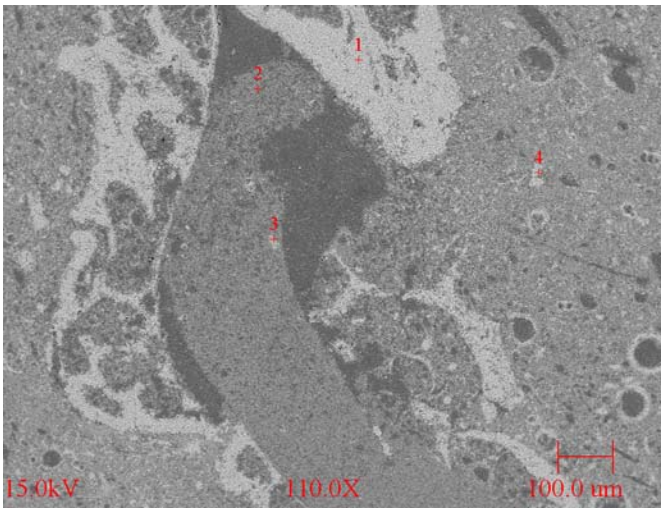

Figure 7.2.4: A closer look at a section of the samples. Qualitative analysis are done at some areas, noted 1-4.

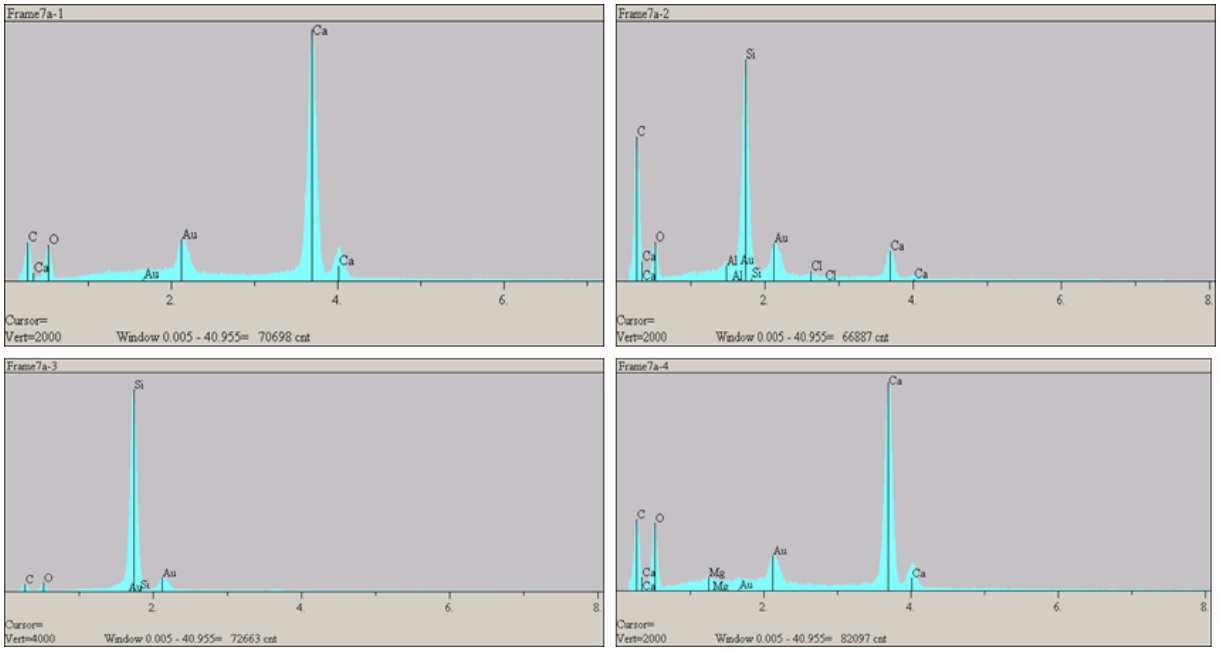

Figure 7.2.5: Qualitative analysis areas 1 to 4 in Figure 7.2.4.

Frame 1 and Frame 4 in Figure 7.2.5 show a large amount of Calcium (Ca), which indicates Calcite. Frame 2 shows a rather high content of Carbon, Chloride and Oxygen (C, Cl and O) which are due to the epoxy. The Silicon is due to quartz, while the Aluminium and Gold (Al and Au) are present due to residues from the polishing. The low content of Magnesium indicates as previously mentioned that the amount of Dolomite is low / negligible.

It would have been interesting to take a look at a sample of the "old type" of chalk plugs, to verify whether these vugs are present in the newer core samples only, or not. Unfortunately, an old plug was not available at the ConocoPhillips Research Centre when these analyses were performed. Therefore, one can only assume that this is a new "phenomenon".

To obtain a comparison to real reservoir chalk, these images are compared with a chalk sample from the Ekofisk Field ("**Tor 2/4, K4**"). An image of this sample is shown in Figure 7.2.6.

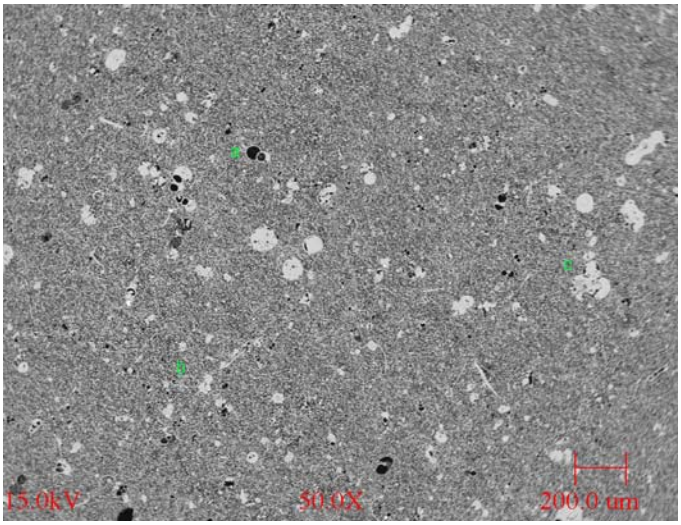

Figure 7.2.6: An image of a chalk-sample from, "Tor 2/4, K4", Ekofisk Field.

When Figure 7.2.6 is compared to the new Rørdal chalk in Figure 7.2.2, one can clearly see that the number/presence of vugs in "Tor 2/4, K4" is lower. In addition, those vugs being present seem to be cemented. To compare the composition of the samples, an EDS was taken of this last image, at the positions marked "a" and "c" in Figure 7.2.6.

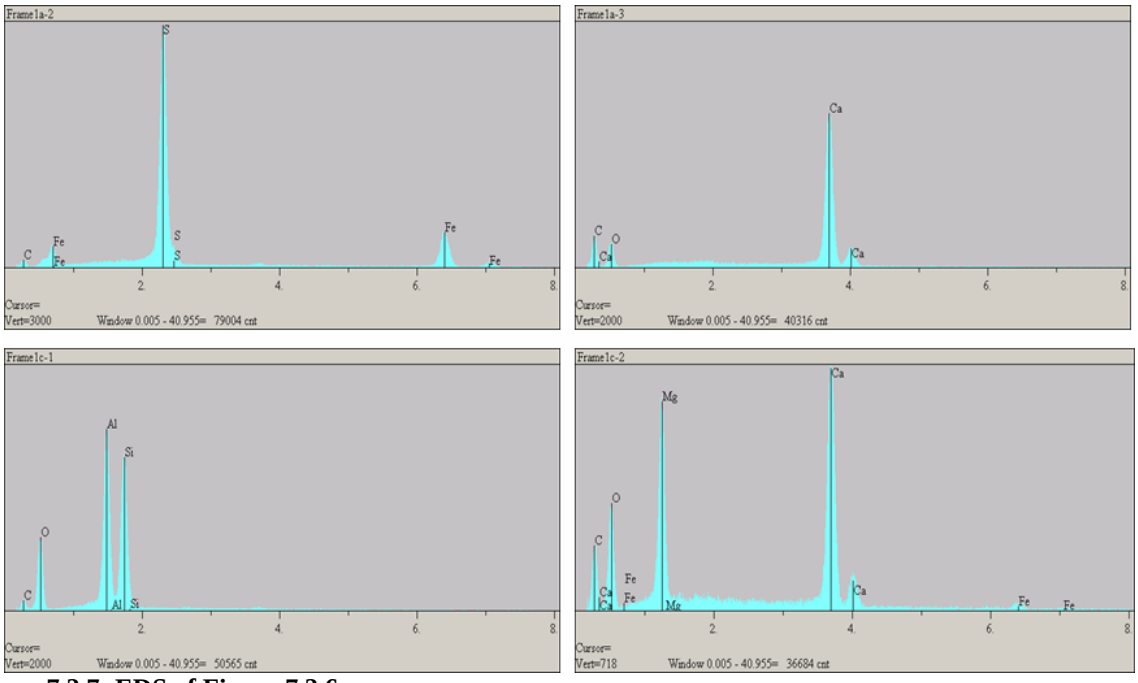

Figure 7.2.7: EDS of Figure 7.2.6.

Frame 1a-2 in Figure 7.2.7 shows traces of Pyrite (FeS_2). Frame 1a-2 indicates Calcite (as is also seen in Figure 7.2.5), and Frame 1c-1 and Frame 1c-2 indicate Kaolinite (clay – Al, Si and O) and Dolomite [Mg – Fe might appear in dolomite as well (James J Howard, Private Communication)].

To sum up; the number of vugs present in the Rørdal outcrop chalk seems to be larger than is the case in the core sample obtained from the well bore core from the Ekofisk Field. There might be several reasons for the presence of these vugs. Most likely this phenomenon arise when water flow through the formation, and fossils present in the chalk dissolve.

7.3 Imbibition Tests and Amott Indices

Some of the cores have been aged using Ekofisk Oil, as described in Chapter 4.6. S_w at different steps of the procedure, time of aging, amount of oil produced by spontaneous and forced imbibition, amount of mobile oil and Amott Indices are presented in Table 7.2.

Table 7.2: Imbibition tests and Amott Indices

Core	S_{wi}	Time of aging [days]	Produced oil by spont. imbibition [ml]	S_w	Produced oil by forced imbibition [ml]	$S_{w,or}$	Mobile oil [ml]	Amott Index	Oil-phase[a]
PO6	0,335*	6	4,30	0,477	9,6	0,796	13,9	0,309	OD
PO7	0,294*	2	3,10	0,395	11,9	0,783	12,0	0,207	OD
PO9	0,336*	2	4,00	0,468	10,0	0,798	14,0	0,286	OD
PO10	0,323*	6	2,80	0,415	12,8	0,838	15,6	0,179	OD
PO11	0,251*	0	8,90	0,543	1,0	0,576	9,9	0,899	OD
PO13	0,249*	0	9,20	0,552	1,0	0,585	10,2	0,902	OD
PO15	0,228	2	8,60	0,519	9,60	0,845	18,20	0,473	D
PO16	0,211	2	7,30	0,459	10,70	0,823	18,00	0,406	D
PO17	0,240	6	3,50	0,356	12,70	0,775	16,20	0,216	D
PO18	0,234	6	3,60	0,356	11,30	0,739	14,90	0,242	D
PO22	0,233	2	7,60	0,480	7,40	0,721	15,00	0,507	D
PO23	0,232	6	3,55	0,349	11,50	0,726	15,05	0,236	D
PO26	0,227	2	9,20	0,527	3,80	0,651	13,00	0,708	D
PO28	0,231	6	2,45	0,311	9,70	0,629	12,15	0,202	D

[a]: The oil used in the imbibition tests is either octadecane (OD) or decane (D).
***: The initial water saturation of the core plugs, whose imbibition tests were performed in USA, was established by using NMR spectroscopy.**

The imbibition tests of PO6 through PO13 are performed at ConocoPhillips Research Centre, Bartlesville, USA using octadecane at 35°C. These tests were performed after finishing the capillary pressure measurements (by the DMS-method). All other imbibition tests are performed at the University of Bergen, using decane.

Decane as the oil phase:

As can be seen from Table 7.2, the "older core plugs" (PO22 through PO28) in general have less mobile oil volume than the "newer core samples". Hence the end point water saturation ($S_{w,or}$) for the new samples are rather high (up to ~85%). This may be an effect of the presence of vugs. Intuitively, one would assume that the vugs would cause trapping; hence a *greater* S_{or} would be expected. What is seen in Table 7.2, is the opposite effect; S_{or} *being smaller*. This may be due to the high amount of pore channels present in chalk, (and possibly mixed wettability?).

From Table 7.2 one can further see that the measured Amott Indices decrease towards less water-wet conditions with increasing aging time. The results show stable wettability conditions, and the reproducibility of the imbibition measurements with Rørdal calk seems to be very good.

Figure 7.3.1 through Figure 7.3.10 illustrates the effects on spontaneous brine imbibition characteristics for core plugs containing **brine and decane** that have been aged in crude oil at 80°C for various length of time. The change in saturation is plotted to logarithmic time.

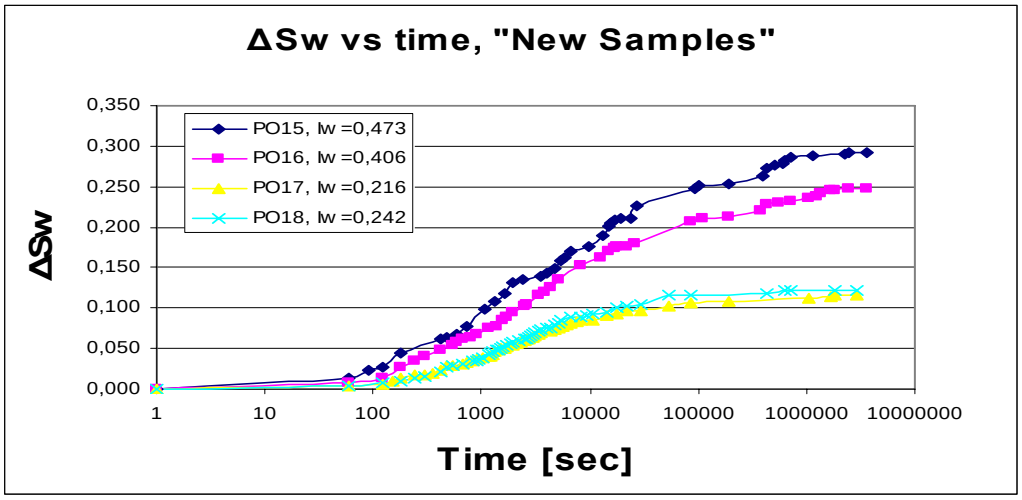

Figure 7.3.1: A semi-logarithmic plot of the change in saturation (new samples) to time [sec].

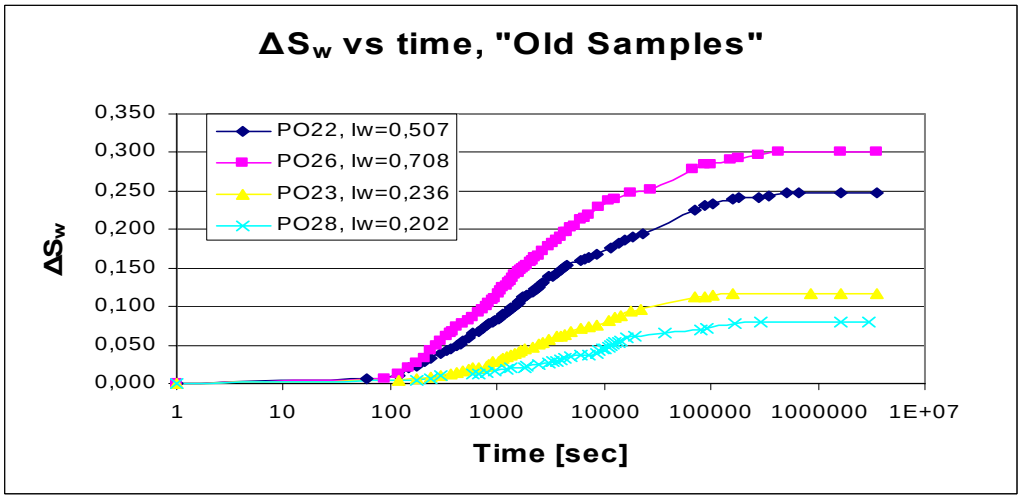

Figure 7.3.2: A semi-logarithmic plot of the change in saturation (old samples) to time [sec].

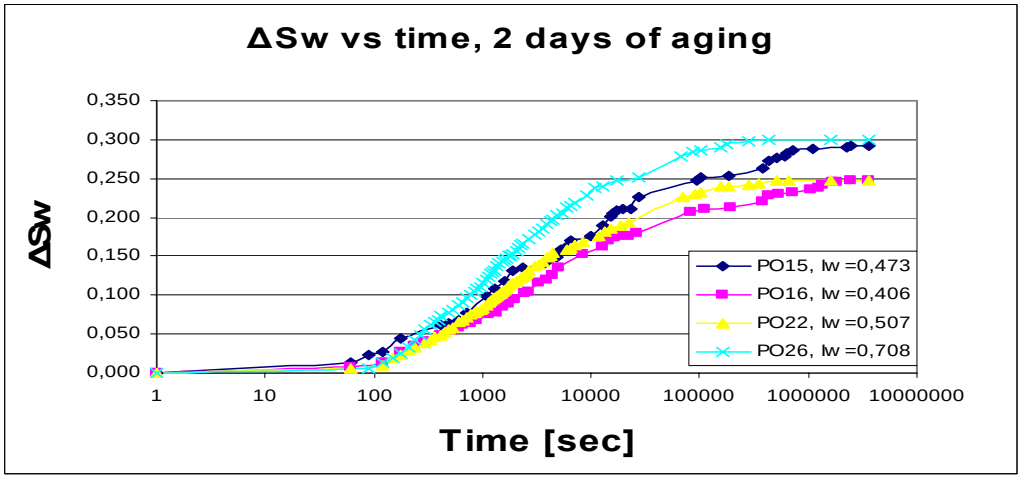

Figure 7.3.3: A semi-logarithmic plot of the change in saturation (two days of aging) to time [sec].

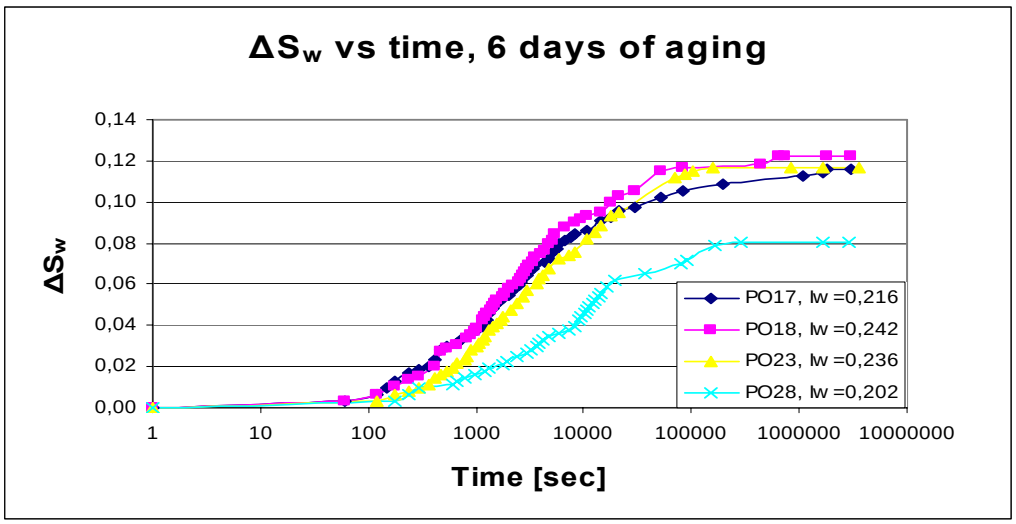

Figure 7.3.4: A semi-logarithmic plot of the change in saturation (six days of aging) to time [sec].

Figure 7.3.1 and Figure 7.3.2 show that the imbibition rate and the imbibition endpoint for the water saturation decrease as the Amott indices decreases. It is also noticeable that the induction time, i.e. time before the imbibition starts, increases as the core plugs are aged to less water-wet conditions.

To demonstrate that the data are consistent, it is necessary to show reproducibility. From Figure 7.3.3 and Figure 7.3.4, where the different types of core samples have been compared, there are no indications that the differences in pore structure affect the change in wettability. The deviation that is seen may be caused by inaccuracy due to reading the volumes and differences/heterogeneities in the core plug and crude oil being used. In Figure 7.3.4, PO28 is most different from the other samples. This core sample was the last one being aged, and from Table 7.2, this one has the lowest Amott Index. One possible reason for this may be that the barrel of crude oil being used in the aging process (Ekofisk oil) was at this point nearly empty, and the relative amount of heavy components may have been increased. This may in turn affect the amount of components being absorbed on the pore walls, and again have effects on the wettability alteration.

In Figure 7.3.5 through Figure 7.3.8, the development of the recovery factor is illustrated.

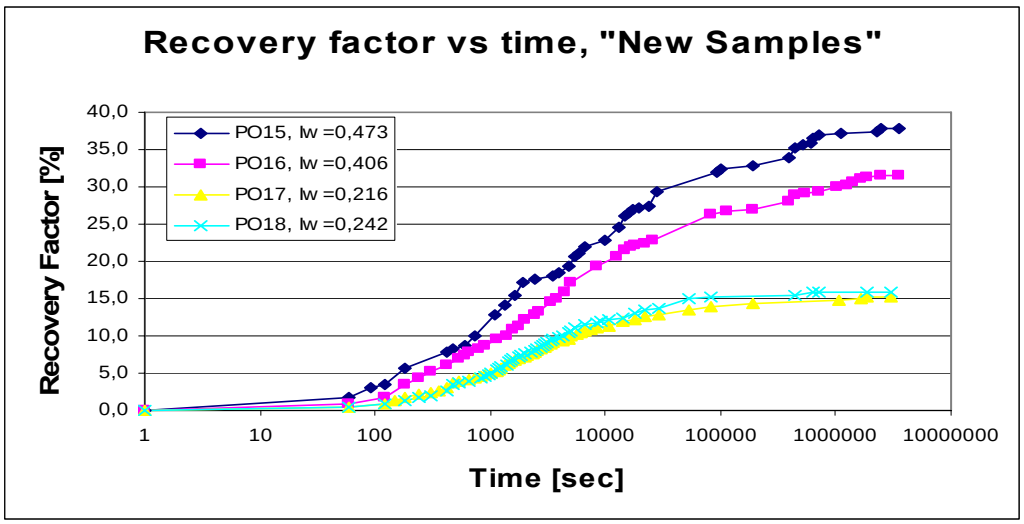

Figure 7.3.5: A semi-logarithmic plot of the recovery factor (new samples) to time [sec].

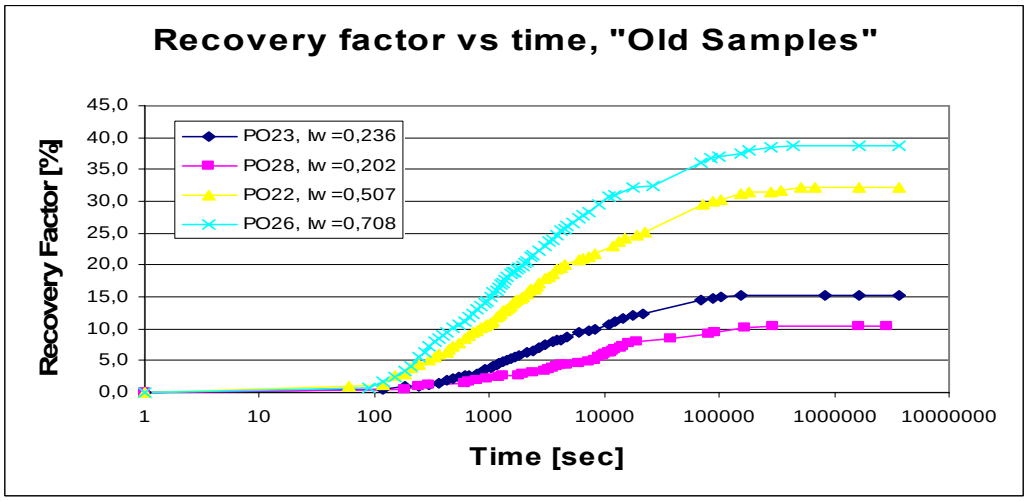

Figure 7.3.6: A semi-logarithmic plot of the recovery factor (old samples) to time [sec].

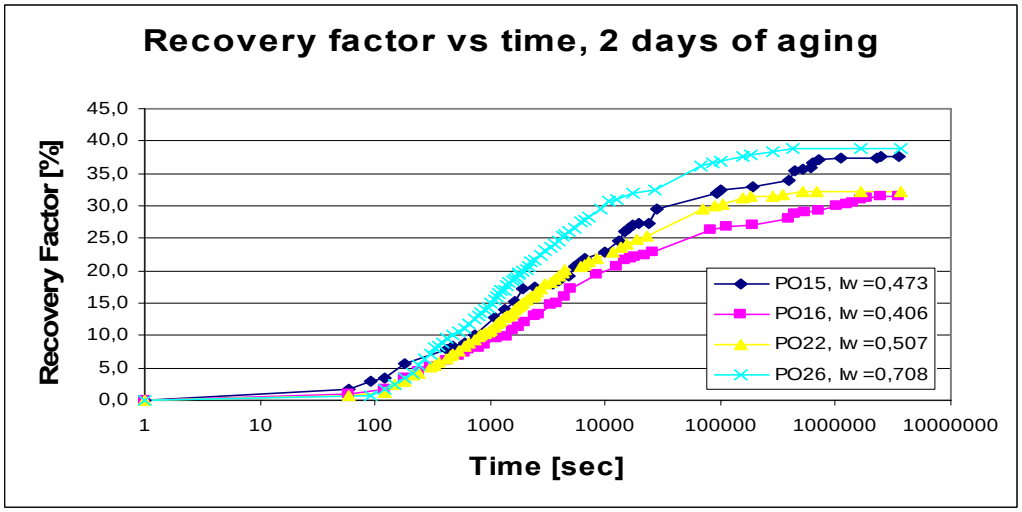

Figure 7.3.7: A semi-logarithmic plot of the recovery factor (two days of aging) to time [sec].

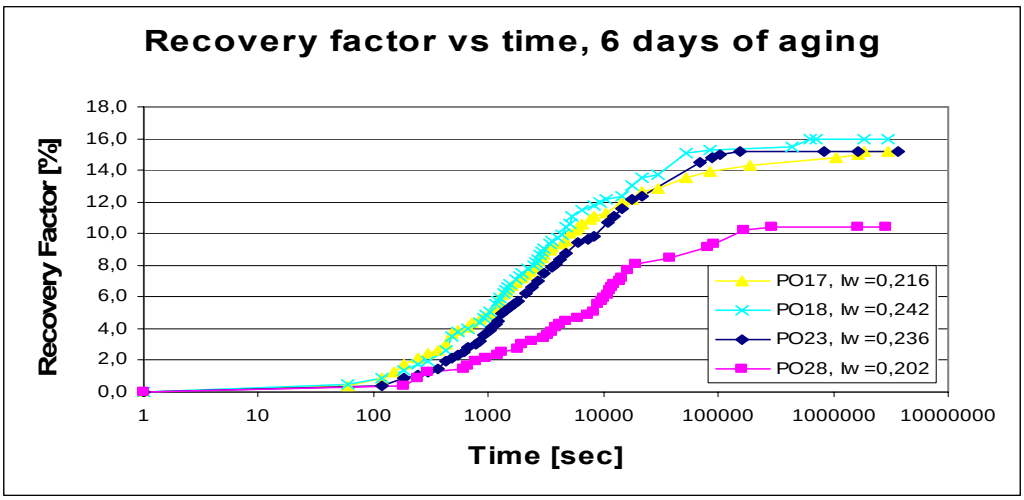

Figure 7.3.8: A semi-logarithmic plot of the recovery factor (six days of aging) to time [sec].

The same tendencies as previously described are seen in these figures, with sample PO28 being most different from the other core samples. In Figure 7.3.6, it is evident that as I_w decreases, the recovery factor decreases as well.

The development of the water saturations through time is shown in Figure 7.3.9 and Figure 7.3.10.

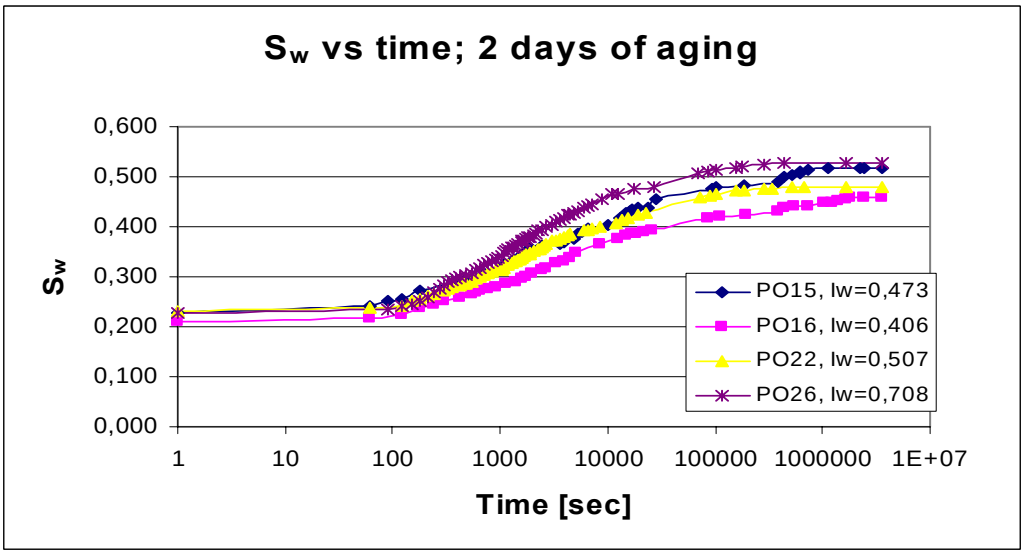

Figure 7.3.9: A semi-logarithmic plot of fractional water saturation to time [sec]. The cores have been aged for 2 days.

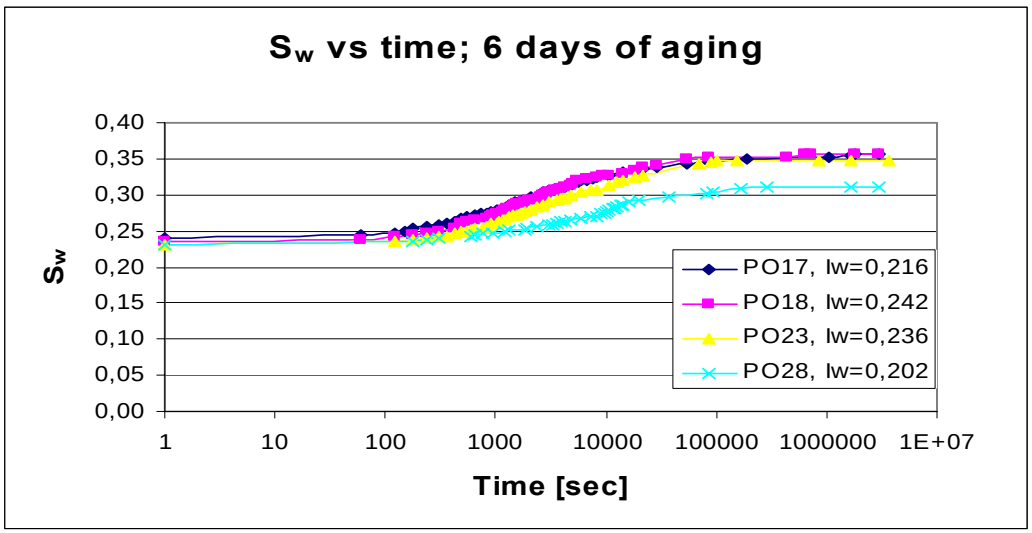

Figure 7.3.10: A semi-logarithmic plot of fractional water saturation to time [sec]. The cores have been aged for 6 days.

These figures show that the end point saturations are fairly consistent. One can see slightly differences in imbibition rate, where PO26 and PO28 stand out from the rest. One reason for this may be a difference in the relative amount of heavy components, as noted earlier.

Octadecane as the oil phase:

The results obtained by use of octadecane, however, are not as consistent. In Table 7.2 it is seen that PO7, being aged for 2 days is found to be less water-wet than PO6, aged for 6 days. This may of course be due to a difference in the amount of wettability-altering components in the crude oil being used. Most likely, however, this is associated with the fact that there is a difference in S_{wi} during aging. PO7 has a lower S_{wi} than PO6, which very well might affect the results [16].

In addition, the fact that octadecane is more viscous than decane, may be reflected in the obtained results. While decane has a viscosity of 0.92 at room temperature, octadecane has a viscosity of 2.46 at ~40^{o}C. This difference may affect the rate of the spontaneous imbibition. The untreated cores; PO11 and PO13, assumed to be strongly water-wet (having an Amott index of $I_w \approx 1.00$) turn out to obtain slightly lower values (I_w=0.899 and I_w=0.902, respectively). In order to improve the comparison of the results, it would have been interesting to perform an imbibition test both by using decane and octadecane on the very same plugs. Then, the effect of variation in viscosity could be further investigated.

In Table 7.2 one can further see that the obtained initial water saturations of these core plugs, being used in the DMS method, are in general higher than what is seen in the other cores. These values have been obtained by using NMR spectroscopy; since the material balance had been lost during the experiments (several displacements had been performed). However, the end point saturations turn out to end up in the same range as the other plugs of the "new type of material", hence there seems to be a consistency. But - the obtained $S_{w,or}$ of the two strongly water-wet core plugs (PO11 and PO13) stand out from the other plugs. These values end up at $S_{w,or}$=0,576 and $S_{w,or}$=0,585, respectively. As previously mentioned, these cores had been exposed to air for quite a while. The air was tried to be removed by using a backpressure

regulator (100 psi, Johnny Jack, Private Communication). But as the results are indicating, the removing of the air may not have turned out to be totally successful, causing relatively low endpoint water saturation.

The results of the spontaneous imbibition obtained of the core samples containing **brine and octadecane** are shown in Figure 7.3.11 through Figure 7.3.13.

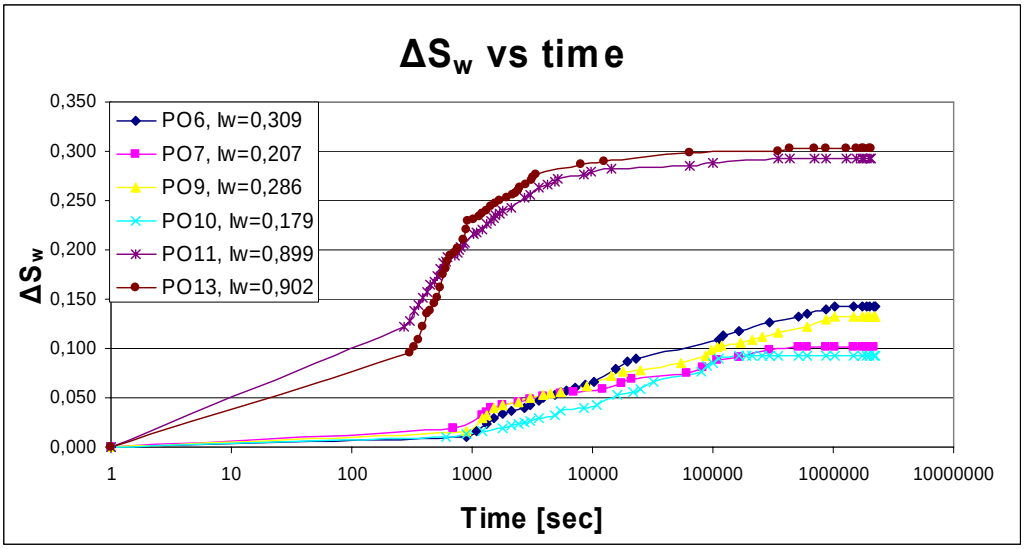

Figure 7.3.11: A semi-logarithmic plot of the change in water saturation to time [sec]. Octadecane being the oil phase.

It is clearly seen that when altering the wettability, the imbibition characteristics will change. As previously discussed, when comparing the time of aging, the results obtained from PO6 and PO7 are opposite of what could be expected: PO7 is found to be less water-wet than PO6, despite the fact that it is exposed to a shorter time of aging.

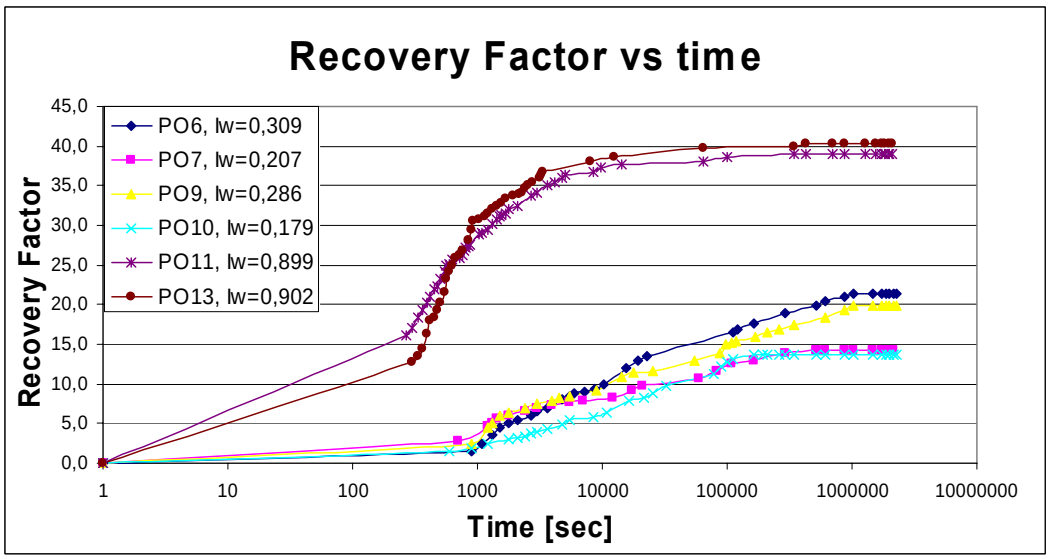

Figure 7.3.12: A semi-logarithmic plot of the recovery factor (six days of aging) to time [sec].

In the figure above, it is seen that the recovery factor at spontaneous imbibition decreases when the wettability is altered to less water-wet conditions. This is consistent with the theory.

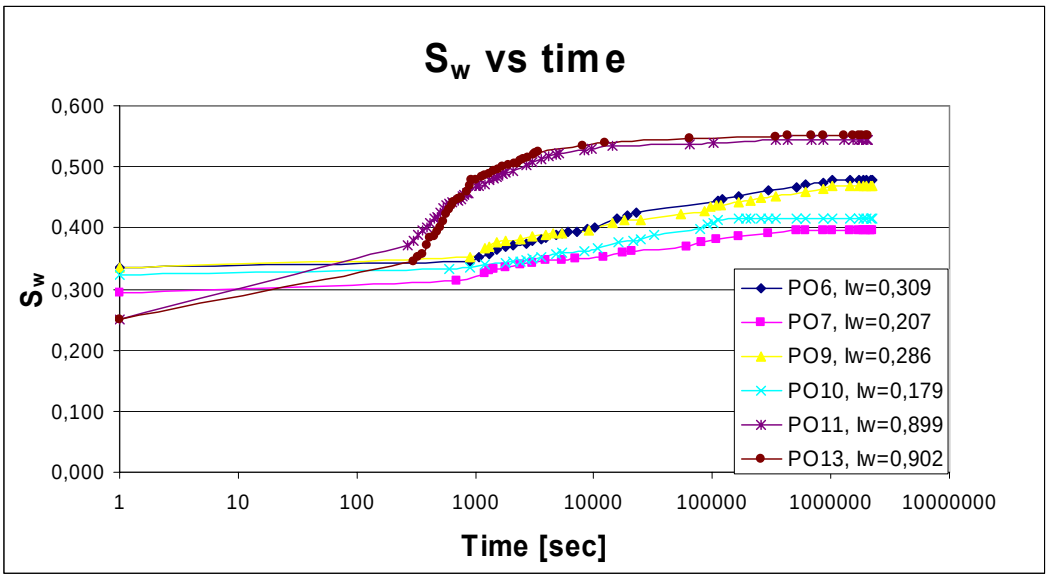

Figure 7.3.13: A semi-logarithmic plot of fractional water saturation to time [sec].

In Figure 7.3.13, the endpoint water saturation is seen to increase with increasing Amott wettability index. The endpoint saturations are relatively consistent. However, as previously mentioned, the $S_{w,or}$ of the two core plugs not being aged; PO11 and PO13, are lower than expected. This may be due to the presence of the air.

There are some variations in the spontaneous imbibition rates seen in Figure 7.3.13. PO11 and PO13, whose wettability has not been altered, are seen to have a higher rate of imbibition than the other plugs. Hence it is evident that the imbibition rate decreases when the plugs are altered to less water-wet conditions.

In Figure 7.3.14, four core plugs with approximately the same wettability conditions are compared.

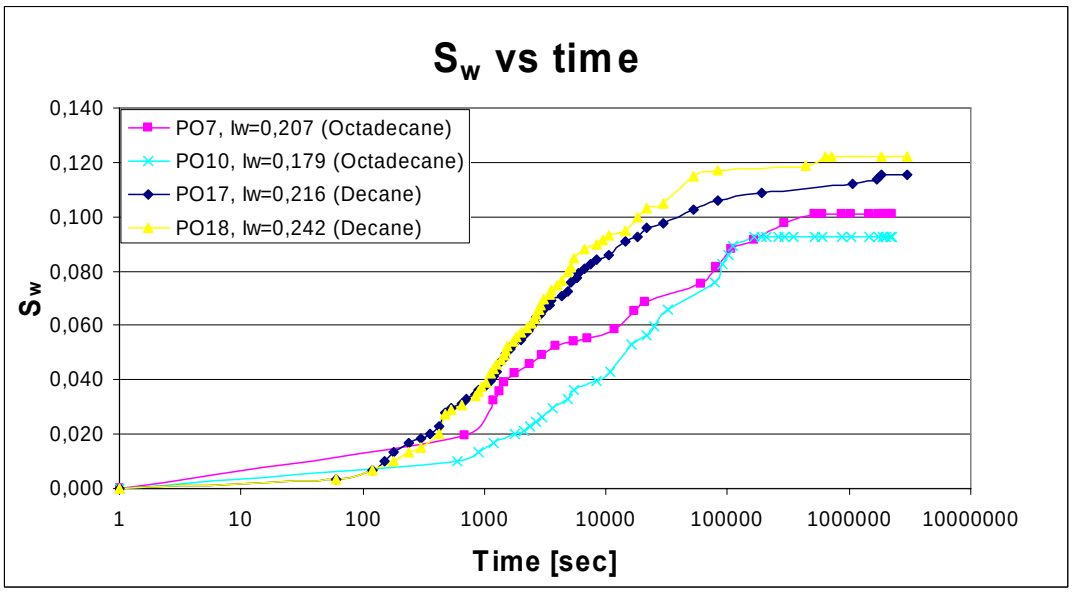

Figure 7.3.14: A semi-logarithmic plot of the spontaneous imbibition of four cores; octadecane and decane are compared.

These curves illustrates that the induction time increases when using octadecane. This may be due to temperature effects. In addition, the rate of imbibition seems to decrease when using octadecane. This is consistent with previous work, which has shown that the imbibition rate decreases with increasing viscosity of the oil phase being used [41].

Despite the assumption that the use of octadecane will not affect the wettability conditions, this could/should have been investigated by performing an imbibition test (e.g. by using decane) both before and after the plugs being in contact with octadecane, to check for possible alteration.

Complementary data are listed in Appendix B.

CHAPTER 8

Measuring P_c-Curves by Use of the DMS-Method

In this chapter, the results from the capillary pressure measurements using the Direct Measurements of Saturation method are presented. This method directly determines the local in-situ saturations and is looked upon as a significant improvement in special core analysis. The main disadvantage of this method is that it requires an oil that solidifies at room temperature.

8.1 Core Preparation

Since the cores had been aged before being shipped to Bartlesville, USA, they were at S_{or} when arriving (due to safety reasons, as mentioned in Chapter 5). Hence they needed to be drained to S_{wi} before imbibition capillary curve measurements could be performed.

The cores were subjected to NMR spectroscopy before and after the drainage process to corroborate the saturations of each phase by plotting response versus T_2 of the NMR analysis. The results from NMR spectroscopy are shown in Figure 8.1.1 and Figure 8.1.2.

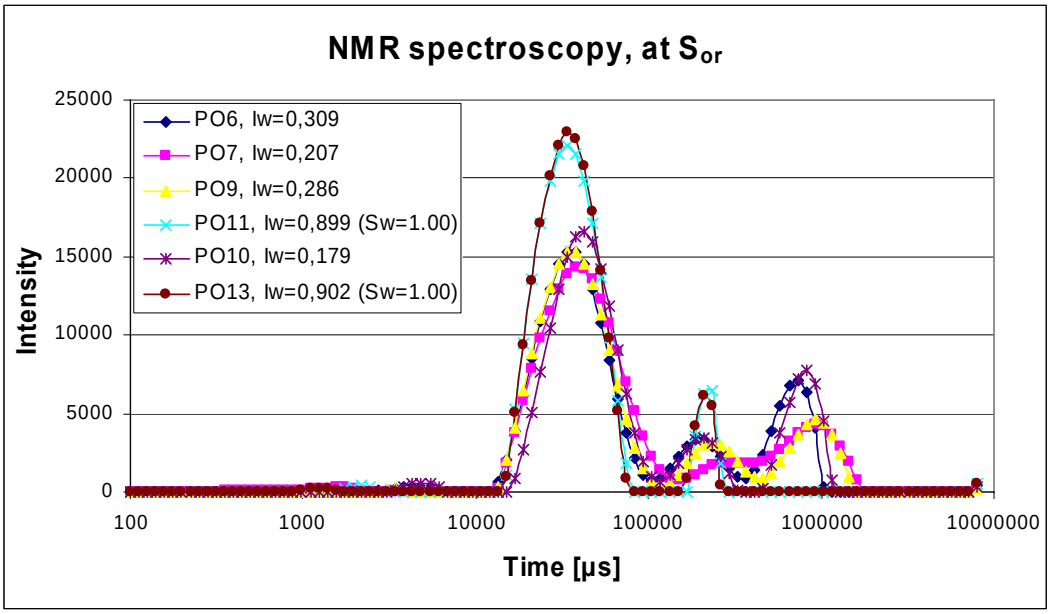

Figure 8.1.1: The NMR spectroscopy of the core samples at S_{or}.

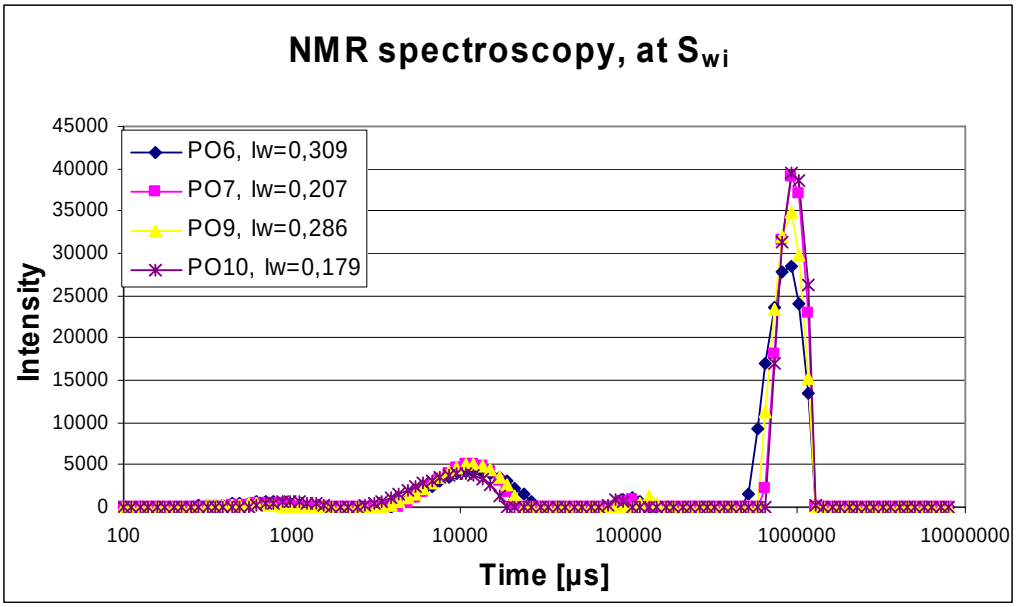

Figure 8.1.2: The NMR spectroscopy of the core samples at S_{wi}.

The first and largest peak in Figure 8.1.1 is due to water. The third peak is due to decane. In Figure 8.1.2 one can see that as the water saturation decreases, the largest peak decreases, while the peak due to decane increases, as expected. In addition, there is a shift in T_2 when the water saturation decreases; T_2 decreases. The reason for this is that as S_w decreases, the water will be situated as a film along the pore walls, hence the surface relaxation will dominate and T_2 will decrease.

In these figures there are some interesting results. The response in the second peak seen in Figure 8.1.1 (at approximately T_2 = 200000 µs) is normally not detectable in such measurements. These results may be due to the vugs, described in Chapter 7. In these vugs the pore diameter is larger than is the case in the rest of the porous media, hence the bulk relaxation manifest itself. This peak is found in all core samples, even in samples PO11 and PO13 which have a water saturation of 1.0. Johansen compared NMR spectroscopy of some core samples gathered in late 1990's and June 2003, and she could not find these second peaks in the "older" samples [46]. Since PO6 through PO13 are all new samples, this enhances the assumption that the aforesaid peak is due to the vugs, which is a phenomenon that is present in these newer core samples. From NMR spectroscopy, it is found that the vugs correspond to approximately 10 % of the total pore volume. That is; a volume of ~3 ml is associated to the vugs.

In Figure 8.1.2, one can further see that this vugs-response decreases as the water saturation decreases. This indicates that the water saturation in the vugs decreases as well.

The NMR-data were used for measuring the saturations. The results are found in Table 8.1.

Table 8.1: Saturation measurements based on material balance and NMR spectroscopy.

	Core	PO6	PO7	PO9	PO10	PO11	PO13
At S_{wi}	$S_{w, mb}$	25,4	19,1	22,7	24,0	16,6	24,9
	$S_{w, NMR}$	25,5	22,4	25,4	26,4	22,1	30,4
	$V_{p, mb}$	30,2	30,7	30,3	30,3	30,5	30,4
	$V_{p, NMR}$	30,3	30,2	30,5	30,0	30,5	30,0
At S_{or}	$S_{w, mb}$	87,4	83,7	86,8	83,5		
	$S_{w, NMR}$	81,7	82,4	85,2	81,6		
	$V_{p, mb}$	30,2	30,7	30,3	30,3	30,5	30,4
	$V_{p, NMR}$	31,3	31,4	30,9	31,1		

From Table 8.1 one can see that there is a corresponding difference in the saturations obtained by material balance and those obtained by use of NMR spectroscopy. There might be several reasons for that. Firstly, the material balances might have been lost while shipping. Secondly, there are uncertainties related to the NMR measurements, such as changes in temperature, etc. Thirdly, the assumption being made that the vugs-response is due to water only and the indistinct partition in the vug-response and decane-response results in additional uncertainties.

8.2 Replacement of Decane by Octadecane

While the core samples are at S_{wi}, the decane needs to be replaced by octadecane. The octadecane solidifies at room temperature; hence it is a suitable oil phase when one needs to calculate the water saturation by use of MRI images. NMR spectroscopy has been used to check the efficiency of the octadecane-decane displacement. Figure 8.2.1 shows the T_2 distribution of PO6 at different stages.

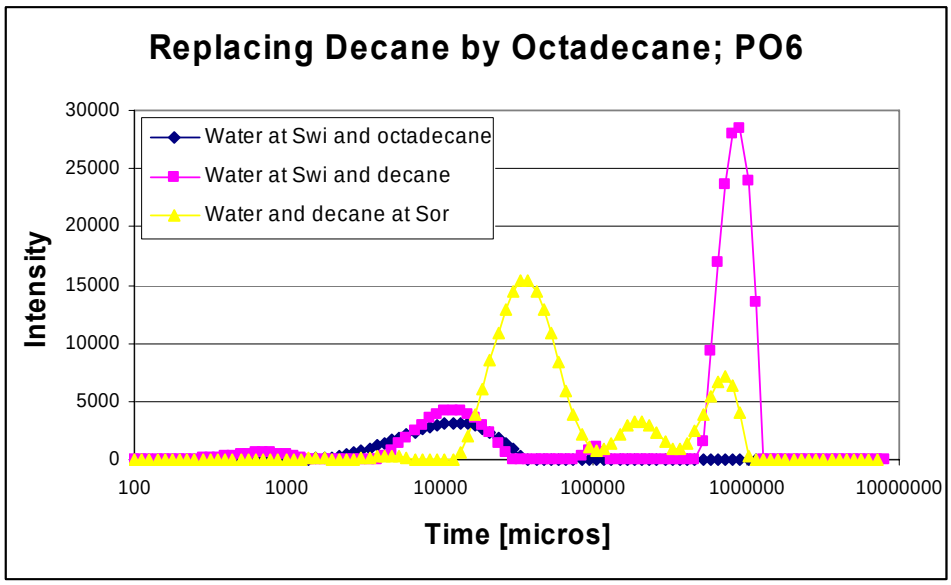

Figure 8.2.1: The cores are subjected to NMR spectroscopy to check the efficiency of the replacement process of decane by octadecane. The figure shows no traces of the decane in sample PO6 after finishing the replacement process.

In Figure 8.2.1 one can easily see that the replacement process of decane by octadecane has been successful. The response due to decane has disappeared, and the water-response is *fairly* the same. One can see that there has been some alteration in the response due to water. The vugs response has disappeared, and the "water-peak" is spread out. This might be a result of the solidification of octadecane, causing changes in T_2 relaxation. In addition, the previously mentioned shift in T_2 due to decreasing S_w is clearly seen.

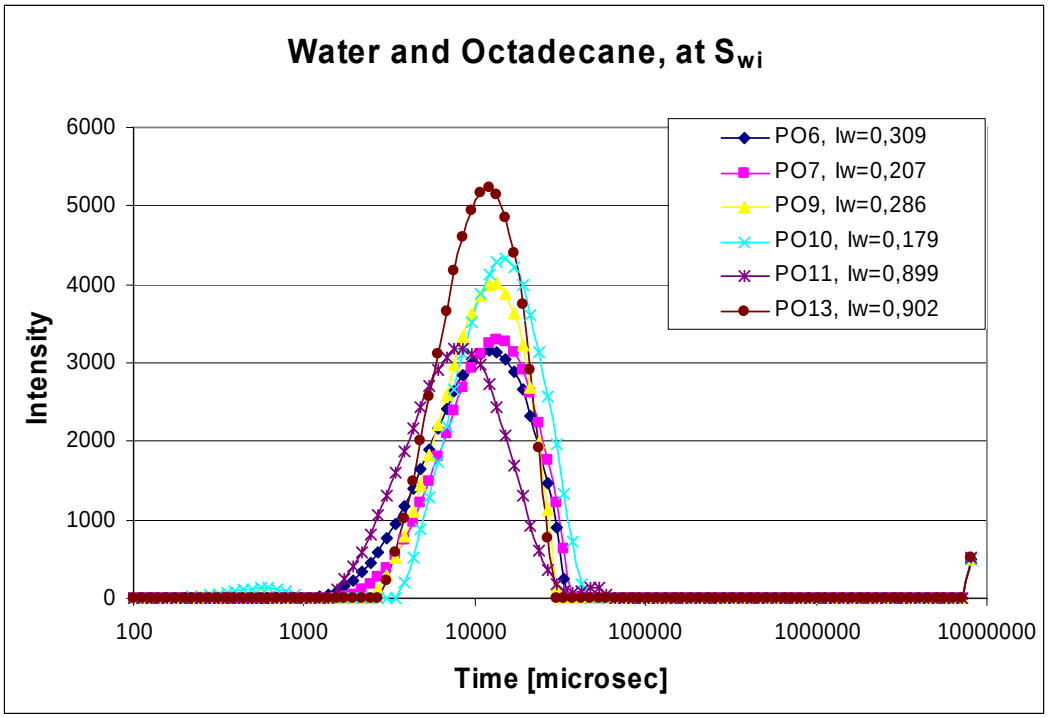

Figure 8.2.2: The NMR spectroscopy of core samples saturated by water and octadecane. The cores are at S_{wi}.

In Figure 8.2.2 the results of the replacement processes are shown for all the core samples. Again, there are no signs of the decane, meaning the octadecane-decane displacements have been successful. One can further notice that the vugs-response has disappeared, which is the case for all core samples.

8.3 Imbibition Capillary Pressure Measurement

After spinning, the cores are subjected to the MRI to calculate the in-situ saturations. Images of sample PO9, at S_{wi} and after imbibition are shown in Figure 8.3.1.

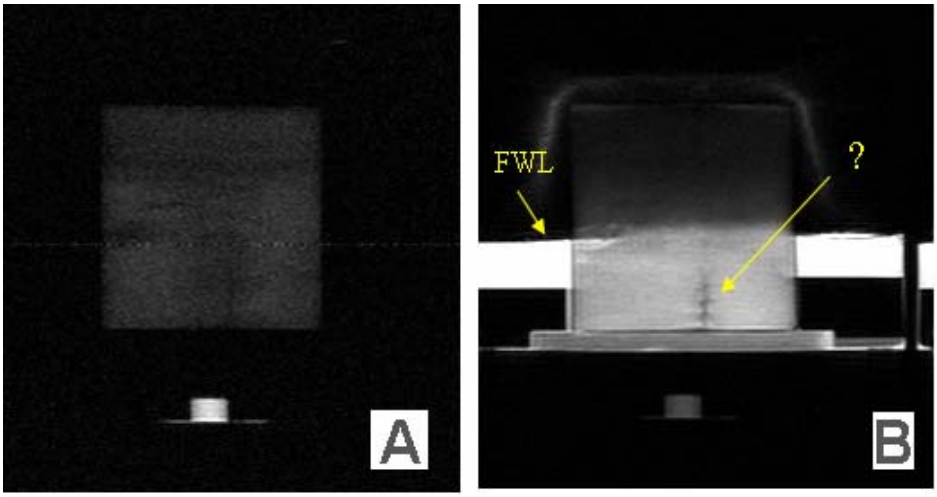

Figure 8.3.1: Images of sample PO9, at A: Swi, and B: after imbibition.

From these images, one can clearly see the change in intensity as the water saturation increases. In the image after imbibition (B), one can clearly see the free water level (FWL); the brightest area outside of the plug represent free water and its uppermost edge is the free water level boundary with the octadecane. Hence the reference point r_2 needed when calculating capillary pressure may easily bee measured.

There is also some sort of heterogeneity in this core. This is most obvious in image B, but one can also see this at S_{wi} (image A). If this vertical "object" is a fracture, this would most likely have been filled with water/brine, and hence have a brighter colour. Since this is obviously not the case, this may be a part of the core with less porosity.

In contrast to what was seen by Spinler and Graue [32] and [47] (see Figure 8.3.2), there is no sign of the concave downward shape of the saturation distribution (due to radial effects) in image B. Hence the wettability alteration method being used in this thesis (continuously flooding crude oil at elevated temperature at low rate in multiple directions) seems to have resulted in a more or less uniform wettability alteration, at least with respect to the radial distribution.

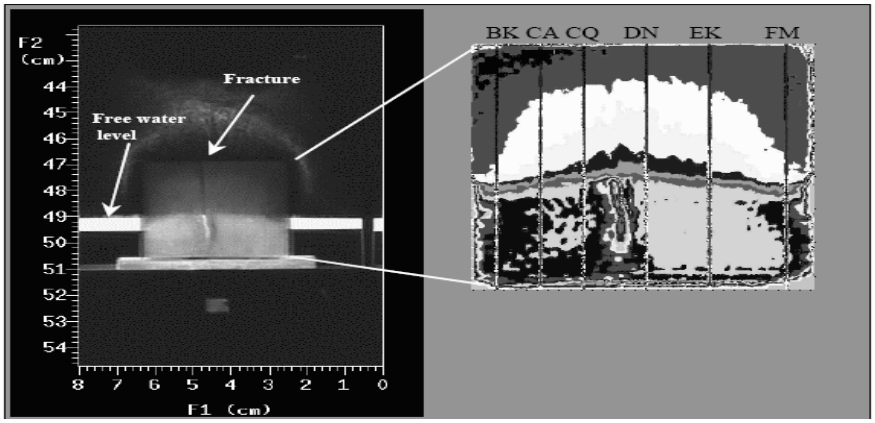

Figure 8.3.2: A concave downward shape of the saturation distributions within the core plug, Spinler et al., 1999)

To calculate the saturation by use of the MRI images, a calibration curve is needed. Basically, to generate a calibration curve, MRI measurements should have been performed at four different states; a dry core plug (to achieve background measurements), at S_{wi}, at S_{or} and a 100% water (brine) saturated core plug. But, as mentioned in Chapter 5.1, the cores were at S_{or} when arriving Bartlesville, USA (because of the wettability alteration), with decane being the oil phase, hence images of the dry and 100% saturated core had not been obtained. Based on experience from earlier work, the background measurements were neglected (Rich Treinen, Private Communication). After the forced imbibition, images were taken at S_{or}. But, unfortunately, the plugs had been tilted while processing, hence these results could not be used. Therefore, the calibration curves were based upon the average intensities at known S_{wi}, and an assumed zero-response of a dry core sample. Previous work by Howard and Spinler has shown that there is no simple linear relation between MRI intensity (response) and water saturation [48]: As S_w > ~50%, the intensity decreases. Thus in order to obtain fairly consistent calibration curve (and compensate for not having measured intensities at S_w>50%), the calibration curves used in these calculations depart from the linear relations; having a curvature for S_w > 50% (Private communication, Rich Treinen). The "Final Calibration Curves" used for calculating saturations of PO6 through PO10 after spinning are shown in Figure 8.3.3 to Figure 8.3.6.

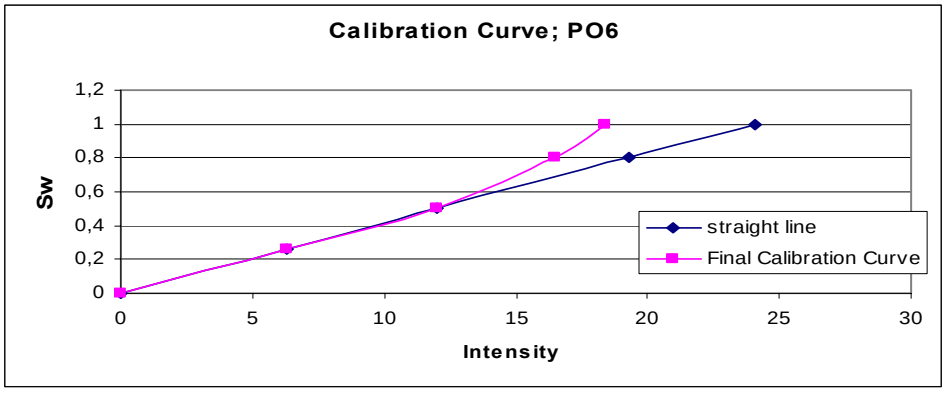

Figure 8.3.3: Calibration curve, core sample PO6.

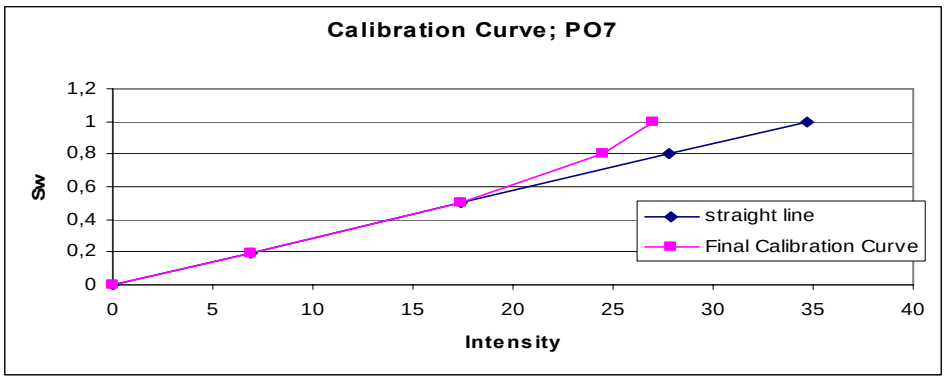

Figure 8.3.4: Calibration curve, core sample PO7.

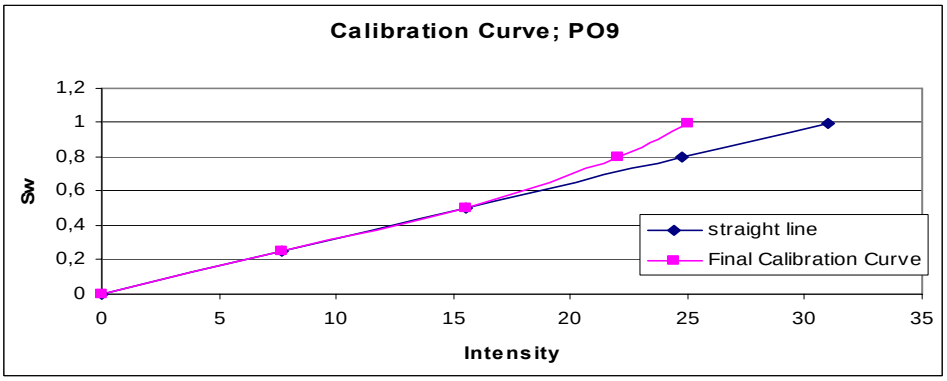

Figure 8.3.5: Calibration curve, core sample PO9.

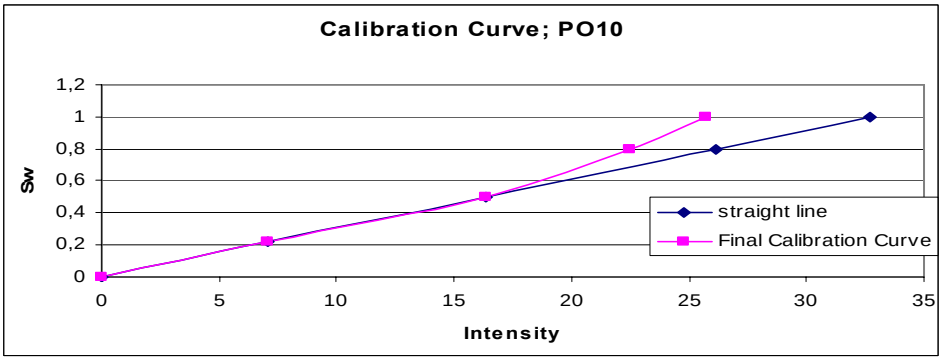

Figure 8.3.6: Calibration curve, core sample PO10.

When the calibration curves were set, and the scaling and calibration of the images were performed, the distribution of saturation could be calculated from the MRI images. The saturations were then again normalized so that the initial water saturations were adjusted to previously achieved S_{wi}. An example of distribution of saturation at S_{wi} and after imbibition measurements are shown in Figure 8.3.7.

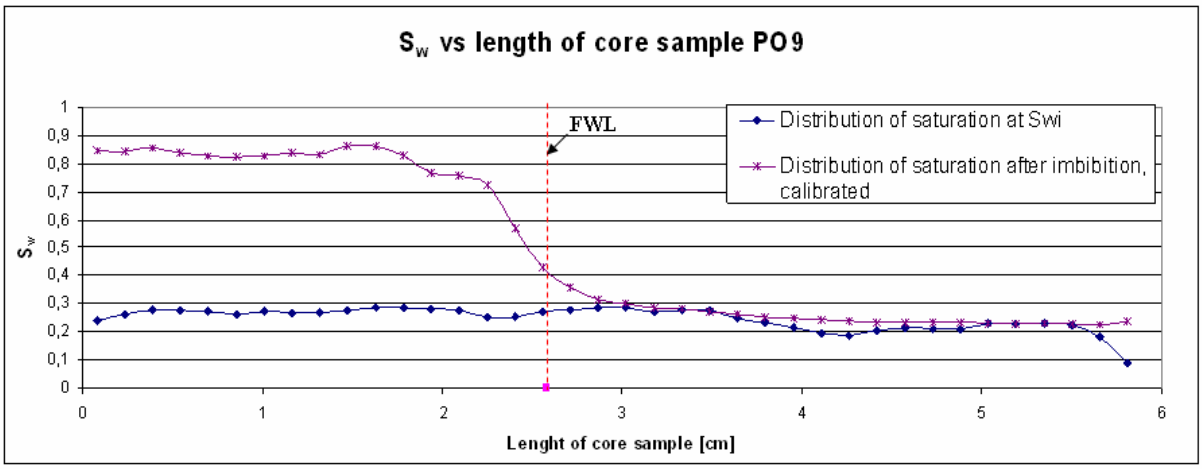

Figure 8.3.7: Distribution of saturation, core sample PO9. The red line is indicating the position of the free-water-level.

The zero point in Figure 8.3.7 is farthest off the centre of rotation. Based on the object seen in Figure 8.3.1, one would expect that there was a decline in saturation near x equals zero, given that the assumption on an area of less porosity was correct. But the distribution in the figure above does not fully confirm this hypothesis (even if there is a small decline), hence this should be reconsidered. On the contrary, the porosity seems to be quite uniform, based on the distribution of saturation at S_{wi}.

One can further see that the endpoint water saturations below the free water level are quite high. $S_w > 0.8$. This may be a result of not using the optimal calibration curve. However, previously obtained end point water saturations after water flooding of these samples have shown higher water saturations than usual; $S_{w,or} \int [0.83, 0{,}88]$. Therefore, since these samples are containing vugs, the rather high $S_{w,or}$ may turn out to be valid.

The calibrated and normalized imbibition capillary pressure curves, based on the saturations obtained by using the calibration curves illustrated above, are shown in Figure 8.3.8.

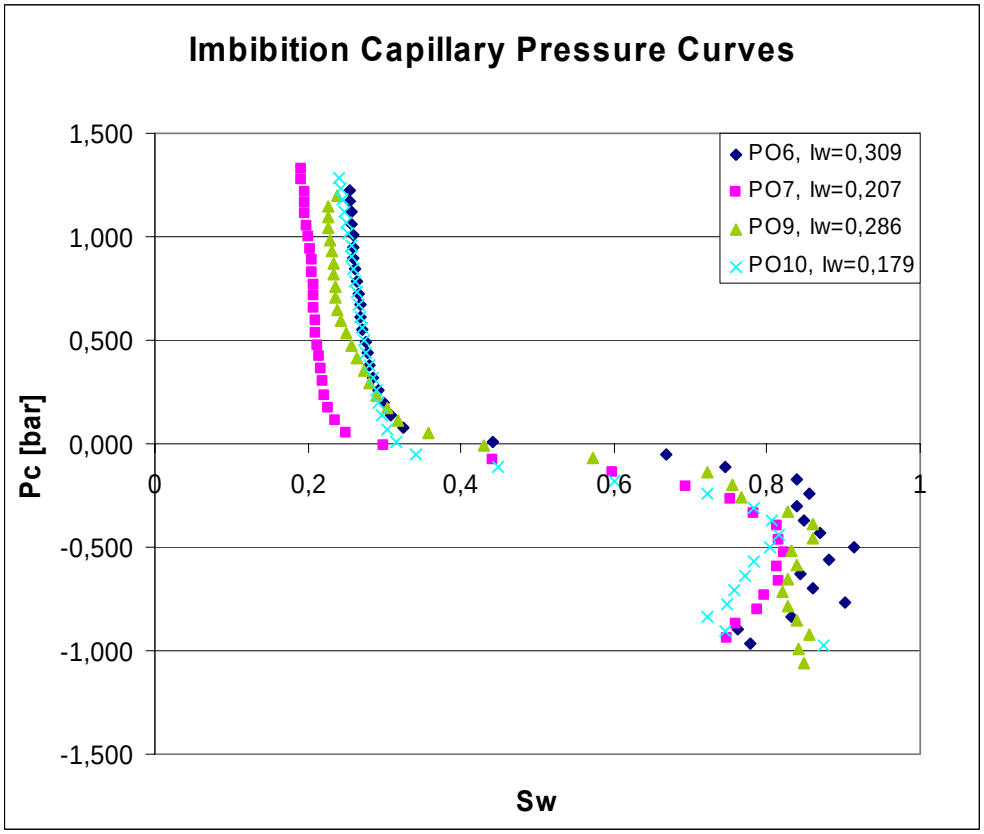

Figure 8.3.8: The imbibition Pc curves, core samples PO6 through PO10.

From Figure 8.3.8 the Amott wettability indices may be calculated, trying to verify the values obtained by the imbibition tests. [The saturations where P_c=0 (endpoint spontaneous imbibition) have been estimated by drawing a straight line through those two points being close to P_c=0 and thereby calculate the point of intersection.] The results are presented in Table 8.2. Results obtained by the originally imbibition curves (i.e. before normalizing - here being noted "uncorrected curves") and the imbibition tests are included for comparison.

Table 8.2: Amott indices based on imbibition capillary pressure curves

Core	V_p [ml]	S_{wi}	$S_{w,Pc=0}$	$S_{w,or}$	I_w	I_w, uncorrected curves	I_w, imbibition test (using octadecane)
PO6	30,2	0,254	0,486	0,874	0,374	0,468	0,309
PO7	30,7	0,191	0,289	0,837	0,152	0,336	0,207
PO9	30,3	0,227	0,420	0,868	0,301	0,461	0,286
PO10	30,3	0,240	0,319	0,835	0,133	0,255	0,179

In Table 8.2, it is seen that the obtained Amott indices demonstrate a tendency: All measurements indicates the same order of wettability alteration: PO6 → PO9 → PO7 → PO10, where PO10 being altered to the least water-wet conditions. However, there are some discrepancies in the obtained Amott indices. The Amott values obtained by using the uncorrected curves are a bit higher, and more in the range of what previously have been found (cf. Table 7.2). The reason for not obtaining a fully consistent result with the imbibition tests may be explained by the uncertainty in the calibration and scaling process. There are also uncertainties in absolute water saturation values due to difficulties with obtaining reliable absolute values of S_w in MRI. Some of the reasons might be:

1. Variation in measured image intensity because of possible software and hardware changes to the MRI.
2. The temperature may have an effect on imaging octadecane.
3. Damaging the plugs while handling causing lost material and fractures may effect the processing of the images to obtain the appropriate S_w.

In addition, according to some studies in the literature [49]-[52], this result may partly be due to differences imposed by the co-current spontaneous imbibition experienced in the centrifuge, compared to counter-current spontaneous imbibition present in a conventional imbibition-test. There has been work on oil recovery in chalk where a discrepancy in the endpoint saturations after spontaneous imbibition has been noticed, depending on whether the process has been obtain in 3D-imbibition cells (counter-current) or in centrifuge measurements / 1D-imbibition experiments (co-current) [24], see Figure 8.3.9. This has also been found at strongly water-wet conditions. Hence the Amott indices based on the imbibition capillary pressure curves should not be immediately accepted.

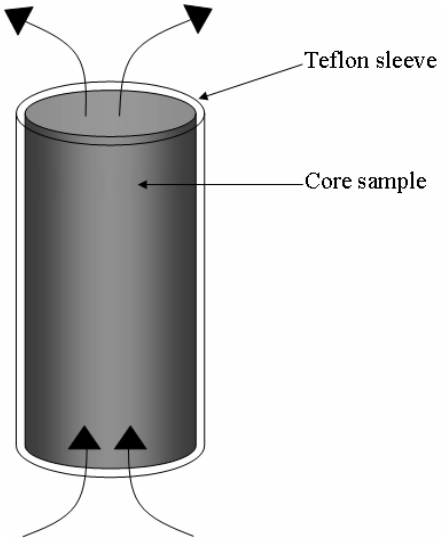

Figure 8.3.9: A teflon sleeve is mounted around the core sample. In this way, fluids may only flow through the inlet and outlet of the core. In this process, the spontaneous imbibition is co-current.

The details on the positive and negative part of the P_c-imbibition curves (Figure 8.3.8) are shown in Figure 8.3.10 and Figure 8.3.11, respectively.

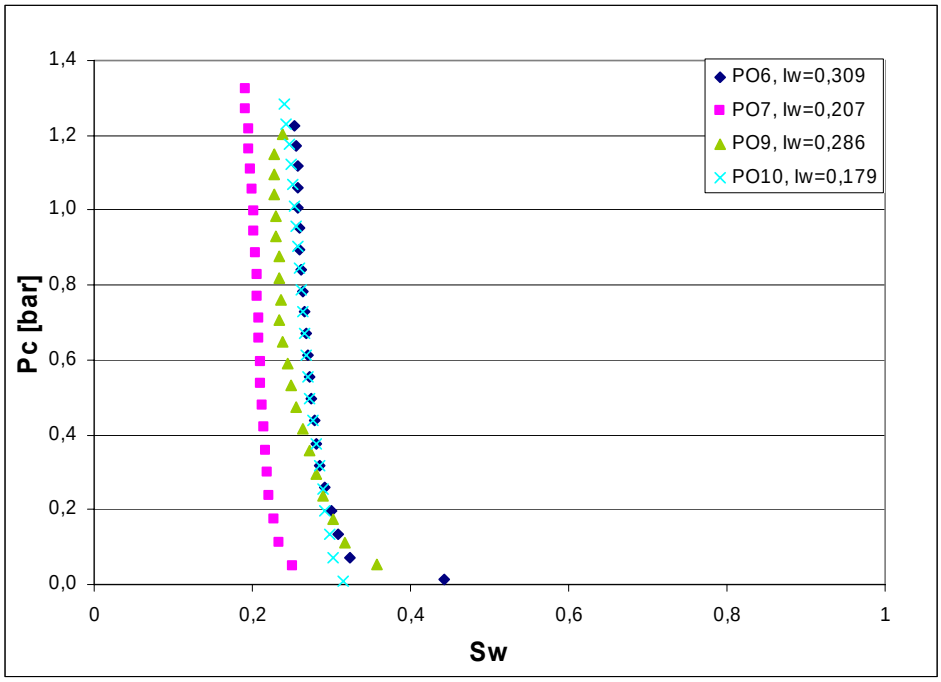

Figure 8.3.10: Comparison of the positive parts of the imbibition curves.

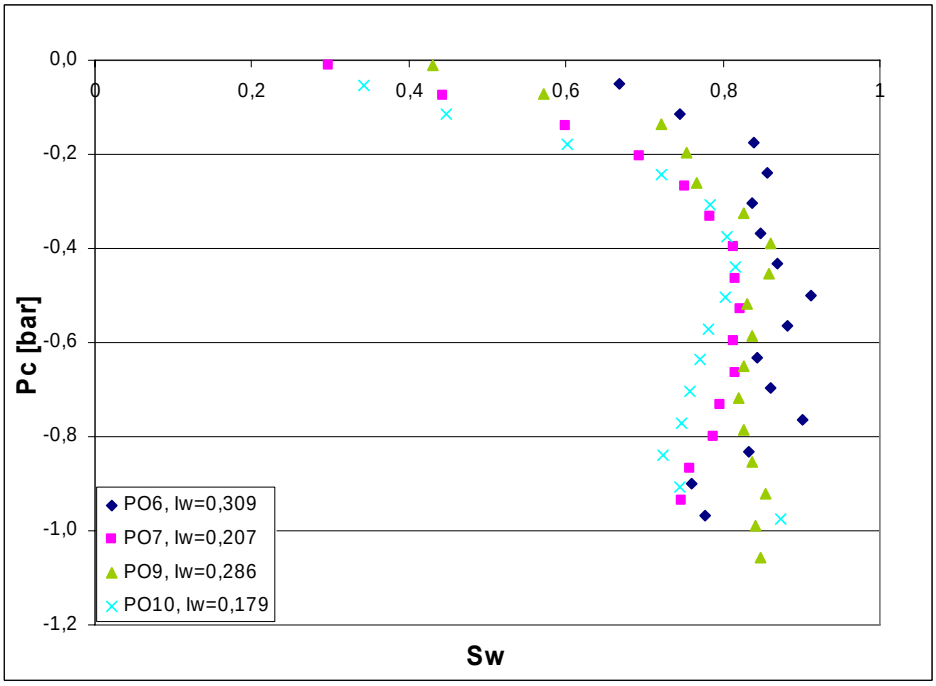

Figure 8.3.11: Comparison of the negative parts of the imbibition curves.

In Figure 8.3.10, one can see that the shape of the upper part of the two cores PO6 and PO9 are quite consistent. This is also the case of PO7 and PO10; the curvature of the spontaneous imbibition curves is not as pronounced as PO6 and PO9. Based on these observations, the two plugs PO7 and PO10 are supposed to be less water-wet than PO6 and PO9. This is consistent with what was found by the imbibition tests.

The discrepancy seen in S_{wi} is due to the normalization: Because of loss in material balance, the curves have been normalized to previously obtained S_{wi}.

What is seen in Figure 8.3.11 is very interesting with respect to enhanced oil recovery. By performing a forced imbibition in a less water-wet reservoir, there will be a considerable increase in the produced amount of oil. The less water-wet conditions, the more oil will be produced by this process. One needs to keep in mind, though, that the calculation of the free-water-level will influence the positioning of the capillary pressure curves. If the height of FWL is overestimated, the correct curves will be shifted upwards. This will lead to increasing Amott indices and not quite as interesting forced displacement curves.

However, it is seen that the saturation values below the free water level vary quite a lot. These variations are generally seen in all plugs. Most likely, the reason for this somewhat odd result may be the previously mentioned possible variance in MRI. The static magnetic field is homogeneous at a distance of 6 cm. If the positioning of the core sample has not been absolutely correct, this may also affect the results. In addition, these variations may be a consequence of not having a perfect calibration curve. Since this variance is found primarily at higher water saturations, this may be due to not having the correct curvature on the curves seen in Figure 8.3.3 to Figure 8.3.6. Another possible explanation is that these observed variations are experimental artefacts caused by wettability variations [47]. In preparation methods applying flow of crude oil, which is the method being used in these experiments, the wettability may vary from one end to the other. This may occur even if the direction of flow during aging is reversed several times [34]. The uniformity may be enhanced, however, if longer core samples had been prepared, and the inlet and outlet face of the plugs had been cut off to obtain the desired core size. There are also possible impurities in the octadecane which may show up at the water / octadecane interface. Hence this may lead to a higher calculated water saturation near $P_c = 0$ (Rich Treinen, Private Communication). And finally, there might be heterogeneities in the outcrop rock, which could lead to a porosity change towards the bottom of the core. Not having a proper slice by slice calibration could in that case result in the saturation change observed. Hence there are a number of possible explanations on this observed phenomenon, and all these may to a greater or lesser degree affect the result.

The obtained curves show that the wettability of these core samples have been altered towards less water-wet conditions. A change in saturation is seen when $P_c < 0$. The end point saturations are found to be at approximately 0.8, which are consistent with previously observed data of this set of core plugs.

8.4 Secondary Drainage Capillary Pressure Measurements

All core plugs in this experiment have been aged to a less water-wet state; hence there are no available capillary pressure primary drainage curves. However, the secondary drainage capillary pressure curves have been measured.

After finishing the secondary drainage process, the cores are subjected to the MRI to be able to calculate the saturation profile. Images of sample PO9 at S_{wi}, after imbibition and after secondary drainage are shown in Figure 8.4.1.

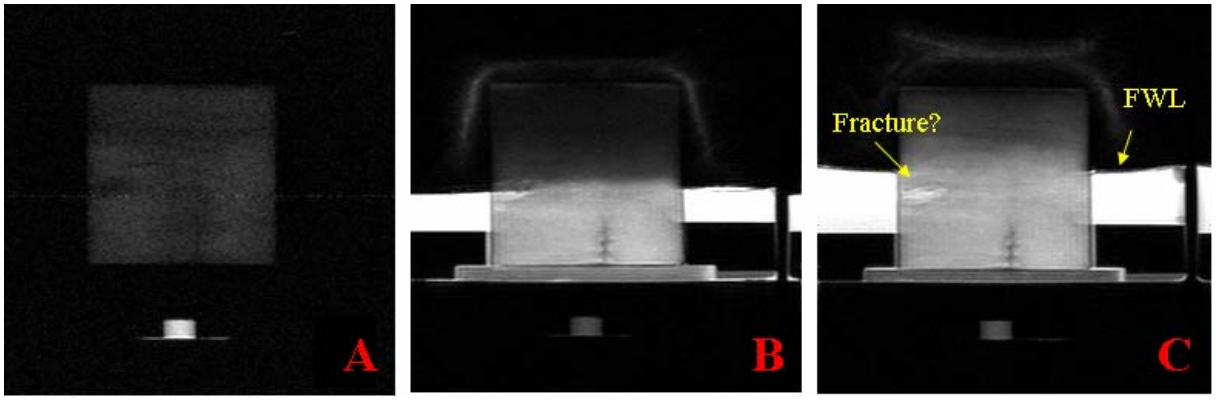

Figure 8.4.1: Images of sample PO9, at A: Swi, B: after imbibition and C: after secondary drainage.

In the figure above, there is a bright cap seen at the top of image B and C. This is most likely impurities in the octadecane (Ken Farmer, Private Communication). In the image taken after secondary drainage (C), two things are worth noticing:

1. A curved water-oil contact is noticed outside the plug. This curvature is not that obvious in image B. Possible explanations for the lack of this curvature in B are; the octadecane has not been properly solidified while spinning (even if the cores were cooled at 15^{o}C over night. -This in turn may have affected the quality of the imbibition P_c-curves), the core holders have been exposed to a change in temperature allowing a redistribution of the surrounding octadecane and water, or - there is a curvature in image B as well, but it is not that easily seen.
2. A bright spot is seen to the left of this image. After removing the teflon sleeve, it turned out that there was a quite large hole in this plug. This is shown in Figure 8.4.2.

Figure 8.4.2: A quite large hole is seen in plug PO9 after removing the teflon sleeve.

Despite the assumption that the water level should not change during experiments, it is clearly seen from Figure 8.4.1 that the heights of FWL are different in the two experiments. That is even if the added amount of water was the same in both cases. From the measurements of the FWL, a deviation of approximately 5 mm has been found. The deviation is most likely due to the imbibition and drainage processes. This assumption may be verified on PO9: Based on the spreadsheet used to obtain the necessary volume of water to add (Appendix A), a difference of 0,5 cm in FWL would correspond to a total volume difference of ~14 ml water. The water saturation of PO9 at S_{wi} is 0.247. After the imbibition (centrifuge) experiment has been performed, the average water saturation is measured to be $\bar{S}_w$=0,492 (by averaging the distinct values). From Table 7.1, the pore volume of PO9 is 30,27ml. The total amount of water having entered the core during this process is:

$$(0{,}492 - 0{,}247) \times 30{,}27ml = \underline{7{,}42ml}$$

The average water saturation of PO9 when the subsequent forced displacement is completed is S_w=0,868. After the secondary drainage imbibition (centrifuge) experiment has been performed, the average water saturation is measured to be $\overline{S}_w$=0,662. The total amount of water having left the core during this process is

$$(0{,}868 - 0{,}662) \times 30{,}27ml = \underline{6{,}11ml}$$

Hence the difference in the amount of water present in image B and C (Figure 8.4.1) should be: ΔV_w = 13.53 ml. This amount is consistent with the value found by using the spreadsheet (~14 ml). The fact the oil-water contact actually has been moved during the imbibition and drainage cycles may in turn have affected the results.

The saturations were calculated by use of the calibration curves, seen in Figure 8.3.3 to Figure 8.3.6. The end point saturations have been scaled based on previously obtained results (by use of the DMS-method) on corresponding core material [24].

The resulting secondary drainage capillary pressure curves are shown in Figure 8.4.3.

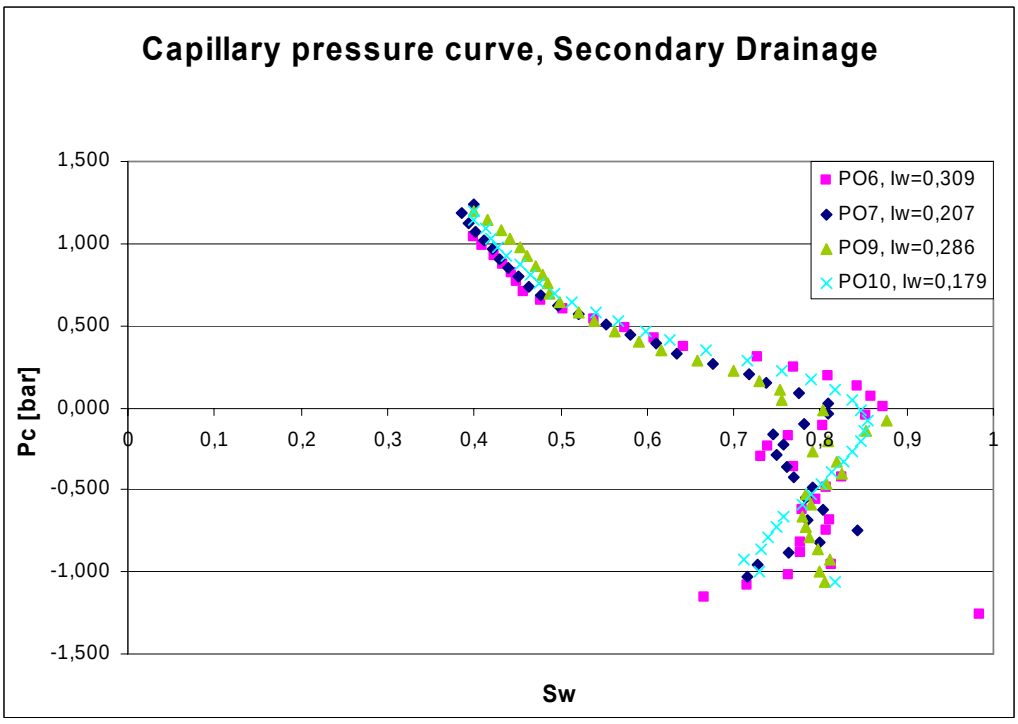

Figure 8.4.3: The secondary drainage Pc curves, core samples PO6 through PO10.

As was seen in the imbibition capillary pressure curves, the variations in the saturations below the water-oil-contact are also found in Figure 8.4.3. The smooth trend in PO10, where the saturations monotonically decrease below FWL is also found in this secondary drainage Pc-curve. The reasons for this may be the same as were discussed in Chapter 8.3. The most interesting part in this figure is what happens above the free-water-level. Hence the positive part of Figure 8.4.3 is illustrated in Figure 8.4.4.

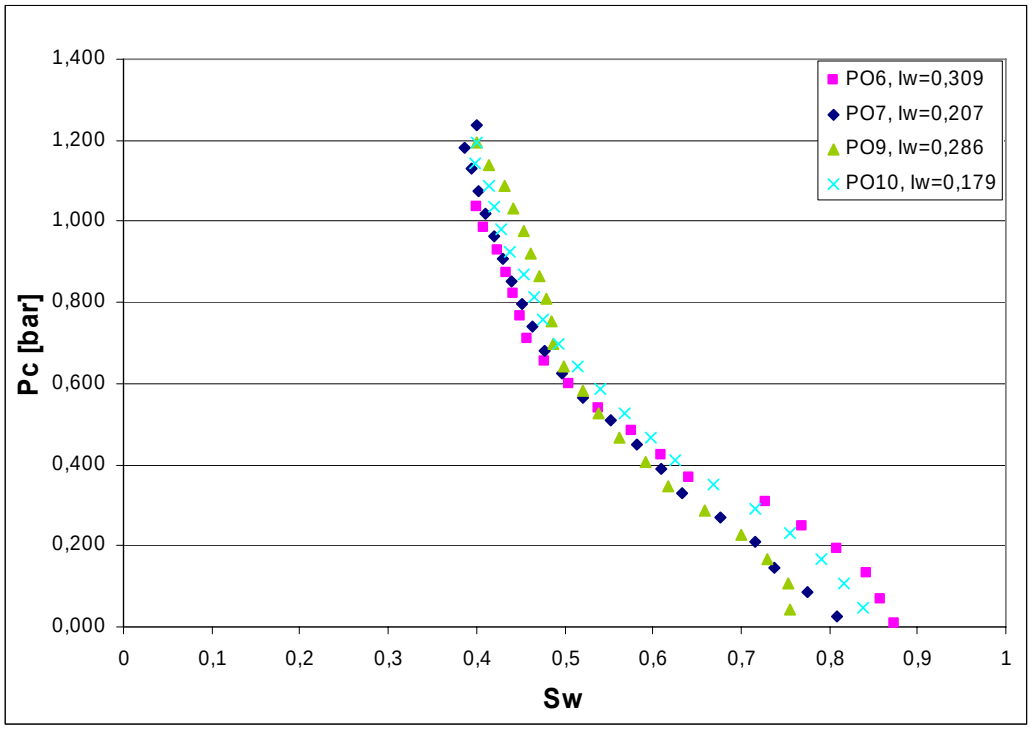

Figure 8.4.4: The positive part of the secondary drainage Pc curves, core samples PO6 through PO10.

Since the capillary pressure curves in Figure 8.4.4 are obtained in a secondary drainage process, the entry pressures are quite low, as expected. This entry pressure appears to be lower for PO7 and PO10, which have been found to be less water-wet than PO6 and PO9. This is as expected, with respect to the theory. However, the variation seen in $S_{w,\,Pc=0}$ makes it difficult to perform an exact evaluation of these threshold pressures. In addition, the element of uncertainty related to the calculation of saturations must be kept in mind. One can further see that after this entry pressure is attained, the saturation decreases rather rapidly with a low change in pressure. At $S_w \approx 0.45$ (and approaching S_{wi}) an increasing change in pressure is needed to attain lower water saturation – the curvature gets sharper. This phenomenon is also consistent with the theory.

As was illustrated in Chapter 2, Figure 2.1.5, the pore size distribution will affect the shape of the drainage P_c-curves. If the core sample is poorly sorted, or in this case; if it contains vugs, there will be a rather wide range of pore sizes. This has been found to result in an almost uniform decline in the wetting phase saturation [4]. In contrast, a well sorted rock sample, which gives a narrow pore size distribution (uniform pore diameters), leads to a significant change in saturation in a limited P_c-interval. Once the entry pressure has been exceeded, fluid invasion increases rapidly for a minor pressure increase until S_{wi} is reached. This curve is typical for a good quality reservoir. The curves shown in Figure 8.4.4 indicates that the pore size distribution is not very narrow, most likely being caused by the presence of vugs. (This is also found in the NMR measurements.)

In Figure 8.4.5, the positive part of the imbibition- and secondary drainage capillary pressure curves are included for comparison.

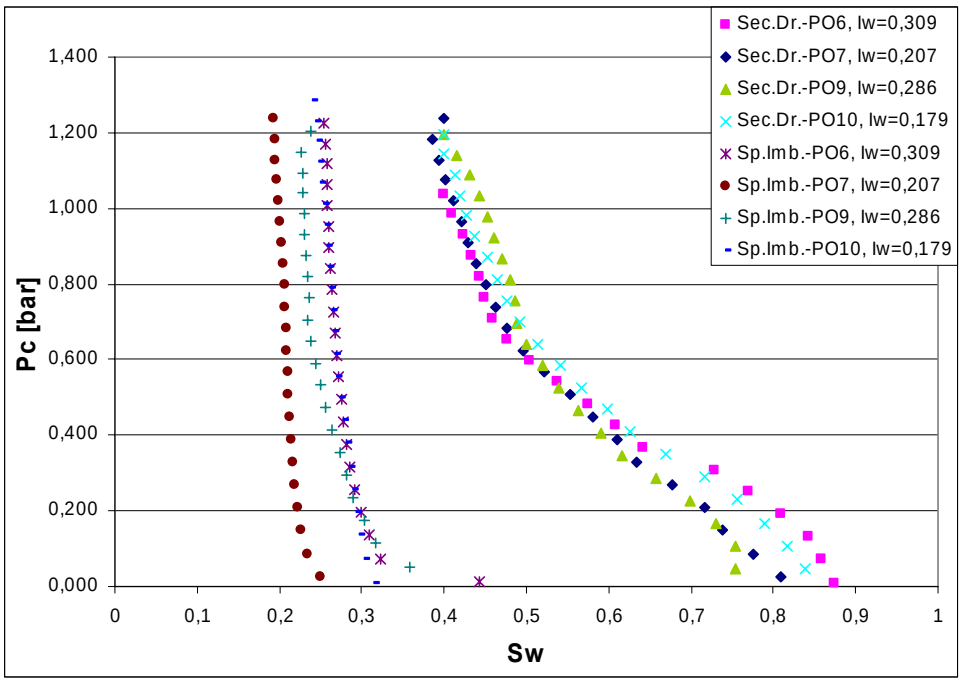

Figure 8.4.5: The positive part of the secondary drainage- and the imbibition capillary pressure curves, obtained by using the DMS method.

Capillary hysteresis can clearly be observed from the secondary drainage and spontaneous imbibition data. Since the final S_{wi} has not been obtained in the secondary drainage process, the final hysteresis loops are not seen.

Complementary data of the capillary pressure curves are found in Appendix C.

CHAPTER 9

Improving the NTIC-Method

While working on this thesis, much effort has been made to improve the Nuclear Tracer Imaging Centrifuge (NTIC) Method of measuring capillary pressure curves. In this chapter, the concepts, modifications and results of this method are presented.

9.1 Introduction to NTIC Method

Since the early work done by Hassler and Brunner [1], the centrifuge has been used to determine capillary pressure curves. However, most of this work has measured the fluid expelled as a function of rotational speed and fit these volumes to a variety of models [29]. There have been several attempts to measure the saturation along the centrifugal axis while the centrifuge is spinning, but for most of this work, the data has been compromised by the limited number of points measured along the axis and/or the lack of adequate saturation resolution. The Direct Measurement of Saturation Method is measuring the saturation along the centrifugal axis and a saturation resolution of about 2% pore volume has been reported, but it required the solidification of the oil phase and removal of the core from the centrifuge for saturation measurements [32].

Like the DMS method, mentioned in the Chapter 2, Chapter 5 and Chapter 8, this Nuclear Tracer Imaging Centrifuge Method measures the in-situ saturations. The in-situ saturations in the core plugs are obtained by use of an imaging system, using nuclear tracers, while spinning in the centrifuge.

There are several advantages of this system compared to existing methods of in-situ measurements of capillary pressures [35].

1. No assumptions are needed to calculate the capillary pressures, since the local fluid saturations are directly measured at various centrifugal radiis along the spinning core, i.e. at various capillary pressures.
2. There is no need to solidify one of the phases and remove the core from the centrifuge to obtain the saturations, as is the case in the DMS method.
3. No restriction on the oil phase, crude oil may be used, even at reservoir conditions.
4. Capillary end effects are directly measurable.

9.2 Set-up

9.2.1 The Centrifuge

The measurements are done with a Beckman J-6B centrifuge. The rotor carries four swinging Exxon core holders, which are capable of holding a confinement pressure up to 300 bars. The centrifuge has a maximum speed of 3500 RPM, which translates to a maximum capillary pressure of about 3.5 bar for a brine/decane system and a 6 cm long core sample. A schematic illustration of the centrifuge is shown in Figure 9.2.1.1.

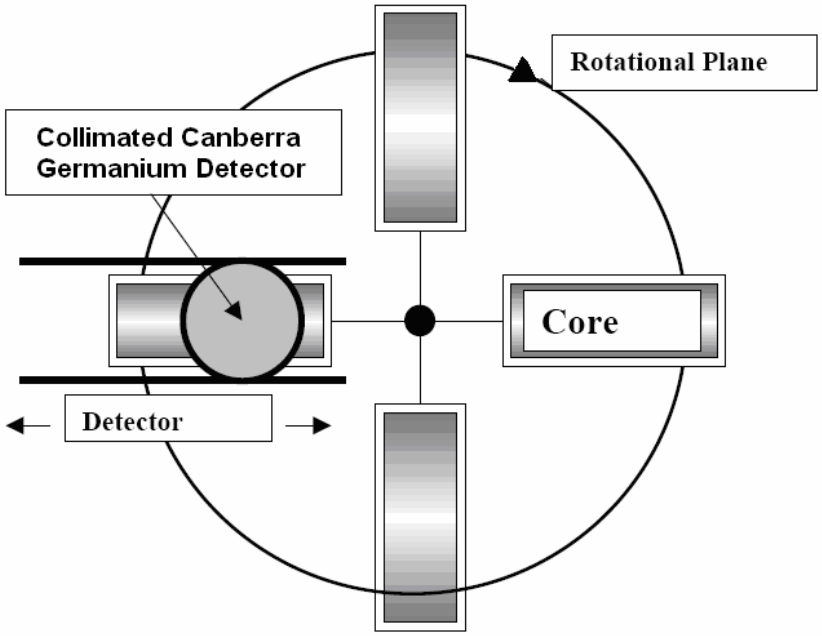

Figure 9.2.1.1: Illustration of the centrifuge, seen from above. The detector will move in the radial direction and measure the in-situ saturation along the centrifugal axis of the core sample.

9.2.2 The Detector and Collimator

The detector being used is a Canberra Germanium Detector, which operates on 3500 V. This is mounted on rig made of aluminium, on the top of the centrifuge, and can be moved horizontally along the centrifugal axis of the core sample while spinning. A collimator, made of lead, is surrounding the detector, the walls being 20 cm thick. This will minimize signal from background radiation, and focus the measurements to a cross-sectional slice of the core plug. See Figure 9.2.2.1.

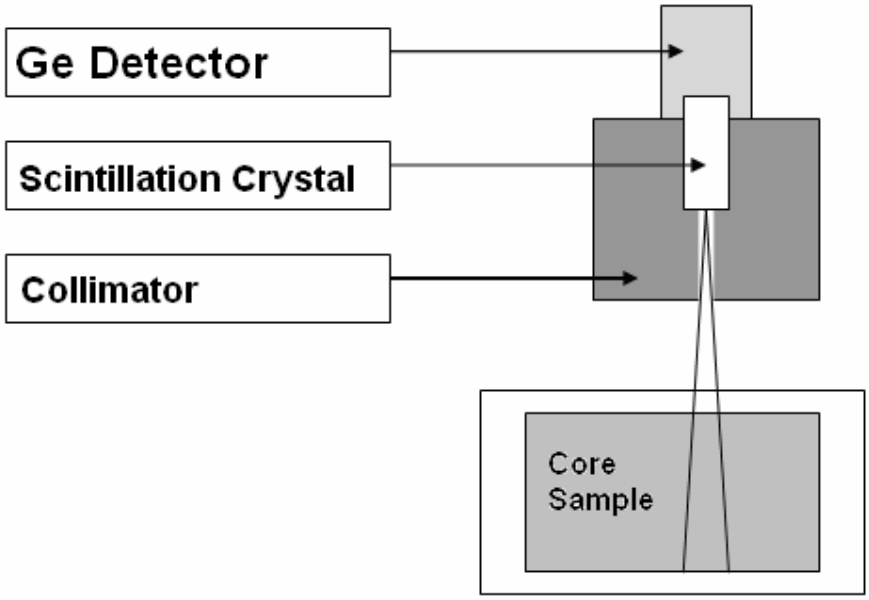

Figure 9.2.2.1: Illustration of the Imaging System. The volume being measured is indicated.

The set-up, seen in Figure 9.2.2.1 and Figure 9.2.2.2, has; depth of collimator opening ("b" in Figure 9.2.2.2): 11 cm; the distance from collimator to top of core sample ("c") is 12.5 cm and the "thickness" of the collimator opening ("a") is 1.5 mm. This is giving A = 0.6 cm, meaning a *focus on a 6 mm cross-section of the core*. Hence, this method is measuring the saturation along the centrifugal axis with ***ten points*** for a 6 cm long core plug.

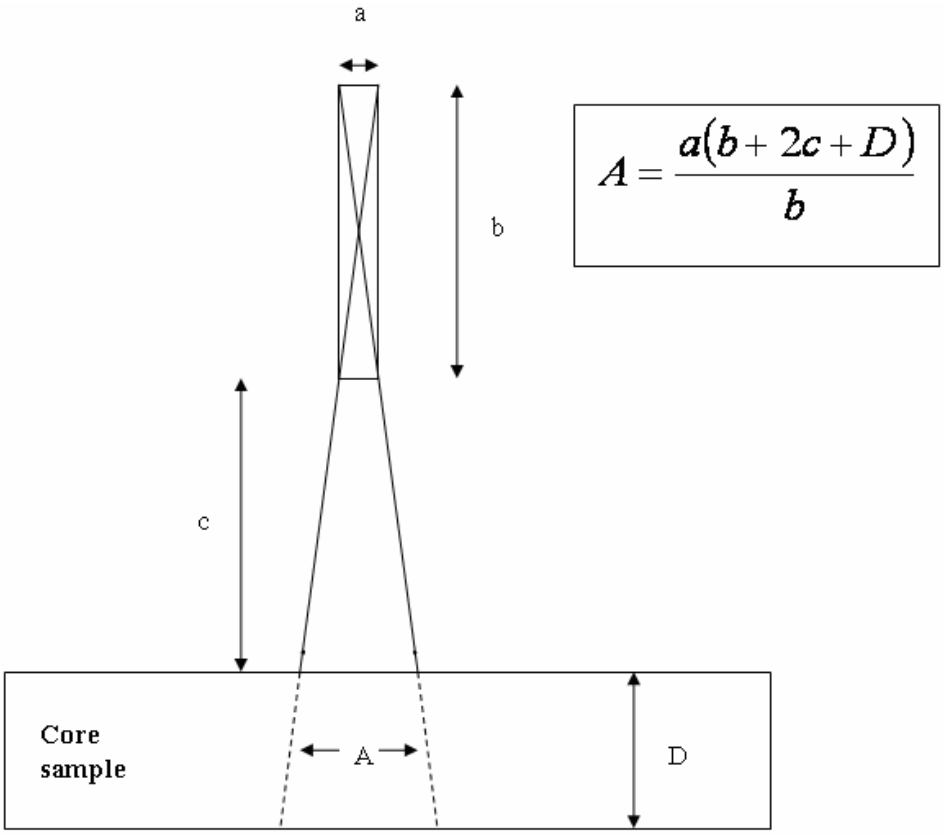

a: collimator thickness
b: collimator depth
c: distance from end of collimator to top of core sample
A: area of sample volume
D: core diameter

Figure 9.2.2.2: The geometry of the collimator opening, seen along the centrifugal axis / radial axis of the centrifuge.

The collimator has further been modified to make sure that the entire diameter of the core sample is within the measuring range. With a collimator opening width of 1.1 cm ("d" in Figure 9.2.2.3), depth ("b") of 11 cm, and a distance of 14.4 cm from end of collimator to centre of core ("e"); the "width" of the measured sample volume is found to be D = 4.0 cm. Hence the entire 1.5'' core sample is within the measuring range (see Figure 9.2.2.3).

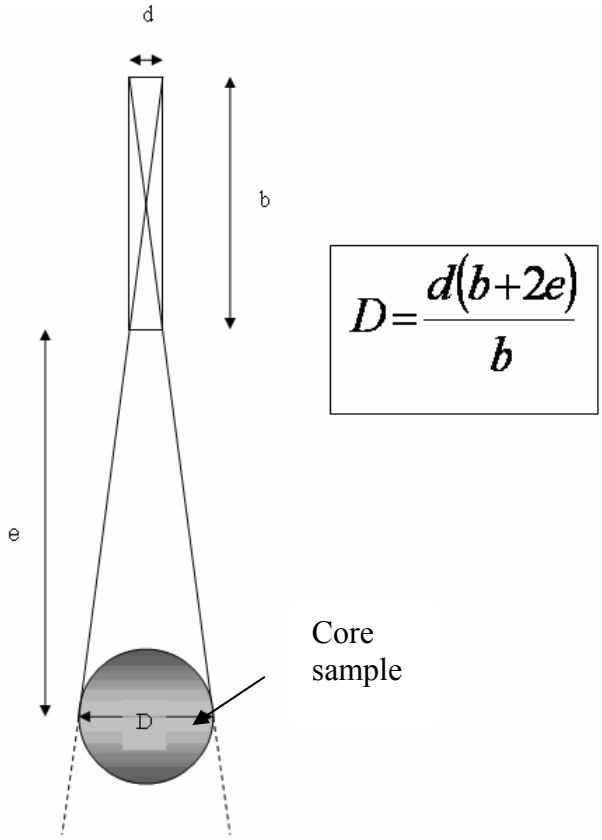

b: collimator depth
d: collimator width
e: distance from end of collimator to centre of core sample
D: width of measured sample volume

Figure 9.2.2.3: The geometry of the collimator opening, seen from the centre of the centrifuge.

In the experiments done in this thesis, only one of the Exxon core holders contained a sample, saturated with a radioactive labelled fluid. To minimize the background radiation, gating of the detector is needed. This is done by mounting steel disk (see Figure 9.2.2.4), tuned to gate the detector, to the bottom of the rotor, together with a photo-diode. The disk is mounted so that the gating starts at the time the core sample is entering the measure range, and stops when the entire sample is out of the area. See Figure 9.2.2.5. In this way, the background radiation is minimized.

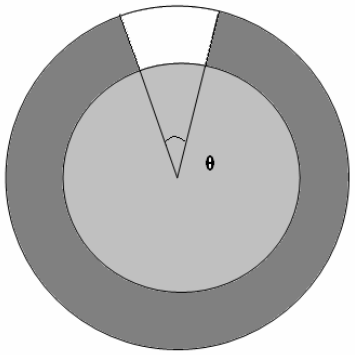

Figure 9.2.2.4: The steel disk being mounted on the bottom of the centrifuge. This has an opening of θ = 40 degrees (white area).

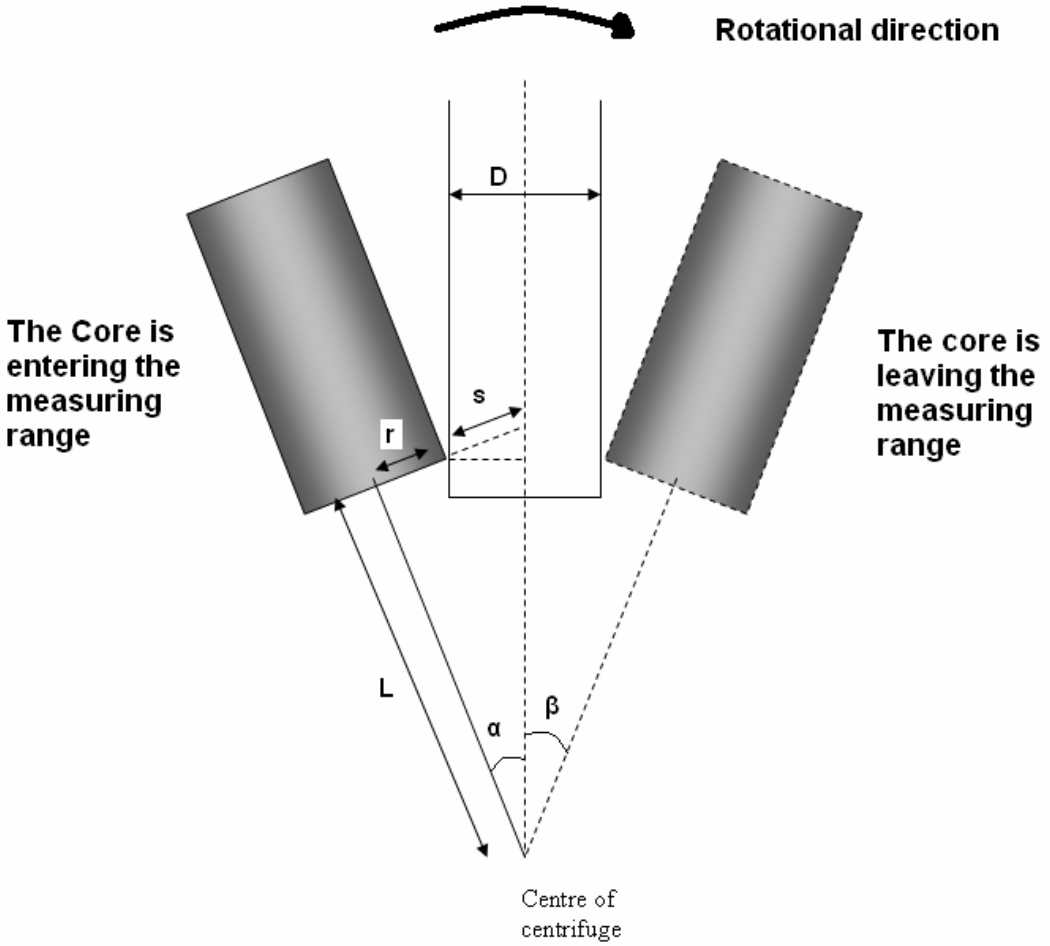

Figure 9.2.2.5: The core sample is entering the measuring range at an angle α, and is leaving the measuring range at an angle β. Measurements are done to verify the gating process.

From the figure above, simple trigonometry yields

$$s = \frac{D/2}{\cos(\alpha)} \qquad (9.2.2.1)$$

To make sure that the entire core sample is outside the measuring range when the gating starts, one need to make sure that:

$$r + s \le L \times \tan(\alpha) \qquad (9.2.2.2)$$

Both α and β are measured to be 20^o. The measured distances are: L = 11.7 cm and r = 1.9 cm. D is found to be 4 cm. By use of equation (9.2.2.1), s is found to be 2.13 cm. Equation (9.2.2.2) then gives:

$$(1.9 + 2.13)cm = 4.03cm \le (11.7 \times \tan 20)cm = 4.26cm$$

which is consistent. Since α and β are equal, there is also a consistency when the sample is leaving the measuring range. In other words; ***the entire core plug is outside the measuring range when the gating starts and the entire core plug is outside when the gating stops.***

9.2.3 The Software

To count and store the signal, a Maestro-32 ORTEC MCA emulator, Model A65 – B32, has been used. The software has been tested to make sure that it was capable of detecting signals at the desired rotational speed. As previously mentioned, the Beckman centrifuge has a maximum rotational speed of 3500 RPM. To verify the capacity of the software, signals corresponding to 6000 RPM were tested. 6000 RPM equals 10 milliseconds per rotation. The measuring time is 40/360 of one rotation (see Figure 9.2.2.4), which in this case equals approximately 1 millisecond per rotation.

This was first tested by use of a signal generator and a square pulse. The measuring time of 1 millisecond per rotation equals a frequency of 10000 Hz (counting rate), hence the period of the square pulse is 100 µs (see Figure 9.2.3.1).

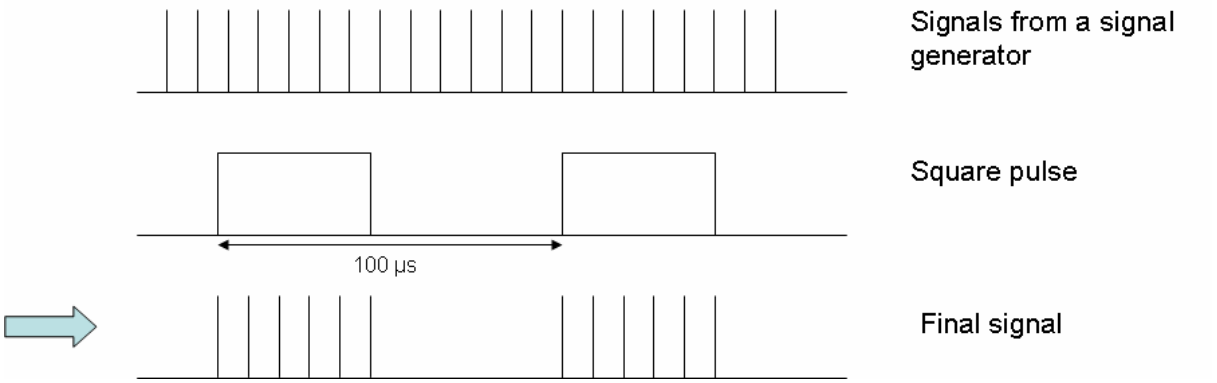

Figure 9.2.3.1: The software was first tested by use of a signal generator and a square pulse. The period of the square pulse was 100 µs.

The software registered the exact number of signals; hence the software seemed to be qualified for the current measurements.

Instead of a square pulse, the software was secondly tested by use of a photo diode and the steel disk seen in Figure 9.2.2.4, since this is the real case. This disk was mounted to a electrical drill, with a rotational speed of 6000 RPM. It was found that an UP-AMP (upgrading amplifier) was necessary for the computer to register the photo-diode, see Figure 9.2.3.2. With this amplifier, the same conclusion as in the first test was found: The software is qualified for the current measurements.

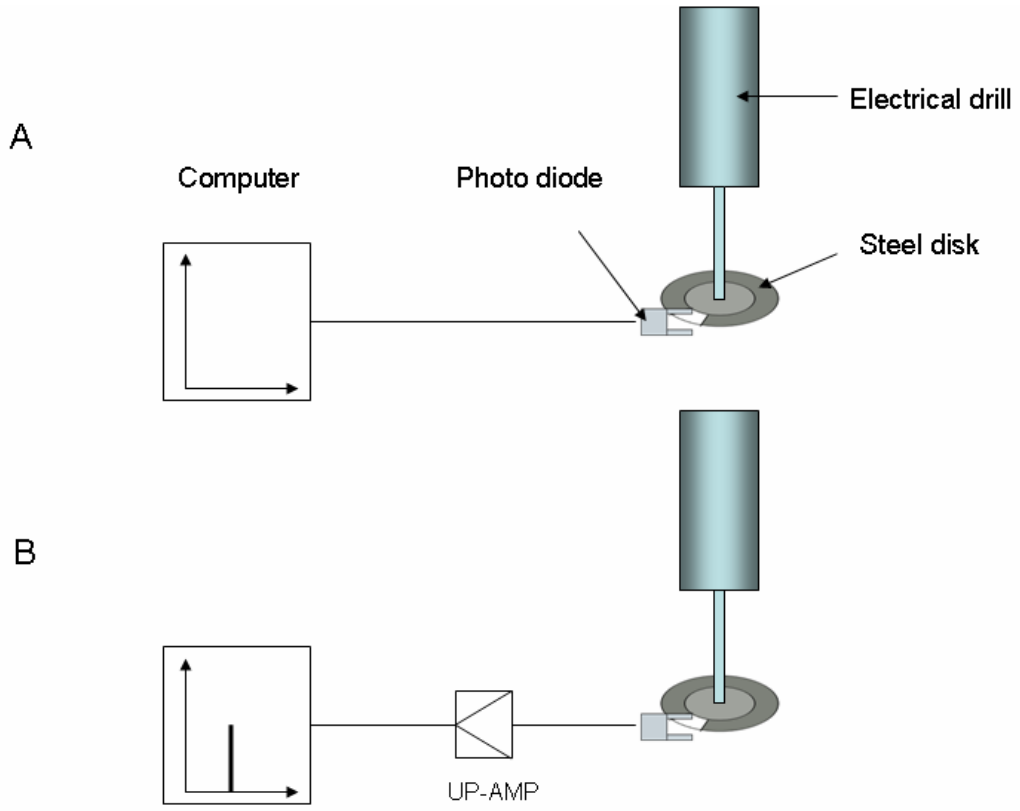

Figure 9.2.3.2: The steel disk is mounted to an electrical drill, which is rotating with a speed of 6000 RPM. A: First, no signal was registered. B: By adding an upgrading amplifier (UP-AMP) to the photo diode, the exact number of signals was registered.

9.2.4 Tracers

To be able to investigate movement of phases, tracers are needed [53]-[54]. In a system of n phases, there will be need for n-1 different tracers, if the in-situ saturation of all the phases should be measured. In this system, only two phases are present; brine and decane, hence only one tracer is needed.

There are some requirements to the tracers. First of all, the attenuation of the radioactivity should be as small as possible, hence only γ emitting isotopes should be used. Next, to avoid large corrections to the activity because of disintegrations, the isotope should have rather long half-life. Necessary corrections are done by the following equation:

$$\frac{N}{N_0} = \exp\left(\frac{-t}{\tau}\right), \qquad (9.2.4.1)$$

where N is the current intensity, N_0 is the original intensity, t is time and τ is half-life.

Thirdly, if more than one tracer is to be used, the energy of the emitted particles needs to be separable. Since only one tracer is being used in this set-up, this does not cause any trouble. In addition, one needs to make sure that the tracer does not change the characteristics of the fluid it shall identify. Based on these requirements, the γ emitting isotope ^{22}Na for the water phase has been chosen. Table 9.1 summarizes the data of the isotope being used.

Table 9.1: Data on the isotope being used.

Isotope	Half-life	Energy γ_1 [keV]	Energy γ_2 [keV]	Labelled phase
^{22}Na	2.6 years	511	1275	brine

To minimize the background radiation and increase the statistics, the 511 keV for ^{22}Na is used. Equation (9.2.4.1) for ^{22}Na is shown graphically in Figure 9.2.4.1.

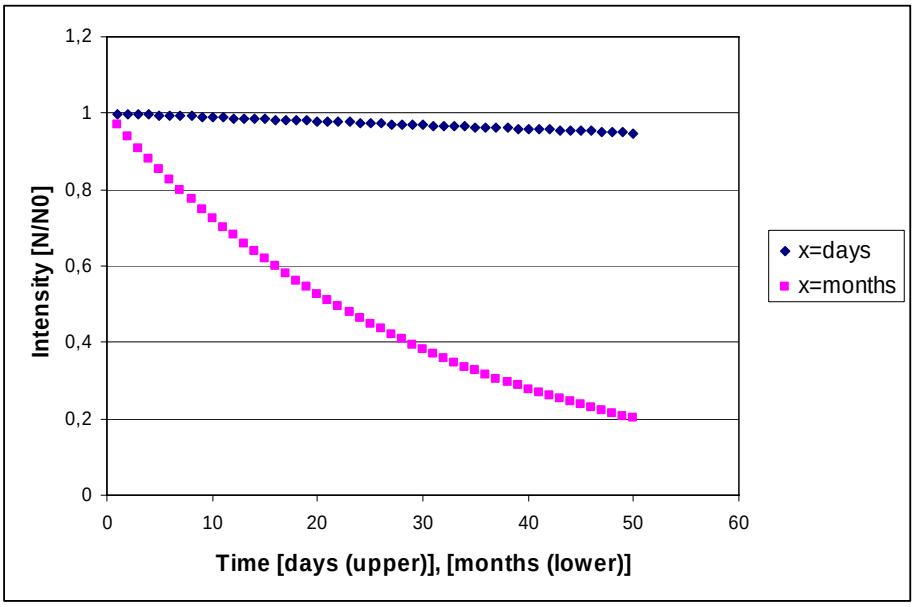

Figure 9.2.4.1: Disintegration of ^{22}Na, half-life=2,6 years. The time axis represents days (upper curve) and months (lower curve).

9.2.5 Calculation of Saturation

To actually calculate the in-situ saturation of the phases, the intensity of the γ-radiation from γ-emitting isotopes is measured. This is done by use of a multi-channel analyser, where the radiation energy of interest (511 keV) is adjusted to channel 2070-2083; a total of 14 channels. For safety reasons, as low radioactivity as possible is used. This set-up uses an intensity of 6 mCu/L. To compensate for this precaution, the distance from the core to the detector is minimized, and the counting time is increased.

With constant collimator opening and distance from collimator to core, the saturation of the labelled phase is proportional to the number of disintegrations registered by the detector (counts per second). Noise is subtracted from the calculated number of counts per seconds as illustrated in the figure below.

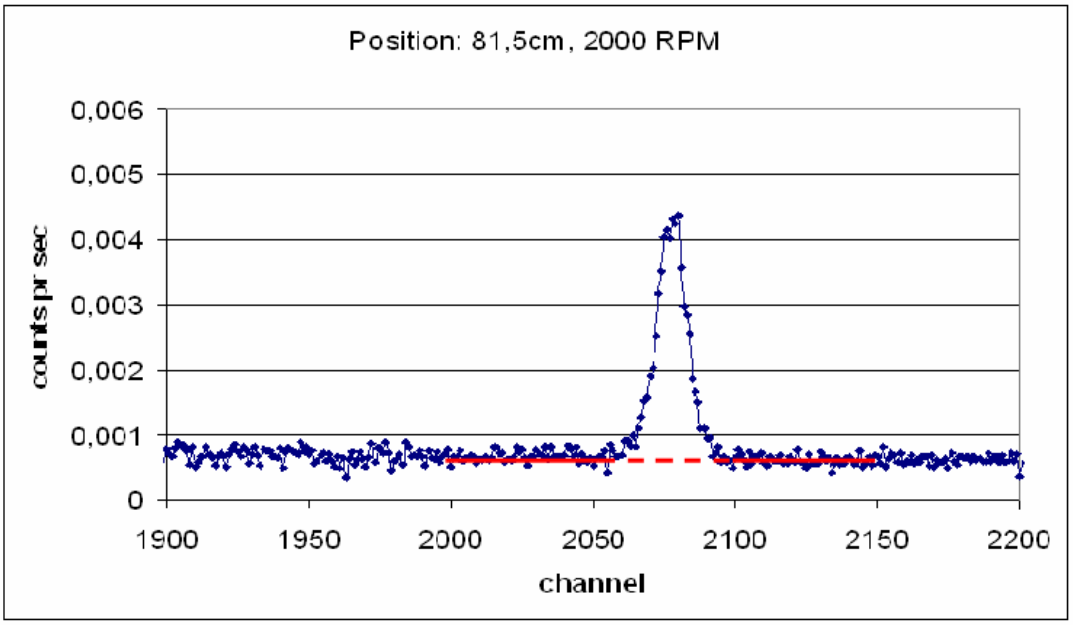

Figure 9.2.5.1: Noise is subtracted from the calculated amount of counts per seconds.

The noise in the region of interest is calculated by first averaging the number of $counts/\sec onds$ in 50 channels both above and below the region, and then again strike an average between these two measurements. The noise is then subtracted from the measured amount of disintegrations (counts per second).

In addition, one needs to take into account the background radiation (due to previously spilled fluid).

Hence the saturation of the labelled phase is calculated by equation (9.2.5.1).

$$S = \frac{counts/\sec onds - background}{counts/\sec onds\,(100\%) - background}, \qquad (9.2.5.1)$$

where *background* and *counts/seconds (100%)* are number of disintegrations without core present and with core 100 % saturated with the radioactive labelled fluid, respectively. The uncertainty is given by the number of disintegrations:

$$\Delta S = \pm \frac{\sqrt{counts}}{counts} \times S \qquad (9.2.5.2)$$

Equation (9.2.5.2) is shown graphically in Figure 9.2.5.2.

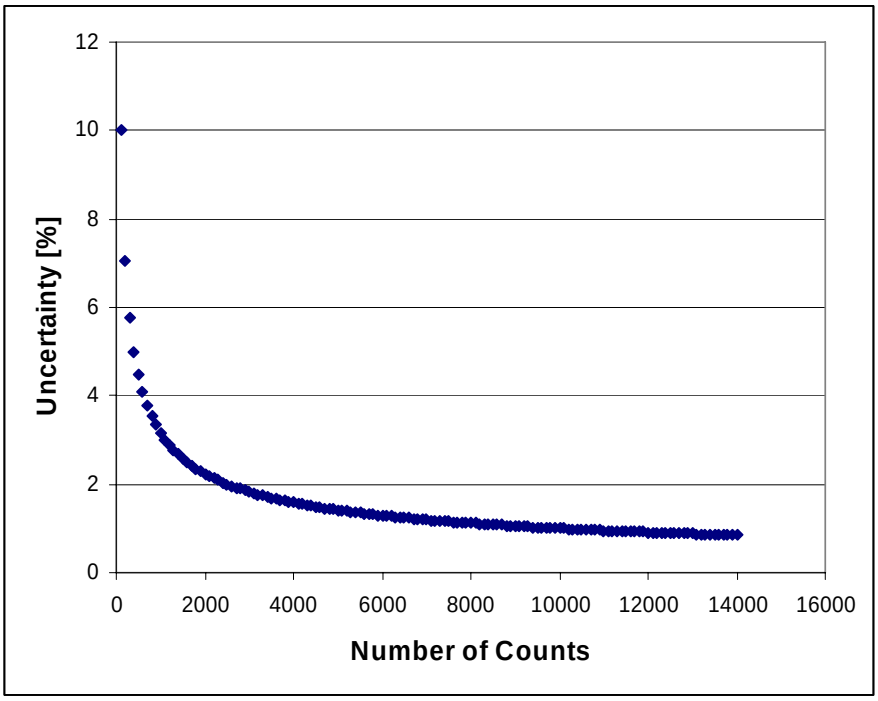

Figure 9.2.5.2: Theoretical uncertainty of the detection process.

The uncertainty described by equation (9.2.5.2), is the principle uncertainty, related to the number of counts registered. In addition, there are uncertainties related to the detection process, signal processing, and variations in temperature, natural radiation and amplifying.

9.3 Calibrations

9.3.1 Measuring Time

Before any further measurements are performed, one needs to establish the minimum measuring time. The detector is placed right above the core sample, and the number of disintegrations per second is measured at different points of time. This is done both when the core holder is lying still (under the detector) and while the centrifuge is spinning at 2000 RPM. The results form measurements carried out at 0 RPM and 2000 RPM are presented in Table 9.2 and Figure 9.3.1.1, and Table 9.3 and Figure 9.3.1.2, respectively.

Table 9.2: Measuring time, at 0 RPM

Time [min]	Number of counts	counts pr sec [sec^{-1}]	Uncertainty [%]
1	58	0,3706	13,1
2	104	0,7614	9,8
3	157	0,7777	8,0
4	218	0,8111	6,8
5	280	0,8373	6,0
6	324	0,7952	5,6
8	414	0,7687	4,9
10	512	0,7561	4,4
12	596	0,7313	4,1
15	733	0,7162	3,7
18	888	0,7235	3,4
20	980	0,7174	3,2
25	1243	0,7024	2,8
30	1443	0,6967	2,6
35	1699	0,6965	2,4
40	1957	0,6997	2,3
45	2141	0,6968	2,2
50	2385	0,6967	2,0
60	2862	0,6973	1,9
70	3357	0,7032	1,7
80	3826	0,7005	1,6
90	4295	0,7012	1,5
100	4786	0,7032	1,4
120	5736	0,7026	1,3
140	6734	0,7076	1,2
160	7792	0,7083	1,1
180	8587	0,7060	1,1
1400	66391	0,6974	0,4

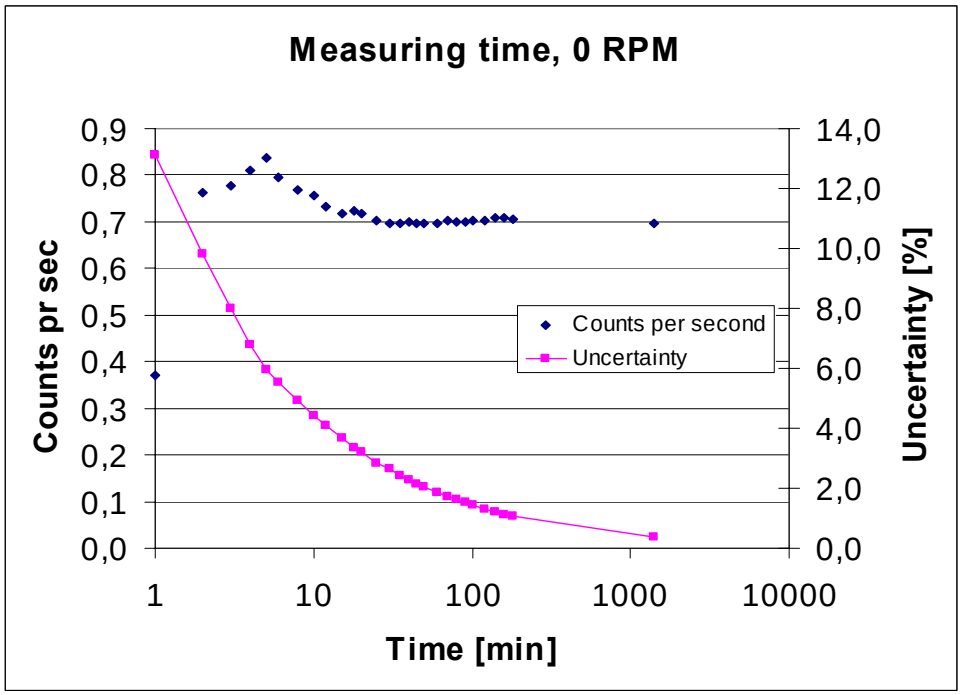

Figure 9.3.1.1: Counts per second and uncertainty for measurements at 0 RPM.

Table 9.3: Measuring time, at 2000 RPM.

Time [min]	Number of counts	Counts pr sec [sec^{-1}]	Uncertainty [%]
30	90	0,03713	10,5
46	137	0,04080	8,5
60	177	0,04116	7,5
75	235	0,04044	6,5
90	273	0,04201	6,1
105	325	0,04407	5,5
120	388	0,04388	5,1
135	423	0,04346	4,9
150	482	0,04327	4,6
165	516	0,04312	4,4
180	577	0,04269	4,2
210	671	0,04213	3,9
240	766	0,04156	3,6
270	833	0,04136	3,5
300	972	0,04287	3,2
330	1077	0,04313	3,0
360	1153	0,04279	2,9
390	1248	0,04261	2,8
420	1359	0,04277	2,7
450	1411	0,04244	2,7
480	1487	0,04207	2,6
540	1597	0,04277	2,5
1200	3782	0,04316	1,6
1260	3977	0,04339	1,6
1290	4026	0,04331	1,6

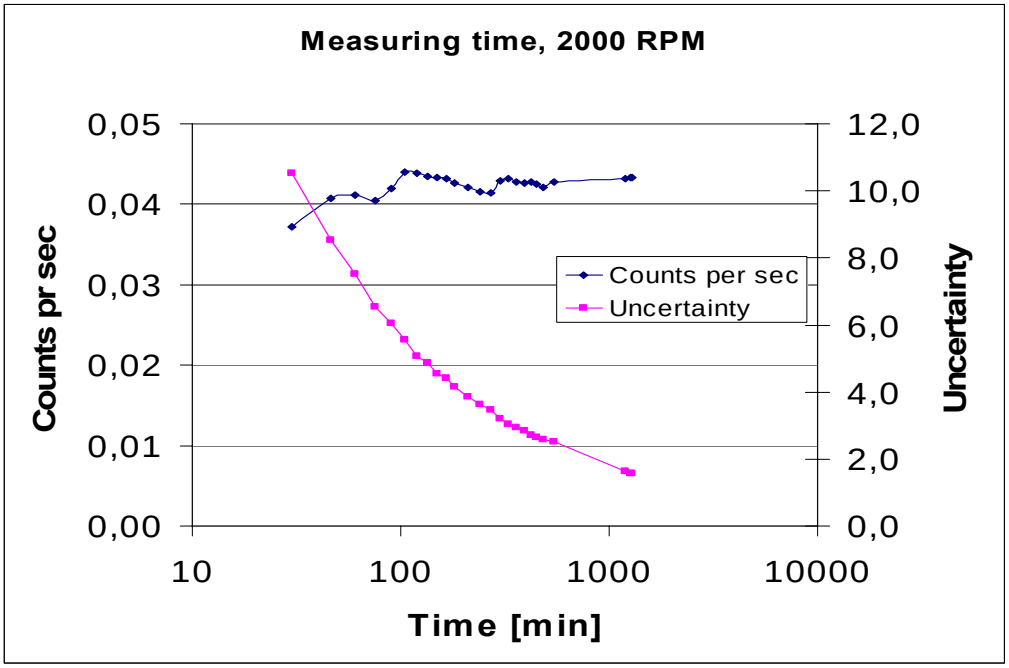

Figure 9.3.1.2: Counts per second and uncertainty for measurements at 2000 RPM.

Based on these measurements, minimum measuring times of 35 minutes when the core is lying still and nine hours when spinning are chosen, giving an uncertainty of ~2.5 %.

9.3.2 Measuring the Collimator Characteristics

Before the experiments are started, one needs to establish the measuring range.

9.3.2.1 Longitudinal Characteristics

The outlet- and inlet endface of the core plug need to be established. Based on previous work by Thomas Bognø and Eirik Aspenes [35], the outer end of the plug is located approximately at position 80cm (position on aluminium rig). With this in mind, measurements are done at a millimetre scale near this position. The length of the core plug is known (6.0 cm), hence analogous measurements are done near the inner end of the core. Results are presented in Table 9.4 and Figure 9.3.2.1.1.

Table 9.4: Longitudinal characteristic of core sample.

Position [cm]	Counts per sec
80,0	0,1954
80,1	0,4198
80,2	0,5714
80,3	0,6638
80,4	0,7645
80,5	0,7853
80,6	0,8246
80,7	0,7582
84,9	0,7649
85,0	0,7424
85,1	0,7772
85,2	0,8131
85,3	0,7985
85,4	0,7696
85,5	0,7806
85,6	0,7661
85,7	0,7360
85,8	0,6452
85,9	0,5951
86,0	0,4837
86,1	0,3743
86,2	0,2222
86,3	0,1088

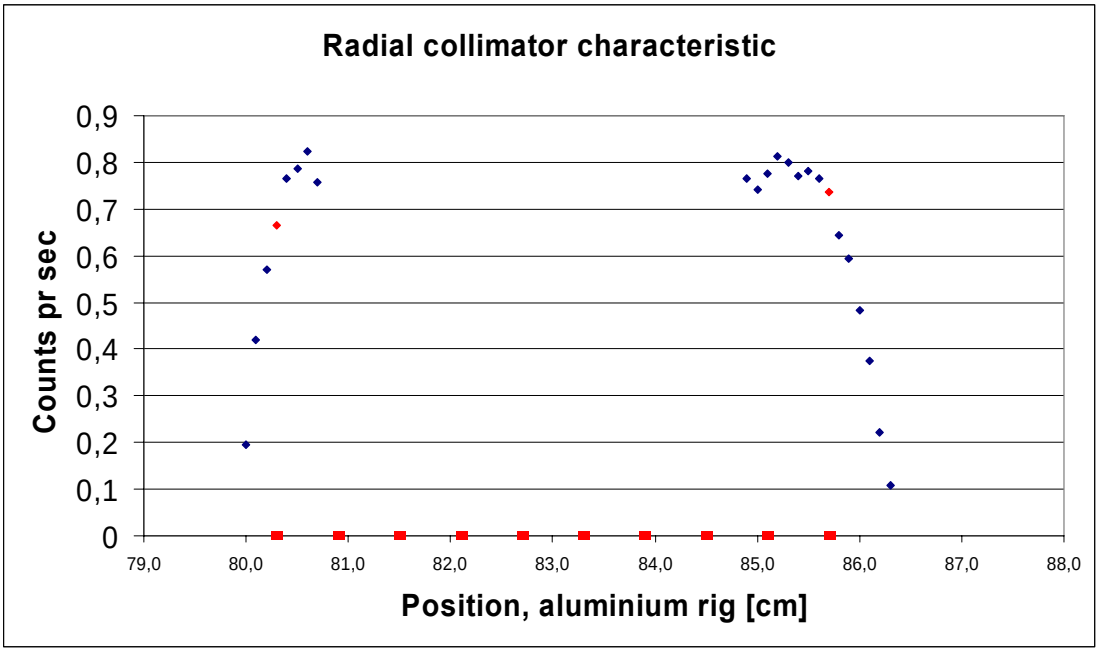

Figure 9.3.2.1.1: Defining the measuring range. Final measuring points are marked red.

Based on these measurements, and the fact that the resolution is set to 6mm, the measuring points are defined as positions [80.3; 80.9; 81.5; 82.1; 82.7; 83.3; 83.9; 84.5; 85.1; 85.7]. These are the red points at the x-axis of Figure 9.3.2.1.1. Assuming the core sample is locked in position during the experiments, these positions are reckoned as settled during the following work.

9.3.2.2 Angular Characteristics

By turning the core holder mounted in the centrifuge, the angular characteristics of the collimator are controlled. Measurements are done both at the inner and outer measuring point of the core sample, see Figure 9.3.2.2.1.

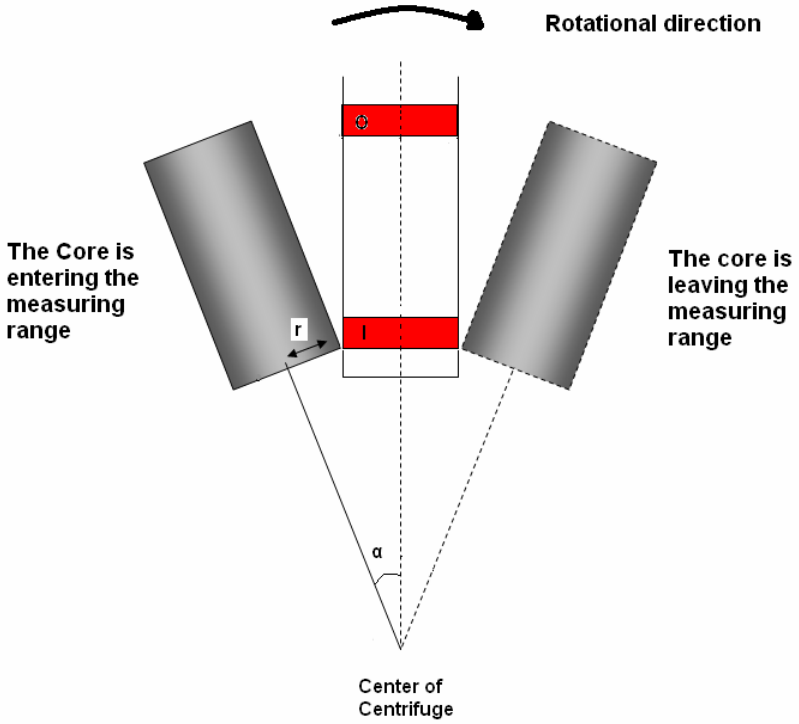

Figure 9.3.2.2.1: To find the angular characteristics of the collimator, measurements are done both at the inner and outer measurement points, marked as I and O, respectively.

The results of the inner and outer measurements are presented in Table 9.5 and Figure 9.3.2.2.2, and Table 9.6 and Figure 9.3.2.2.3, respectively.

Table 9.5: Data from inner measuring point.

Na1 peak; 511 keV	
Angle [degrees]	**Counts per sec**
-20	0,043
-15	0,149
-10	0,503
-5	0,886
0	1,179
5	1,004
10	0,552
15	0,226
20	0,115

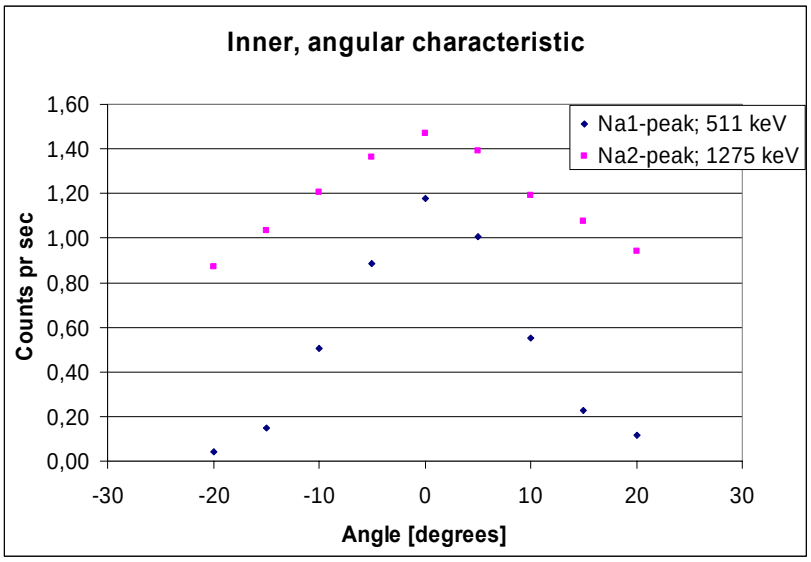

Figure 9.3.2.2.2: The inner angular characteristics. Both measurements of the 511keV and 1275 keV are included.

Table 9.6: Data from outer measuring point.

Na1-peak; 511 keV	
Angle [Degrees]	**Counts per sec**
-20	0,022
-15	0,023
-10	0,159
-5	0,546
0	0,975
5	0,713
10	0,144
15	0,025
20	0,026

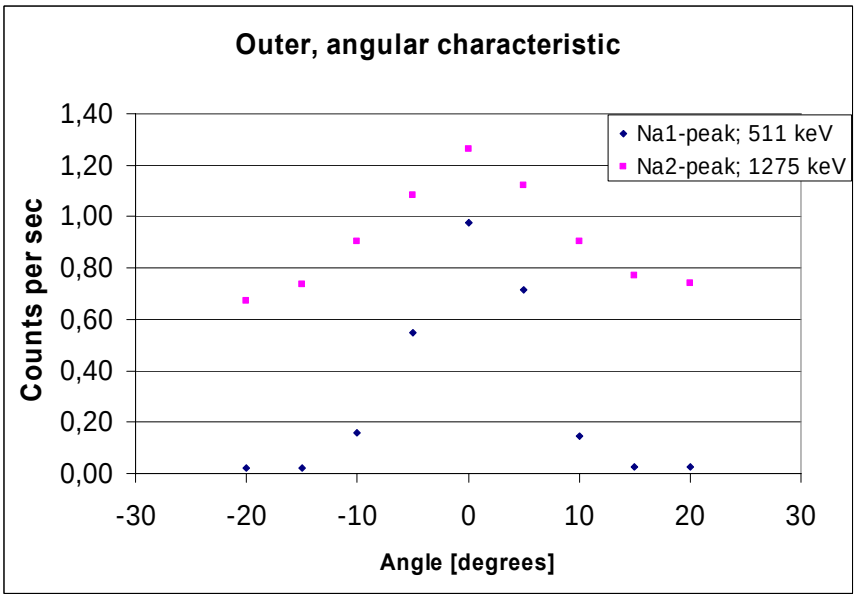

Figure 9.3.2.2.3: The outer angular characteristics. Both measurements of the 511keV and 1275 keV are included.

These measurements indicate why the 511 keV is to prefer. From Figure 9.3.2.2.2 and Figure 9.3.2.2.3 one can see that the collimator is more able to stop the 511 keV radiations than is the case for the more energetic 1275 keV radiation. Hence to minimize the background radiation, all calculations are performed by use of the 511 keV radiations.

As expected, the "strongest" signals are obtained at the inner measuring point, since a larger part of the core sample is inside the measuring range than is the case at the outer measuring point (for $|\alpha| > 0$, see Figure 9.3.2.2.1).

One can further see that the plots are not totally symmetrical. There might be several reasons for that. Firstly, the angles are based on a visual estimate, and there may therefore be a tolerance to the referred value. Secondly, since we are dealing with a porous material, the porosity may vary as well, and as a result of this, the measurements would not be totally homogenous.

9.3.3 Correction Coefficients

The radius from the centre of the centrifuge to each measuring point varies, hence the time which the core sample being inside the measuring range varies. Thus the innermost measuring point will give more detections than the outermost point. In order to be able to compare the measurements performed at 0 and 2000 RPM, a correction coefficient is needed (to compensate for the measurements obtained at 2000 RPM), see Figure 9.3.3.1.

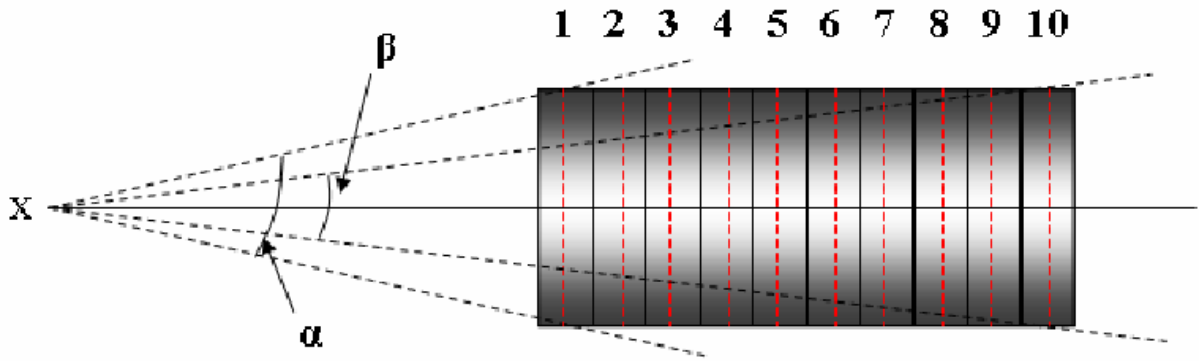

Figure 9.3.3.1: Calculating the correction coefficients. Each angle from α to β is calculated. Using α as reference point, each coefficient is calculated.

This coefficient is calculated by using the innermost measuring point (point 1 in Figure 9.3.3.1) as a reference point. The distance from the centre of the centrifuge to the centre of point 1 is (11.7 + 0.3) cm = 12.0 cm (The resolution being 6 mm). The radius of the core sample is 1.9 cm. This gives $\theta_1 = \alpha = 18.0^o$. The corresponding values of point 10 is [11.7 + (9.5 x 0.6)] cm = 14.7 cm, r: 1.9 cm. This gives $\theta_{10} = \beta = 12.5^o$. Each correction coefficient is calculated by use of the following equation:

$$f_i = \frac{\theta_1}{\theta_i} \qquad (9.3.3.1)$$

The correction values of each point are listed in Table 9.7.

Table 9.7: The correction coefficients.

	Angle (degrees)		Factor of correction
θ_A	20,0	f_A	**0,902**
θ_B	18,9	f_B	**0,951**
θ_1	18,0	f_1	**1,000**
θ_2	17,2	f_2	**1,049**
θ_3	16,4	f_3	**1,098**
θ_4	15,7	f_4	**1,148**
θ_5	15,0	f_5	**1,197**
θ_6	14,4	f_6	**1,246**
θ_7	13,9	f_7	**1,296**
θ_8	13,4	f_8	**1,345**
θ_9	12,9	f_9	**1,394**
θ_{10}	12,5	f_{10}	**1,444**
θ_C	12,1	f_C	**1,493**
θ_D	11,7	f_D	**1,543**

As seen in Table 9.7, two additional points on each side of the core sample are included. These are to be used when measurements are done outside the core.

9.4 Measurements of a 100% Water Saturated Core Plug

9.4.1 At 0 RPM

When knowing the minimum measuring time and the positions of the measuring points, a scan of the 100 % water saturated (radioactive labelled brine) core plug while lying still (0 RPM) may be performed. The minimum measuring time is set to 35 minutes, based on the previous measurements. A total of 14 points are measured, four outside the core plug (two on each side) and 10 points across the plug. The results of measurements on PO30 and PO31 are presented in Table 9.8 and Figure 9.4.1.1 and Table 9.9 and Figure 9.4.1.2, respectively.

Table 9.8: 100 % Sw, PO30

Position	Number of counts	Counts per sec	Uncertainty (counts pr sec)	Uncertainty [%]
79,1	322	0,058	0,003	5,6
79,7	362	0,059	0,003	5,3
80,3	2675	0,676	0,013	1,9
80,9	2291	0,748	0,016	2,1
81,5	45264	0,743	0,003	0,5
82,1	2014	0,687	0,015	2,2
82,7	1950	0,722	0,016	2,3
83,3	1895	0,759	0,017	2,3
83,9	2476	0,761	0,015	2,0
84,5	2442	0,779	0,016	2,0
85,1	2231	0,803	0,017	2,1
85,7	2285	0,803	0,017	2,1
86,3	658	0,165	0,006	3,9
86,9	372	0,049	0,003	5,2

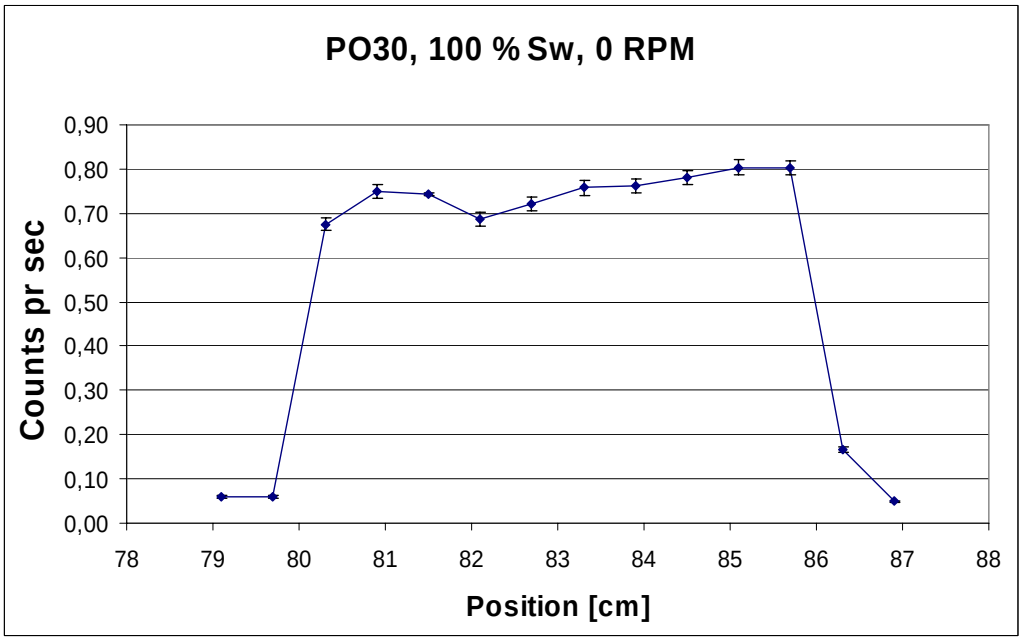

Figure 9.4.1.1: The scanned profile of PO30, at 0 RPM.

From Figure 9.4.1.1, one can see that the scanned profile is rather uniform throughout the length of the core; hence the plug seems quite homogenous. The uncertainties are acceptable.

Table 9.9: 100 % Sw, PO31.

Position	Number of counts	Counts per sec	Uncertainty (counts pr sec)	Uncertainty [%]
79,1	225	0,040	0,003	6,7
79,7	219	0,080	0,005	6,8
80,3	1864	0,592	0,014	2,3
80,9	2191	0,591	0,013	2,1
81,5	1212	0,626	0,018	2,9
82,1	1835	0,664	0,016	2,3
82,7	35626	0,657	0,004	0,5
83,3	1031	0,669	0,021	3,1
83,9	2520	0,662	0,013	2,0
84,5	1335	0,636	0,017	2,7
85,1	1521	0,667	0,017	2,6
85,7	1636	0,562	0,014	2,5
86,3	356	0,032	0,002	5,3
86,9	37472	0,032	0,0002	0,5

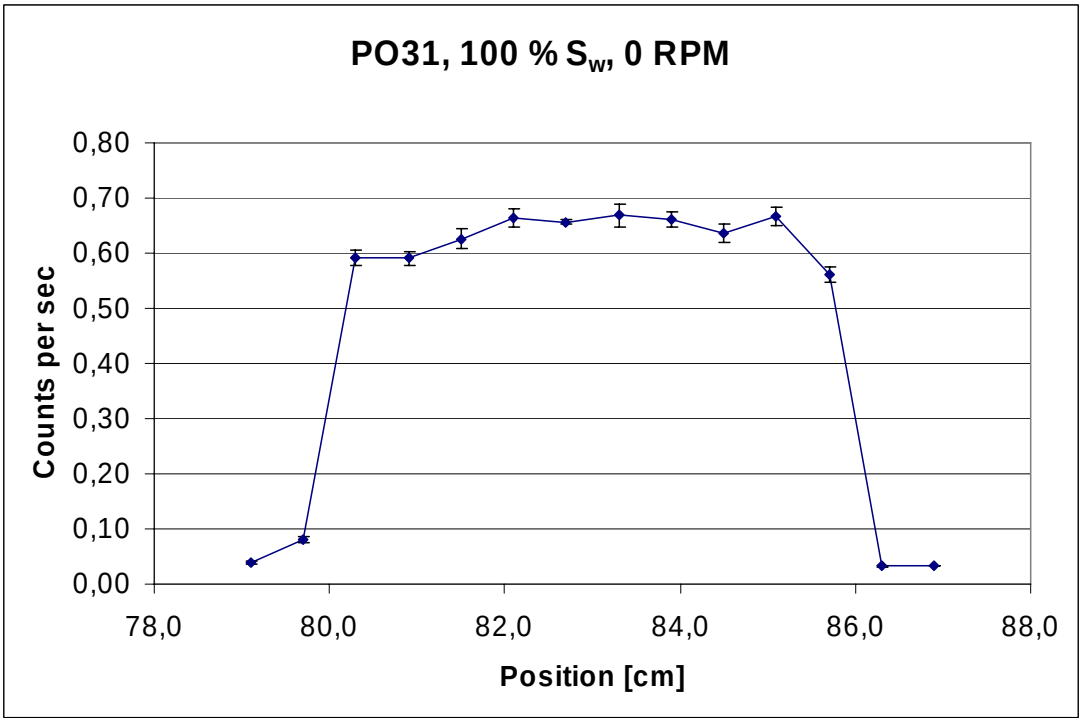

Figure 9.4.1.2: The scanned profile of PO31, at 0 RPM.

The figure above indicates a rather homogenous core plug, with respect to the porosity. However, Figure 9.4.1.2 shows generally lower values of counts per second than is the case in Figure 9.4.1.1. This may be a result of variations in temperature, which may affect the multi-channel analyzer (the region of interest-ROI). In addition, it may be a result of not achieving a 100 % effective RWAT. An effluent profile has not been taken (due to lack of available equipment), hence the replacement of brine by radioactive labelled brine may not have been 100 % effective.

9.4.2 At 2000 RPM

After taking a saturation profile when core sample is lying still, another profile is taken while the core sample is spinning. The centrifugal speed chosen is 2000 RPM. It is now need for gating, which means the software needs to be set to MCB-properties → Gating → Coincidence.

9.4.2.1 Theoretical Calculations

The expected number of counts per second when the centrifuge is spinning can be estimated theoretically.

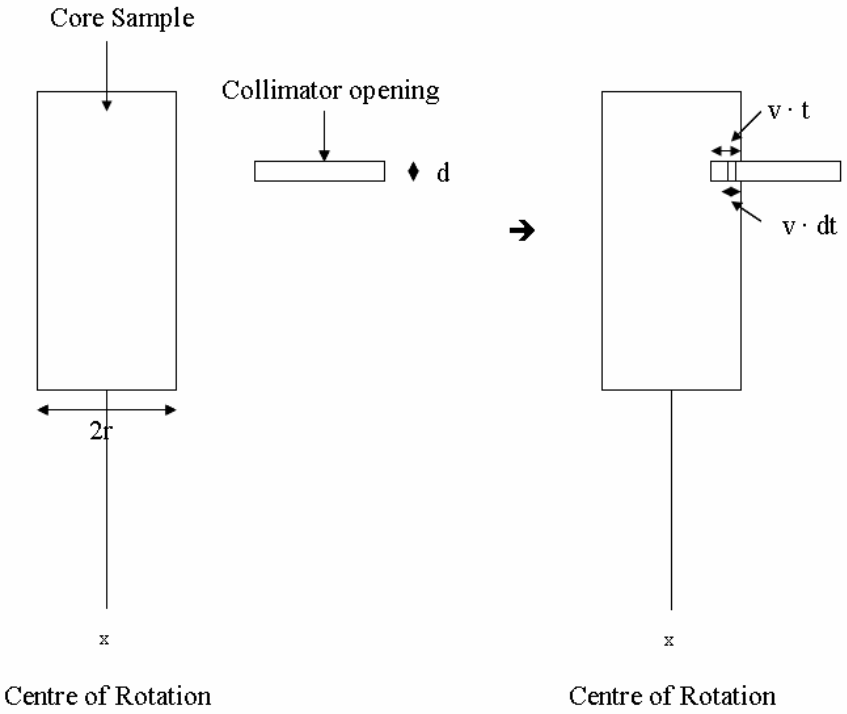

Figure 9.4.2.1.1: Core Sample entering the measuring range; v=velocity, t=time, d=the measuring range (6mm).

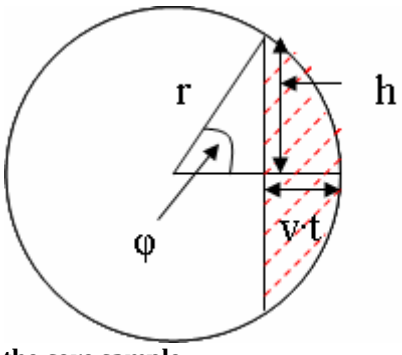

Figure 9.4.2.1.2: A cross-section of the core sample.

Trigonometric relations from Figure 9.4.2.1.2 (v=velocity, t=time and r=radius of core plug):

$$\cos\varphi = \frac{r - vt}{r} \tag{9.4.2.1.1}$$

$$\sin\varphi = \frac{h}{r} \Rightarrow h = r \cdot \sin\varphi \tag{9.4.2.1.2}$$

Derivation of (9.4.2.1.1) gives (a constant velocity is assumed):

$$-\sin\varphi \cdot d\varphi = \frac{-v \cdot dt}{r} \Rightarrow dt = \sin\varphi \cdot \frac{r}{v} \cdot d\varphi \tag{9.4.2.1.3}$$

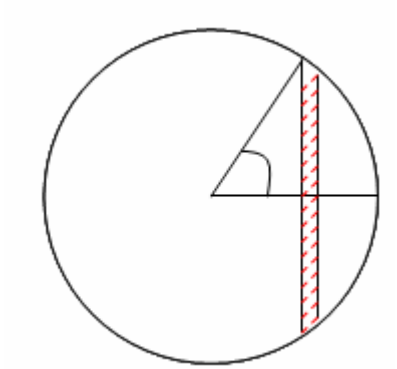

Figure 9.4.2.1.3: A cross-section of the core sample.

The volume of the shaded field is given by:

$$dV = v \cdot dt \cdot d \cdot 2r\sin\varphi = 2dvr\sin\varphi\, dt\,, \tag{9.4.2.1.4}$$

where the area and height of the shaded field is given by v·dt·d and 2·rsin φ, respectively.

The volume of the shaded field in Figure 9.4.2.1.2 is given by

$$V(t) = \int 2dvr\sin\varphi\, dt \tag{9.4.2.1.5}$$

By use of (9.4.2.1.1) and (9.4.2.1.3):

$$V(t) = \int_0^{ar\cos\left(\frac{r-vt}{r}\right)} 2dvr\sin\varphi \cdot \sin\varphi \frac{r}{v} d\varphi = \underline{2r^2 d \int_0^{ar\cos\left(\frac{r-vt}{r}\right)} \sin^2\varphi \cdot d\varphi}$$

By use of a calculation program, this yields:

$$V(t) = -rd\left[\sqrt{\left(vt\frac{2r-vt}{r^2}\right)r} - \sqrt{\left(vt\frac{2r-vt}{r^2}\right)vt} - \left(ar\cos\frac{r-vt}{r}\right)r\right]$$

This gives the relation of volume and time.

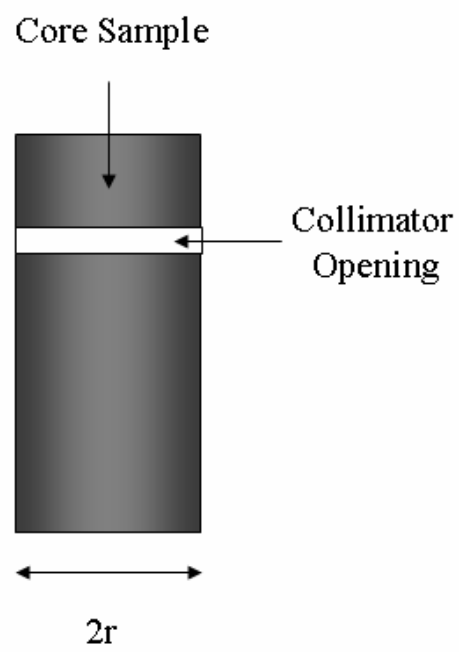

Figure 9.4.2.1.4: The entire diameter of the core is within the collimator opening.

The time it takes until the entire diameter of the core sample is within the collimator opening (see Figure 9.4.2.1.4), is given by

$$t = \frac{2r}{v} \qquad (9.4.2.1.6)$$

We define

$$n = \frac{number\ of\ counts}{m^3 \cdot s} \qquad (9.4.2.1.7)$$

The total number of counts *from the moment the sample is entering the collimator opening until the entire sample is inside* is given by [from the expression of V(t) and equations (9.4.2.1.6) and (9.4.2.1.7)]

$$N' = n \cdot \int_0^{2r/v} V(t)dt = 2\frac{r^3}{v}d\pi \cdot n \qquad (9.4.2.1.8)$$

The velocity, v, is equivalent to

$$v = l \cdot \omega, \tag{9.4.2.1.9}$$

where l is the distance from the centre of rotation, and ω is the angular velocity.

Because the number of counts when the sample is *leaving* the collimator opening is analogous to equation (9.4.3.1.8), the total number of counts is given by

$$N = 4\frac{r^3}{l\omega} d\pi \cdot n$$

During a time T, the core sample is entering (and leaving) the measuring range a number of X times. X is given by

$$X = \frac{T \cdot \omega}{2\pi} \tag{9.4.2.1.10}$$

Hence the total number of counts is

$$N_{tot} = N \cdot X = 2\frac{r^3}{l} d \cdot n \cdot T$$

And the total number of counts per second, $\overline{N}_{tot}$, is given by

$$\overline{N}_{tot} = 2\frac{r^3}{l} d \cdot n \tag{9.4.2.1.11}$$

The number of counts per second when the collimator opening is located directly above the core sample is given by

$$N_0 = \pi r^2 d \cdot n$$

The relation between $\overline{N}_{tot}$ and N_0 can be written

$$\begin{aligned} &\overline{N}_{tot} = 2\frac{r^3}{l} d \cdot n = 2\frac{r}{l\pi} \cdot \pi r^2 d \cdot n \\ &\Rightarrow \underline{\underline{\overline{N}_{tot} = 2\frac{r}{l\pi} \cdot N_0}} \end{aligned} \tag{9.4.2.1.12}$$

Hence the number of counts per second when spinning should *theoretically* be a factor $2\frac{r}{l\pi}$ of the values obtained at 0 RPM.

9.4.2.2 Experimental Measurements

At a rotational speed of 2000 RPM, the experimental results of samples PO30 and PO31 are presented in Table 9.10 and Figure 9.4.2.1, and Table 9.11 and Figure 9.4.2.2, respectively. The theoretically obtained values, based on the calculations in Chapter 9.4.2.1, are included for comparison.

Table 9.10: Experimental and theoretical results of PO30

Core:	**PO30**							
Porosity [%]:	**44,5**							
Permeability [mD]:	**4,5**							
Swi [%]	**100**							
	Experimental					**Theoretical**		**Deviation**
	At 0 RPM		**At 2000 RPM**			**At 2000 RPM**		**Experiment-**
Position	**Counts pr. sec**	**±**	**Counts pr sec**	**Corrected Counts pr sec**	**±**	**Counts pr sec**	**Corrected Counts pr sec**	**Theory [%]**
79,1	0,058	0,003	0,005	0,0074	0,0006	0,004	0,006	-26
79,7	0,059	0,003	0,007	0,0104	0,0004	0,004	0,006	-78
80,3	0,676	0,013	0,036	0,0524	0,0011	0,046	0,067	22
80,9	0,748	0,016	0,041	0,0570	0,0008	0,053	0,074	23
81,5	0,743	0,003	0,039	0,0534	0,0009	0,054	0,074	28
82,1	0,687	0,015	0,039	0,0514	0,0014	0,052	0,068	25
82,7	0,722	0,016	0,038	0,0482	0,0009	0,057	0,071	33
83,3	0,759	0,017	0,045	0,0542	0,0013	0,062	0,075	28
83,9	0,761	0,015	0,050	0,0570	0,0010	0,065	0,075	24
84,5	0,779	0,016	0,047	0,0518	0,0012	0,070	0,077	33
85,1	0,803	0,017	0,038	0,0396	0,0008	0,075	0,079	50
85,7	0,803	0,017	0,028	0,0279	0,0008	0,079	0,079	65
86,3	0,165	0,006	0,006	0,0054	0,0002	0,017	0,016	67
86,9	0,049	0,003	0,005	0,0041	0,0003	0,005	0,005	15

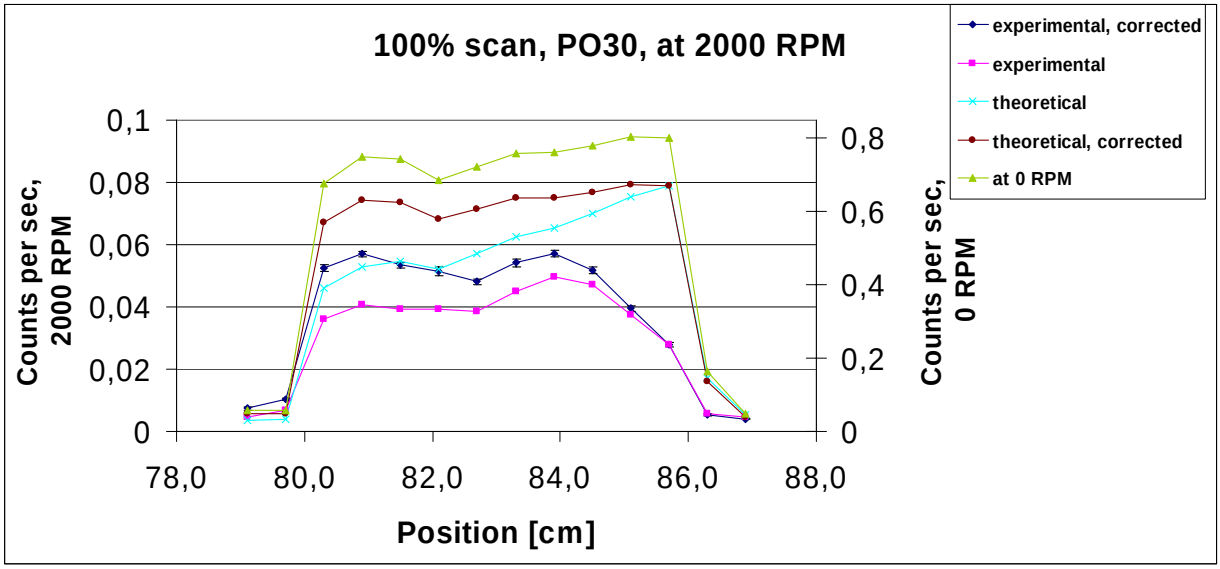

Figure 9.4.2.1: The experimentally- and theoretically obtained results of PO30, at 0 and 2000 RPM.

In Table 9.10, the area of interest is found between the two dashed lines. That is the range of the core sample, found in Chapter 9.3.2.1. In addition, two points at each side of the plug are included for comparison.

In Figure 9.4.2.1, the use of the correction coefficient is seen to obtain the wanted effect. The shape of the corrected experimentally obtained saturation profile measured at 2000 RPM seems to be in good agreement with the shape of the experimentally obtained saturation profile measured at 0 RPM. However, the part of the saturation curve being closest to the centre of rotation is gradually decreasing. This result is not seen in the profile obtained at 0 RPM. After finishing the experiment, a small amount of water was seen in the receiving cup (approximately 4.5 ml). Hence the output of the core sample had not been completely sealed when spinning. This would lead to a decrease in the water saturation of the plug, which is obtained in Figure 9.4.2.1. In addition, the area where the decline is seen is in accordance with the fact that the capillary pressure has its maximum closest to the centre of rotation. Hence, a decrease in water saturation (water has being replaced by air) will at first be detectable in this range. To verify this assumption, the measured numbers of counts per second are summarized. This yields a total of 0.4387 counts per second (from Table 9.10; only the region of interest is included). If the results of position 85,1 and 85,7 are normalized to 0,05 (an estimate of what might be expected), this yields a total of 0.5254 counts per second. Hence a difference of ~16% is obtained. The amount of water being produced during spinning corresponds to a decrease in S_w of ~15%, hence the values are consistent.

When comparing the theoretical and experimentally obtained saturation profile at 2000 RPM, a deviation between the curves is found. The discrepancy is found to be ~25-30% (from Table 9.10), (the positions affected by air have been neglected). There may be several reasons for this discrepancy. First of all, there very well might be moments in the theoretical deduction which have not been taken into account. Secondly, in experimental work, there will always be certain aspects of uncertainty. In these experiments, uncertainties are related to variation in temperature (which might affect amplifier and cause a movement of the region of interest), radioactive decay, variation in real time / live time, etc. Since the measurements were done in the course of approximately one month, the effect of radioactive decay should be insignificant (cf. Figure 9.2.4.1).

Table 9.11: Experimental and theoretical results of PO31

Core:	**PO31**							
Porosity [%]:	**44,3**							
Permeability [mD]:	**3,4**							
Swi [%]	**100**							
	Experimental					**Theoretical**		**Deviation**
	At 0 RPM		**At 2000 RPM**			**At 2000 RPM**		**Experiment-**
Position	**Counts pr. sec**	**±**	**Counts pr sec**	**Corrected Counts pr sec**	**±**	**Counts pr sec**	**Corrected Counts pr sec**	**Theory [%]**
79,1	0,040	0,003	0,004	0,0061	0,0002	0,003	0,004	-54
79,7	0,080	0,005	0,012	0,0174	0,0007	0,005	0,008	-118
80,3	0,592	0,014	0,036	0,0525	0,0010	0,040	0,059	11
80,9	0,591	0,013	0,038	0,0532	0,0013	0,042	0,059	9
81,5	0,626	0,018	0,039	0,0522	0,0010	0,046	0,062	16
82,1	0,664	0,016	0,042	0,0549	0,0013	0,051	0,066	17
82,7	0,657	0,003	0,044	0,0549	0,0012	0,052	0,065	16
83,3	0,668	0,021	0,048	0,0572	0,0012	0,055	0,066	13
83,9	0,662	0,013	0,049	0,0566	0,0012	0,057	0,065	13
84,5	0,636	0,017	0,049	0,0544	0,0012	0,057	0,063	13
85,1	0,667	0,017	0,054	0,0571	0,0013	0,063	0,066	13
85,7	0,562	0,014	0,048	0,0481	0,0014	0,055	0,055	13
86,3	0,032	0,002	0,004	0,0042	0,0002	0,003	0,003	-32
86,9	0,032	0,000	0,004	0,0035	0,0002	0,004	0,003	-12

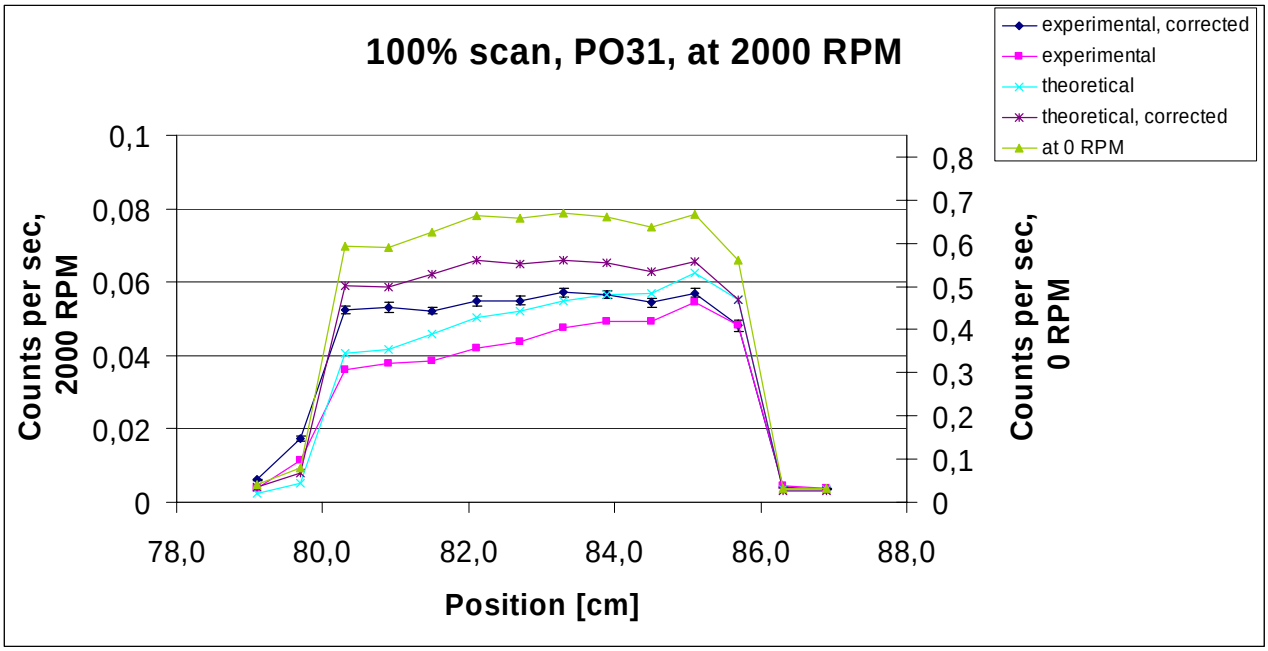

Figure 9.4.2.2: The experimentally- and theoretically obtained results of PO31, at 0 and 2000 RPM.

In the figure above, it is seen that by using the correction coefficient, the shape of the saturation profiles obtained at 0 and 2000 RPM are more or less the same. As was the case for PO30, there is a deviation in the theoretically and experimentally obtained saturation profiles at 2000 RPM for this plug as well. However, this latter deviation is not that significant. The reason for this "improved" result is most likely due to the difference between the saturation curves seen in Figure 9.4.1.1 and Figure 9.4.1.2: Since the profiles being obtained at 2000 RPM are quite stable (insignificant difference in the obtained result of PO30 versus PO31), and the theoretical calculations are based upon the measurements obtained at 0 RPM (where a larger deviation is seen), there will be a difference. This difference will in turn affect the theoretically obtained values.

The problems with an unsealed outlet were also seen when spinning PO31. An amount of 4 ml of water was produced, even when effort had been made to seal the outlet of the core holder. Hence the obtained saturation profile was decreasing towards the inlet endface of the plug. This result, however, has been corrected in Figure 9.4.2.2: The core holder containing the plug was removed from the centrifuge after spinning, and approximately 2 pore volumes of the radioactive labelled fluid was injected by using a backpressure regulator to compress and remove the unwanted air (Private Communication, Arne Graue). Another measurement was then performed close to the inlet endface of the plug and it was verified that the initial water saturation had been re-established. Hence the saturation profile could be normalized.

9.4.3 Capillary Pressure Measurements

The aims of these experiments were to perform both primary drainage- and forced imbibition capillary pressure measurements, and then compare the obtained results by using this Nuclear Tracer Imaging Centrifuge Method with the conventional P_c-curves, measured simultaneously. The maximum speed of rotation was primarily set to 3500 RPM (cf. centrifuge manual). However, at this maximum rotational speed, it turned out that the receiving cup mounted at the outlet endface of the core holder could not handle the stress, and the cup was crushed. Since this happened while performing experiments on PO30, and before reaching the final equilibrium, no scanning profiles had been obtained, hence only the *conventional* primary drainage P_c-curve was obtained from this core plug. The capillary pressure is plotted versus mean saturation, and Hassler-Brunner saturations. These latter saturations were obtained by using the following equation (from Chapter 2):

$$S_{w,HB}(P_{ci}) = \bar{S}_w(P_{ci}) + P_{ci}\frac{d\bar{S}_w(P_{ci})}{dP_{ci}}$$

The capillary pressure is calculated by

$$P_c = \frac{1}{2}\Delta\rho\omega^2\left(r_2^{\,2} - r_1^{\,2}\right)$$

Where r_2 is the distance from the centre of rotation to the outer endface of the plug, and r_1 is the distance from the centre to the inlet endface og the plug.The results are presented in Table 9.12 and Figure 9.4.3.1.

Table 9.12: Capillary pressure measurements, PO30; the conventional method.

Core:	PO30							
Porosity [%]	44,5							
Permeability [mD]	4,5							
PV [ml]	29,9							
			Mean Saturation				Hassler-Brunner Saturation	
RPM	Ow	±	Sw	±	Pc [bar]	±	Sw	
560	0,0	0,5	1,00	0,03	0,10	0,00	1,00	
800	0,0	0,5	1,00	0,03	0,20	0,01	1,00	
980	0,5	0,5	0,98	0,03	0,30	0,01	0,96	
1360	1,0	0,5	0,97	0,03	0,57	0,02	0,91	
1620	2,0	0,5	0,93	0,03	0,81	0,02	0,83	
1940	4,5	0,5	0,85	0,03	1,16	0,03	0,45	
2260	9,0	0,5	0,70	0,03	1,58	0,04	0,17	
2600	14,0	0,5	0,53	0,03	2,09	0,05	0,16	
3000	18,0	0,5	0,40	0,03	2,78	0,07	0,07	
3250	19,5	0,5	0,35	0,03	3,26	0,09	0,05	
3500	?	?	?	?	3,79	0,10	?	

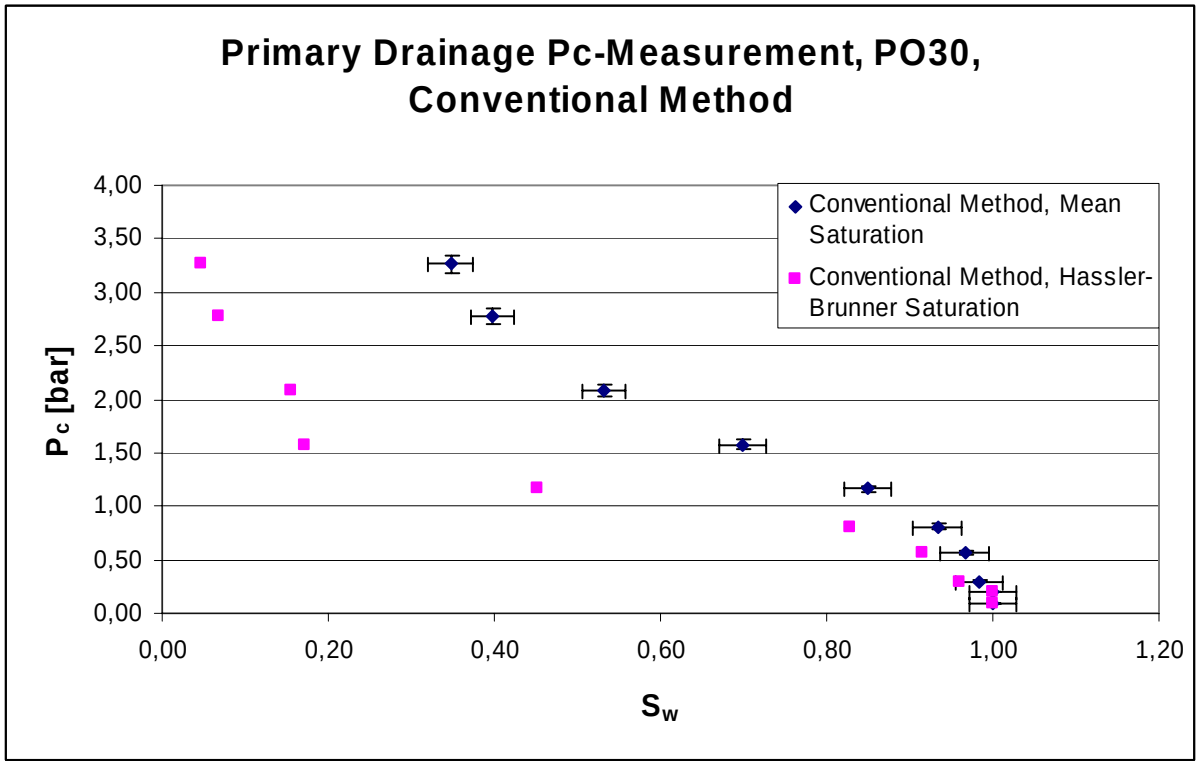

Figure 9.4.3.1: The primary drainage Pc-curve, PO30, obtained by use of the conventional method.

As expected, it is seen that by calculating the Hassler-Brunner saturations, and plotting the obtained values to the calculated capillary pressure, the P_c-curve is shifted to the left. Previous studies on capillary pressure curves reported similar tendencies [26]. However, the obtained values of $S_{w,HB}(P_{ci})$ might be a bit too low. The quality of the data could have been improved by increasing the number of data points. In that way, the $\frac{d\bar{S}_w(P_{ci})}{dP_{ci}}$ would have been more accurate, hence the quality of $S_{w,HB}(P_{ci})$ would have been improved.

In Figure 9.4.3.1, the threshold pressure of this sample is approximately at 0.5 bar, which is a bit lower than what might be expected. However, the curvature of this curve is consistent with the theory. It is seen that by further increasing the capillary pressure (that is; increasing the speed of rotation) S_w would most likely continue decreasing. Hence the final S_{wi} is probably not obtained. But, unfortunately, these measurements performed on plug PO30 could not be compared to the NTI method, because of the previously mentioned incident.

Because of this incident, the initial plan needed to be reconsidered. Due to the time consuming work of preparing for another measurement (cleaning the centrifuge to minimize background radiation, performing RWAT, calibration, performing a scan of a 100% water saturated plug, etc.) the plan was modified into performing one primary drainage capillary pressure measurement. In order to avoid this happening again, the maximum speed of rotation was limited to 3000 RPM. The buckets were balanced as seen in Table 9.13 [The core of interest (PO31) was placed in bucket no. 1.]

Table 9.13: Balancing the buckets

Bucket #	Basis weight [g]	Lead [g]	Final weight [g]
1	2452,9	0,0	2452,9
2	2431,5	21,4	2452,9
3	2432,0	20,9	2452,9
4	2436,8	16,1	2452,9

As was the case in PO30, the conventional Pc-curve was measured by varying the speed of rotation. After reaching a velocity of 3000 RPM, the in-situ saturation was measured by the NTIC Method, and the resulting P_c-curves were compared. The results achieved by the conventional- and the NTIC-Method are presented in Table 9.14 and Figure 9.4.3.2, and Table 9.15 and Figure 9.4.3.3, respectively.

Table 9.14: Capillary pressure measurements, PO31; the conventional method.

Core:	PO31								
Porosity [%]	44,3								
Permeability [mD]	3,4								
PV [ml]	29,8								
			Mean Saturation					Hassler-Brunner Saturation	
RPM	Qw	±	Sw	±	Pc [bar]	±		Sw	
550	0,0	0,4	1,00	0,03	0,09	0,00		1,00	
800	0,0	0,4	1,00	0,03	0,20	0,01		1,00	
1000	0,5	0,4	0,98	0,03	0,31	0,01		0,96	
1300	1,0	0,4	0,97	0,03	0,52	0,01		0,92	
1600	2,0	0,4	0,93	0,03	0,79	0,02		0,83	
1875	3,5	0,4	0,88	0,03	1,08	0,03		0,58	
2140	8,5	0,4	0,71	0,03	1,41	0,04		0,21	
2400	13,0	0,4	0,56	0,03	1,78	0,05		0,14	
2720	18,0	0,4	0,40	0,03	2,28	0,06		0,12	
3000	19,5	0,4	0,35	0,03	2,78	0,07		0,10	

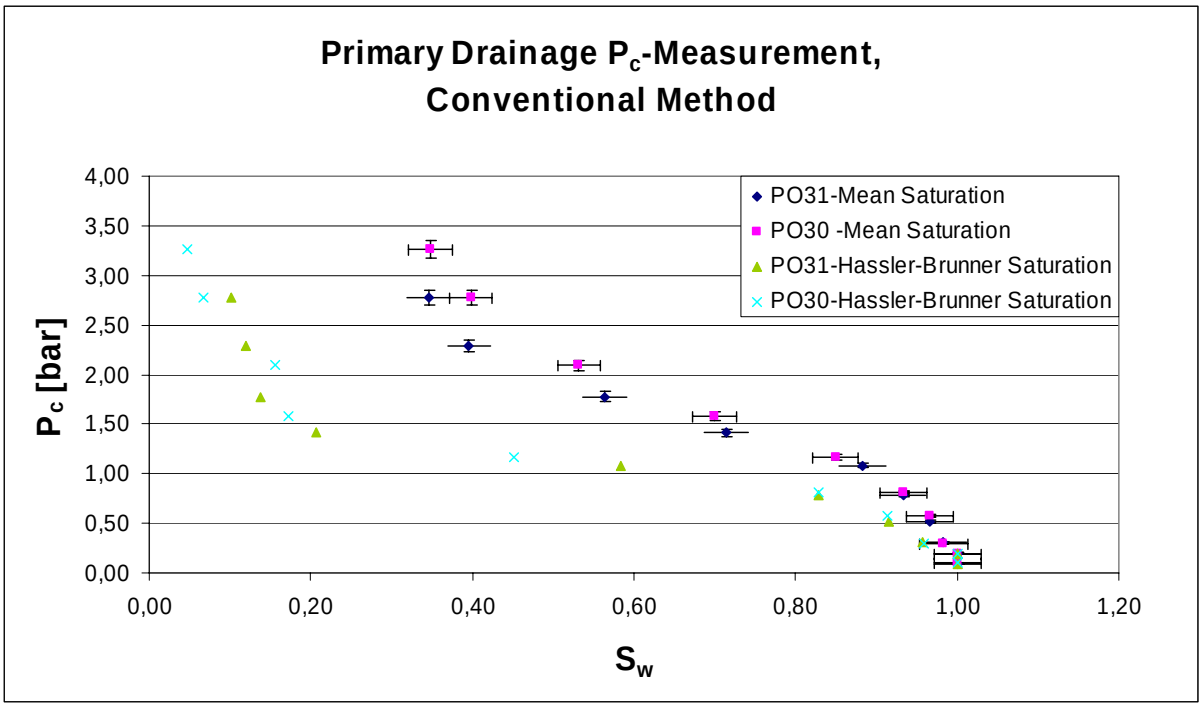

Figure 9.4.3.2: The primary drainage Pc-curves, PO31, obtained by use of the conventional method. The results obtained on PO30 are included for comparison.

In Figure 9.4.3.2, it is seen that the results obtained by the conventional centrifuge method appear to be consistent. That seems to be the case both by using the mean saturations and the Hassler-Brunner saturations. As was the case in Figure 9.4.3.1, the quality of the data could have been improved by increasing the number of data-points.

Table 9.15: Capillary Pressure measurements, the Nuclear Tracer Imaging Centrifuge Method, PO31.

Core:	PO31						
PV [ml]	29,8						
Φ [%]	44,3						
K_{abs} [mD]	3,4						
	S_w=1.00		Drainage				
Position	Counts/sec	Corrected Counts/sec	Counts/sec	Corrected Counts/sec	S_w	Sw corrected (-b.g)	Pc [bar]
80,3	0,052	0,052	0,0250	0,0237	0,477	0,463	2,66
80,9	0,053	0,053	0,0310	0,0296	0,582	0,571	2,43
81,5	0,052	0,052	0,0168	0,0155	0,322	0,305	2,19
82,1	0,055	0,055	0,0127	0,0113	0,230	0,211	1,93
82,7	0,055	0,055	0,0102	0,0089	0,185	0,165	1,67
83,3	0,057	0,057	0,0099	0,0086	0,173	0,153	1,39
83,9	0,057	0,057	0,0088	0,0075	0,156	0,136	1,10
84,5	0,054	0,054	0,0082	0,0068	0,150	0,129	0,80
85,1	0,057	0,057	0,0069	0,0056	0,121	0,100	0,49
85,7	0,048	0,048	0,0062	0,0049	0,130	0,105	0,17
				Average saturation:	0,253	0,234	
				Average saturation (mb):	(0,35 ± 0,3)	(0,35 ± 0,3)	

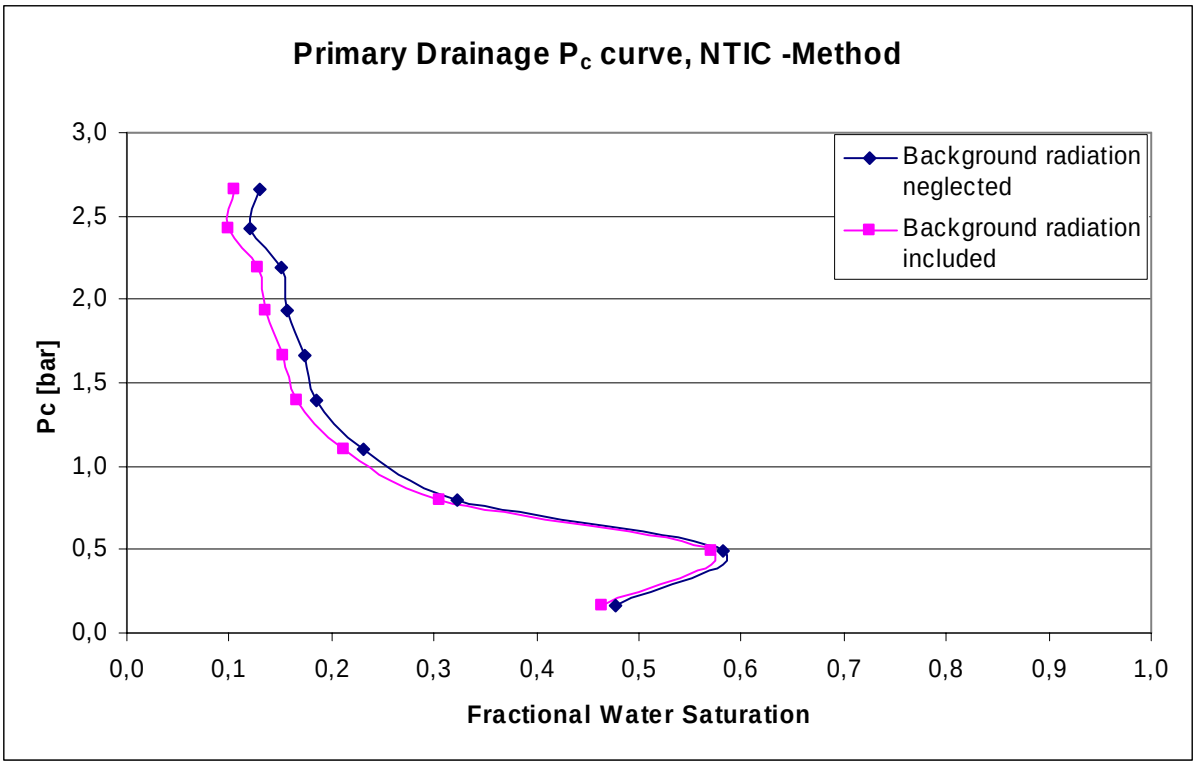

Figure 9.4.3.3: The primary drainage capillary pressure curve obtained by using the Nuclear Tracer Imaging Centrifuge Method. Comparisons are made of results obtained by including and neglecting the measured background radiation.

In Figure 9.4.3.3 it is seen that the water saturation decreases as the capillary pressure increases. This is consistent with the theory. It is further seen that by including the background radiation, a certain decrease in the measured saturation is observed. The deviation decreases as the water saturation increases. The observed deviation, however, is not of an alarming size. [In addition, it is worth noticing that the normalization of the secondary drainage curves obtained by using the DMS method (1bar → $S_w \approx 0.4$) seems to be valid.]

A significant low water saturation is observed at the measuring point being nearest to the outlet endface of the core holder. This phenomenon is most likely due to a movement of the measuring range. Before the drainage process was started, the core holder needed to be exchanged in order to fit the receiving cup properly. Since these measurements are performed on a millimetre scale, a small change in the positioning of the core plug could significantly change the results.

Table 9.15 shows that there is a discrepancy in the average water saturation observed by using the NTIC Method and the average water saturation given by the material balance. This is partly an effect of the movement of the measuring range. If the water saturation at the point being nearest to the outlet endface of the core holder is set to 1.00, the average water saturation obtained by using the NTIC method will increase to 0.305. The average water saturation obtained by using the material balance is found to be (0.35 ± 0.03). Hence the results are quite consistent.

The capillary pressure drainage curve obtained by using the NTIC Method (corrected) is then compared to the curve obtained by using the conventional centrifuge technique. The results are presented in Figure 9.4.3.4.

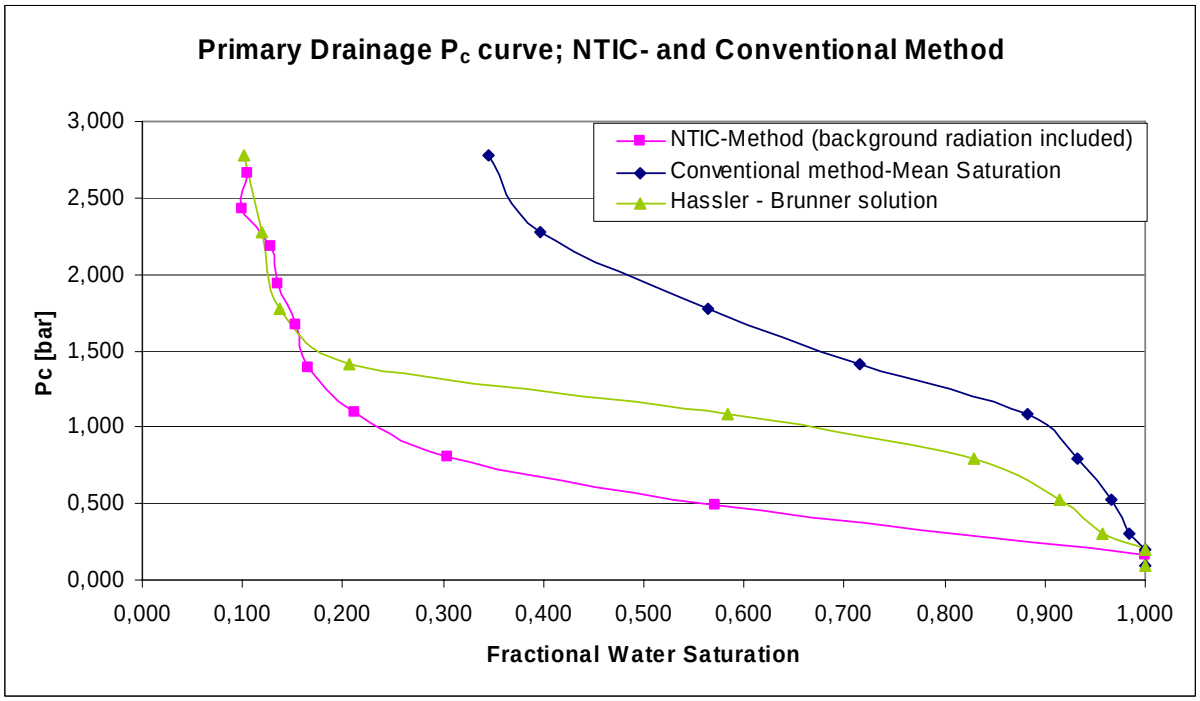

Figure 9.4.3.4: Comparison of the NTIC- and the conventional centrifuge method.

In the figure above it is seen that the results from the NTIC measurements are fairly consistent with the results obtained by using the conventional centrifuge technique (the Hassler-Brunner solution). The average saturation given by the Pc-curves are shown in Table 9.16.

Table 9.16: Average water saturation

Method	$S_{w,average}$
Conventional Method, Mean Saturation	0,35
Hassler-Brunner Solution	0,58
NTIC Method	0,30*

*** The measuring point being nearest to the outlet endface is set to 1.00**

Hence the capillary pressure curve obtained by using the NTIC method seems to be pretty close to the "true" P_c-curve.

As previously mentioned, if the number of data points had been increased (in the conventional method), the quality of the observed results (the Hassler-Brunner saturations) would most likely have been improved.

Chapter 10

Conclusions and Further Work

10.1 Conclusions

Experiments have been performed both on plugs from chalk material obtained at the Portland Quarry in Ålborg, Denmark in the late 1990's and in June 2003. It was observed that:

- The core material obtained in June 2003 was containing vugs, which seemed to cause significant lower residual oil saturation then what was previously observed.

12 of the core plugs in this study were altered to less water-wet conditions. The following conclusions were obtained:

- The wettability conditions were successfully altered by a continuous multidirectional flow of crude oil (Ekofisk) at elevated temperature through the core plugs.
- The wettability alteration by applying the multidirectional flow technique of crude oil at elevated temperature provided reproducible and stable wettability conditions.
- The wettability alteration was seen to be dependent on the initial water saturation, not only the time of aging.
- The spontaneous imbibition characteristics obtained by use of octadecane were found to differ from those obtained by use of the less viscous decane. However, the tendencies were the same when moving towards less water-wet conditions.

Capillary pressure measurements have been performed by using the Direct Measurement of Saturation (DMS) Method. The obtained results were concluded with:

- Capillary pressure curves obtained by the DMS method demonstrated consistent trends when moving towards less water-wet conditions and reproducible results were obtained for the capillary pressure data.
- Shift in end point saturations for spontaneous imbibition demonstrated consistent results at the different wettability conditions investigated.
- Spontaneous imbibition capillary pressure curves for decreasing water-wet conditions exhibited a less sharp curvature near S_{wi}.
- In order to obtain good quality data, a complete calibration curve (saturation versus intensity) was needed.
- The Amott indices calculated by using the imbibition curve were found to differ from the values obtained by the imbibition tests.

The following conclusions were drawn after performing capillary pressure measurements by using the Nuclear Tracer Imaging Centrifuge (NTIC) Method:

- The NTIC Method were improved and put into operation.
- Geometrical calculations were performed and the collimator was modified to successfully decrease the background radiation.
- The background radiation was minimized by gating the detector; hence the measurements were improved.
- The maximum speed of rotation in the Beckman J-6B centrifuge was limited to 3000 RPM.
- The obtained fluid distribution when the centrifuge was spinning at 2000 RPM (with a sealed outlet endface) was consistent with what is obtained at 0 RPM.
- Theoretical calculations were performed in order to estimate the number of counts per second to be expected when the centrifuge was spinning compared to the measurements at 0 RPM. A discrepancy of approximately 15% was found in the theoretically obtained calculations compared to the experimentally obtained measurements.
- The primary drainage capillary pressure curve obtained by using the NTIC Method demonstrated consistent trends when compared to the conventional centrifuge method.

10.2 Further Work

The improvements of the Nuclear Tracer Imaging Centrifuge Method and comparisons of methods measuring the capillary pressure curves are not completed with this thesis. A great deal of work needs to be added in order to obtain correct capillary pressure curves, and thereby enhance the understanding of the oil recovery processes. However, a master thesis must end some time, within the limited time available.

In order to make a proper comparison of the different methods for measuring capillary pressure, the methods ought to be performed on the very same core plugs. Hence the experimental procedure should be well planned.

To generate a calibration curve (response ↔ saturation), which is needed for the Direct Measurements of Saturation method, MRI measurements should be performed at all four states: a dry core plug (to obtain background measurements), at S_{wi}, at S_{or} and a 100% water (brine) saturated core plug. Hence, it might be wise to start out with the DMS method. In addition, one should make an extra effort trying to equalize the initial water saturations and the Amott indices when comparisons are made. This will simplify the part of comparison.

With respect to the Nuclear Tracer Imaging Centrifuge Method, further modifications may be performed to improve the measurements. The drainage capillary pressure curve and the negative part of the capillary pressure imbibition curve are obtainable with the present system. In order to obtain the spontaneous imbibition capillary pressure curve, additional planning is required.

Nomenclature

A:	cross sectional area
c:	concentration
C:	Celsius
cm:	centimetre
d:	diameter
D:	diffusion coefficient
DMS:	direct measurement of saturation
F:	formation factor
FWL:	free-water-level
K:	absolute permeability
k_{eff}:	effective permeability
k_{rw}:	relative permeability, water
k_{ro}:	relative permeability, oil
I_o:	Amott displacement-by-oil ratio
I_w:	Amott displacement-by-water ratio
I:	Amott-Harvey relative displacement index
J:	flux
$J(P_c)$:	Leveretts J-function
L:	length of core plug
mD:	millidarcy
m_{dry}:	mass of dry core
MHz:	megahertz
Ml:	millilitre
mm:	millimetre
MRI:	magnetic resonance imaging
$m_{tot.sat}$:	mass of totally saturated core
NMR:	nuclear magnetic resonance
NTI:	nuclear tracer imaging
NTIC:	nuclear tracer imaging centrifuge (-method)
ΔP:	pressure difference
P_c:	capillary pressure
P_{ci}:	capillary pressure at the inlet endface
P_{nw}:	pressure in the non-wetting phase
P_w:	pressure in the wetting phase
PV:	pore volume
R:	radius of core plug
RF:	recovery factor
ROI:	region of interest
RPM:	rotations per minute
RWAT:	inactive water is replaced by radioactive water
Q:	rate of flow
S_{nwr}:	residual non-wetting phase saturation
S_o:	oil saturation
S_{or}:	residual oil saturation
S_w:	water saturation
S_{wi}:	initial water saturation
$S_{w,or}$:	end point water saturation

ΔS_w: change in water saturation
S_T: reference liquid saturation
v: velocity
V_b: bulk volume
V_{osp}: volume of oil spontaneously displaced by water
V_{ot}: total volume of oil displaced by water
V_p: pore volume
V_{wsp}: volume of water spontaneously displaced by oil
V_{wt}: total volume of water displaced by oil
W: USBM wettability index
%: percent
°: degrees

Greek letters:
γ: gamma radiation
δ_w: displacement-by-water ratio
δ_o: displacement-by-oil ratio
θ_a: apparent contact angle
θ_a: contact angle
θ_{rec}: receding contact angle
θ_T: contact angle on a flat surface
μ: viscosity
ρ: density
$\Delta\rho$: density difference
ρ_{nw}: density in the non-wetting fluid
ρ_w: density in the wetting fluid
σ: surface tension
φ: porosity
φ_{eff}: effective porosity
ω: angular velocity

References:

1. *Hassler, G.L. and Brunner, E., "Measurements of Capillary Pressure in Small Core Samples", Trans AIME, 160, (114-123), 1945.*

2. *Forbes, P.L, "Centrifuge Data Analysis Techniques: An SCA Survey on the Drainage Capillary Pressure Curves from Centrifuge Measurements", SCA-9714, in 1997 International Symposium Proceedings: Society of Professional Well Log Analysts, Society of Core Analysts, Chapter-at-Large, 19 p.*

3. *Baldwin, B.A. and Spinler, E.A., "A direct method for simultaneously determining Positive and Negative Capillary Pressure Curves in Reservoir Rock", Journal of Petroleum Science and Engineering (1998) 20, 161-165.*

4. *Selley, Richard C., "Elements of Petroleum Geology", 2nd edition, 1998.*

5. *Schlumberger oilfield glossary, http://www.glossary.oilfield.slb.com/*

6. *Marle, C.M., "Multiphase Flow in Porous Media", Editions Technips, Paris, 1981.*

7. *Graue A, "Fys 224, Experimental Reservoir Physics", Dept. of Physics, University of Bergen, 1992.*

8. *Craig, F.F., "The Reservoir Engineering Aspects of Waterflooding", Monograph Series, SPE, Richardson TX (1971), 3.*

9. *Salathiel, R.A., "Oil Recovery by Surface Film Drainage in Mixed Wettability Rocks", JPT (Oct. 1973), 1216-24.*

10. *Anderson, W.G., "Wettability Literature Survey – Part 1: Rock/Oil/Brine Interactions and the Effects of Core Handling on Wettability", JPT (Oct. 1986) 1125-1149.*

11. *Anderson, W.G., "Wettability Literature Survey – Part 2: Wettability Measurement", JPT (Nov. 1986) 1246-1262.*

12. *Anderson, W.G., "Wettability Literature Survey – Part 3: The Effects of Wettability on the Electrical Properties of Porous Medium", JPT (Dec. 1986) 1371-1378).*

13. *Anderson, W.G., "Wettability Literature Survey – Part 4: Effects of Wettability on Capillary Pressure", JPT (Oct. 1987) 1283-1300.*

14. *Anderson, W.G., "Wettability Literature Survey – Part 5: The Effects of Wettability on Relative Permeability", JPT (Nov. 1987) 1453-1468.*

15. *Anderson, W.G., "Wettability Literature Survey – Part 6: The Effects of Wettability on Waterflooding", JPT (Dec. 1987) 1605-1622.*

16. *Graue, A., Bognø, T., Moe, R.W., Baldwin, B.A., Spinler, E.A., Maloney, D., Tobola, D.P., "Impacts of Wettability on Capillary Pressure and Relative Permeability", SCA-9907, Phillips Petroleum Company Norway, 1999.*

17. *Amott, E., "Observations Relating to the Wettability of Porous Rocks", Petroleum Transactions of AIME 216, 1959, p. 156-162.*

18. *Donaldson, E.C., Thomas, R.D. and Lorenz, P.B., "Wettability Determination and Its Effect on Recovery Efficiency", SPEJ, 1969, p. 13-20 (March).*

19. *Sharma, M.M and, Wunderlich, R.W., ""The Alteration of Rock Properties Due to Interactions with Drilling Fluid Components", SPE 14302, SPE Annual Technical Conference and Exhibition, Las Vegas, 1985, p. 22-25.*

20. *3.1.1 Diffusion and Point Defects, http://www.techfak.uni-kiel.de/matwis/amat/def_en/kap_3/backbone/r3_1_1.html*

21. *Skjæveland, S.M., Kleppe, J.,"SPOR Monograph, Recent Advances in Improved Oil Recovery Methods for North Sea Sandstone Reservoirs", Norwegian Petroleum Directorate, Stavanger 1992.*

22. *Holmes, S., "Capillary Pressure & Relative Permeability Petrophysical Reservoir Models", Digital Formation INC., USA, May 2002.*

23. *Leverett, M.C., "Capillary Behaviour in Porous Solids", Trans AIME (1941), 142, 159-69.*

24. *Bognø, T., Aspenes, E., Graue, A., Spinler, E.A. and Tobola, D., "Comparison of Capillary Pressure Measurements at Various Wettabilities using the Direct Measurement of Saturation Method and Conventional Centrifuge Techniques", 2001 International Symposium of Core Analysts, Edinburgh, Scotland, Sept. 17-19, 2001.*

25. *Spinler, E.A. and Graue, A., "Capillary Pressure Scanning Curves by Direct Measurement of Saturation", SCA-9705, 1997.*

26. *Forbes, P.L., Chen, Z.A. and Ruth, D.W., "Quantitative Analysis of Radial Effects on Centrifuge Capillary Pressure Curves", SPE 28182, presented at the 69th SPE annual conference in New Orleans, LA, 25-28 September 1994.*

27. *Chen, Z.A. and Ruth, D.W., "The Effect of Gravity Degradation on Low-Speed Centrifuge Capillary Pressure Data", AIChE J., 41, No. 3, 469, 1995.*

28. *Christiansen, R.L., "Geometric Concerns for Accurate Measurements of Capillary Pressure Relationships with Centrifuge Methods", SPE Formation Evaluation, 7, p.311-314, 1992.*

29. *Ruth, D. and Chen, Z., "Measurement and Interpretation of Centrifuge Capillary Pressure Curves – The SCA Survey", The Log Analyst, Sept.-Oct., 1995, 21-33.*

30. *Fishbane, P.M., Gasiorowicz, S. and Thornton, S.T., "Physics for Scientists and Engineers", 2nd ed., 1996.*

31. *Chardaire-Riviere, C., Forbes, P., Zhang, J.F. and Chavent, G., "Improving the Centrifuge Technique by Measuring Local Saturation", SPE 24882, 1992.*

32. *Spinler, E.A., Baldwin, B.A. and Graue, A., "Simultaneous Measurement of Multiple Capillary Pressure Curves from Wettability and Rock Property Variations within Single Rock Plugs", SCA 9957, Reviewed Proc.: 1999 International Symposium of Core Analysts Golden, Co, USA, Aug., 1-4.*

33. *Fassi-Fihri, O., Robin, M. and Rosenberg, E., "Wettability Studies at the Pore Level: A New Approach by the Use of Cryo-Scanning Electron Microscopy", SPE 22596, 66th Annual Tech. Conf. and Exhib. Of SPE, 1991*

34. *Graue, A., Aspenes, E., Bognø, T., Moe, R.W. and Ramsdal, J., "Alteration of Wettability and Wettability Heterogeneity", Reviewed Proc.: 6th International Symposium on Evaluation of Reservoir Wettability and Its Effect on Oil Recovery, Socorro, NM, USA. Journal of Petroleum Science and Engineering, Volume 33, April 2002, 3-17*

35. *Graue, A., Bognø, T., Spinler, E.A. and Baldwin, B.A., "A Method for Measuring In-Situ Capillary Pressures at Different Wettabilities Using Live Crude Oil at Reservoir Conditions, Part 1: Feasibility Study", SCA2002-18, Monteray, 2002.*

36. *Lien, J.R., "En kort innføring i NMR-logging", Universitetet i Bergen, 2002.*

37. *Coates, G.R., Xiao, L., and Prammer, M.G., "NMR logging, Principles & Applications", Halliburton Company, 1998.*

38. *Lie, Marianne, "Evaluering av dagbruddsbergarter som analoger til kalksteinreservoarer I Nordsjøen", 1995.*

39. *Ekdale, A.A. and, Bromley, R.G., "Trace Fossils and Ichnofabric in the Kjølby Gaard Marl, Uppermost Cretaceous, Denmark", Bull Geol. Soc. Denmark, Vol. 31., Copenhagen, Mar. 7, 1993, 107-119.*

40. *Graue, A., Viksund, B.G., and Baldwin, B., "Reproducible Wettability Alteration of Low-Permeable Outcrop Chalk", SPE 39662, Proc. 1998 SPE/DOE International Symposium, Tulsa, OK, USA (April 1998).*

41. *Graue, A., Tonheim, E. and Baldwin, B., "Control and Alteration of Wettability in Low-Permeable Chalk", Rev. Proc., 3rd International Symposium on Evaluation of Reservoir Wettability and Its Effect on Oil Recovery, Laramie, Wyoming, USA, Sept. 1994.*

42. *Cuiec, L., "Wettability and Oil Reservoirs", Institut Francais Du Petrole, 1987*

43. *Aspenes, E., Graue, A. and Ramsdal, J., "In-Situ Wettability Distribution and Wetting Stability in Outcrop Chalk Aged in Crude Oil", Journal of Petroleum Science and Engineering 39, 2003, p. 337-350.*

44. *Sawaruddin, M., Torsæter, O. and Skauge, A., "Comparing Different Methods for Capillary Pressure Measurements", paper 2051, 2000 International Symposium Proceedings, Society of Core Analyst, 2000.*

45. *ImageJ – an image analyzing program.*

46. *Johannesen, E., B., "Oljeutvinning i kalkstein og NMR-karakterisering av fuktforhold etablert ved bruk av ulike råoljer", June 2004.*

47. *Spinler, E. A., Baldwin, B. A and Graue, A., "Experimental Artifacts Caused by Wettability Variations in Chalk., JPSE 33 (1-3), 49-59, 2002*

48. *Howard, J.J. and Spinler, E.A., "Nuclear Magnetic Resonance Measurements of Wettability and Fluid Saturations in Chalk", SPE 26471, 1993 Annual Technical Conference and Exhibition Proceedings, (Formation Evaluation and Reservoir Geology), p. 565-573. Later published in 1995 in SPE Advanced Technology Series, v. 3, no.1, p. 60-65.*

49. *Cuiec, L.E., Bourbiaux, B. and Kalaydjian, F., "Imbibition in Low-Permeability Porous Media: Understanding and Improvement of Oil Recovery", presented at the SPE/DOE Seventh Symposium on Enhanced Oil Recovery, Tulsa, Oklahoma, USA, April, 1990.*

50. *Bourbiaux, B. and Kalaydjian, F., "Experimental Study of Co-Current and Counter-Current Flows in Natural Porous Media", SPERE (August, 1990), pp. 361-368*

51. *Terez, I.E. and Firoozabadi, A., "Water Injection in Water-Wet Fractured Porous Media: Experiments and a New Model Using Modified Buckley-Leverett Theory", SPE/DOE Improved Oil Recovery Symposium Proceedings, SPE 39605, 1996.*

52. *Spinler, E.A. and Maloney, D.R., "Application of Linear X-Ray Analysis Using Adsorption Coefficients For Direct Determination of In-Situ Core Saturation for Pc-Measurements", presented at 2001 SCA Symposium, Sept 17-19, Edinburgh, Scotland, 2001.*

53. *Lien, J., Graue, A., Kolltveit, K., "A Nuclear Imaging Technique for Studying Multiphase Flow in a Porous Medium at Oil Reservoir Conditions", Nuclear Instruments and Methods in Physical Research, A271 (1988), 693-700.*

54. *Graue, A., "Nuclear Tracer Saturation Imaging of Fluid Displacement in Low-Permeable Chalk", SPE 25899, Denver, 1993.*

Appendices

Appendix A

The spreadsheet used to calculate the free water level.

Kashagan Pc: Volume water to add for Imbibition runs (The method of Rich Treinen)

Dimensions:		
Cup Inner Diameter:	7,640	A
Plug Holder OD:	7,635	B
Plug Holder Bore:	3,964	C
Frit Thickness:	0,434	t_f
Frit Diameter:	5,161	d_f
Frit Porosity:	0,250	ϕ_f
Base Height:	1,503	b
Post X:	1,917	x_p
Post Y:	2,367	y_p

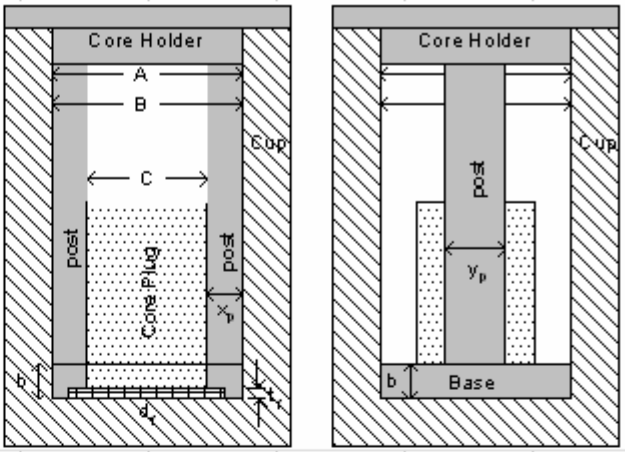

User Input				
	KE-2	KW-1	KW-1	KW-1
Plug ID	po6	po7	po9	po10
Plug Length (cm)	6	6	5,992	6
Plug Diameter (cm)	3,78	3,786	3,78	3,78
Water Addition (cc) to:				
1/4 Height =	14,567	14,513	14,516	14,567
1/3 Height =	27,340	27,269	27,272	27,340
2/5 Height =	37,558	37,473	37,477	37,558
1/2 Height =	52,886	52,779	52,784	52,886
Volumes:				
Inner Cup at 1/4 H:	88,661	88,661	88,569	88,661
Inner Cup at 1/3 H:	111,583	111,583	111,461	111,583
Inner Cup at 2/5 H:	129,920	129,920	129,773	129,920
Inner Cup at 1/2 H:	157,426	157,426	157,243	157,426
Frit:	6,809	6,809	6,809	6,809
Holder Base Volume:	46,541	46,541	46,541	46,541
Posts at 1/4 H:	3,911	3,911	3,893	3,911
Posts at 1/3 H:	8,449	8,449	8,425	8,449
Posts at 2/5 H:	12,079	12,079	12,050	12,079
Posts at 1/2 H:	17,524	17,524	17,488	17,524
Plug Volume at 1/4 H:	16,833	16,887	16,811	16,833
Plug Volume at 1/3 H:	22,444	22,515	22,414	22,444
Plug Volume at 2/5 H:	26,933	27,019	26,897	26,933
Plug Volume at 1/2 H:	33,666	33,773	33,621	33,666

Appendix B

Complementary Data from Imbibition Tests

Core	PO6				
V_p [ml]	30,2				
Swi	0,335				
OOIP [ml]	20,1				
$M_{bef.\ sp.imb}$ [g]	121,440				
$M_{aft.\ sp.imb}$ [g]	123,093				
$V_{o,spon.imb.}$ [ml]	4,3				
$S_{w,after\ sp.imb}$	0,477				
$M_{aft.\ for.imb}$ [g]	124,966				
$V_{o,forced\ disp}$ [ml]	9,6				
$S_{w,after\ for.imb}$	0,796				
Amott	0,309				
Time [min]	Time [sec]	Vo prod [ml]	Sw	ΔSw	RF [%]
0	1	0,00	0,335	0,000	0,0
15	900	0,30	0,345	0,010	1,5
18	1080	0,50	0,352	0,017	2,5
22	1320	0,70	0,358	0,023	3,5
25	1500	0,90	0,365	0,030	4,5
30	1800	1,00	0,368	0,033	5,0
35	2100	1,10	0,371	0,036	5,5
45	2700	1,20	0,375	0,040	6,0
50	3000	1,30	0,378	0,043	6,5
60	3600	1,40	0,381	0,046	7,0
65	3900	1,50	0,385	0,050	7,5
80	4800	1,60	0,388	0,053	8,0
90	5400	1,70	0,391	0,056	8,5
100	6000	1,75	0,393	0,058	8,7
120	7200	1,80	0,395	0,060	9,0
145	8700	1,90	0,398	0,063	9,5
170	10200	2,00	0,401	0,066	10,0
260	15600	2,40	0,415	0,080	12,0
320	19200	2,60	0,421	0,086	13,0
380	22800	2,70	0,424	0,089	13,5
1860	111600	3,30	0,444	0,109	16,4
2040	122400	3,40	0,448	0,113	16,9
2760	165600	3,55	0,453	0,118	17,7
4920	295200	3,80	0,461	0,126	18,9
8640	518400	4,00	0,468	0,133	19,9
10080	604800	4,10	0,471	0,136	20,4
14400	864000	4,20	0,474	0,139	20,9
17280	1036800	4,30	0,477	0,142	21,4
24480	1468800	4,30	0,477	0,142	21,4
28800	1728000	4,30	0,477	0,142	21,4
31680	1900800	4,30	0,477	0,142	21,4
33120	1987200	4,30	0,477	0,142	21,4
36000	2160000	4,30	0,477	0,142	21,4
37440	2246400	4,30	0,477	0,142	21,4

Core	PO7				
V_p [ml]	30,7				
Swi	0,294				
OOIP [ml]	21,6				
$M_{bef.\ sp.imb}$ [g]	121,953				
$M_{aft.\ sp.imb}$ [g]	123,481				
$V_{o,spon.imb.}$ [ml]	3,1				
$S_{w,after\ sp.imb}$	0,395				
$M_{aft.\ for.imb}$ [g]	125,381				
$V_{o,forced\ disp}$ [ml]	11,9				
$S_{w,after\ for.imb}$	0,783				
Amott	0,207				
Time [min]	Time [sec]	Vo prod [ml]	Sw	ΔSw	RF [%]
0	1	0,00	0,294	0,000	0,0
15	700	0,60	0,314	0,020	2,8
20	1200	1,00	0,327	0,033	4,6
22	1320	1,10	0,330	0,036	5,1
24	1440	1,20	0,333	0,039	5,5
30	1800	1,30	0,336	0,042	6,0
40	2400	1,40	0,340	0,046	6,5
50	3000	1,50	0,343	0,049	6,9
65	3900	1,60	0,346	0,052	7,4
90	5400	1,65	0,348	0,054	7,6
195	7000	1,70	0,349	0,055	7,9
200	12000	1,80	0,353	0,059	8,3
290	17400	2,00	0,359	0,065	9,2
350	21000	2,10	0,363	0,069	9,7
1000	60000	2,30	0,369	0,075	10,6
1360	81600	2,50	0,376	0,082	11,6
1800	108000	2,70	0,382	0,088	12,5
2760	165600	2,80	0,385	0,091	12,9
4920	295200	3,00	0,392	0,098	13,9
8640	518400	3,10	0,395	0,101	14,3
10080	604800	3,10	0,395	0,101	14,3
14400	864000	3,10	0,395	0,101	14,3
17280	1036800	3,10	0,395	0,101	14,3
24480	1468800	3,10	0,395	0,101	14,3
28800	1728000	3,10	0,395	0,101	14,3
31680	1900800	3,10	0,395	0,101	14,3
33120	1987200	3,10	0,395	0,101	14,3
36000	2160000	3,10	0,395	0,101	14,3
37440	2246400	3,10	0,395	0,101	14,3

Core	P09				
V_p [ml]	30,3				
Swi	0,336				
OOIP [ml]	20,1				
$M_{bef.\ sp.imb}$ [g]	121,150				
$M_{aft.\ sp.imb}$ [g]	122,510				
$V_{o,spon.imb.}$ [ml]	4,0				
$S_{w,after\ sp.imb}$	0,468				
$M_{aft.\ for.imb}$ [g]	124,789				
$V_{o,forced\ disp}$ [ml]	10,0				
$S_{w,after\ for.imb}$	0,798				
Amott	0,286				
Time [min]	Time [sec]	Vo prod [ml]	Sw	ΔSw	RF [%]
0	1	0,00	0,336	0,000	0,0
15	900	0,50	0,353	0,017	2,5
20	1200	0,90	0,366	0,030	4,5
22	1320	1,00	0,369	0,033	5,0
25	1500	1,20	0,376	0,040	6,0
30	1800	1,30	0,379	0,043	6,5
40	2400	1,40	0,382	0,046	7,0
50	3000	1,50	0,386	0,050	7,5
65	3900	1,60	0,389	0,053	8,0
75	4500	1,65	0,391	0,055	8,2
90	5400	1,70	0,392	0,056	8,5
150	9000	1,85	0,397	0,061	9,2
240	14400	2,20	0,409	0,073	10,9
300	18000	2,30	0,412	0,076	11,4
420	25200	2,35	0,414	0,078	11,7
900	54000	2,60	0,422	0,086	12,9
1440	86400	2,80	0,428	0,092	13,9
1620	97200	3,00	0,435	0,099	14,9
1800	108000	3,05	0,437	0,101	15,2
1980	118800	3,10	0,438	0,102	15,4
2790	167400	3,20	0,442	0,106	15,9
3540	212400	3,30	0,445	0,109	16,4
4320	259200	3,40	0,448	0,112	16,9
5760	345600	3,50	0,452	0,116	17,4
10080	604800	3,70	0,458	0,122	18,4
14400	864000	3,90	0,465	0,129	19,4
17280	1036800	4,00	0,468	0,132	19,9
24480	1468800	4,00	0,468	0,132	19,9
28800	1728000	4,00	0,468	0,132	19,9
31680	1900800	4,00	0,468	0,132	19,9
33120	1987200	4,00	0,468	0,132	19,9
36000	2160000	4,00	0,468	0,132	19,9
37440	2246400	4,00	0,468	0,132	19,9

Core	PO10				
V_p [ml]	30,3				
Swi	0,323				
OOIP [ml]	20,5				
$M_{bef.\ sp.imb}$ [g]	121,240				
$M_{aft.\ sp.imb}$ [g]	122,492				
$V_{o,spon.imb.}$ [ml]	2,8				
$S_{w,after\ sp.imb}$	0,415				
$M_{aft.\ for.imb}$ [g]	125,455				
$V_{o,forced\ disp}$ [ml]	12,8				
$S_{w,after\ for.imb}$	0,838				
Amott	0,179				
Time [min]	Time [sec]	Vo prod [ml]	Sw	ΔSw	RF [%]
0	1	0,00	0,323	0,000	0,0
10	600	0,30	0,333	0,010	1,5
15	900	0,40	0,336	0,013	2,0
20	1200	0,50	0,340	0,017	2,4
30	1800	0,60	0,343	0,020	2,9
35	2100	0,65	0,344	0,021	3,2
40	2400	0,70	0,346	0,023	3,4
45	2700	0,75	0,348	0,025	3,7
50	3000	0,80	0,349	0,026	3,9
60	3600	0,90	0,353	0,030	4,4
80	4800	1,00	0,356	0,033	4,9
90	5400	1,10	0,359	0,036	5,4
140	8400	1,20	0,363	0,040	5,9
180	10800	1,30	0,366	0,043	6,3
270	16200	1,60	0,376	0,053	7,8
360	21600	1,70	0,379	0,056	8,3
420	25200	1,80	0,382	0,059	8,8
540	32400	2,00	0,389	0,066	9,8
1320	79200	2,30	0,399	0,076	11,2
1500	90000	2,50	0,406	0,083	12,2
1680	100800	2,60	0,409	0,086	12,7
1860	111600	2,70	0,412	0,089	13,2
2760	165600	2,80	0,415	0,092	13,7
3180	190800	2,80	0,415	0,092	13,7
3510	210600	2,80	0,415	0,092	13,7
4320	259200	2,80	0,415	0,092	13,7
4920	295200	2,80	0,415	0,092	13,7
5760	345600	2,80	0,415	0,092	13,7
8640	518400	2,80	0,415	0,092	13,7
10080	604800	2,80	0,415	0,092	13,7
14400	864000	2,80	0,415	0,092	13,7
17280	1036800	2,80	0,415	0,092	13,7
24480	1468800	2,80	0,415	0,092	13,7
28800	1728000	2,80	0,415	0,092	13,7
31680	1900800	2,80	0,415	0,092	13,7
33120	1987200	2,80	0,415	0,092	13,7
36000	2160000	2,80	0,415	0,092	13,7
37440	2246400	2,80	0,415	0,092	13,7

Core	PO11				
V_p [ml]	30,5				
Swi	0,251				
OOIP [ml]	22,8				
$M_{bef\ sp.Imb}$ [g]	122,600				
$M_{aft\ sp.Imb}$ [g]	125,570				
$V_{o,spon.Imb.}$ [ml]	8,9				
$S_{w,after\ sp.Imb}$	0,543				
$M_{aft\ for.Imb}$ [g]	125,924				
$V_{o,forced\ disp}$ [ml]	1,0				
$S_{w,after\ for.Imb}$	0,576				
Amott	0,899				
Time [min]	Time [sec]	Vo prod [ml]	Sw	ΔSw	RF [%]
0,0	1	0,00	0,251	0,000	0,0
4,5	270	3,70	0,372	0,121	16,2
5,0	300	3,90	0,379	0,128	17,1
5,5	330	4,20	0,389	0,138	18,4
6,0	360	4,40	0,395	0,144	19,3
6,5	390	4,60	0,402	0,151	20,2
7,0	420	4,80	0,409	0,158	21,0
7,5	450	5,00	0,415	0,164	21,9
8,0	480	5,10	0,418	0,167	22,4
8,5	510	5,30	0,425	0,174	23,2
9,0	540	5,50	0,432	0,181	24,1
9,5	570	5,70	0,438	0,187	25,0
10,0	600	5,75	0,440	0,189	25,2
10,5	630	5,85	0,443	0,192	25,6
12,0	720	5,90	0,445	0,194	25,9
12,5	750	6,00	0,448	0,197	26,3
13,0	780	6,10	0,451	0,200	26,7
13,5	810	6,20	0,455	0,204	27,2
14,0	840	6,25	0,456	0,205	27,4
14,5	870	6,30	0,458	0,207	27,6
17,0	1020	6,60	0,468	0,217	28,9
18,0	1080	6,65	0,469	0,218	29,1
20,0	1200	6,70	0,471	0,220	29,4
22,0	1320	6,90	0,478	0,227	30,2
24,0	1440	7,00	0,481	0,230	30,7
25,0	1500	7,10	0,484	0,233	31,1
26,0	1560	7,15	0,486	0,235	31,3
28,0	1680	7,20	0,487	0,236	31,6
30,0	1800	7,30	0,491	0,240	32,0
35,0	2100	7,40	0,494	0,243	32,4
45,0	2700	7,70	0,504	0,253	33,7
50,0	3000	7,80	0,507	0,256	34,2
60,0	3600	8,00	0,514	0,263	35,1
70,0	4200	8,10	0,517	0,266	35,5
80,0	4800	8,20	0,520	0,269	35,9
85,0	5100	8,30	0,523	0,272	36,4
140,0	8400	8,40	0,527	0,276	36,8
160,0	9600	8,50	0,530	0,279	37,3
240,0	14400	8,60	0,533	0,282	37,7
1080,0	64800	8,70	0,537	0,286	38,1
1680,0	100800	8,80	0,540	0,289	38,6
5760,0	345600	8,90	0,543	0,292	39,0
7200,0	432000	8,90	0,543	0,292	39,0
11520,0	691200	8,90	0,543	0,292	39,0
14400,0	864000	8,90	0,543	0,292	39,0
21600,0	1296000	8,90	0,543	0,292	39,0
25920,0	1555200	8,90	0,543	0,292	39,0
28800,0	1728000	8,90	0,543	0,292	39,0
30240,0	1814400	8,90	0,543	0,292	39,0
33120,0	1987200	8,90	0,543	0,292	39,0
34560,0	2073600	8,90	0,543	0,292	39,0

Core	PO13				
V_p [ml]	30,4				
Swi	0,249				
OOIP [ml]	22,8				
$M_{bef.\ sp.imb}$ [g]	121,550				
$M_{aft.\ sp.imb}$ [g]	124,586				
$V_{o,spon.imb.}$ [ml]	9,2				
$S_{w,after\ sp.imb}$	0,552				
$M_{aft.\ for.imb}$ [g]	124,586				
$V_{o,forced\ disp}$ [ml]	1,0				
$S_{w,after\ for.imb}$	0,585				
Amott	0,902				
Time [min]	Time [sec]	Vo prod [ml]	Sw	ΔSw	RF [%]
0,0	1	0,00	0,249	0,000	0,0
5,0	300	2,90	0,344	0,095	12,7
5,5	330	3,10	0,351	0,102	13,6
6,0	360	3,30	0,358	0,109	14,5
6,5	390	3,70	0,371	0,122	16,2
7,0	420	4,10	0,384	0,135	18,0
7,5	450	4,20	0,387	0,138	18,4
8,0	480	4,40	0,394	0,145	19,3
8,5	510	4,60	0,400	0,151	20,2
9,0	540	4,90	0,410	0,161	21,5
9,5	570	5,30	0,424	0,175	23,2
10,0	600	5,50	0,430	0,181	24,1
10,5	630	5,70	0,437	0,188	25,0
11,0	660	5,90	0,443	0,194	25,9
12,0	720	6,00	0,447	0,198	26,3
12,5	750	6,10	0,450	0,201	26,7
14,0	840	6,40	0,460	0,211	28,1
15,0	900	6,70	0,470	0,221	29,4
15,5	930	6,95	0,478	0,229	30,5
17,0	1020	7,00	0,479	0,230	30,7
19,0	1140	7,10	0,483	0,234	31,1
20,0	1200	7,20	0,486	0,237	31,6
22,0	1320	7,30	0,489	0,240	32,0
24,0	1440	7,40	0,493	0,244	32,4
26,0	1560	7,50	0,496	0,247	32,9
28,0	1680	7,60	0,499	0,250	33,3
32,0	1920	7,70	0,503	0,254	33,8
36,0	2160	7,75	0,504	0,255	34,0
38,0	2280	7,80	0,506	0,257	34,2
40,0	2400	7,90	0,509	0,260	34,6
42,0	2520	8,00	0,512	0,263	35,1
46,0	2760	8,10	0,516	0,267	35,5
52,0	3120	8,20	0,519	0,270	36,0
54,0	3240	8,30	0,522	0,273	36,4
56,0	3360	8,40	0,526	0,277	36,8
135,0	8100	8,70	0,535	0,286	38,1
210,0	12600	8,80	0,539	0,290	38,6
1080,0	64800	9,05	0,547	0,298	39,7
5760,0	345600	9,10	0,549	0,300	39,9
7200,0	432000	9,20	0,552	0,303	40,3
11520,0	691200	9,20	0,552	0,303	40,3
14400,0	864000	9,20	0,552	0,303	40,3
21600,0	1296000	9,20	0,552	0,303	40,3
25920,0	1555200	9,20	0,552	0,303	40,3
28800,0	1728000	9,20	0,552	0,303	40,3
30240,0	1814400	9,20	0,552	0,303	40,3
33120,0	1987200	9,20	0,552	0,303	40,3
34560,0	2073600	9,20	0,552	0,303	40,3

Core	PO15				
M_m	94,4	g			
V_P	29,52	ml			
V_v prod. by drainage	22,8	ml			
S_{wi}	0,228				
OOIP [ml]	22,8	ml			
V_o prod. by sp.imb.	8,6	ml			
S_w after sp.imb.	0,519				
V_o prod by f.imb.	9,600	ml			
$S_{w,e.p.}$	0,844				

Time [min]	Time [sec]	Vo prod	Sw	ΔS_w	RF [%]
	1	0,00	0,228	0,000	0,0
1	60	0,40	0,241	0,014	1,8
1,5	90	0,70	0,251	0,024	3,1
2	120	0,80	0,255	0,027	3,5
3	180	1,30	0,272	0,044	5,7
7	420	1,80	0,289	0,061	7,9
8	480	1,90	0,292	0,064	8,3
10	600	2,00	0,295	0,068	8,8
12	720	2,30	0,305	0,078	10,1
18	1080	2,90	0,326	0,098	12,7
22	1320	3,20	0,336	0,108	14,0
27	1620	3,50	0,346	0,119	15,4
32	1920	3,90	0,360	0,132	17,1
40	2400	4,00	0,363	0,136	17,5
59	3540	4,10	0,366	0,139	18,0
66	3960	4,20	0,370	0,142	18,4
80	4800	4,40	0,377	0,149	19,3
89	5340	4,70	0,387	0,159	20,6
98	5880	4,80	0,390	0,163	21,1
110	6600	5,00	0,397	0,169	21,9
165	9900	5,20	0,404	0,176	22,8
215	12900	5,60	0,417	0,190	24,6
250	15000	5,95	0,429	0,202	26,1
265	15900	6,05	0,433	0,205	26,5
285	17100	6,15	0,436	0,208	27,0
325	19500	6,20	0,438	0,210	27,2
395	23700	6,25	0,439	0,212	27,4
460	27600	6,70	0,455	0,227	29,4
1560	93600	7,30	0,475	0,247	32,0
1680	100800	7,40	0,478	0,251	32,5
3135	188100	7,50	0,482	0,254	32,9
6460	387600	7,75	0,490	0,263	34,0
7305	438300	8,05	0,500	0,273	35,3
8595	515700	8,15	0,504	0,276	35,7
10095	605700	8,20	0,505	0,278	36,0
10485	629100	8,35	0,510	0,283	36,6
12045	722700	8,45	0,514	0,286	37,1
18705	1122300	8,50	0,516	0,288	37,3
37905	2274300	8,55	0,517	0,290	37,5
40545	2432700	8,60	0,519	0,291	37,7
59445	3566700	8,60	0,519	0,291	37,7

Core	PO16				
M_m	94,5	g			
V_p	29,42	ml			
V_v prod. by drainage	23,2	ml			
S_{wi}	0,211				
OOIP [ml]	23,200	ml			
V_o prod. by sp.imb.	7,3	ml			
S_w after sp.imb.	0,460				
V_o prod by f.imb.	10,7	ml			
$S_{w,e.p.}$	0,823				

Time [min]	Time [sec]	Vo prod	Sw	ΔS_w	RF [%]
0	1	0,00	0,211	0,000	0,0
1	60	0,20	0,218	0,007	0,9
2	120	0,40	0,225	0,014	1,7
3	180	0,80	0,239	0,027	3,4
4	240	1,00	0,245	0,034	4,3
5	300	1,20	0,252	0,041	5,2
7	420	1,40	0,259	0,048	6,0
9	540	1,60	0,266	0,054	6,9
10	600	1,70	0,269	0,058	7,3
11	660	1,80	0,273	0,061	7,8
13	780	1,90	0,276	0,065	8,2
15	900	2,00	0,279	0,068	8,6
19	1140	2,20	0,286	0,075	9,5
23	1380	2,30	0,290	0,078	9,9
26	1560	2,50	0,296	0,085	10,8
29	1740	2,60	0,300	0,088	11,2
33	1980	2,80	0,307	0,095	12,1
41	2460	3,00	0,313	0,102	12,9
44	2640	3,10	0,317	0,105	13,4
55	3300	3,40	0,327	0,116	14,7
64	3840	3,50	0,330	0,119	15,1
73	4380	3,70	0,337	0,126	15,9
85	5100	4,00	0,347	0,136	17,2
140	8400	4,50	0,364	0,153	19,4
210	12600	4,80	0,375	0,163	20,7
245	14700	5,00	0,381	0,170	21,6
280	16800	5,10	0,385	0,173	22,0
300	18000	5,15	0,386	0,175	22,2
370	22200	5,20	0,388	0,177	22,4
435	26100	5,30	0,392	0,180	22,8
1400	84000	6,10	0,419	0,207	26,3
1875	112500	6,20	0,422	0,211	26,7
3200	192000	6,25	0,424	0,212	26,9
6435	386100	6,50	0,432	0,221	28,0
7280	436800	6,70	0,439	0,228	28,9
9080	544800	6,75	0,441	0,229	29,1
12020	721200	6,80	0,443	0,231	29,3
17240	1034400	6,95	0,448	0,236	30,0
20600	1236000	7,00	0,449	0,238	30,2
23060	1383600	7,10	0,453	0,241	30,6
27730	1663800	7,20	0,456	0,245	31,0
30500	1830000	7,25	0,458	0,246	31,3
40520	2431200	7,30	0,460	0,248	31,5
59420	3565200	7,30	0,460	0,248	31,5

Core	PO17				
M_m	95,7	g			
V_p	30,27	ml			
V_v prod. by drainage	23	ml			
S_{wi}	0,240				
OOIP [ml]	23,000	ml			
V_o prod. by sp.imb.	3,5	ml			
S_w after sp.imb.	0,356				
V_o prod by f.imb.	12,7	ml			
$S_{w,e.p.}$	0,775				
$k_{ro,or}$					

Time [min]	Time [sec]	Vo prod	Sw	ΔS_w	RF [%]
0	1	0,00	0,240	0,00	0,0
1	60	0,10	0,243	0,00	0,4
2	120	0,20	0,247	0,01	0,9
2,5	150	0,30	0,250	0,01	1,3
3	180	0,40	0,253	0,01	1,7
4	240	0,50	0,257	0,02	2,2
5	300	0,55	0,258	0,02	2,4
6	360	0,60	0,260	0,02	2,6
7	420	0,70	0,263	0,02	3,0
8	480	0,85	0,268	0,03	3,7
9	540	0,90	0,270	0,03	3,9
11	660	0,95	0,272	0,03	4,1
12	720	1,00	0,273	0,03	4,3
14	840	1,05	0,275	0,03	4,6
15	900	1,10	0,277	0,04	4,8
17	1020	1,15	0,278	0,04	5,0
19	1140	1,20	0,280	0,04	5,2
20	1200	1,25	0,281	0,04	5,4
21	1260	1,30	0,283	0,04	5,7
22	1320	1,40	0,286	0,05	6,1
24	1440	1,45	0,288	0,05	6,3
25	1500	1,50	0,290	0,05	6,5
27	1620	1,55	0,291	0,05	6,7
29	1740	1,60	0,293	0,05	7,0
33	1980	1,65	0,295	0,05	7,2
35	2100	1,70	0,296	0,06	7,4
39	2340	1,75	0,298	0,06	7,6
41	2460	1,80	0,300	0,06	7,8
43	2580	1,85	0,301	0,06	8,0
45	2700	1,90	0,303	0,06	8,3
49	2940	1,95	0,305	0,06	8,5
51	3060	2,00	0,306	0,07	8,7
57	3420	2,05	0,308	0,07	8,9
59	3540	2,10	0,310	0,07	9,1
72	4320	2,15	0,311	0,07	9,3
80	4800	2,20	0,313	0,07	9,6
85	5100	2,30	0,316	0,08	10,0
95	5700	2,35	0,318	0,08	10,2
100	6000	2,40	0,319	0,08	10,4
110	6600	2,45	0,321	0,08	10,7
125	7500	2,50	0,323	0,08	10,9
140	8400	2,55	0,324	0,08	11,1
175	10500	2,60	0,326	0,09	11,3
240	14400	2,75	0,331	0,09	12,0
300	18000	2,80	0,333	0,09	12,2
360	21600	2,90	0,336	0,10	12,6
490	29400	2,95	0,338	0,10	12,8
885	53100	3,10	0,343	0,10	13,5
1400	84000	3,20	0,346	0,11	13,9
3195	191700	3,30	0,349	0,11	14,3
17720	1063200	3,40	0,352	0,11	14,8
27830	1669800	3,45	0,354	0,11	15,0
30530	1831800	3,50	0,356	0,12	15,2
49430	2965800	3,50	0,356	0,12	15,2

Core	PO18				
M_m	97	g			
V_p	29,52	ml			
V_v prod. by drainage	22,6	ml			
S_{wi}	0,234				
OOIP [ml]	22,600	ml			
V_o prod. by sp.imb.	3,6	ml			
S_w after sp.imb.	0,356				
V_o prod by f.imb.	11,3	ml			
$S_{w,e.p.}$	0,739				
$k_{ro,or}$					

Time [min]	Time [sec]	Vo prod	Sw	ΔS_w	RF [%]
0	1	0,00	0,2344	0,000	0,0
1	60	0,10	0,2378	0,003	0,4
2	120	0,20	0,2412	0,007	0,9
3	180	0,30	0,2446	0,010	1,3
4	240	0,40	0,2480	0,014	1,8
5	300	0,45	0,2497	0,015	2,0
7	420	0,60	0,2547	0,020	2,7
8	480	0,80	0,2615	0,027	3,5
9	540	0,85	0,2632	0,029	3,8
11	660	0,90	0,2649	0,030	4,0
14	840	1,00	0,2683	0,034	4,4
15	900	1,05	0,2700	0,036	4,6
16	960	1,10	0,2717	0,037	4,9
17	1020	1,15	0,2734	0,039	5,1
19	1140	1,25	0,2768	0,042	5,5
20	1200	1,30	0,2785	0,044	5,8
21	1260	1,35	0,2801	0,046	6,0
23	1380	1,40	0,2818	0,047	6,2
24	1440	1,45	0,2835	0,049	6,4
25	1500	1,50	0,2852	0,051	6,6
26	1560	1,55	0,2869	0,053	6,9
29	1740	1,60	0,2886	0,054	7,1
31	1860	1,65	0,2903	0,056	7,3
33	1980	1,70	0,2920	0,058	7,5
37	2220	1,75	0,2937	0,059	7,7
41	2460	1,80	0,2954	0,061	8,0
43	2580	1,85	0,2971	0,063	8,2
45	2700	1,90	0,2988	0,064	8,4
47	2820	1,95	0,3005	0,066	8,6
49	2940	2,00	0,3022	0,068	8,8
51	3060	2,05	0,3039	0,069	9,1
57	3420	2,10	0,3056	0,071	9,3
59	3540	2,15	0,3072	0,073	9,5
66	3960	2,20	0,3089	0,075	9,7
72	4320	2,25	0,3106	0,076	10,0
80	4800	2,35	0,3140	0,080	10,4
85	5100	2,40	0,3157	0,081	10,6
90	5400	2,50	0,3191	0,085	11,1
110	6600	2,60	0,3225	0,088	11,5
140	8400	2,65	0,3242	0,090	11,7
155	9300	2,70	0,3259	0,091	11,9
175	10500	2,75	0,3276	0,093	12,2
240	14400	2,80	0,3293	0,095	12,4
300	18000	2,95	0,3343	0,100	13,1
360	21600	3,05	0,3377	0,103	13,5
490	29400	3,10	0,3394	0,105	13,7
885	53100	3,40	0,3496	0,115	15,0
1400	84000	3,45	0,3513	0,117	15,3
7250	435000	3,50	0,3530	0,119	15,5
10610	636600	3,60	0,3564	0,122	15,9
12050	723000	3,60	0,3564	0,122	15,9
30530	1831800	3,60	0,3564	0,122	15,9
49430	2965800	3,60	0,3564	0,122	15,9

Core	PO22				
M_m	97,6	g			
V_p	30,75	ml			
V_v prod. by drainage	23,6	ml			
S_{wi}	0,233				
OOIP [ml]	23,60	ml			
V_o prod. by sp.imb.	7,6	ml			
S_w after sp.imb.	0,480				
V_o prod by f.imb.	7,4	ml			
$S_{w,e.p.}$	0,720				

Time [min]	Time [sec]	Vo prod	Sw	ΔS_w	RF [%]
0	1	0,00	0,233	0,000	0,0
1	60	0,20	0,239	0,007	0,8
2	120	0,30	0,242	0,010	1,3
2,5	150	0,60	0,252	0,020	2,5
3	180	0,70	0,255	0,023	3,0
3,5	210	0,90	0,262	0,029	3,8
4	240	1,00	0,265	0,033	4,2
5	300	1,20	0,272	0,039	5,1
5,5	330	1,30	0,275	0,042	5,5
6	360	1,40	0,278	0,046	5,9
7	420	1,50	0,281	0,049	6,4
7,5	450	1,60	0,285	0,052	6,8
8	480	1,70	0,288	0,055	7,2
9	540	1,80	0,291	0,059	7,6
10	600	2,00	0,298	0,065	8,5
11	660	2,10	0,301	0,068	8,9
12	720	2,20	0,304	0,072	9,3
13	780	2,30	0,307	0,075	9,7
14	840	2,40	0,311	0,078	10,2
15	900	2,45	0,312	0,080	10,4
16	960	2,50	0,314	0,081	10,6
17	1020	2,55	0,315	0,083	10,8
18	1080	2,65	0,319	0,086	11,2
19	1140	2,80	0,324	0,091	11,9
20	1200	2,85	0,325	0,093	12,1
21	1260	2,90	0,327	0,094	12,3
22	1320	3,00	0,330	0,098	12,7
23	1380	3,05	0,332	0,099	12,9
24	1440	3,10	0,333	0,101	13,1
25	1500	3,15	0,335	0,102	13,3
26	1560	3,20	0,337	0,104	13,6
27	1620	3,30	0,340	0,107	14,0
28	1680	3,35	0,341	0,109	14,2
29	1740	3,45	0,345	0,112	14,6
31	1860	3,50	0,346	0,114	14,8
32	1920	3,55	0,348	0,115	15,0
35	2100	3,65	0,351	0,119	15,5
37	2220	3,75	0,354	0,122	15,9
39	2340	3,80	0,356	0,124	16,1
41	2460	3,85	0,358	0,125	16,3
43	2580	3,95	0,361	0,128	16,7
45	2700	4,05	0,364	0,132	17,2
50	3000	4,25	0,371	0,138	18,0
55	3300	4,30	0,372	0,140	18,2
60	3600	4,40	0,376	0,143	18,6
65	3900	4,55	0,380	0,148	19,3
70	4200	4,65	0,384	0,151	19,7
75	4500	4,75	0,387	0,154	20,1
100	6000	4,90	0,392	0,159	20,8
110	6600	4,95	0,393	0,161	21,0
120	7200	5,05	0,397	0,164	21,4
140	8400	5,15	0,400	0,167	21,8
195	11700	5,40	0,408	0,176	22,9
225	13500	5,60	0,415	0,182	23,7
255	15300	5,70	0,418	0,185	24,2
315	18900	5,85	0,423	0,190	24,8
375	22500	5,95	0,426	0,193	25,2
1185	71100	6,95	0,459	0,226	29,4
1485	89100	7,10	0,463	0,231	30,1
1725	103500	7,15	0,465	0,233	30,3
2625	157500	7,35	0,472	0,239	31,1
3045	182700	7,40	0,473	0,241	31,4
4725	283500	7,45	0,475	0,242	31,6
5745	344700	7,50	0,476	0,244	31,8
8685	521100	7,60	0,480	0,247	32,2
11265	675900	7,60	0,480	0,247	32,2
27165	1629900	7,60	0,480	0,247	32,2
60525	3631500	7,60	0,480	0,247	32,2

Core	PO23				
M_m	98,4	g			
V_p	30,46	ml			
V_v prod. by drainage	23,4	ml			
S_{wi}	0,232				
OOIP [ml]	23,40	ml			
V_o prod. by sp.imb.	3,55	ml			
S_w after sp.imb.	0,348				
V_o prod by f.imb.	11,5	ml			
$S_{w,e.p.}$	0,726				

Time [min]	Time [sec]	Vo prod	Sw	ΔS_w	RF [%]
0	1	0,00	0,232	0,000	0,0
2	120	0,10	0,235	0,003	0,4
3	180	0,20	0,238	0,007	0,9
4	240	0,25	0,240	0,008	1,1
5	300	0,30	0,242	0,010	1,3
6	360	0,35	0,243	0,011	1,5
7	420	0,45	0,247	0,015	1,9
8	480	0,50	0,248	0,016	2,1
9	540	0,55	0,250	0,018	2,4
10	600	0,60	0,251	0,020	2,6
11	660	0,65	0,253	0,021	2,8
13	780	0,70	0,255	0,023	3,0
14	840	0,75	0,256	0,025	3,2
15	900	0,85	0,260	0,028	3,6
17	1020	0,90	0,261	0,030	3,8
18	1080	0,95	0,263	0,031	4,1
19	1140	1,00	0,265	0,033	4,3
20	1200	1,05	0,266	0,034	4,5
22	1320	1,15	0,270	0,038	4,9
24	1440	1,20	0,271	0,039	5,1
26	1560	1,25	0,273	0,041	5,3
28	1680	1,30	0,274	0,043	5,6
30	1800	1,35	0,276	0,044	5,8
35	2100	1,45	0,279	0,048	6,2
40	2400	1,55	0,283	0,051	6,6
45	2700	1,65	0,286	0,054	7,1
50	3000	1,75	0,289	0,057	7,5
60	3600	1,85	0,293	0,061	7,9
65	3900	1,90	0,294	0,062	8,1
70	4200	1,95	0,296	0,064	8,3
80	4800	2,05	0,299	0,067	8,8
100	6000	2,20	0,304	0,072	9,4
120	7200	2,25	0,306	0,074	9,6
140	8400	2,30	0,307	0,076	9,8
180	10800	2,50	0,314	0,082	10,7
210	12600	2,60	0,317	0,085	11,1
240	14400	2,70	0,320	0,089	11,5
300	18000	2,85	0,325	0,094	12,2
360	21600	2,90	0,327	0,095	12,4
1170	70200	3,40	0,343	0,112	14,5
1470	88200	3,45	0,345	0,113	14,7
1710	102600	3,50	0,347	0,115	15,0
2610	156600	3,55	0,348	0,117	15,2
14130	847800	3,55	0,348	0,117	15,2
27150	1629000	3,55	0,348	0,117	15,2
60510	3630600	3,55	0,348	0,117	15,2

Core	PO26				
M_m	97,8	g			
V_P	30,65	ml			
V_v prod. by drainage	23,7	ml			
S_{wi}	0,227				
OOIP [ml]	23,70	ml			
V_o prod. by sp.imb.	9,2	ml			
S_w after sp.imb.	0,527				
V_o prod by f.imb.	3,8	ml			
$S_{w,e.p.}$	0,651				

Time [min]	Time [sec]	Vo prod	Sw	ΔS_w	RF [%]
0	1	0,00	0,227	0,000	0,0
1,5	90	0,20	0,233	0,007	0,8
2	120	0,40	0,240	0,013	1,7
2,5	150	0,60	0,246	0,020	2,5
3	180	0,80	0,253	0,026	3,4
3,5	210	1,00	0,259	0,033	4,2
4	240	1,30	0,269	0,042	5,5
4,5	270	1,50	0,276	0,049	6,3
5	300	1,70	0,282	0,055	7,2
5,5	330	1,90	0,289	0,062	8,0
6	360	2,00	0,292	0,065	8,4
6,5	390	2,10	0,295	0,069	8,9
7	420	2,25	0,300	0,073	9,5
8	480	2,40	0,305	0,078	10,1
9	540	2,50	0,308	0,082	10,5
10	600	2,65	0,313	0,086	11,2
11	660	2,80	0,318	0,091	11,8
12	720	2,95	0,323	0,096	12,4
13	780	3,10	0,328	0,101	13,1
14	840	3,20	0,331	0,104	13,5
15	900	3,30	0,334	0,108	13,9
16	960	3,40	0,338	0,111	14,3
17	1020	3,55	0,343	0,116	15,0
18	1080	3,70	0,347	0,121	15,6
19	1140	3,80	0,351	0,124	16,0
20	1200	3,90	0,354	0,127	16,5
21	1260	4,00	0,357	0,131	16,9
22	1320	4,05	0,359	0,132	17,1
23	1380	4,20	0,364	0,137	17,7
24	1440	4,30	0,367	0,140	18,1
26	1560	4,40	0,370	0,144	18,6
27	1620	4,45	0,372	0,145	18,8
28	1680	4,50	0,374	0,147	19,0
29	1740	4,60	0,377	0,150	19,4
30	1800	4,65	0,378	0,152	19,6
32	1920	4,70	0,380	0,153	19,8
34	2040	4,80	0,383	0,157	20,3
36	2160	4,90	0,387	0,160	20,7
38	2280	5,05	0,392	0,165	21,3
40	2400	5,10	0,393	0,166	21,5
45	2700	5,30	0,400	0,173	22,4
50	3000	5,45	0,405	0,178	23,0
55	3300	5,60	0,409	0,183	23,6
60	3600	5,70	0,413	0,186	24,1
65	3900	5,85	0,418	0,191	24,7
70	4200	6,00	0,423	0,196	25,3
75	4500	6,05	0,424	0,197	25,5
80	4800	6,20	0,429	0,202	26,2
90	5400	6,30	0,432	0,206	26,6
100	6000	6,50	0,439	0,212	27,4
110	6600	6,60	0,442	0,215	27,8
120	7200	6,70	0,445	0,219	28,3
150	9000	7,00	0,455	0,228	29,5
180	10800	7,30	0,465	0,238	30,8
210	12600	7,35	0,467	0,240	31,0
290	17400	7,60	0,475	0,248	32,1
450	27000	7,70	0,478	0,251	32,5
1140	68400	8,55	0,506	0,279	36,1
1440	86400	8,70	0,511	0,284	36,7
1680	100800	8,75	0,512	0,285	36,9
2580	154800	8,90	0,517	0,290	37,6
3000	180000	9,00	0,520	0,294	38,0
4680	280800	9,10	0,524	0,297	38,4
7200	432000	9,20	0,527	0,300	38,8
27120	1627200	9,20	0,527	0,300	38,8
60480	3628800	9,20	0,527	0,300	38,8

Core	PO28				
M_m	98,2	g			
V_p	30,56	ml			
V_v prod. by drainage	23,5	ml			
S_{wi}	0,231				
OOIP [ml]	23,50	ml			
V_o prod. by sp.imb.	2,45	ml			
S_w after sp.imb.	0,311				
V_o prod by f.imb.	9,7	ml			
$S_{w,e.p.}$	0,629				

Time [min]	Time [sec]	Vo prod	Sw	ΔS_w	RF [%]
0	1	0,00	0,231	0,000	0,0
3	180	0,10	0,234	0,003	0,4
4	240	0,20	0,238	0,007	0,9
5	300	0,30	0,241	0,010	1,3
10	600	0,35	0,242	0,011	1,5
11	660	0,40	0,244	0,013	1,7
13	780	0,45	0,246	0,015	1,9
16	960	0,50	0,247	0,016	2,1
20	1200	0,55	0,249	0,018	2,3
22	1320	0,60	0,251	0,020	2,6
30	1800	0,65	0,252	0,021	2,8
32	1920	0,70	0,254	0,023	3,0
40	2400	0,75	0,256	0,025	3,2
50	3000	0,80	0,257	0,026	3,4
55	3300	0,85	0,259	0,028	3,6
60	3600	0,90	0,260	0,029	3,8
65	3900	0,95	0,262	0,031	4,0
70	4200	1,00	0,264	0,033	4,3
80	4800	1,05	0,265	0,034	4,5
100	6000	1,10	0,267	0,036	4,7
120	7200	1,15	0,269	0,038	4,9
140	8400	1,20	0,270	0,039	5,1
150	9000	1,30	0,274	0,043	5,5
160	9600	1,35	0,275	0,044	5,7
170	10200	1,40	0,277	0,046	6,0
180	10800	1,45	0,278	0,047	6,2
190	11400	1,50	0,280	0,049	6,4
200	12000	1,55	0,282	0,051	6,6
210	12600	1,60	0,283	0,052	6,8
230	13800	1,65	0,285	0,054	7,0
240	14400	1,70	0,287	0,056	7,2
270	16200	1,80	0,290	0,059	7,7
325	19500	1,90	0,293	0,062	8,1
625	37500	2,00	0,296	0,065	8,5
1345	80700	2,15	0,301	0,070	9,1
1525	91500	2,20	0,303	0,072	9,4
2785	167100	2,40	0,310	0,079	10,2
4800	288000	2,45	0,311	0,080	10,4
27360	1641600	2,45	0,311	0,080	10,4
48960	2937600	2,45	0,311	0,080	10,4

Appendix C

Complementary Data, DMS - Method

Core: PO6

Imbibition Capillary Pressure Data				Secondary Drainage Capillary Pressure Data			
Sw	Sw calibrated	Height above endpoint [m]	Pc [bar]	Sw	Sw calibrated	Height above endpoint [m]	Pc [bar]
0,777	0,777	0,002	-0,968	0,666	0,666	0,002	-1,155
0,761	0,761	0,004	-0,900	0,715	0,715	0,004	-1,086
0,833	0,833	0,005	-0,832	0,764	0,764	0,005	-1,019
0,901	0,901	0,007	-0,765	0,813	0,813	0,007	-0,951
0,861	0,861	0,009	-0,697	0,778	0,778	0,009	-0,884
0,843	0,843	0,010	-0,631	0,778	0,778	0,010	-0,817
0,881	0,881	0,012	-0,565	0,808	0,808	0,012	-0,751
0,913	0,913	0,013	-0,499	0,812	0,812	0,013	-0,686
0,870	0,870	0,015	-0,434	0,779	0,779	0,015	-0,620
0,848	0,848	0,016	-0,369	0,795	0,795	0,016	-0,555
0,838	0,838	0,018	-0,304	0,807	0,807	0,018	-0,491
0,856	0,856	0,019	-0,240	0,824	0,824	0,019	-0,427
0,838	0,838	0,021	-0,176	0,770	0,770	0,021	-0,363
0,745	0,745	0,022	-0,113	0,732	0,732	0,022	-0,300
0,668	0,668	0,024	-0,050	0,739	0,739	0,024	-0,237
0,442	0,442	0,026	0,012	0,763	0,763	0,026	-0,175
0,324	0,324	0,027	0,074	0,803	0,803	0,027	-0,113
0,265	0,309	0,029	0,135	0,854	0,854	0,029	-0,051
0,222	0,299	0,030	0,196	0,873	0,873	0,030	0,010
0,190	0,291	0,032	0,257	0,859	0,859	0,032	0,071
0,167	0,286	0,033	0,317	0,831	0,843	0,033	0,131
0,150	0,281	0,035	0,377	0,772	0,809	0,035	0,191
0,136	0,278	0,036	0,437	0,704	0,769	0,036	0,250
0,122	0,275	0,038	0,496	0,632	0,727	0,038	0,309
0,111	0,272	0,040	0,554	0,484	0,642	0,040	0,367
0,101	0,270	0,041	0,612	0,427	0,609	0,041	0,426
0,093	0,268	0,043	0,670	0,369	0,575	0,043	0,483
0,086	0,266	0,044	0,727	0,304	0,538	0,044	0,541
0,079	0,264	0,046	0,784	0,246	0,504	0,046	0,598
0,069	0,262	0,047	0,841	0,200	0,477	0,047	0,654
0,061	0,260	0,049	0,897	0,166	0,458	0,049	0,710
0,057	0,259	0,050	0,952	0,151	0,449	0,050	0,766
0,055	0,259	0,052	1,007	0,140	0,442	0,052	0,821
0,053	0,258	0,054	1,062	0,124	0,434	0,054	0,875
0,050	0,257	0,055	1,117	0,107	0,423	0,055	0,930
0,043	0,256	0,057	1,171	0,081	0,409	0,057	0,984
0,036	0,254	0,058	1,224	0,066	0,400	0,058	1,037

Core: PO7

Imbibition Capillary Pressure Data				Secondary Drainage Capillary Pressure Data			
Sw	Sw calibrated	Height above endpoint [m]	Pc [bar]	Sw	Sw calibrated	Height above endpoint [m]	Pc [bar]
0,748	0,748	0,001	-0,936	0,716	0,716	0,001	-1,025
0,759	0,759	0,002	-0,867	0,727	0,727	0,002	-0,956
0,788	0,788	0,004	-0,799	0,763	0,763	0,004	-0,888
0,797	0,797	0,005	-0,731	0,800	0,800	0,005	-0,820
0,816	0,816	0,007	-0,664	0,843	0,843	0,007	-0,753
0,813	0,813	0,009	-0,597	0,785	0,785	0,009	-0,686
0,823	0,823	0,010	-0,530	0,802	0,802	0,010	-0,619
0,815	0,815	0,012	-0,464	0,783	0,783	0,012	-0,553
0,813	0,813	0,013	-0,398	0,792	0,792	0,013	-0,487
0,783	0,783	0,015	-0,333	0,769	0,769	0,015	-0,422
0,752	0,752	0,016	-0,268	0,762	0,762	0,016	-0,357
0,694	0,694	0,018	-0,204	0,749	0,749	0,018	-0,292
0,599	0,599	0,019	-0,139	0,758	0,758	0,019	-0,228
0,442	0,442	0,021	-0,076	0,745	0,745	0,021	-0,164
0,298	0,298	0,022	-0,012	0,782	0,782	0,022	-0,101
0,180	0,251	0,024	0,050	0,808	0,808	0,024	-0,038
0,142	0,235	0,026	0,113	0,809	0,809	0,026	0,024
0,122	0,227	0,027	0,175	0,747	0,775	0,027	0,086
0,110	0,222	0,029	0,236	0,681	0,738	0,029	0,148
0,103	0,219	0,030	0,297	0,643	0,717	0,030	0,209
0,096	0,216	0,032	0,358	0,571	0,677	0,032	0,269
0,090	0,214	0,033	0,418	0,494	0,634	0,033	0,330
0,086	0,212	0,035	0,478	0,451	0,610	0,035	0,389
0,083	0,211	0,036	0,537	0,399	0,581	0,036	0,449
0,080	0,210	0,038	0,597	0,347	0,552	0,038	0,508
0,077	0,209	0,040	0,655	0,291	0,521	0,040	0,566
0,075	0,208	0,041	0,713	0,246	0,496	0,041	0,625
0,073	0,207	0,043	0,771	0,212	0,477	0,043	0,682
0,070	0,206	0,044	0,828	0,187	0,463	0,044	0,739
0,067	0,205	0,046	0,885	0,165	0,451	0,046	0,796
0,062	0,203	0,047	0,942	0,144	0,440	0,047	0,853
0,059	0,201	0,049	0,998	0,127	0,430	0,049	0,909
0,054	0,199	0,050	1,053	0,110	0,421	0,050	0,965
0,048	0,197	0,052	1,109	0,093	0,411	0,052	1,020
0,044	0,195	0,054	1,163	0,077	0,402	0,054	1,075
0,044	0,195	0,055	1,218	0,062	0,394	0,055	1,129
0,037	0,192	0,057	1,272	0,047	0,386	0,057	1,183
0,033	0,191	0,058	1,325	0,073	0,400	0,058	1,236

Core: PO9

Imbibition Capillary Pressure Data				Secondary Drainage Capillary Pressure Data			
Sw	Sw calibrated	Height above endpoint [m]	Pc [bar]	Sw	Sw calibrated	Height above endpoint [m]	Pc [bar]
0,848	0,848	0,001	-1,057	0,805	0,805	0,001	-1,065
0,841	0,841	0,002	-0,988	0,800	0,800	0,002	-0,996
0,855	0,855	0,004	-0,920	0,811	0,811	0,004	-0,928
0,838	0,838	0,005	-0,852	0,798	0,798	0,005	-0,860
0,827	0,827	0,007	-0,785	0,788	0,788	0,007	-0,793
0,821	0,821	0,009	-0,718	0,783	0,783	0,009	-0,726
0,827	0,827	0,010	-0,651	0,779	0,779	0,010	-0,659
0,838	0,838	0,012	-0,585	0,789	0,789	0,012	-0,593
0,832	0,832	0,013	-0,519	0,783	0,783	0,013	-0,527
0,859	0,859	0,015	-0,454	0,807	0,807	0,015	-0,462
0,861	0,861	0,016	-0,389	0,826	0,826	0,016	-0,397
0,827	0,827	0,018	-0,325	0,819	0,819	0,018	-0,333
0,766	0,766	0,019	-0,261	0,792	0,792	0,019	-0,269
0,754	0,754	0,021	-0,197	0,809	0,809	0,021	-0,205
0,723	0,723	0,022	-0,134	0,853	0,853	0,022	-0,142
0,571	0,571	0,024	-0,071	0,876	0,876	0,024	-0,079
0,430	0,430	0,026	-0,009	0,804	0,804	0,026	-0,017
0,302	0,358	0,027	0,053	0,755	0,755	0,027	0,045
0,229	0,317	0,029	0,114	0,753	0,753	0,029	0,106
0,203	0,303	0,030	0,175	0,709	0,730	0,030	0,167
0,178	0,289	0,032	0,236	0,650	0,699	0,032	0,228
0,164	0,281	0,033	0,296	0,571	0,658	0,033	0,288
0,149	0,273	0,035	0,356	0,492	0,617	0,035	0,348
0,134	0,264	0,036	0,415	0,442	0,591	0,036	0,407
0,119	0,256	0,038	0,474	0,387	0,562	0,038	0,466
0,107	0,249	0,040	0,533	0,342	0,539	0,040	0,525
0,098	0,244	0,041	0,591	0,307	0,520	0,041	0,583
0,088	0,238	0,043	0,648	0,267	0,500	0,043	0,640
0,082	0,235	0,044	0,706	0,245	0,488	0,044	0,698
0,083	0,235	0,046	0,762	0,240	0,486	0,046	0,754
0,081	0,234	0,047	0,819	0,230	0,480	0,047	0,811
0,079	0,233	0,049	0,875	0,213	0,471	0,049	0,867
0,074	0,231	0,050	0,930	0,194	0,461	0,050	0,922
0,073	0,230	0,052	0,986	0,178	0,453	0,052	0,978
0,069	0,228	0,053	1,040	0,157	0,442	0,053	1,032
0,069	0,228	0,055	1,095	0,137	0,432	0,055	1,087
0,068	0,227	0,057	1,149	0,105	0,415	0,057	1,141
0,087	0,238	0,058	1,202	0,076	0,400	0,058	1,194

Core: PO10

Imbibition Capillary Pressure Data				Secondary Drainage Capillary Pressure Data			
Sw	Sw calibrated	Height above endpoint [m]	Pc [bar]	Sw	Sw calibrated	Height above endpoint [m]	Pc [bar]
0,873	0,873	0,001	-0,976	0,818	0,818	0,001	-1,065
0,746	0,746	0,002	-0,908	0,729	0,729	0,002	-0,996
0,723	0,723	0,004	-0,839	0,711	0,711	0,004	-0,928
0,748	0,748	0,005	-0,772	0,732	0,732	0,005	-0,860
0,758	0,758	0,007	-0,704	0,739	0,739	0,007	-0,793
0,771	0,771	0,009	-0,637	0,750	0,750	0,009	-0,726
0,783	0,783	0,010	-0,570	0,758	0,758	0,010	-0,659
0,804	0,804	0,012	-0,504	0,779	0,779	0,012	-0,593
0,815	0,815	0,013	-0,439	0,789	0,789	0,013	-0,527
0,806	0,806	0,015	-0,373	0,802	0,802	0,015	-0,462
0,783	0,783	0,016	-0,308	0,813	0,813	0,016	-0,397
0,721	0,721	0,018	-0,244	0,827	0,827	0,018	-0,332
0,601	0,601	0,019	-0,180	0,838	0,838	0,019	-0,268
0,448	0,448	0,021	-0,116	0,847	0,847	0,021	-0,204
0,342	0,342	0,022	-0,053	0,852	0,852	0,022	-0,141
0,265	0,315	0,024	0,010	0,855	0,855	0,024	-0,079
0,228	0,303	0,026	0,072	0,839	0,846	0,026	-0,016
0,213	0,297	0,027	0,134	0,825	0,838	0,027	0,046
0,198	0,292	0,029	0,196	0,789	0,817	0,029	0,108
0,187	0,289	0,030	0,257	0,743	0,790	0,030	0,169
0,175	0,284	0,032	0,318	0,684	0,756	0,032	0,229
0,166	0,281	0,033	0,378	0,617	0,716	0,033	0,289
0,152	0,277	0,035	0,438	0,534	0,669	0,035	0,349
0,142	0,273	0,036	0,497	0,461	0,626	0,036	0,409
0,134	0,270	0,038	0,556	0,414	0,598	0,038	0,468
0,126	0,268	0,040	0,615	0,360	0,567	0,040	0,526
0,121	0,266	0,041	0,673	0,314	0,540	0,041	0,584
0,114	0,264	0,043	0,731	0,269	0,514	0,043	0,642
0,108	0,261	0,044	0,788	0,231	0,492	0,044	0,699
0,103	0,260	0,046	0,845	0,204	0,476	0,046	0,757
0,097	0,258	0,047	0,901	0,185	0,465	0,047	0,813
0,093	0,256	0,049	0,957	0,165	0,453	0,049	0,869
0,084	0,253	0,050	1,013	0,138	0,438	0,050	0,925
0,077	0,251	0,052	1,068	0,120	0,427	0,052	0,980
0,070	0,248	0,053	1,123	0,107	0,420	0,054	1,034
0,063	0,246	0,055	1,177	0,096	0,413	0,055	1,089
0,055	0,243	0,057	1,231	0,071	0,399	0,057	1,143
0,046	0,240	0,058	1,285	0,073	0,400	0,058	1,196